Model Based Fault Detection and Isolation Approach for Actuator and Sensor Faults in a UAV

by

Potego J. Madutlela

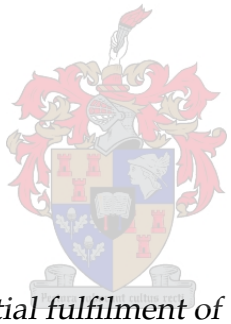

Thesis presented in partial fulfilment of the requirements for the degree of Master of Engineering (Electrical) in the Faculty of Engineering at Stellenbosch University

Supervisor: Dr. JAA. Engelbrecht

December 2021

Stellenbosch University https://scholar.sun.ac.za

Declaration

By submitting this thesis electronically, I declare that the entirety of the work contained therein is my own, original work, that I am the sole author thereof (save to the extent explicitly otherwise stated), that reproduction and publication thereof by Stellenbosch University will not infringe any third party rights and that I have not previously in its entirety or in part submitted it for obtaining any qualification.

Date: December 2021

Copyright © 2021 Stellenbosch University
All rights reserved.

Stellenbosch University https://scholar.sun.ac.za

Abstract

This thesis presents the design and validation of model-based fault detection and isolation (FDI) approach for unmanned aerial vehicles (UAV). In safety-critical systems such as chemical, nuclear plants and passenger aircraft, FDI is typically founded on hardware redundancy. In hardware redundancy, multiple actuators are spatially distributed to localise faults quickly, and sensor measurements are compared for consistency. The primary drawback with hardware redundancy is the increased installation complexity, weight, and costs. With modern computing technologies, model-based FDI offers a cost-effective, iterative and efficient FDI design process, verifiable with high fidelity computer-aided simulation (CAS).

This thesis investigates the application of the Two-Stage Kalman filter (TSKF) to the problem of FDI. The TSKF solves the main deficiencies faced with the augmented state Kalman filter (ASKF), namely, numerical instability in ill-conditioned systems, and computational inefficiency where large parameter vectors are augmented. The TSKF approach utilises two parallel reduced-order KFs to estimate the system state and the parameter vectors separately. The UAV's two rudders are not "isolable" because they produce identical moments. A novel active FDI (AFDI) method is proposed to isolate rudder actuator faults.

The FDI displays high noise sensitivity under the severe Dryden turbulence model, resulting in high false detection and missed detection rates. A novel adaptive technique is proposed to improve the robustness and sensitivity of the FDI. Unlike most methods which rely on a single scaling factor, the proposed adaptation technique employs multiple factors to weight the spread of fault parameter covariance matrix in the direction of flow of information, resulting in selective adaptation.

Fault parameter variations are nonuniform in time and space. A static alarm threshold will induce high false alarms or missed alarms when set to low or too high, respectively. A novel adaptive threshold based on the normalised innovation squared (NIS) is proposed. A Monte Carlo campaign is carried out to validate the FDI while fault-sizes, the aircraft's physical parameters, and disturbances are scattered, each with a distinct mean dispersion. The proposed strategy exhibits high robustness to noise and sensitivity to faults which indicates a reliable FDI.

Stellenbosch University https://scholar.sun.ac.za

Uittreksel

Hierdie tesis beskryf die ontwerp en validering van 'n model-gebaseerde foutopsporing en isolasie ("fault deteciton and isolation (FDI)") tegniek vir onbemande lugvoertuie ("unmanned aerial vehicles (UAVs)"). In veiligheidskritieke stelsels soos chemiese aanlegte, kernkragaanlegte, en passasiersvliegtuie, word FDI gewoonlik gebaseer op hardeware-oortolligheid. Vir hardeware-oortolligheid word verskeie aktueerders ruimtelik versprei om foute vinnig op te spoor, en sensormetings word vergelyk vir ooreenstemming. Die primêre nadeel van hardeware-oortolligheid is die verhoogde installasie-kompleksiteit, gewig en koste. Met moderne rekenaartegnologieë bied model-gebaseerde FDI 'n koste-effektiewe, iteratiewe en doeltreffende FDI-ontwerpproses met 'n hoë betroubaarheid wat bevestig kan word met rekenaargesteunde simulasie.

Hierdie tesis ondersoek die toepassing van die twee-stadium Kalman filter ("two-stage Kalman filter (TSKF)") op die probleem van FDI. Die TSKF los die belangrikste tekortkominge van die uitgebredie-toestand Kalman-filter ("augmented state Kalman filter (ASKF)") op, naamlik numeriese onstabiliteit in swak gekondisioneerde stelsels, en berekeningsondoeltreffendheid waar groot parametervektore bygevoeg word. Die TSKF-benadering gebruik twee parallelle Kalman filters met verminderde orde om die stelseltoestand en die parametervektore afsonderlik af te skat. Die UAV se twee roere ("rudders") is egter nie "isoleerbaar" nie omdat dit hulle identiese draaimoment veroorsaak. 'n Nuwe aktiewe FDI-metode (AFDI) word voorgestel om die roeraktueerderfoute te isoleer.

Die FDI vertoon hoë sensitiwiteit vir geraas vanaf erge turbulensie soos gemodelleer deur die Dryden-turbulensie-model, wat lei tot 'n groot aantal vals deteksies en gemiste deteksies. 'n Nuwe aanpassingstegniek word voorgestel om die robuustheid en sensitiwiteit van die FDI te verbeter. Anders as die meeste metodes wat op een enkele skaalfaktor staatmaak, gebruik die voorgestelde aanpassingstegniek verskeie faktore om die verspreiding van die foutparameterkovariansiematriks in die rigting van informasievloei te weeg, wat lei tot selektiewe aanpassing.

Foutparametervariasies is nie eenvormig in tyd of ruimte nie. 'n Statiese alarmdrempel sal hoë vals deteksies of gemiste deteksies veroorsaak as dit onderskei-

Stellenbosch University https://scholar.sun.ac.za

delik óf te laag óf te hoog gestel is. ’n Nuwe aanpassingsdrempel wat gebaseer is op die genormaliseerde innovasie kwadraat (NIS) word voorgestel. ’n Monte Carlo simulasieveldtog is uitgevoer om die FDI te toets met die foutgroottes, die fisiese parameters van die vliegtuig, en die steurings lukraak gevarieer elk met ’n duidelike gemiddelde verspreiding. Die voorgestelde strategie vertoon ’n hoë robuustheid vir geraas en sensitiwiteit vir foute, wat dui op ’n betroubare FDI.

Stellenbosch University https://scholar.sun.ac.za

Acknowledgements

- I can never express enough gratitude to Dr Japie Engelbrecht. I feel extremely lucky that I was able to have a supervisor who is so dedicated, humble and extremely friendly. Doing an off-campus MEng was always going to be tricky and I could not have asked for a better mentor. Baie dankie Dr Japie!
- I would like to thank my partner in crime, Sung Misong, for her continued love and support. 나는 당신이없는 세상을 상상할 수 없습니다. 내 뼈의 뼈와 내 살의 살. 널 너무나도 사랑해.
- I want to thank my mother for her endless love, her prayers, her dedication and influence on me. I could not have asked for a better super Mom, love you so much.
- I would like to thank the rest of the crew, the A-team, my siblings, Tumishi, Paahla, Makatoloshe, Boledi, Mahlako, Meladi and Baleseng being my family, supportive and hardworking and setting such a good example for me to follow.
- 저를 그렇게 두 팔 벌려 가족으로 맞이해 주신 부모님과 자매님의 사랑과 지원과 친절에 감사드립니다. 제출 후 한국어를 배우겠다고 약속합니다.

Stellenbosch University https://scholar.sun.ac.za

Dedications

To the men and women in Science and Engineering, and to the dissemination of knowledge and eradication of poverty and suffering in the world. To Vaughn Benjamin and to Midnite, thank you for your influence on my life and your contribution to world peace. Ras Vaughn, see you in the morning.

Stellenbosch University https://scholar.sun.ac.za

Contents

Stellenbosch University https://scholar.sun.ac.za

Stellenbosch University https://scholar.sun.ac.za

Stellenbosch University https://scholar.sun.ac.za

Stellenbosch University https://scholar.sun.ac.za

List of Figures

Stellenbosch University https://scholar.sun.ac.za

Stellenbosch University https://scholar.sun.ac.za

Stellenbosch University https://scholar.sun.ac.za

List of Tables

Stellenbosch University https://scholar.sun.ac.za

Nomenclature

Abbreviations and Acronyms

AFDI Active Fault Detection and Isolation

AFTCS Active Fault Tolerant Control System

AMM Autonomous Mission Management

AoA Angle of Attack

AWGN Additive White Gaussian Noise

CA Control Allocation

CAS Computer Aided Simulation

CBM Condition Based Maintenance

CFIT Controlled flight into Terrain

CG Centre of Gravity

CSIR Council for Scientific and Industrial Research

DCM Direction Cosine Matrix

DOF Degree of Freedom

DUKF Dual Unscented Kalman Filter

EA Eigenstructure Assignment, Elevator-Aileron

EKF Extended Kalman Filter

ER Elevator-Rudder

ERSG European Remotely Piloted Aircraft Systems Steering Group

ESL Electronic Systems Laboratory

Stellenbosch University https://scholar.sun.ac.za

ESTEC European Space Research and Technology Centre

FD Fault Detector

FDD Fault Detection and Diagnosis

FDI Fault Detection and Isolation

FDIR Fault/Failure Detection, Isolation and Recovery

FEEP Field Emission Electric Propulsion

FMEA Fault Mode and Effect Analysis

FTC Fault-Tolerant Control

GLR Generalised Likelihood Ratio

GNC Guidance Navigation Control

GPS Global Positioning System

ICAO International Civil Aviation Organisation

IFAC International Federation of Automatic Control

IMM Interacting Multiple Models

IMU Inertial Measurement Unit

ISTAR Intelligence, Surveillance, Target Acquisition, and Reconnaissance

IVHM Integrated Vehicle Health Management

JUKF Joint-Unscented Kalman Filter

KF Kalman Filter

LIP Locked in Place

LOC-I Loss of Control In-Flight;

LoE Loss of Effectiveness

LTI Linear Time-Invariant

LTV Linear Time-Varying

LQR Linear Quadratic Regulator

Stellenbosch University https://scholar.sun.ac.za

MC Monte Carlo

MM Multiple Model

MMST Multiple Model Switching and Tuning

MPC Model Predictive Control

NASA National Aeronautics and Space Administration

PFTCS Passive-Fault Tolerant Control System

PIM Pseudo-Inverse Method

RAX Remote Agent

RMSE Root Mean Square Error

RPV Remotely Piloted Vehicle

RS Runway safety

SACAA South African Civil Aviation Authority

SARP Standards and Recommended Practices

SESAR-JU Single European Sky Air traffic management Research Joint Undertaking

SHM System Health Management

TSKF Two-Stage Kalman Filter

UA Unmanned Aircraft

UAS Unmanned Aerial System

UAV Unmanned Aerial Vehicle

UIO Unknown Input Observer

UKF Unscented Kalman Filter

URTM Unmanned Road Traffic Management

VLL Very Low-level

Stellenbosch University https://scholar.sun.ac.za

Atmospheric disturbance parameters

W_{20}	Wind speed at 20 feet	[m/s]
u_g	Disturbance velocity along the x-axis	[m/s]
v_g	Disturbance velocity along the y-axis	[m/s]
w_g	Disturbance velocity along the z-axis	[m/s]
p_g	Disturbance angular velocity about the x-axis	[rad/s]
q_g	Disturbance angular velocity about the y-axis	[rad/s]
r_g	Disturbance angular velocity about the z-axis	[rad/s]
L_u	Scale length of u_g	[m]
L_v	Scale length of v_g	[m]
L_w	Scale length of w_g	[m]
σ_u	Root-mean-square intensity of u_g	[ ]
σ_v	Root-mean-square intensity of v_g	[ ]
σ_w	Root-mean-square intensity of w_g	[ ]

Times

t	general notation for a continuous time	[s]
t_F	time of fault occurrence	[s]
t_D	time of fault detection time	[s]
t_{dt}	fault detection time (delay)	[s]
t_{it}	fault isolation time (delay)	[s]
k	discrete time instance $t_k = kT$	[ ]
Ts	sampling time	[s]

State variables

α	angle of attack	[rad]
β	sideslip angle	[rad]
ϕ	roll angle	[rad]
θ	pitch angle	[rad]
ψ	yaw angle	[rad]
p	roll rate	[rad/s]
q	pitch rate	[rad/s]
r	yaw rate	[rad/s]
x_n	position north	[m]

Stellenbosch University https://scholar.sun.ac.za

y_e	position east	[m]
z_d	position down	[m]
h	altitude	[m]
u	longitudinal velocity	[m/s]
v	lateral velocity	[m/s]
w	normal velocity	[m/s]
V_T	total airspeed	[m/s]

Surfaces and engine controls input

δ	collective representation of all control inputs	[ ]
δ_{Er}	right elevator deflection	[rad]
δ_{El}	left elevator deflection	[rad]
δ_{Ar}	right aileron deflection	[rad]
δ_{Al}	left aileron deflection	[rad]
δ_{Rr}	right rudder deflection	[rad]
δ_{Rl}	left rudder deflection	[rad]
δ_{prop}	engine propulsion setting	[ ]

Aircraft parameters

m	aircraft mass	[kg]
$\boldsymbol{I}$	Moment of inertia	[kg.m^2]
I_{xx}	Moment of inertia about the roll axis	[kg.m^2]
I_{yy}	Moment of inertia about the pitch axis	[kg.m^2]
I_{zz}	Moment of inertia about the yaw axis	[kg.m^2]
I_{xy}	Roll and pitch product of inertia	[kg.m^2]
I_{xz}	Roll and yaw product of inertia	[kg.m^2]
I_{zy}	Pitch and yaw product of inertia	[kg.m^2]
S_{ref}	wing platform area	[m^2]
b_{ref}	wing span	[m]
$\bar{c}$	mean aerodynamic chord	[m]
AR	Wing Aspect ratio	[ ]
e	Oswald Efficiency Factor	[ ]

Coordinate systems

Stellenbosch University https://scholar.sun.ac.za

$\mathcal{F}_b = (x_b, y_b, z_b)$ body-axes coordinate system . . . . . [ ]

$\mathcal{F}_s = (x_s, y_s, z_s)$ stability-axes coordinate system . . . . . [ ]

$\mathcal{F}_w = (x_w, y_w, z_w)$ wind-axes coordinate system . . . . . [ ]

$\mathcal{F}_{NED} = (x_E, y_E, z_D)$ North-east-down coordinate system . . . . . [ ]

Universal and atmospheric constants

$g = \quad 9.81\,\mathrm{m/s^2}$

$\rho = \quad 1.1323\,\mathrm{Km^{-3}}$

$p_0 = \quad 1013 \times 10^2\,\mathrm{Nm^{-2}}$

$a = \quad -6.5 \times 10^{-3}\,\mathrm{K/m}$

$T_0 = \quad 288.15\,\mathrm{K}$

$R = \quad 287.3\,\mathrm{m^2K^{-1}s^{-2}}$

Stellenbosch University https://scholar.sun.ac.za

Chapter 1

Introduction

This chapter begins with a brief introduction of unmanned aerial vehicles (UAVs) and their applications. Next, the chapter presents a brief overview of past, current, and emerging advancements and innovations in UAV applications. New challenges facing UAVs are discussed to highlight the need for the work presented in this thesis. The subject of this study is then introduced, research objectives are defined, and a detailed literature review of previous research in related fields is presented. The chapter concludes with an overview of the research project and an outline of how the thesis is structured.

1.1 Unmanned Aerial Vehicles

Unmanned aerial vehicles (UAVs) have gained unprecedented levels of popularity and attention in various sectors over the past few decades. UAVs are a subset of unmanned systems (US), which are artificially powered vehicles operating either in air, maritime or ground, and more importantly, *do not carry a human operator onboard*. The term UAV refers both to fully autonomous aerial vehicles (that operate on their own) and remotely piloted vehicles (RPVs).

Since their inception, the terminologies concerning UAVs have evolved along with the aircraft. In the context of formal definitions, one of the earliest references to UAVs came out of the Protocol of 15 June 1929, which was an amendment to the Paris Convention of 13 October 1919, amending Article 15 to include "aircraft without a pilot". At the Convention on International Civil Aviation of 1944, which replaced the Paris Convention, the new phrase "pilotless aircraft" was adopted. Today, there are several definitions concerning UAVs from different contexts, which present new

Stellenbosch University https://scholar.sun.ac.za

challenges. Some definitions may be interpreted to classify recreational toy drones in the same category as state-of-the-art military UAVs. From a legislative viewpoint, it is clear that different regulations should apply to recreational drones than to military or application UAVs. The burden of establishing consistency in definitions has forced some regulators to define what UAVs are not, in addition to defining what they are [6]. Generally, the term UAV does not include unmanned free balloons or model aircraft used for recreational purposes and whose flight cannot be managed in real-time.

A broader and recent definition is found in documents from the International Civil Aviation Organisation (ICAO), namely unmanned aircraft (UA), defined as "an aircraft which is intended to operate with no pilot on board" [6]. Another common term is unmanned aircraft system (UAS) which is an umbrella term encompassing the aircraft and its supporting systems, such as the onboard and ground flight equipment, sensors, electronics, software, ground-stations, controls, and communications systems.

Several organisations such as the ICAO, European Organisation for the Safety of Air Navigation (Eurocontrol), European Aviation Safety Agency (EASA), and others have dedicated serious efforts to establish harmony and uniformity in the terminologies mentioned above, mainly to establish internationally accepted regulations based on Standards and Recommended Practices (SARPs). However, today the terms UA, UAV, UAS, RPV and sometimes drone, are often used interchangeably.

Due to their versatility, UAVs have historically been mainly directed at military application. Indeed, the military sector has spearheaded UAV developments for many decades since their introduction. This is primarily due to the high costs associated with UAV acquisition, operation and maintenance. Moreover, the loss of UAVs has historically been more accepted than the loss of passenger aircraft and aircrew. Removing the human component from the aircraft has been indispensable in enabling the earliest and main applications of UAVs, namely, undertaking "dull, dirty and dangerous"[7] or D^3 missions. Dull refers to long-endurance operations that can last for several days, and perhaps in the future, for weeks or even months. Dirty refers to hazardous assignments such as inspecting chemical agents or post-disaster sites, which presents known health risks. Dangerous refers to deployments to environments with known exposures and risks of immediate loss of life (e.g. military missions). Modern conflicts have demonstrated the utility of UAVs in carrying out these operations.

Stellenbosch University https://scholar.sun.ac.za

In addition to enabling D^3, the absence of aircrew in controlled flight has enabled exploring other uses in UAVs, which would have otherwise been riskier, unsafe, expensive or impossible with human-crewed aircraft. The requirements for an onboard pilot results in additional design constraints, requiring the aircraft to have a minimum size, weight, human safety features, and some level comfort during flight, to mention a few. These design requirements are absent in UAVs, which has extraordinarily expanded capabilities and reach of aviation. Other advantages of UAVs over their piloted counterparts include the flexibility of design, manoeuvrability, reduced cost and time to manufacture, operate and maintain air vehicles [8] and the ability to operate air vehicles in urban or remote environments. As such, the fascination with UAV continues to grow amongst researchers, manufactures and operators. With recent technological advancements, the spectrum of UAV application is expected to continue to expand. UAVs have already found utilisation in a wide range of applications, including:

- Media and filming
- Scanning and analysis of crop yields in agriculture.
- Inspection of construction sites and activities
- Transportation and delivery of goods
- Monitoring and analysis of forests and wildlife
- UAS Road Traffic Management (URTM)
- Intelligence, surveillance, target acquisition, and reconnaissance (ISTAR)
- Inspections of marine activities, power lines, mines or dams.
- Search and rescue operations.
- Aerial imaging and mapping of environments and systems.
- Customs and Border Protection (CBP)

While D^3 originated from military applications where UAVs proved more efficient than piloted aircraft, UAVs are displaying their D^3 qualities in civilian airspace where they are performing increasingly complex assignments autonomously in unknown environments.

1.2 The Future and UAVs

The application of UAVs in the civilian airspace is still a subject of much ongoing research. Due to their versatility, there is growing interest to use

Stellenbosch University https://scholar.sun.ac.za

UAVs or drones to drive innovation, new services and business models, and global economic growth. Currently, Europe is spearheading global efforts to establish UAV operational plans, standardisation and policy initiatives. The European Remotely Piloted Aircraft Systems Steering Group (ERSG) produced a UAV integration roadmap in 2013 entitled "*Roadmap for Integration of Civil Remotely Piloted Aircraft Systems into the European Aviation System*"[9]. In the same year, the U.S Federal Aviation Administration produced their UAV roadmap entitled "*Integration of Civil Unmanned Aircraft Systems in the National Airspace System*"[10]. These roadmaps aimed to establish standard procedures and guidelines to ensure safe and regulated deployment of UAVs into the respective airspace system.

The Single European Sky Air traffic management Research Joint Undertaking (SESAR-JU) was established in 2015 for the purpose of developing new European air traffic management (ATM) systems and establishing a blueprint to enable safe, secure and environmentally friendly operation of UAVs in low-level airspace. Recent developments in SESAR-JU includes the U-space Blueprint [11] and European ATM Master Plan [12]. In summary, U-space institutes a structured approval plan for operating UAV services in the European airspace. The approval process is split into four stages, starting with the definition or conception of UAV services, and ending at a fully integrated UAV operation. U-space works by digitising and automating processes and tools to facilitate safe and secure integration of drones into airspace, including very low-level (VLL) drone operations. On the other hand, the European ATM Master Plan focuses on providing guidelines on key drone-related research and development (R & D) activities that must be prioritised to support the expansion of UAV markets and align with the integration plans.

The business benefits of establishing regulated UAV airspace are obvious. Major technology companies like Google and Amazon have initiated projects to investigate the integration of delivery drones in the civilian airspace, extending to the consumer's doorstep[13–15]. By leveraging the latest technological advancements in computing, communication systems, and connectivity of network systems, UAVs could transform the modern world and available services.

Local research on UAV operation includes a study by Ingham in 2008[16], who proposed a roadmap for operating UAVs in the South African airspace in his PhD thesis at Stellenbosch University. In 2010, Maneschijn[17] investigated frameworks for carrying out airworthiness certification of UAV's for their safe integration into civilian airspace, in his PhD thesis at Stellen-

Stellenbosch University https://scholar.sun.ac.za

Table 1.1: UAVs vs Piloted Aircrafts Mishap Rate per 100, 000 hrs

Aircraft	Cumulative Mishap Rate
Pioneer	334
Hunter	55
Predator	32
General Aviation Aircrafts	1
Regional/Commuter Airliners	0.1
Larger Airliners	0.01

bosch University. In terms of local legislation, the South African Civil Aviation Authority (SACAA) has issued regulations for operating a"Remotely piloted aircraft", "Toy aircraft" and "Model aircraft" [18] which the SACAA has acknowledged may require reworking.

1.3 Reliability Considerations for UAVs

Today, there are still several challenges that remain unresolved before a routine safe integration of UAVs into civilian airspace can be realised. In addition to cost, supply-and-demand issues, a major stumbling block facing UAVs is their history of poor reliability [4] and the lack of accepted regulations and standards for their certification, integration and safe operation. In particular, the lack of airworthiness certification for UAVs has been a primary impediment [16, 17]. This has prevented a routine integration of UAVs to operate within unsegregated civilian airspace, despite the apparent benefits. Other issues for affecting progress are ethical impact and social acceptance, lack of legal framework, including criminal or civil liability and insurance, which are all a subject of ongoing research.

The U.S Office of Defense investigated the reliability of UAVs in a report released in 2005 [19], which reported that 17% of UAV accidents were attributable to human factors. The remaining 83% of accidents were due to faults in the propulsive system, control surfaces, sensors, or extreme environmental phenomena. The study also reported on class A accidents ("*significant aircraft damage or total loss*") per 100,000 hours of flight for UAVs. The data is reproduced in Table 1.1, with corresponding data for passenger aircraft tabled alongside for comparison. As seen from the comparative data, the reliability of UAVs requires improvement when compared to passenger aircraft. While UAVs and passenger aircraft typically undertake entirely different assignments, it is noteworthy that Pioneer

Stellenbosch University https://scholar.sun.ac.za

suffers 33 000% more mishaps than the safest airliner aircraft. References [17, 19–24] can be consulted for historical data on aircraft accidents.

Although passenger aircraft are more reliable than UAVs, similar reliability and safety concerns have been highlighted in commercial aviation. From analysing accident data on scheduled commercial flights, ICAO specified three accident categories that they classified as high-risk, to be prioritised in their Global Aviation Safety Plan (GASP) for 2017 - 2019. The three high failure categories are

- Runway safety (RS) related events
- Controlled flight into terrain (CFIT).
- Loss of Control In-Flight (LOC-I); and

The charts in Figure 1.1 show statistical data relating to these high-risk accident categories until 2019. Accidents attributed to RS accounted for almost 50 % of the total accidents while LOC-I accounted for just less than 40 %. In particular, the trends show that LOC-I accidents have not decreased in many years. This observation and similar observations with UAV failure rates have led to this conclusion; to use available computing and aviation technologies to recover aircraft in these accident situations automatically.

Thus, reliability, maintainability, recoverability, and survivability are to be among the primary focus areas when designing future aerial vehicles. The U.S Department of Defense's UAVs Roadmap 2005-2030 calls for new designs focusing on self-repairing, smart flight-control systems. Developing self-repairing control systems is probably the most critical milestone in aerial vehicles attaining total and sustainable autonomy. Such vehicles should have capabilities to be deployed to unfamiliar, unexpected, or hazardous environments, and complete their mission despite suffering component failure, or even a wilful attack. A key enabler towards achieving this level of autonomy will be the development of adaptable control systems which take into account the *health status* and performance capabilities of the aircraft in real-time, adjust and adapt the control system to maintain some minimum performance and safety.

Robust control has been effectively applied to a wide class of control systems to explicitly deal with uncertainties, bounded modelling errors and system faults. However, severe system or component failures, such as a damaged wing or stuck (locked-in-place) control surface in a UAV, can drastically alter the aircraft's behaviour and render it uncontrollable, leading to more catastrophic failures. Thus, new and enhanced enabling tech-

Stellenbosch University https://scholar.sun.ac.za

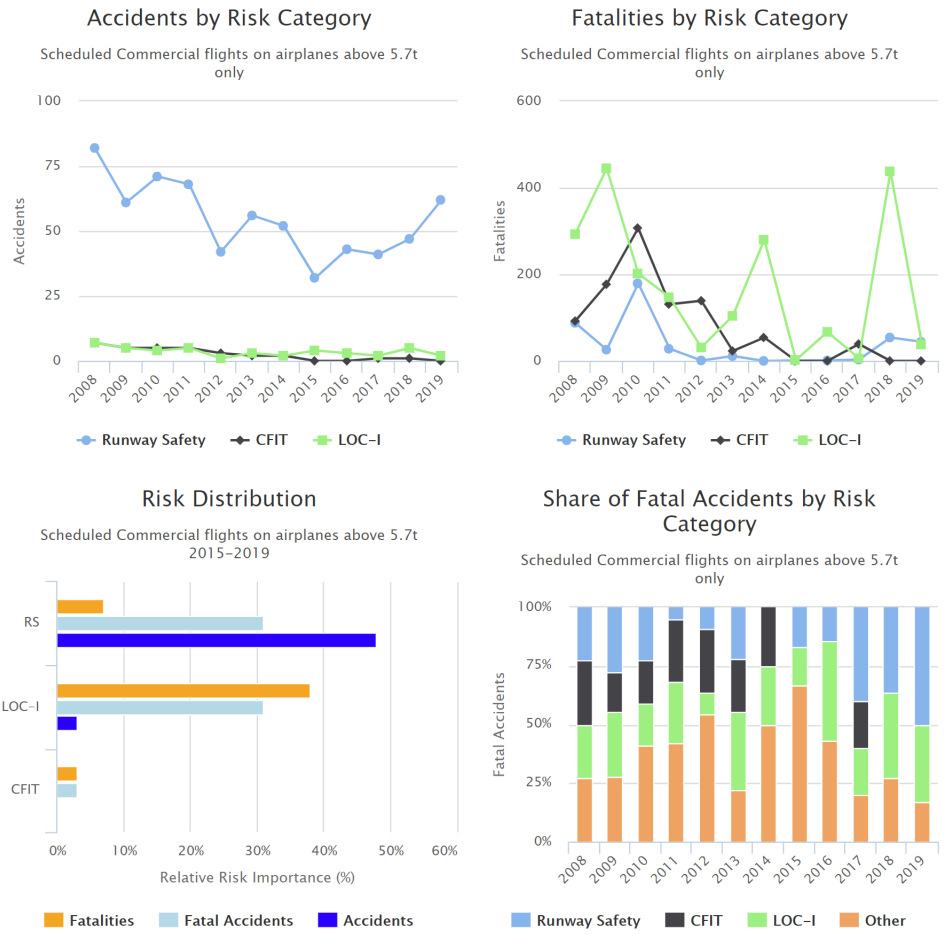

Figure 1.1: Commercial flights accident and fatality statistics from 2008 to 2019. Source: Adapted from [1]

nologies and control systems are required to realise "*self-repairing, smart-control systems*". Fault Tolerant Control (FTC) is one such enabling technology. FTC employs reconfigurable and adaptive control laws that automatically detect and accommodate faults to ensure the continued safe operation of the system in the presence of some *manageable* system faults.

1.4 Fault Tolerant Control

FTC is an emergent sub-component of control systems, which focuses on tolerance to systems faults. The main idea in FTC is to develop fault adaptation control laws designed to maintain intended or safe operation of the

Stellenbosch University https://scholar.sun.ac.za

controlled system, typically at reduced performance levels, rather than failing entirely in the event that some part of the system is faulty. In aerial vehicles, faults may result from wear and tear of old equipment, loss of communication, sensor failures, damage from accidents, or the interaction with the environment such as dust, severe wind gusts or icing [21, 22, 24].

The most effective FTC systems (FTCS) include a real-time "*system health* " monitoring functionality for fault detection and isolation (FDI). The primary objective of the FDI system is to automatically *detect* faults as soon as they occur, *isolate* their location, source or type, thereby enabling a supervisory control system to minimise or eliminate their effects on the overall system, to avoid loss of control or a more catastrophic failure. The FDI provides fault information to the FTC system, which reconfigures the controller to accommodate and adapt to the system's faulty conditions.

Fault tolerance has historically been founded on hardware (equipment) redundancy, especially for safety-critical systems such as chemical, nuclear plants or passenger aircraft. In this approach, additional (secondary, tertiary, etc.) spare equipment and software are installed in parallel with the primary, such that in the event of a failure of the primary, the control system may switch to the secondary for fault tolerance. Hardware redundancy can be extremely effective; however, its main drawback is increased installation complexity, cost, weight, and maintenance, which makes it unsuitable for small, low-cost UAVs.

1.5 Previous Research at Stellenbosch University

The Electronic Systems Laboratory (ESL), which operates at Stellenbosch University has been engaged in research on advanced control systems in UAVs and passenger aircraft. For research on Fault Tolerant Control, the ESL has utilised the Meraka modular UAV as a testbed, amongst other UAVs. The Meraka UAV was developed by Meraka Institute of the Council for Scientific and Industrial Research (CSIR) and is fitted with an autopilot developed at Stellenbosch University, to carry out research focusing mainly on Single Fault Survivability (SFS)[25].

The Meraka UAV is especially suited for FTC due to its intrinsic redundancy built into its geometry and control surfaces configuration. The UAV has eight control surfaces, namely, two elevators, two flaps, two rudders and two ailerons.

All control surfaces can be controlled independently. The right and left ailerons/elevators can be deflected up or down independently while the

Stellenbosch University https://scholar.sun.ac.za

Figure 1.2: Potograph of the Meraka UAV

left and right rudders can be deflected right or left independently. The Meraka UAV design also allows for a pitching moment to be produced with ailerons and a rolling moment with elevators, a property which offers further redundancy. Due to being located above the centre of gravity, any rudder deflection will produce a pitching moment, in addition to rolling and yawing. The redundant configuration of the Meraka UAV can be easily comprehended by examining its geometry, as seen in Figure 1.2.

Fault Tolerant Control research at Stellenbosch University originated with the focus to develop tools and architectures for an FTC system capable of rescuing an aircraft from undesirable flight conditions and component failures. Figure 1.3 shows the five-layer FTC architecture developed at Stellenbosch University, which is described in reference [26]. This thesis contributes to the Physical Aircraft Layer, whose purpose includes system identification for the health monitoring of the physical aircraft.

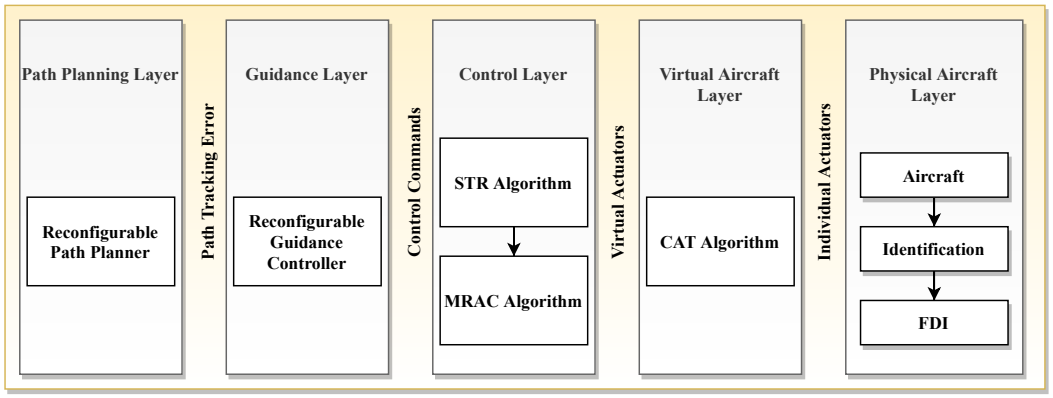

Figure 1.3: Fault Tolerant Control (FTC) architecture

Some FDI and FTC procedures have already been proposed and successfully validated with flight tests by various students at Stellenbosch

Stellenbosch University https://scholar.sun.ac.za

University. In 2011, [27] Willem Basson utilised Adaptive Control to recover longitudinal stability in an aircraft following a damage-induced shift in the aircraft's centre of gravity. In 2011, Lionel Basson [28] presented his work on a control allocation system, which focused on minimising the impact of faults on the reconfiguration of the guidance, navigation and control (GNC) system in the FTC architecture described above. The approach relied on minimising the difference between the desired and achievable aircraft performance parameters. Pietersen and Appel [26, 29] both investigated UAV parameter estimation using recursive least-square approaches for FTC. However, these works did not investigate the detection or isolation of faults.

Odendaal [3] presented his work on fault isolation by utilising the multiple-model (MM) approach. The method required a bank of nine extended Kalman filters, with each responsible for the isolation of each control surface. Multiple-model approaches have high computational requirements. However, modern computing technologies allowed MM approaches to gain popularity. The parallel structure of the MM framework provides an intrinsic fast isolation property but requires further statistical analysis of each filter to isolate faults. Recently in 2017, Hugo [30] successfully implemented an autonomous landing design for a UAV after a partial loss of the wing, horizontal and vertical stabilisers.

1.6 Research Objectives

The primary objective of this thesis is the design and validation of model-based FDI approaches for UAVs. The complete design of an FTCS is outside the scope of this thesis. Rather, the research focuses on developing a reliable FDI design, allowing a reliable FTCS design. This study only considers faults occurring in sensors and actuators. Such faults can be realistically modelled, resulting in a convenient FDI design that can be cheaply and rigorously tested in computer simulations before prototyping or implementation. The FDI techniques presented are based on the mathematical analysis of the aircraft's dynamic model. Catastrophic failures such as structural damage may render the UAV uncontrollable, in which case special emergency landing procedures such as by parachute have been proposed for UAV recovery[31, 32]. Liu et al. proposed a method for unpowered emergency landing of a UAV by spiral drop after engine failure [33]. Catastrophic structural failures in the airframe are not considered in this thesis.

Stellenbosch University https://scholar.sun.ac.za

In UAVs, actuators are used to deflect the elevators, ailerons, flaps, and rudders for flight control. Among known actuator faults, the loss of effectiveness (gain-loss), offset (bias) and locked-in-place (stuck), are among the most common faults in actuators. Therefore this study focuses on the detection and diagnosis of actuator bias, locked-in-place (LIP) and loss of effectiveness (gain-loss) faults in actuators. The FDI strategy developed is highly robust and capable of detecting multiple actuator faults of any magnitude within deflection saturation limits, including faults occurring concurrently. The FDI algorithm is formulated within the Two-Stage Kalman Filter. The algorithm is further extended to enable the detection of sensor faults by extracting fault signatures from the innovation sequence of the TSKF.

In larger passenger aircraft, fault tolerance is typically based on hardware redundancy, where multiple actuators, computers and sensors are deployed in parallel, in a duplex, triplex or higher redundancy configuration to function in parallel or as backups. In this approach, identical or related actuators are spatially distributed in a strategic way to localise faults quickly, and sensor measurements are compared for consistency. However, an FTCS design in small, low-cost UAVs should not significantly increase the number of actuators, computing devices, sensors, design or installation complexity involved. For this reason, this thesis considers model-based FDI.

Even without hardware redundancy, a reliable FDI should detect faults quickly and accurately. This is particularly important in aerial vehicles where system states can change significantly in very short periods. Moreover, different faults produce different effects which must be dealt with in specific ways. Parametric faults such as a shift in the centre of mass can be addressed with robust feedback control. However, a stuck actuator represents a discrete fault, which affects system dynamics and changes the system mode or behaviour differently than parametric faults. Actuator faults in a UAV must be detected and isolated very quickly, and detection must be done among the continuous mode changes to ensure realtime control reconfiguration and recovery of the aircraft. The fast isolation of faults is in aerial vehicles is especially critical as recovery must be almost immediate.

Moreover, it is typically required to maintain the aircraft close to some desired or equilibrium trajectory. Actuator faults can significantly upset the aircraft's trajectory and nudge it into highly nonlinear behaviours, which may cause linearly derived algorithms to fail. In this study, a linear

Stellenbosch University https://scholar.sun.ac.za

analysis of the Meraka UAV reveals open-loop instability in the phugoid and spiral modes as well as heavy coupling between the longitudinal and lateral motions. If actuator faults are not detected and isolated very quickly, the aircraft may assume highly nonlinear motions, resulting in reduced control capabilities. A reliable and fast FDI system is required to enable the FTCS to respond swiftly to faults and maintain vehicle control. Moreover, unaccommodated faults cause unnecessary structural loads during flight, which is undesirable for energy efficiency, aircraft life-cycle and reliability. FDI allows the opportunity to power-down failed components or optimise flight set-points, which can reduce structural load and improve energy efficiency, thereby contributing to the European Vision 2020 directives aimed at "greening" aircraft [2].

The design considerations and limitations relating to the proposed FDI approach are as follows.

- The FDI algorithms developed should be simple enough to implement in small, low-cost UAVs.
- The phugoid and spiral modes of the Meraka UAV show open-loop instability. Unaccounted actuator faults will degrade closed-loop capabilities. Therefore, faults must be isolated quickly to ensure fault recovery and stability.
- Additional redundant computing devices, actuators, and sensors will increase the overall weight of the aircraft, which is undesirable for small UAVs. Instead of hardware redundancy, this study considers analytical redundancy, which relies on the mathematical characterisation of the UAV and only requires the standard avionics already available for guidance, navigation and control (GNC) to realise FDI.
- Although the positions of the actuators are not measured, their fault statuses are tracked in realtime.
- The UAV is equipped with an autopilot which has a masking effect on faults. An active FDI approach is developed to isolate masked faults.
- The abrupt nature of actuator faults induce the strongly coupled behaviour between the longitudinal and the lateral axes. Moreover, the redundant control surfaces have identical effects in the moments produced, which makes fault isolation in these surfaces nontrivial. However, the FDI developed can distinguish between faults occurring in the left or right control surfaces.

Stellenbosch University https://scholar.sun.ac.za

- The two rudders always produce identical moments due to being mathematically equivalent. To distinguish between faults in the right and left rudder faults requires active FDI strategies, which are developed in this study.
- The FDI proposed in this thesis can handle multiple faults, and by making simple changes on parts of the analytical model, the FDI approach can handle different classes of faults, namely, bias, LoE, and LIP actuator faults. Thus, the FDI can be tuned for varying systems and classes of faults by basic adjustments in the model definition.
- In real-life application, the KF state can be affected by the intermittent loss of sensor signals or spurious data. To add resilience and robustness to the FDI algorithm, sensor fault detection is incorporated into the FDI design. Sensor faults are detected, regardless of type, so that intermittent, unreliable sensor measurements can be discarded to maintain accurate state estimates.
- Faults are by nature hidden or absent in the system until they appear abruptly. Thus model-based FDI is a self-contradictory objective to find an algorithm that tracks slow-changing and fast-changing parameters at the same time. Within the KF algorithm, this translates to selecting an additive covariance matrix for the fault parameter, that is neither too high nor too low. Solutions relying on the optimisation of the two requirements may not always result in a reliable FDI where fast decisions are needed. In this thesis, several adaptive techniques are incorporate into the FDI to ensure both sensitivity and robustness, based on the level of variation in the fault parameters.

Fault information computed by the FDI is not instantaneously available to the FTCS for control reconfiguration. The FDI requires a certain amount of time to detect, isolate and reconstruct occurring faults. It is thus necessary to define some parameters to evaluate the reliability, accuracy and the time taken by the FDI to isolate faults. Performance indices are defined to evaluate the performance of the proposed FDI strategy.

The previous FDI approaches proposed at ESL reviewed in preceding sections are incapable of handling multiple-concurrent faults (faults occurring at the same time). More precisely, these approaches assume a single fault at any given time and require that the initial fault be rectified before having the ability to detect the next fault. Indeed most techniques available do not attempt to isolate multiple faults concurrently. The FDI techniques presented in this thesis can isolate multiple faults occurring

Stellenbosch University https://scholar.sun.ac.za

concurrently. Moreover, only two filters are required to track all the faults in the UAV, which is advantageous from a computing and hardware point of view.

1.7 Research Methodology

This research considers the problem of FDI for small-sized UAVs. The project begins with a rigorous review of existing FDI and FTC methods commonly encountered in literature. From among the FDI methods investigated, model-based FDI, also called analytical redundancy, is preferred due to meeting the main objectives of this research. Model-based FDI offers opportunities for a low-cost, iterative design and testing in a simulated environment, without significant hardware upgrades or installations, which would have been required in the case of hardware redundancy. Without additional hardware, there is no added weight to the existing UAV. The FDI design can be cheaply tested in a simulated environment as many times as necessary before implementation.

The main drawback with model-based FDI is that a highly accurate mathematical model of the aircraft is required. A six-degrees-of-freedom (6-DoF) nonlinear model of the Meraka UAV is developed in MATLAB® and Simulink® software packages, as a simulated testbed for the FDI. Dryden turbulence models, discrete gusts, and wind shears are added to the nonlinear model to mimic real-world disturbances. A linearised version of the UAV model is also developed to enable linear FDI design.

There are notable differences between the aircraft model developed in this study, and the classical aircraft model formulation. Typically, fixed-wing aircraft have multiple elevators and ailerons to the left and right of the fuselage. However, their mathematical description usually combines the effects of two or more related control surfaces to create some virtual control surface equivalent. For example, the effect of the two right and left elevators on the pitching moment are often combined to produce one virtual elevator effect as follows:

$$\bar{q}S_{ref}\bar{c}C_{m_{\delta_E}}\delta_E = \bar{q}S_{ref}\bar{c}C_{m_{\delta_{E_r}}}\delta_{E_r} + \bar{q}S_{ref}\bar{c}C_{m_{\delta_{E_l}}}\delta_{E_l} \tag{1.7.1}$$

Assuming equal contribution due to the aircraft's symmetric design $C_{m_{\delta_{E_r}}} = C_{m_{\delta_{E_l}}} = \frac{C_{m_{\delta_E}}}{2}$. The classical formulation, which is on the LHS of Equation (1.7.1), does not distinguish between pitching the moment contributed by the right and left elevators separately, and is therefore not suitable for the FDI and FTC problem. A split-surface model, having the form

Stellenbosch University https://scholar.sun.ac.za

on the RHS of Equation (1.7.1) is developed in this thesis to ensure that moments induced by the left and right control surfaces are monitored separately and are distinguishable in real-time. For example, a negative (upward) deflection in the right aileron will not only cause a positive rolling moment but will also generate a small positive pitching moment. On the other hand, the same negative (downward) deflection in the left aileron will also generate a positive rolling moment, but produce a negative pitching moment in contrast. These subtle distinctions in aerodynamical effects produced by each individual control surface are necessary to permit their isolation based on the mathematical characterisation.

The FDI strategy developed in this thesis utilises Kalman filtering (KF) techniques to estimate system states and the fault parameters jointly. Augmenting the fault parameters into the state vector will significantly increase the computational load requirements and may cause numerical problems in ill-conditioned systems. In the proposed approach, this problem is eliminated by estimating system states and fault parameters separately in two parallel coupled Kalman filters, rather than by augmenting the fault parameter into the state vector. This approach is called the Two-Stage Kalman Filter (TSKF). Chapter 4 discusses the advantages of the TSKF over the Augmented KF (AKF) approach in greater detail.

The control surfaces induce symmetric and identical moments that are indistinguishable with a direct application of a single TSKF. In model-based FDI, it is necessary to consider the concepts of detectability and isolability. When parameters can be jointly computed and isolated using one mathematical model, it is said that they are identifiable, or isolable by that model. In references [34, 35] detectability and isolability were derived for the Unknown Input Observer formulation based on the concepts of observability and controllability.

For the case of the Meraka UAV studied in this thesis, the isolability condition is not satisfied for all control surfaces when a single TSKF is utilised to estimate all fault parameters. When all faults are not isolable, multiple estimators may be utilised. Therefore, the FDI problem is split into two separate filters, which in this thesis, are termed as the elevator-aileron (EA) filter and an elevator-rudder (ER) filter. By applying the EA and ER filters in parallel, all the control surfaces become isolable at all times. The EA filter is capable of tracking and isolating all faults occurring in the elevators and ailerons, including multiple faults occurring at the same time. The ER filter is selected purposely to ensure fault isolation of the left and right rudders using active FDI techniques.

Stellenbosch University https://scholar.sun.ac.za

Unlike with the elevators and ailerons, all the moments generated by the right and left rudders are always identical, making it challenging to isolate rudder faults by only tracking their effects on the moments. This is due to the two rudders being equivalent in their mathematical modelling. To achieve rudder fault isolation, active FDI (AFDI) algorithms are developed. In the case of a bias fault, the nonlinear relationship between rudder deflection and pitching moment is assessed online to extract fault signatures. Due to the rudders being located above the centre of mass on the Meraka UAV, any rudder deflection in any direction will cause a positive pitching moment. The rudder-induced pitching moment is modelled as a function of the absolute value of rudder deflection in this study, i.e. $C_m = \boldsymbol{f}(\mid \delta_R \mid)$, for the nonlinear simulation model.

The AFDI technique developed to isolate rudder bias faults functions by tracking the effects the rudders on the pitching moment. A bias fault on one of the rudders will offset trim and cause unwanted pitching. Because the UAV is fitted with a feedback controller, the elevator will compensate for the rudder induced pitch and find a new "biased" elevator trim setting. As a result, the ER filter will falsely estimate an elevator bias (this "false" elevator bias will henceforth be called a *pseudo-elevator bias* in this thesis), which in truth, represents right or left rudder fault. Also, the ER filter will still detect and reconstruct rudder faults, but attribute half of the actual bias magnitude to both rudders, regardless of which of the two is faulty. The AFDI approach monitors this behaviour in the *pseudo-elevator bias* to determine which rudder is truly faulty.

Firstly, the FDI algorithm is able to identify the presence of *pseudo-elevator bias* and distinguish it from a real elevator bias, given the fact that the EA already correctly tracks the real elevator faults. In other words, if there is a real (true) elevator fault, it will appear in the EA filter and will be isolated correctly. In the case of the ER filter, observe that since a fault in any of the rudders will induce the *pseudo-elevator bias*, the same faulty rudder can be used to remove the *pseudo-elevator bias* by forcing the faulty rudder to a correct trim setting that induces no pitch. This is realised with an active FDI strategy which injects auxiliary signals into the rudders in order to remove any rudder induced pitching moment.

The rudder whose auxiliary excitation restores or approximates the original "pre-fault" elevator trim setting (the rudder whose auxiliary manipulation can eliminate the *pseudo-elevator bias*) is declared as the rudder with a bias fault. Note that if the "healthy" rudder is actively injected, the *pseudo-elevator bias* can only increase. In contrast, if the faulty rudder is in-

Stellenbosch University https://scholar.sun.ac.za

jected with an auxiliary signal, the *pseudo-elevator bias* can either increase or decrease down to zero. This is the distinguishing factor that allows the active isolation of the faulty rudder. The decrease in the *pseudo-elevator bias* to zero lets the FDI know that the biased rudder was deflected back to the unbiased trim or zero deflection, resulting in the elevator reverting to the original trim setting. With the elevator back at the trim setting, the *pseudo-elevator bias* disappears, and the rudder that removed it is declared as the one having a bias fault.

In the case of stuck rudders, the same isolability problem exists. The AFDI approach for this case involves exciting each rudder with a precalculated auxiliary signal having a specific frequency, and monitoring the presence of such frequency in the system states or computed signals. If the healthy rudder is excited, the frequency of the excitation signal will induce moments which propagate through the system and appear in measured signals and calculated parameters. If a stuck rudder is excited, there will be no induced moments or system response, and the excitation signal frequency will not be present in the processed signals. The rudder inducing no response in the system is declared as faulty by the AFDI algorithm.

Performance indices are calculated to evaluate the effectiveness and reliability of the FDI. Once developed, the FDI is tested on the nonlinear stochastic computer-simulated UAV model. The three fault classes, namely, bias, LoE and LIP, are routinely tested under single fault and multiple fault scenarios for different fault sizes. With each test scenario, the FDI performance indices are calculated, and the simulated results are plotted. Furthermore, to test the robustness and reliability of the FDI, a Monte Carlo (MC) campaign of 1000 fault cases ($n_{MC} = 1000$), equality distributed between the six (6) control surfaces, is carried out. Each MC run is performed with randomly distributed shifts in c.o.g, change in mass, sensor errors, and aerodynamical coefficients. This procedure is carried out for the bias, LoE and LIP fault cases. Simulation results from the MC campaign are presented in this thesis. To conclude the research, related work which could not be completed within this thesis is considered. Recommendations are made for future researchers who may be focusing on similar problems considered in this study.

1.8 Contributions in the Thesis

The research project makes the following contributions.

Stellenbosch University https://scholar.sun.ac.za

- A novel adaptation procedure (henceforth referenced as $\boldsymbol{Q}^{\gamma}-$ *Adaptation* in this thesis) is developed to improve both the sensitivity and robustness of the FDI. The additive covariance matrix for the fault parameter estimates needs to be large enough to track abrupt changes in the fault parameters, and at the same time, it needs to be small enough to reduce sensitivity to disturbances in the "no-fault" conditions to avoid high false alarm rates. However, a fixed (time-invariant) covariance is not ideal because it is guaranteed to be either too small or too large during different fault scenarios. That is, a covariance matrix that is ideal for the "no-fault" scenario is not ideal for the "in-fault" scenario. Moreover, the rate of variation of all parameters will not be the same during the entire evolution of the controlled system. Indeed, the rate of variation in affected parameters will grow significantly during faults, while unaffected parameters remain slow varying. Thus a selective approach is needed to adaptive $\boldsymbol{Q}^{\gamma}$ based on affected parameters. An adaptive procedures based on a single scaling (or forgetting) factor is unsuitable in a multivariate system, as is the Meraka UAV, because not all fault parameters have the same variation rate. The adaptation procedure proposed is based on scaling the eigenvalues of the $\boldsymbol{Q}^{\gamma}$ covariance matrix by multiple forgetting (scaling) factors in the direction of parameter variations. The multiple-factor approach is advantageous over a single factor approach, as it avoids scaling all parameters equally which would lead the the "blow-up" [36] phenomena due to the algorithm being too noise sensitive.
- Typically, a single FDI system is designed and tailored to detect a specific, single type of fault. In this study, a multi-mode hybrid switching model is developed to track both bias, LoE and LIP faults within a single model-based FDI design.
- A novel adaptive threshold technique is developed for enhanced fault isolation. The rate of variation of faults is random and non-uniform in time and space. If a static alarm (an alarm to flag the presence of faults) threshold is set too low, there will be high false alarms rate cause by noise in the parameters. If set too high, there will be high missed detections. In highly coupled multivariable nonlinear systems, abrupt faults will induce transient behaviour, typically a spike response, in the other system states and parameters. This transient behavior can cause momentary jumps in fault parameters, which would trigger false alarms. In this thesis, an adaptive threshold is de-

Stellenbosch University https://scholar.sun.ac.za

veloped, based on the normalised innovation squared (NIS), which represents the biasedness in the TSKF. The NIS allows setting the fault isolation threshold probabilistically for a specific level of confidence, owing to the NIS's χ^2 distribution properties.

- A novel active FDI strategy is developed to distinguish between bias, LoE and LIP faults. The hybrid multi-mode model needs to switch appropriately to reconstruct the correct magnitude of the fault parameter in the case of a LIP or LoE actuator fault. The nominal (default) FDI model is set up to detect bias, LoE and LIP faults. However, only the bias fault parameters will be reconstructed accurately with the nominal model. To reconstruct LIP and LoE after their detection, the hybrid model must switch appropriately. The switching logic relies on the controlled system's response to AFDI excitation strategy. Whenever a fault is detected, sinusoidal auxiliary excitation signals whose magnitudes are selected from the kernel of the linearised input ($\boldsymbol{B}$) matrix, at a frequency ω, are injected into the controls. If the fault is a bias type, there will be no response in the system due to the orthogonal signals cancelling each other out, in which case a bias fault is declared and isolated using the procedures described in Chapter 4. If the fault is a LoE or LIP type, the auxiliary controls cannot fulfil $\boldsymbol{u}_{ex} \in ker(\boldsymbol{B})$ and the excitation signal frequency ω will propagate through the system and appear in the measured signals and computed parameters. To distinguish between LIP and LoE faults, another sinusoidal is injected into the faulty actuator's input. If there's no response the fault is declared as LIP type, and otherwise an LoE type. Next the model switches appropriately for LIP or LoE faults. In the case of a LIP fault, the switching removes the effect of the stuck rudder from controls input by nulling the corresponding row in the $\boldsymbol{B}$ matrix, which allows the stuck position to be estimated entirely as part of the system states.
- A novel active FDI strategy is developed to isolate rudder bias faults As described in preceding sections, this procedure works by removing rudder induced pitching moment by deflecting the biased rudder to the trim setting. The rudder with which this is achieved can only be the one with a bias fault.
- An adaptive state estimation procedure based on multiple scaling factors, adapting the KF's estimate error covariance matrix is proposed. This formulation improves on popular techniques that use

Stellenbosch University https://scholar.sun.ac.za

a single scaling factor. A single factor is undesirable in large multivariate systems where state variations are not evenly spread. Once biasedness is detected (once the NIS exceeds a preset threshold), the algorithm generates multiple scaling factors based on matching the sampled innovation covariance with the theoretical covariance within the KF algorithm.

1.9 Thesis Outline

The remainder of this thesis is structured as follows:

- *Chapter 2* presents a general literature review in the field of FDI and FTCS. The chapter focuses on FDI and FTCS techniques typically applied to aerial vehicles and UAVs. The chapter concludes with a review of model-based FDI techniques commonly encountered the literature.
- *Chapter 3* presents the nonlinear 6-DoF model of the Meraka UAV. The chapter develops wind, gust and turbulent models to allow to mimic real flight in high fidelity simulation. The chapter concludes with a linearised version of the Meraka UAV model to which is utilised in the proposed FDI designs.
- *Chapter 4* defines the structure of the Two-Stage Extended Kalman filter (TSEKF), which is to be used to estimate bias, LoE and LIP actuator faults. Formulations of the fault models for the three cases are presented. Adaptive techniques are proposed to introduce robustness to the FDI. The Joint-Unscented Kalman filter and Dual-Unscented Kalman filter are presented and tested for comparison with the TSKF. The fault isolation technique used in this thesis is then presented.
- In *Chapter 5*, extensive simulations of fault scenarios of different types and magnitudes of faults are carried out to validate the FDI approach. The presented FDI algorithms are compared and evaluated.
- The thesis is concluded with *Chapter 6*, which makes recommendations for future research in related fields. Several appendices are included to reference related material.

Stellenbosch University https://scholar.sun.ac.za

Chapter 2

Literature Review

This chapter presents the literature review of some of the typical methods encountered in the fault-tolerant control (FTC) and fault detection and isolation (FDI). In aligning with the presented research work, this chapter focuses mainly on model-based fault diagnosis and active fault-tolerant control (AFTC). The chapter starts with a brief discussion of the various terminologies in FTC that are used throughout this study.

The complete review of FTC and FDI techniques in research and industry is beyond the scope of this thesis. For complete coverage of these techniques, the reader is referred to several survey papers which have appeared since the 1990s [37–48].

2.1 Definition of Fault-tolerant Systems

2.1.1 Faults and Failures

There are some existing and established terminologies in the field of FTC which are reviewed in this section. The International Federation of Automatic Control (IFAC) SAFEPROCESS Technical Committee has guided standardisation efforts relating to FTC. IFAC proposed the below definitions which are now accepted as standard.

- **Fault:** An unpermitted deviation of at least one characteristic property or parameter of the system from the acceptable / usual / standard condition.
- **Failure:** A permanent interruption of a system's ability to perform a required function under specified operating conditions.

In alignment with the above definitions, faults are understood in this thesis as unwanted events that alter the aircraft at component or system

Stellenbosch University https://scholar.sun.ac.za

level, inducing unexpected behaviour that impede the full operation of the affected components of systems. Events that result in the airframe completely losing its aerodynamical properties are considered catastrophic *failures* and are not considered for FDI in this study. A stuck actuator is an example of a fault treated in this study; however, a complete wing loss represents a catastrophic failure that could result in a complete loss of aircraft.

In large-scale control systems, faults may not manifest in the observable system behaviour immediately, but may ultimately lead to system failure if not corrected. Some faults have hidden or slow effects on the system, which makes their detection difficult. Consequently, with the exception of accidents, most failures are usually a manifestation of undetected or unattended system faults. A proven strategy to prevent system failures is by implementing appropriate maintenance regimes. FDI can improve maintenance regimes by enabling condition-based maintenance (CMB) whereby maintenance is carried out on particular components once faults have been detected, and the proof test interval can be reviewed.

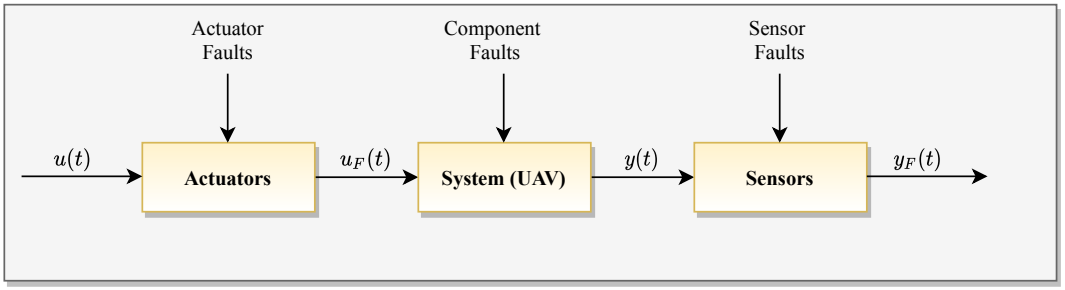

Figure 2.1: Different sources of faults in control systems

In Figure 2.1 is shown three possible sources of faults in the controlled system. A UAV can be considered a plant comprised of distinct subsystems, namely, actuators, process components, and sensors. The malfunctioning of a servo motor is an example of an actuator fault. A damaged wing or other UAV structural changes indicate process faults, while overly exaggerated sensor readings indicate sensor faults. The objective of an FDI system is to detect and locate faults, distinguish between the system components, and locate (isolate) the faulty component early enough to avoid complete system failure. Faults can also be classified according to their time-variant characteristics as follows (see Figure 2.2):

Stellenbosch University https://scholar.sun.ac.za

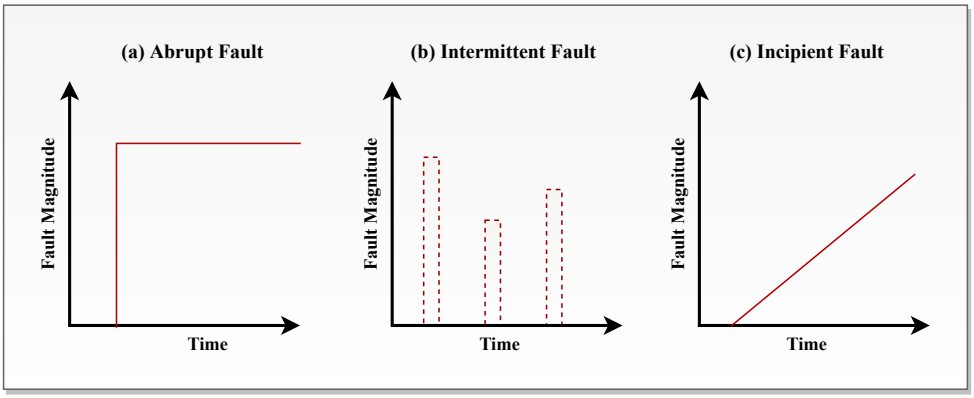

Figure 2.2: The types of faults in control systems

- **Abrupt faults:** an unwanted abrupt jump in the system parameter value when the fault occurs
- **Incipient faults:** a gradual evolution of a fault into a significant a value
- **Intermittent faults:** the fault appear and disappear repeatedly and/or randomly

Abrupt faults are characterised by a step-like jump in the behaviour of the system, while incipient faults drift gradually, typically at a slow rate. Intermittent faults are the repeated occurrences of transient faults characterised by appearing and reappearing randomly. An example of a hidden fault is a fault on standby equipment, which can only be visible on when this equipment is activated.

2.1.1.1 Sensor Faults

UAVs are typically fitted with several types of sensing equipment for system identification, guidance, navigation and control. Unattended sensor faults can lead to more severe failures of the UAV, especially in the absence of redundancy. Figure 2.3 shows typical faults found in sensors, namely, bias, accuracy loss or calibration error, drifting measurement and frozen

Stellenbosch University https://scholar.sun.ac.za

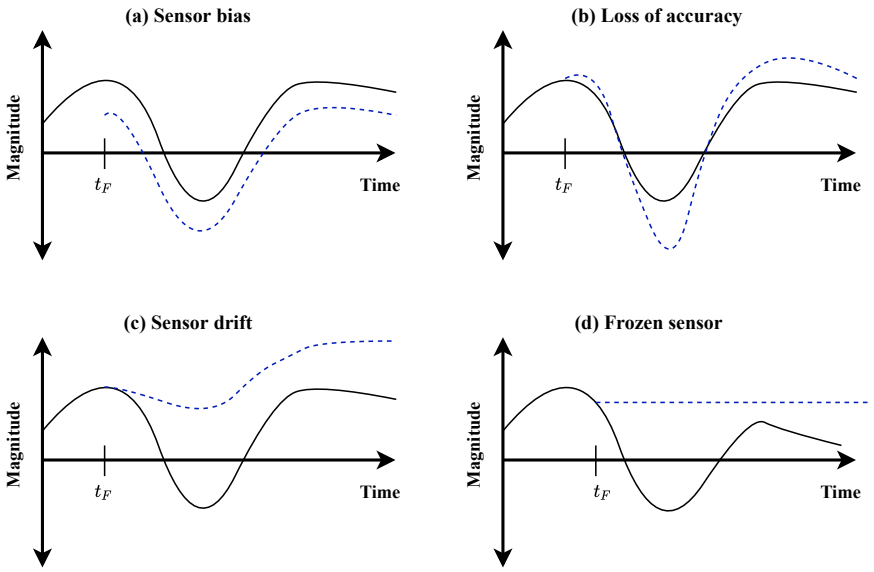

Figure 2.3: Typical faults in sensors occurring at t_F; dashed - measured, and solid - true state

measurement. The sensor faults in Figure 2.3 are represented mathematically in 2.1.2.

$$y = \begin{cases} x_j(t) & & \forall t \geqslant t_{F_j} & \text{Fault} \\ x_j(t) + \dot{b}_j(t) & \dot{b}(t) = 0, b_j(t_{F_j}) \neq 0 & \forall t \geqslant t_{F_j} & \text{Bias} \\ x_j(t) + b_j(t) & |b(t)| = a_j t, 0 < a_j < \varepsilon & \forall t \geqslant t_{F_j} & \text{Drift} \\ x_j(t) + b_j(t) & |b(t)| \leq \bar{b_j}, b_j(t) \in L^\infty & \forall t \geqslant t_{F_j} & \text{LoA} \\ x_j(t_{F_j}) & & \forall t \geqslant t_{F_j} & \text{Frozen} \end{cases} \tag{2.1.1}$$

where t_F denotes the instant when the fault appears in the i_{th} sensing device, while b_j is the coefficient of deviation such that $b_j \in [-\bar{b}, \bar{b}]$ where $b_j > 0$.

2.1.1.2 Actuator Faults

In control systems, actuators are used to generate forces or moments, drive control system and achieve some desired dynamic behaviour. In an aircraft, they are used to deflect control surfaces such as elevators, ailerons, rudders, engine throttle or to operator the landing-gear mechanism. Particularly in UAVs, the failure to detect and recover from actuator faults

Stellenbosch University https://scholar.sun.ac.za

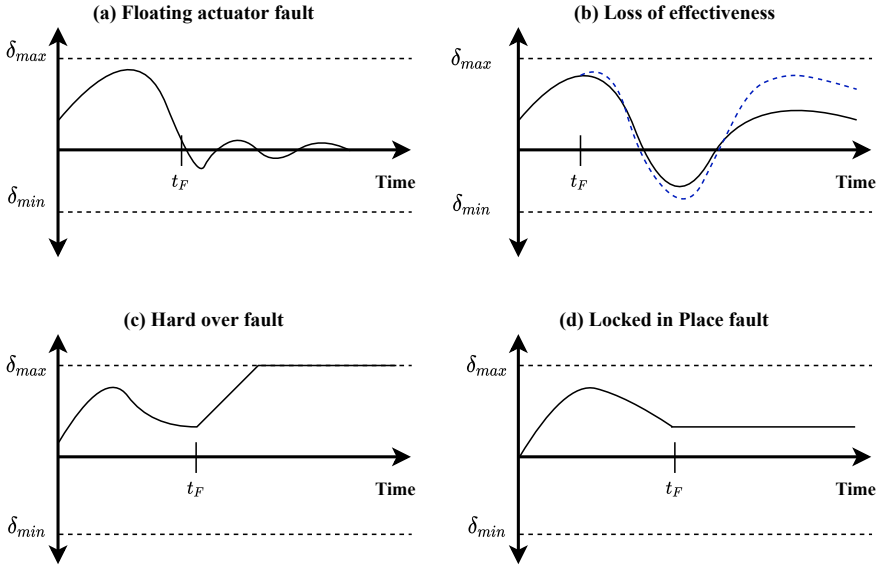

Figure 2.4: Typical faults in actuators occurring at t_F; dashed - desired, and solid - true actuator position

will lead to catastrophic events. Figure 2.4 shows the typical faults occurring in actuators. These fault types in actuator are expressed as follows:

$$u_i^a(t) = \begin{cases} u_i^c(t) & \forall t & \text{No Fault} \\ \gamma_i u_i^c(t) & 0 < \gamma < 1, \forall t \geqslant t_{F_i} & \text{LoE} \\ 0 & \forall t \geqslant t_{F_i} & \text{Floating} \\ u_{i_{min}} \vee u_{i_{max}} & \forall t \geqslant t_{F_i} & \text{LIP} \\ x_i(t_{F_i}) & \forall t \geqslant t_{F_i} & \text{HOF} \end{cases} \tag{2.1.2}$$

This signal $u_i^a(t)$ is the actual actuation command to the i_{th} control surface, while $u_i^c(t)$ is the control command signal given for the same surface. t_{F_i} denotes the instance when the fault occurs in the i_{th} control surface. Finally $u_{i_{min}}$ and $u_{i_{max}}$ represents the saturation levels of the control surfaces. The above faults can be represented mathematically as follows:

$$u_i^a(t) = \delta_i \gamma_i u_i^c(t) + (1 - \delta_i)\bar{u}_i \tag{2.1.3}$$

where $\delta_i = 1$, $\gamma_i = 1$ during the no fault conditions, while $\delta_i = 1$, $0 < \gamma_i < 1$ during LOE type fault and $\delta_i = 0$ during other type faults (float, LIP and HOF). The $\bar{u}_i$ is the position at which the actuator is locked.

Stellenbosch University https://scholar.sun.ac.za

2.2 Fault Tolerant Control System

The past four decades have seen growing demands for the safety, reliability, maintainability, and survivability in control systems; the result of which has been increased interest for research in fault detection and diagnosis (FDD) and Fault-Tolerant Control. Over the years, FTC has gained recognition from both industry and academia due to allowing collaborative research and technologies focused on improving safety, productivity, efficiency, and permanence. While FTC was mainly aimed at traditionally safety-critical systems, such as chemical, nuclear plants or aircraft, technological advancement has enabled FTC in a broader range of engineering applications.

A fault-tolerant control system (FTCS) is a control system that is designed with the ability to automatically accommodate (or tolerate) system component faults while maintaining stability and safe operation, possibly at some reduced performance levels. The primary goal of fault tolerance is to prevent the prolongation and effect of system faults from causing abnormal or unsafe system behaviour. An FTCS compensates for the effects of system faults by reconfiguring the control laws or adjusting the control structure to recover system performance. To have fault-tolerant capabilities, an FTCS may offer sub-optimal performance during normal system operation. There are generally two frameworks for FTC, namely, passive FTC and active FTC.

2.2.1 Passive Tolerant Control

Passive fault-tolerant control (PFTC) is analogous to robust control and does not require fault detection and isolation (FDI) or control reconfiguration for fault-tolerant capabilities. In PFTC, a single *super* robust control law is deployed with the ability to compensate for model uncertainties, system parameter variations and system disturbances, and maintain stability and acceptable performance levels for some class of expected of faults. In complex control systems, the cost of deploying a robust controller will be the sub-optimal performance of the system in the fault-free conditions. Severe system variations due to sensor or actuator faults can also lead to instability in some control systems. Active FTC strategies are necessary to overcome these limitations.

Stellenbosch University https://scholar.sun.ac.za

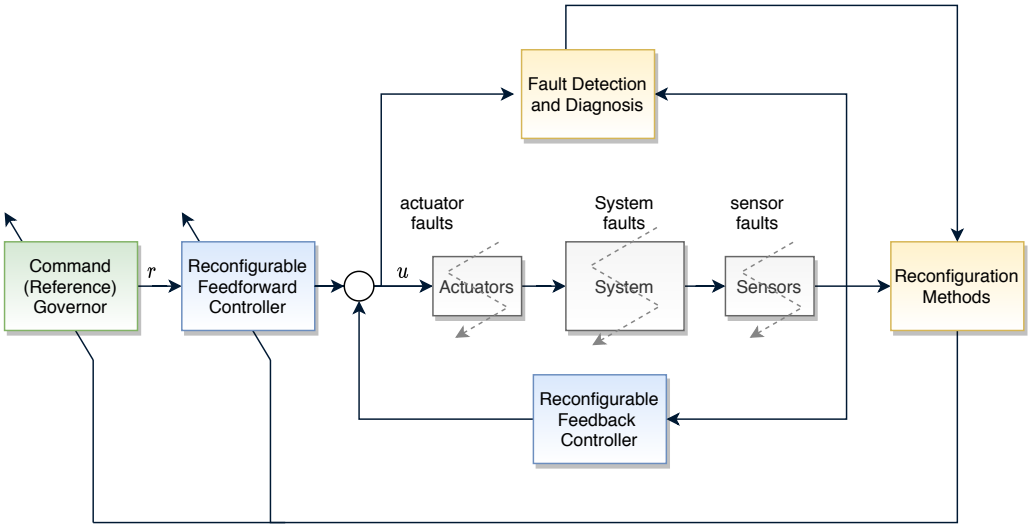

Figure 2.5: A general FTC architecture with FDI and control reconfiguration

2.2.2 Active Tolerant Control

In contract to passive FTC, an active fault-tolerant control (AFTC) system actively adapts to occurring system faults on-line by reconfiguring the controller to maintain stability and acceptable system performance levels. An AFTC system can accommodate faults by either selecting precomputed control laws or synthesising new control laws in real-time based on information about the *health status* of the system. Figure 2.5 depicts the overall architecture of an AFTC system, which has four functional blocks or subsystems. Generally, an AFTC can be categorised into four subsystems.

- Fault detection and diagnosis (FDD) or fault detection and isolation (FDI) system.
- Re-configurable controller.
- Controller reconfiguration mechanism.
- Reference governing system.

The main feature that differentiates the AFTCS from a PFTCS is the incorporation of FDI and a reconfigurable control structure in the former, which are absent (or passive) in the latter. In AFTCS, the FDI detects and isolates faults, estimates the fault parameters (timestamp, type and magnitude). FDI may include fault diagnosis functionality which estimates some set of system parameters under fault conditions to enable the reconstruction of a "post-fault" system model. This information must

Stellenbosch University https://scholar.sun.ac.za

be estimated on-line in real-time and made available to the controller reconfiguration system. Based on the fault data, the FTCS must automatically reconfigure its structure and maintain stability and desired dynamic performance. Reconfiguration here does not merely refer to the controller adjusting some parameters, but to also to changing its structure (type or order) or transitioning to a different set of controllers. Next, a module is needed to evaluate the performance capabilities of the entire system, considering the degraded conditions of the system after the fault. The reference governor system serves this function by setting reference trajectory limits and adjusting control objectives to ensure the best possible system performance.

2.2.3 Active Fault-tolerant Control Approaches

This section reviews some of the AFTC strategies commonly encountered in literature in the field of fault-tolerant and reconfigurable flight control systems.

2.2.3.1 Multiple-Model Approach

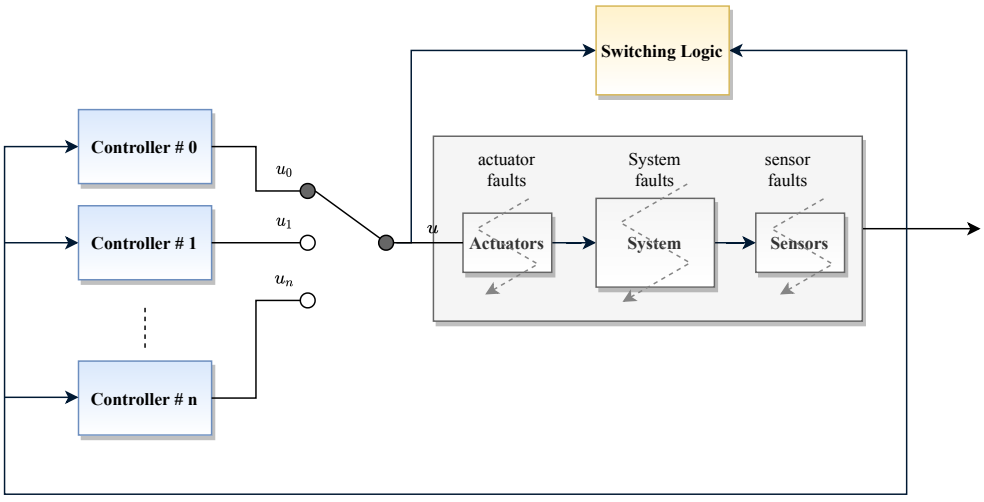

Figure 2.6: Multiple model based AFTC approach

A single robust controller may not always guarantee the desired system performance or stability. In this case, a multiple-model (MM) approach AFTC may be implemented. In the MM approach, a set of precalculated control algorithms are deployed in parallel, and each controller is fine-tuned to handle a specific, type, set or class of expected faults.

Stellenbosch University https://scholar.sun.ac.za

While each controller is designed to cater for the specific scenario, controllers are typically deployed one at a time. Therefore MM approaches also include a *no-fault* scenario controller that is designed to optimize performance under the *fault-free* conditions. The ideas behind MM based AFTC schemes are illustrated in Figure 2.6

A switching logic is required to oversee the transitioning between preset control modes based on information regarding the system health status. The MM approach can be extended to operate in an adaptive fashion. The controllers should also have bumpless switching.

Adaptation and Learning Using Multiple Models, Switching, and Tuning

This approach relies on the control system switching between a set of pre-calculated control laws depending on the detected fault condition. The approach is depicted in Figure 2.7. A dedicated model from the MM set describes the dynamics of each fault scenario. Each model is associated with a pre-computed control law, designed off-line. During a fault, the control system reconfigures by selecting the model-controller pair predesigned to archive the desired system performance in that fault scenario. A switching logic module computes a cost function based on matching the real system with each model. Based on this function, the system selects the model best describing current conditions in real-time.

A reconfigurable scheme may also include a system tuning based on parameter identification techniques and the updating of the models online. These algorithms have the advantages ca be efficient, fast and stable provided occurring faults match the predefined fault scenarios. The main drawback with the approach is that when unmodeled or multiple fault scenarios appear, the method may fail. Moreover, for large systems with many different possible faults, the number of models and controllers to be designed may be impractical.

2.2.3.2 Automatic Design

This approach encompasses schemes which rely on performing a complete re-design of the control algorithm after a fault has been identified. This approach is different from the MM approach in that, rather than switching to or adjusting a predefined controller, a complete controller structure changes are carried out online. Various controller re-design methods have been proposed and are available in literature [49]. To mention a few, these include Pseudo-inverse Method (PIM), eigenstructure assign-

Stellenbosch University https://scholar.sun.ac.za

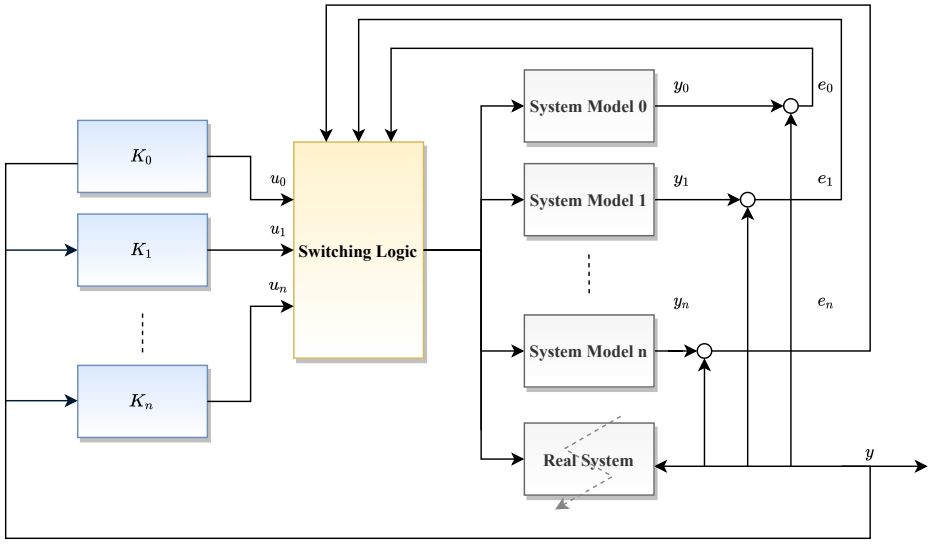

Figure 2.7: Multiple model switching and tuning approach

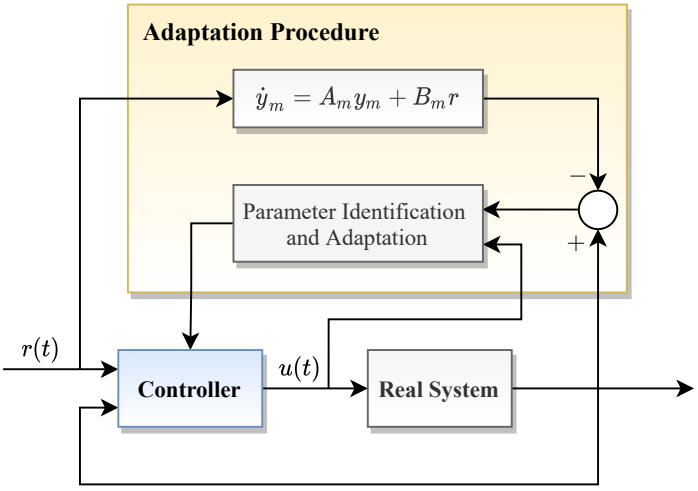

Figure 2.8: The Model Reference Approach

ment, Linear Quadratic Regulator (LQR) design, state-feedback $\mathcal{H}_\infty$ control or model predictive control.

2.2.3.3 Adaptive Control: The Model Reference Approach

This approach can be effective in handling components and structural faults. The method may be reliant on other complex control systems and functions by integrating information generated from such systems. The main idea in this approach is that the controlled system should track the designed reference model. For the matching of the real system and its

Stellenbosch University https://scholar.sun.ac.za

model, the controller must adapt and adjust online as depicted in Figure 2.8.

Model reference methods can be categorised into direct, indirect or a combination of the two. In the indirect adaptive control technique, the controlled system's parameters are identified, based on which some certainty-equivalence control schemes are derived. For parameter identification, techniques such the recursive least-squares or neural networks have been utilised. In the direct adaptive control techniques, the control system's parameters are directly adjusted without the explicit identification of the plant's unknown parameters.

2.3 FTC and FDI in Aerial Vehicles

Aerial vehicles can be considered mission-critical systems mainly because failures and accidents can easily result in catastrophic or total destruction if not managed. Disastrous failures result in loss of mission, investments, and in the case of passenger vehicles, loss of life. As such, the aviation industry utilises state of the art FDI and FTC architectures that are heavily reliant on redundancy. In this section, FTC and FDI procedures typically utilised in aviation systems are discussed.

2.3.1 Passenger Aircraft

Especially for passenger aircraft where human life is involved, the most reliable and proven methods for FTC and FDI must be adopted. Such methods have historically relied on hardware and software redundancy to handle faults easily and quickly. Hardware and software redundancy have been used extensively on aircrafts such as Boeing 777 and Airbus A320/A330/A340 [50–52]. Another aircraft relying heavily on redundancy is the Airbus A380, which is equipped with four engines, two rudders, four elevators, six flaps, six ailerons, sixteen spoilers, eighteen slats and a surplus sensing equipment and onboard computers. The main idea in hardware redundancy is to compare parallel information generated by multiple hardware and transition to redundant (spare) hardware during faults and failures.

Boeing[53] and Airbus[54] have owned patents in hardware redundancy technologies for several years. Due to the cost, weight, energy consumption, increased installation and maintenance requirements associated with hardware redundancy, these organisations are actively engaged in model-based approaches for FDI[2]. Hence the use of observer-based

Stellenbosch University https://scholar.sun.ac.za

oscillatory failure detection scheme in the A380 aircraft[55]. However, even model-based FDI level in larger aircraft must be broken down to component level to improve reliability. In reference [2] for example, model-based FDD is carried out on an Electro-Hydro Actuator (EHA) of the Airbus 380, to diagnose it for oscillatory faults that appear due to malfunctioning of actuator servo-loops. The architecture for the FDD is depicted in Figure 2.9. The FDD design requires sensors in three separate places (each with redundancy), wiring to the sensors and computing equipment for monitoring of the system. This FDD infrastructure monitors just one of the many control surfaces in the Airbus A380, with each control surface having its own independent FDD algorithm.

The above works sought to reduce the computational and installation burdens associated with the traditional hardware redundancy approaches in passenger aircraft; however, the computational and hardware requirements are still too demanding to deploy in small-sized UAVs. Further reductions in hardware and computational capacity are necessary for FDI designs suitable for small UAVs. To detect actuator faults, a potentiometer based sensing device could be used to measure positions of control surfaces, or wired off the existing potentiometer on the aircraft servo, which would greatly simplify the involved algorithms. However, this option is not always available and is not considered in this study. In this thesis, control surface faults are monitored by modelling tracking their aerodynamical effects using the system states, and without the need to measure the actual position of the actuators.

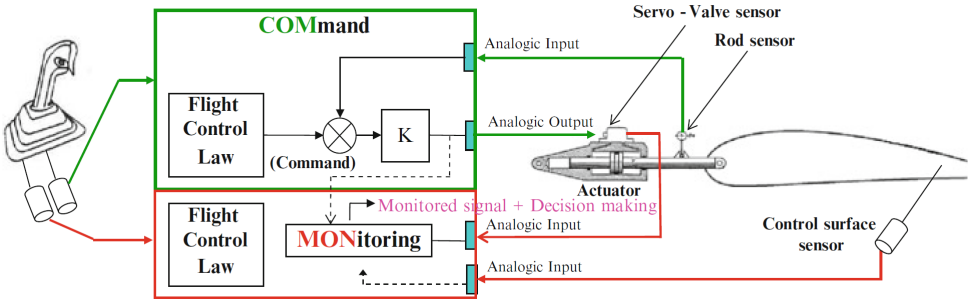

Figure 2.9: Model based FDD applied to Aibrus A380 Electro-Hydro Actuator (EHA) - Adapted from [2]

It is noted that model-based fault diagnosis at a component level results improves the reliability of the FDI as it demonstrated with various types of faults in reference [2]. This is because there is more variability or

Stellenbosch University https://scholar.sun.ac.za

errors to be expected with a wholistic model describing the entire system, than with a subcomponent modelling. Moreover, passenger aircraft make use of high cost, state of the art system components (actuators or sensors) whose analytical models have usually been studied extensively and validated experimentally, and their technical specifications and data are available. This may not be the case in UAVs, and model-based FDI should be based on a "text-book" model representing the UAV's flight dynamics.

2.3.2 Space Vehicles

Deep space vehicles may involve long communication delays, and as such, would greatly benefit from automated FDD and FTC functionalities. Considering the high cost of re-initiating any single deep-space mission (which typically follow a single-shot approach), there is unequalled need for space vehicles to be equipped with fault tolerance capabilities. One of NASA's New New Millennium Program projects called The Deep Space 1, involved investigating advanced technologies for onboard fault diagnosis and recovery[56]. In the same project, NASA also tested their remote self-repair software. The Jet Propulsion Laboratory called the Remote Agent (RAX), was the first artificial intelligence control system to control a spacecraft without human supervision[57, 58]. Remote Agent showed the capabilities to plan its mission and accurately detect faults in the spacecraft components.

2.3.3 Unmanned Aerial Vehicles

In UAVs, the FDI architecture mostly used is the integrated vehicle health management (IVHM) which includes prognosis and maintenance planning [59]. The IVHM performs online system identification by tracking the UAV's time-varying parameters to monitor and estimate (identify) system faults via FDI techniques. For fault tolerance, the IVHM is usually deployed in conjunction with the automated contingency management (ACM) layer. The ACM uses the vehicle's health information to evaluate system capabilities and set new constraints based on reduced system functionality, which may include flight envelope adjustments, mission optimization or complete re-planning, or emergency landing. With these new constraints, the ACM will reconfigure the control laws and adapt them to new constraints to achieve newly optimized mission objectives.

IVHM and ACM enable better autonomy and survivability during impaired operating conditions. Due to limited space and computing power in low-cost UAVs, model-based FDI is an attractive option. A potentiome-

Stellenbosch University https://scholar.sun.ac.za

ter based sensor could be fitted to the control surfaces to measure their position for FDI. However, deploying additional sensors on control surfaces and servo actuators in small, low-cost UAVs require additional wiring and processors. The proposed model-based FDI requires no additional sensing equipment and uses the standard sensing equipment for guidance, navigation and control (GNC)

2.4 Fault Detection and Isolation

Fault Diagnosis gained primary focus during the 1970s in the United States after their Apollo program endured a series of equipment failures, which led to the tragedy of April 1967 [60]. FDD and FTC have since been studied extensively in the field aviation, and a large body of literature is now available. Surveys on the state of the art literature of FTC and FDD can be found in [37–48].A review of FDI techniques applicable to aerial vehicles can be found in [2, 61, 62].

A fault detection and isolation system is a system that can detect the presence of a fault and determine its location within a reasonable time to allow for control reconfiguration. When an FDI system is also capable of estimating the severity of the fault, it is called a Fault Detection, Isolation and Identification (FDII) system, or Fault Detection and Diagnosis (FDD) system. Because the FDI developed in this study is capable of fault *diagnosis*, FDI and FDD are used interchangeably.

Below are more terminologies relating to FTC as defined by the IFAC Technical Committee SAFEPROCESS

- **Fault detection:** Determination of the faults present in a system and the time of detection.
- **Fault isolation:** Determination of the kind, location and time of detection of a fault. Follows fault detection.
- **Fault identification:** Determination of the size and time-variant behaviour of a fault. Follows fault isolation.
- **Fault diagnosis:** Determination of the kind, size, location and time of detection of a fault. Follows fault detection. Includes fault isolation and identification.

Fault detection refers to the FDI making a binary decision on whether or not a fault has occurred. Isolation is distinguishing faulty components from fault-free ones and locating (isolating) their source. Identification is determining the size, type, time or severity of the fault. Where redundant

Stellenbosch University https://scholar.sun.ac.za

sensors/actuators are used for AFTC, identification may not be a prerequisite for control reconfiguration. Moreover, identification may be inherent within the isolation algorithms if the fault is estimated as part of its detection, as is the case in this thesis.

FDI systems can also be categorised into two types, namely the passive FDI (PFDI) and the active FDI (AFDI). PFDI simply monitors the system, waits for the presence of a fault to be apparent within the system and then performs necessary techniques to detect and isolate the fault. Thus the PFDI is a reactive approach to FDI. A pro-active approach is the AFDI, which actively excites the system using actuation or auxiliary signal injection with the purpose of "*scanning*" the system for faults and extracting faults signatures.

2.4.1 Basic Requirements of an FDD System

A reliable FDI must be able to detect small (or hidden), abrupt, incipient faults and isolate them within sufficient time to allow the FTC to counteract the fault, such as reconfiguration, maintenance or shut-down. The following performance criteria are for consideration when designing a reliable FDI.

- **Detectability:** Detectability refers to whether a fault can be detected or not with the given sensing. This is a characteristic of the system given the instrumentation available. Undetected faults may result in catastrophic failure if untreated. A reliable FDI should detect faults quickly to allow time for corrective action.
- **Isolability:** An FDI must distinguish between different faults to a component level and correctly locate (isolate) them. Isolability is particularly difficult in a UAV in systems where symmetry and redundant actuators exist.
- **Identifiability/Diagnosis:** An FDI system must accurately estimate the severity of the fault. In the absence of redundancy, reconfigurable controls may require a quantitative description of the fault to generate fault-tolerant controller.
- **Sensitivity:** An FDI system must be highly sensitive to reliably detect even small (hidden) faults and incipient faults. However, and overly sensitive FDI may also lead to robustness problems and report higher rates of false alarms.
- **Robustness:** While being highly sensitive, the FDI system must also be robust against measurement noise, system disturbances, model

Stellenbosch University https://scholar.sun.ac.za

uncertainties and system variations. Robustness in FDI means maximising detectability, isolability and sensitivity to faults while minimising false detection. The key problem is distinguishing between out-of-spec system behaviour induced by disturbances, noise, unmodelled parameters from those induced by actual faults. Consequently, robustness is a contradictory objective to minimise missed detection and at the same time, false alarms. A good FDI solution is the optimisation of these two requirements

- **Multiple Faults:** An ideal FDI should also detect and isolate multiple faults. If temporal separation between faults is assumed, the design of a multiple-fault detection and isolation algorithm can be simplified. In UAVs, the difficulty in detecting multiple concurrent faults lies in the nonlinearities, coupling that exists between system states, symmetry and redundant actuators producing identical moments.

2.4.2 FDD Systems Performance Evaluation

Before deployment for real application, an FDI system should be tested and validated for effectiveness and reliability. An FDI will include a Boolean decision logic used to decide the declaring of faults. The Boolean function may be governed by a statistical analysis of generated residuals or fault signatures, and the two processes should be tuned carefully. Nevertheless, the Boolean decision logic will not 100 % effective in declaring faults, and some false alarms or missed faults can be expected.

In this study, the FDI is tested for reliability by carrying out a Monte Carlo (MC) simulation ($n_{MC} = 1000$). With each run, some FDI performance indices are calculated and recorded. To calculate the performance indices, a *benchmark zone* is first specified (see Figure 2.10) , starting at time t_{on} and ending at the benchmark horizon t_{hor}. Before the benchmark zone, a short period until t_{on} is allowed for the FDI to startup and reach steady-state behaviour.

- **Detection Time** (t_{dt}): the time taken from the occurrence of a fault t_F to the true and permanent detection of the same fault t_D. As can be seen, the first three temporary detection are unsure and therefore are not taken into account when determining t_D

$$t_{dt} = t_D - t_F \tag{2.4.1}$$

- **Detection decision** ($\boldsymbol{DD}$): a binary signal representing the decision that a fault has been detected in the system.

Stellenbosch University https://scholar.sun.ac.za

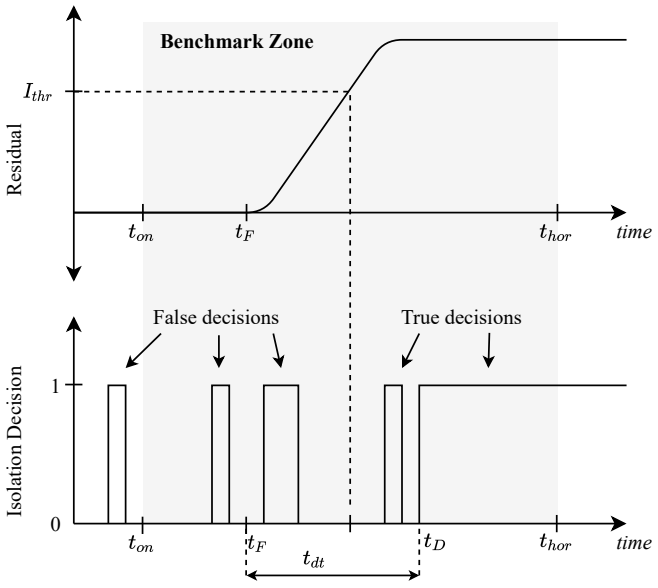

Figure 2.10: Benchmark diagram for FDI performance

- **Isolation decision** (***ID***): a binary signal representing the decision that a fault has been isolated in the system.
- **False Detection Rate** (r_{dt}): can be define as follows

$$r_{fd} = \frac{\sum_i t_{fd}^{i,DD}}{t_{hor} - t_F} \tag{2.4.2}$$

where t_{fd}^i is the period of the i_{th} false detection during the fault-free conditions. This index is used to quantify false alarms in the system. In an ideal FDI system, this parameter should be close to zero.

- **True Detection Rate** (r_{td}) : can be define as follows

$$r_{td} = \frac{\sum_i t_{td}^{i,DD}}{t_F - t_{on}} \tag{2.4.3}$$

where t_{td}^i is the period of the i_{th} true fault detection. This parameter represents the efficiency of the FDI. In an ideal FDI system, this index should be close to 1.

- **Isolation Time** (t_{it}) : is the time spanned from when the fault occurs to when it is isolated.
- **False Isolation Rate** (r_{fi}) : can be defined as follows

$$r_{fi} = \frac{\sum_i t_{fi}^{i,ID}}{t_F - t_{on}} \tag{2.4.4}$$

where t_{fi}^i the period of the i_{th} false fault isolation

Stellenbosch University https://scholar.sun.ac.za

- **True Isolation Rate** (r_{ti}) : is define as follows

$$r_{ti} = \frac{\sum_i t_{ti}^{i,ID}}{t_{hor} - t_F} \tag{2.4.5}$$

The above indices will be used to evaluate the FDI's performance in this study.

2.5 Classification of Fault Detection and Isolation Methods

FDI techniques can be grouped into three categories, namely, hardware redundancy schemes, analytical redundancy (model-based approach) and data-based approach. Model-based and data-based techniques can both be used to yield qualitative or quantitative fault information. The quantitative approach relies on developing mathematical models, used to generate fault information in a quantified manner (such as elevator stuck at 1 degree). The quantitative approached employ techniques such as; fault trees, trend analysis, fuzzy logics or pattern recognition to isolate or classify faults by type, levels of severity (such as moderate, severe or critical). Next, the three categories of FDI are discussed.

2.5.1 Hardware Redundancy

In this approach, fault diagnosis realised by deploying auxiliary (redundant) hardware, such as sensing devices, software, computing hardware and actuators. The redundant hardware is deployed in parallel with the primary hardware to perform the same operation or serve as a backup. Fault detection and diagnosis is achieved by consistency checks by comparing measured data and trends using voting schemes between parallel hardware. The main benefit of hardware redundancy is that direct and fast isolation is archived very reliably, and redundant hardware is readily available for FTC.

Hardware redundancy has become an industry standard for FDI and conforms well into safety and industrial certification processes. The obvious disadvantages of this method increased complexity in hardware architecture, increased weight, cost of installation, repair and maintenance and thus it is unsuitable for low cost, low weight (limited space) UAV applications. Due to the drawbacks noted above, hardware redundancy is usually dedicated exclusively for critical components in UAVs.

Stellenbosch University https://scholar.sun.ac.za

2.5.2 Model-Free (Data-based) Approach

When an appropriate mathematical model of the system is unattainable, data-based approaches are a powerful alternative for FDI. These methods rely on analysing data describing system behaviour measured either in realtime or analysing historical data offline. The functionality of these methods relies on expert knowledge on the expected behaviour to detect the presence of faults. The applicable techniques include pattern recognition, fuzzy-logics, signal processing, neural networks (NN) and statistical analysis.

Neural networks use either online or offline measurement data describing system behaviour under faulty and fault-free conditions to learn the system modes. Trained NN can mimic system behaviour very accurately, identify its fault symptoms and predict the system modes. Neural networks have shown high accuracy levels and robustness to disturbances even is large scale highly nonlinear systems. A major drawback with the NN approach is that data collected during fault conditions may be required to train the NN. Sometimes this requires failing the system of interest several times to allow the NN to learn the failure modes, which may take a considerable amount of iterations and failure scenario to allow sufficient learning. Besides, NN is a black-box approach which limits the availability of intuitive parameters to characterise the real system.

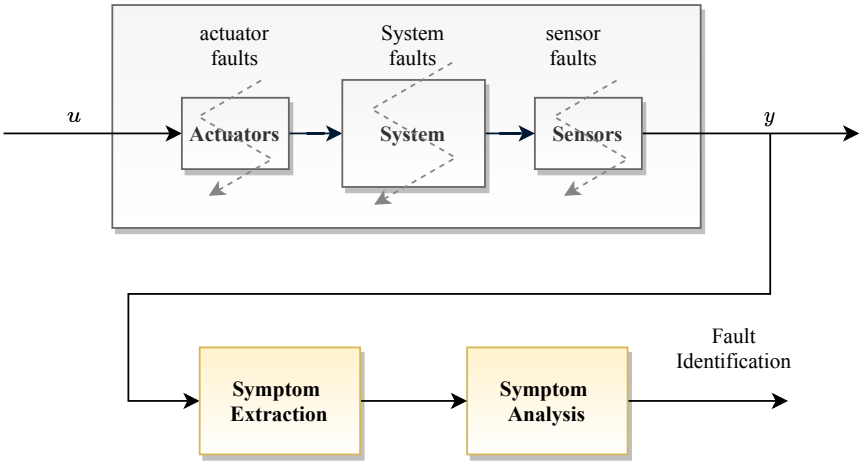

Figure 2.11: Schematic description of the signal based FDI schemes

Signal processing techniques have been widely used especially in machinery components such as gearboxes bearings to extract fault *signatures* [42] from these systems. The methods work by subjecting the system to

Stellenbosch University https://scholar.sun.ac.za

some pre-defined signal processing techniques and observing the outcome. The technique relies on the concept that the faults of interest in the system will manifest in the processed signals. Popular techniques include time-domain analyses approaches, such as amplitude distribution, limit or envelope checks, and trend analysis. The statistics of the measurable states and outputs of the system are compared with nominal operational limits. Frequency analysis of measured signals such as spectral power densities and frequency spectral lines are evaluated to make conclusions about the presence of faults. A noteworthy drawback with these strategies is that the mathematical models describing system dynamics are disregarded, which may often be useful in quantifying the fault and enabling FTC.

2.5.3 Analytical Redundancy Approach

Analytical redundancy is analogous to model-based FDI in the FDI literature. Beard is typically regarded as the first to have put forward the idea of analytical redundancy in his PhD work in 1971 at MIT[63, 64]. The idea relied on using a mathematical model to evaluate the system conditions, rather than using redundant hardware. The key advantage of this approach is that no additional hardware is needed to archive fault diagnosis. Figure 2.12 depicts the general structure of an analytical redundancy based FDI schemes. The approach usually involves two stages, namely (i) residual generation and (ii) residual evaluation.

The method generates residuals by comparing the output predicted by the analytical model with the measured outputs of the system of interest. The residuals are expected to be small under fault-free conditions. The term "small" depends on the system and the FDI design. The residual is expected to dramatically deviate from the "small" value in the presence of faults.

In the residual evaluation stage, residuals are checked for signs of faults. The presence of faults is determined based on some predetermined decision algorithm. The typical procedures can range threshold checks on the realtime values or rolling averages of the residuals, to generalised likelihood ratio (GLR) testing or sequential probability ratio test. The objective is to provide a Boolean decision regarding the presence of faults.

Decision algorithms typically require threshold tuning, which is usually a trade-off between ensuring fault sensitivity (minimising missed faults) and robustness (minimising false alarms). The reliance on an accurate

Stellenbosch University https://scholar.sun.ac.za

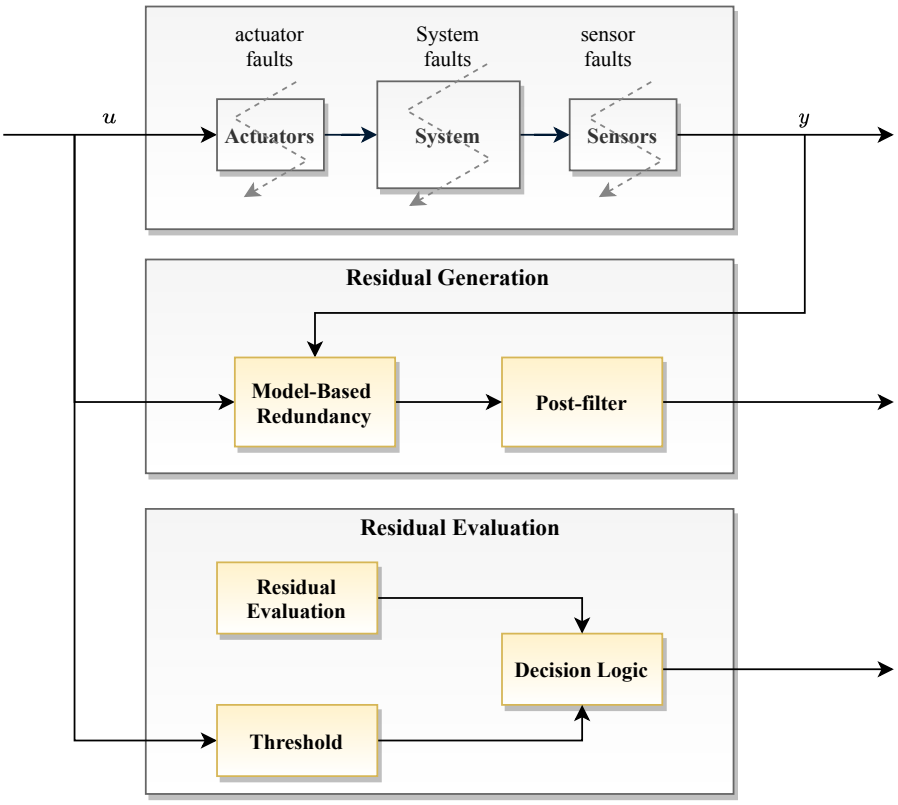

Figure 2.12: Analytical redundancy based FDI scheme

model will often have a direct impact on the quality of the FDI in the analytical redundancy approaches, regardless of which techniques are utilised. Unmodelled parameter variations and disturbances can trigger false alarms. These factors may be addressed by appropriate fault isolation decision rules.

There are two levels at which robustness to system disturbances can be handled, namely, during residual generation or during its evaluation. In the former case, the design shall ensure disturbances are decoupled from the residual and the approach is robust to model uncertainties. In the later, the decision thresholds may incorporate some adaptive scheme using some statistical knowledge of the system to minimise the effect of uncertainties, transient behaviour and effects of unknown inputs.

2.6 Model-based Fault Detection and Isolation

With the availability of modern computers, model-based fault diagnosis offers a cost-effective, iterative, and easily implementable FDI systems design process. The section presents methods typically encountered in the

Stellenbosch University https://scholar.sun.ac.za

field of model-based fault diagnosis. Due to the vast body of literature available, the presented approaches are described briefly. Model-based FDI techniques can be categorised into state estimation techniques, parameter estimation techniques, parity space techniques and decoupling strategies.

2.6.1 Parity Space Approach

In the parity space methods, party checks are carried on the consistency of the parity equation. The system equations are modified into the parity relations, derived based on measured signals from the system. The idea with the parity relations is to decouple the generated residuals from the system states and each other. This gives the parity relations the ability to detect faults by examining the parity relations for inconsistencies. Parity relations can either be formulated with a state-space framework [65], or formulated by the use of transfer function describing the system [66–69]. A comprehensive review and analyses of parity space methods are given in [42, 70].

2.6.2 State Estimation

This approach relies on tracking the controlled system states and generating residuals by comparing calculated states with measured system signals. If the presence of a fault is detected in the residual, an isolation procedure must distinguish one fault from another. While a single residual can be sufficient for fault detection, a set of residuals are may be necessary for fault isolation. If the condition is satisfied that a particular fault is dissimilar from other faults by examining a single residual vector, fault isolation can be archived evaluating that residual set. The generated residuals can be thought to span some residual space [47]. There are two frameworks for evaluation residuals for fault isolation, namely the residual directional set and the structured residual set

1. **Directional residuals**. In this approach, the residuals are generated within a geometric framework. The residual space spanned by a residual vector is expected to match fault-free residual space. Next, fault isolation is facilitated by defining residual directional vectors such that in the occurrence of a particular fault will characterise a specific direction in the residual place, which is unique for each occurring fault. By designating specific faults to unique directional vector, fault isolation is archived.

Stellenbosch University https://scholar.sun.ac.za

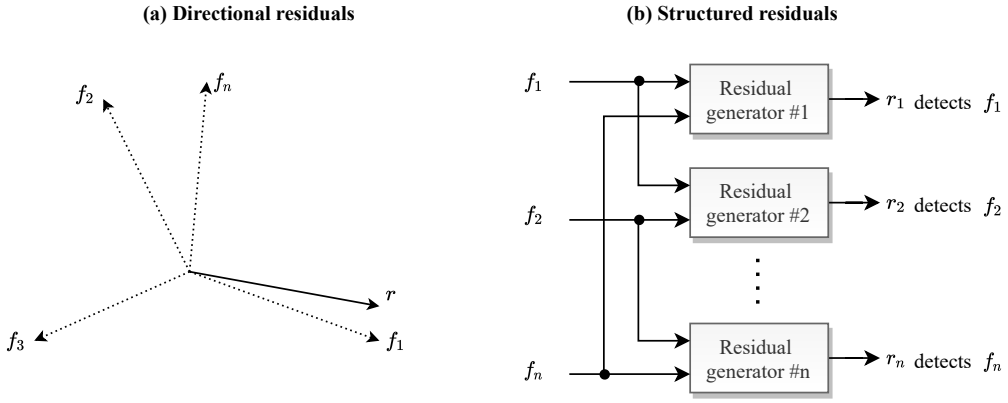

Figure 2.13: Fault isolation by residuals. Adapted from [3]

2. **Structured residual set**. In this approach, a set of residuals are designed to be sensitive to a set of faults, while maintaining insensitivity to other faults. Fault isolation is archived by specifying the sensitivity and insensitivity association between residuals and faults.

The concepts of the directional and structured residual approaches are depicted in Figure 2.13

2.6.3 Stochastic Approach

Most systems in practice, such as a UAV, exhibit nonlinear and stochastic properties. Filtering techniques are a popular way if estimating stochastic systems' internal states, physical parameters or unknown inputs. Kalman filtering can be used for system identification in stochastic systems. In the fault-free conditions, the Kalman filter's innovation is expected to be white noise with a zero mean and a known covariance. To archive isolation, multiple filters can be utilised in the multiple model (MM) framework, the multiple model adaptive estimation (MMAE) or the interacting multiple model (IMM) framework [71, 72].

In these MM approaches, a bank of filters, with each filter representing a unique fault condition (including the fault-free case), are designed to run in parallel. The statistical information available in the KF algorithm allows computing the probability of each fault as they occur, leading to reliable isolation capabilities. MMAE has been successfully tested for FDI in UAVs [72] and has also been studies on the Meraka UAV at ESL [3]. The IMM approach, initially proposed in [73] also uses a bank of filter estimators and modal probabilities to weight the input and outputs of a bank of filters at each instant, switching between interacting models in a proba-

Stellenbosch University https://scholar.sun.ac.za

bilistic way. The main drawback with the multiple model approaches is high computational requirements. For the case of a UAVs, reference [42], utilised a bank of 12 filters while reference [3], utilised a bank of 9 filters.

The Kalman filter's limitations can be addressed by linearisation of the controlled system around the current mean estimate, resulting in the extended Kalman filtering (EKF) approach. The Unscented Kalman Filter (UKF) also called the sigma point filter (SPF) (Julier and Uhlmann[74]) is a further and the latest extension to the Kalman filter. Instead of linearising the system model, unscented transformation is used to compute the statistic of a random variable as it undergoes a nonlinear transformation. The UKF characterises the mean and covariance of the GRV using a set of sample points selected through a deliberate procedure and passed through the nonlinear function to accurately capture posterior mean and covariance the 3rd order for any nonlinearity. [74–77]. The algorithms for the KF, EKF and UKF are presented later in this thesis.

The Kalman filtering techniques discussed above either assume or approximate a Gaussian probability distribution. The particle filter (PF) can resolve nonlinearity and non-Gaussian distribution while accurately tracking system behaviour. However, PF approaches have excessive computational requirements.

Stellenbosch University https://scholar.sun.ac.za

Chapter 3

Nonlinear Aircraft Model

This chapter presents detailed description of the nonlinear kinematic and dynamic equations used to design the high fidelity simulation of the Meraka UAV in Simulink ®. This simulation model will serve as a testbed to test and validate the proposed FDI design. The aerodynamic coefficients of the Meraka were determined by simulation in [3]. The nonlinear model assumes rigid body dynamics. To mimic the UAV's interaction with the real world, atmospheric disturbances are incorporate into the model in the form of; steady wind, turbulences, discrete gusts and wind shears. A linearised version of the nonlinear model is derived, to allow the design of the TSKF based FDI.

3.1 Reference Frames and Coordinate Transformations

The translational and rotational motion of a rigid body aircraft can be described by a set of nonlinear simultaneous differential equations [78]

$$\dot{\boldsymbol{x}}(t) = \boldsymbol{f}\left(\boldsymbol{x}(t), \boldsymbol{u}(t)\right) \tag{3.1.1}$$

where $\boldsymbol{x}(t)$ is a 12-dimensional time-varying state vector and $\boldsymbol{u}(t)$ is an l dimensional control vector. The observation equation describing the measurements of the vehicle state is written as

$$\boldsymbol{y}(t) = \boldsymbol{g}\left(\boldsymbol{x}(t), \boldsymbol{u}(t)\right) \tag{3.1.2}$$

where $\boldsymbol{y}(t)$ is a time-varying state observation vector. The equations describing the motion of an aircraft can be formulated more broadly than described above; however, the above formulation will be sufficient to de-

Stellenbosch University https://scholar.sun.ac.za

scribe the UAV accurately. For the UAV problem, the state vector is composed of four 3×1 sub-vectors describing the vehicle's translational velocity, rotational velocity, attitude and its location in a $3-$dimensional space:

$$\boldsymbol{x} = (\boldsymbol{x}_1, \boldsymbol{x}_2, \boldsymbol{x}_3, \boldsymbol{x}_4)^T \tag{3.1.3}$$

where

$$\boldsymbol{x}_1 = (V, \alpha, \beta)^T \tag{3.1.4}$$
$$\boldsymbol{x}_2 = (p, q, r)^T \tag{3.1.5}$$
$$\boldsymbol{x}_3 = (\phi, \theta, \psi)^T \tag{3.1.6}$$
$$\boldsymbol{x}_4 = (x, y, z)^T \tag{3.1.7}$$

where $\boldsymbol{x}_1$ and $\boldsymbol{x}_2$ are defined in the body-fixed axis and $\boldsymbol{x}_3$ and $\boldsymbol{x}_4$ are defined in the earth-fixed inertial frame for convenience. To accurately express the motion of a UAV, it is necessary to express the orientation and motion of multiple bodies or systems with respect to each other. To speak again, the orientation of the UAV ought to be expressed with respect to the orientation of other systems, such as the runway or a ground station. Thus, several coordinate systems are first defined to characterise the motion and orientation of the various UAV systems. The main reasons for transformations between coordinate systems are:

- Newton's equations of motion are founded in the inertial reference frame. It is typically easier for various reasons, to express the UAV's motion in a body-fixed coordinate frame.
- It is also easier to express the forces and moments acting on the UAV in a body-fixed coordinate frame
- The sensing equipment of the UAV, such as the accelerometers and rate gyros are fitted and measure data in the vehicle's body coordinate frame. Whereas for UAV guidance navigation control (GNC), the GPS measures position, course angle and ground speed with respect to the inertial frame.
- Mission planning in controlled flight relies on trajectories and map information which are typically specified in the inertial frame. This information has to be resolved into the aircraft's body-fixed frame to be usable by onboard systems.

Stellenbosch University https://scholar.sun.ac.za

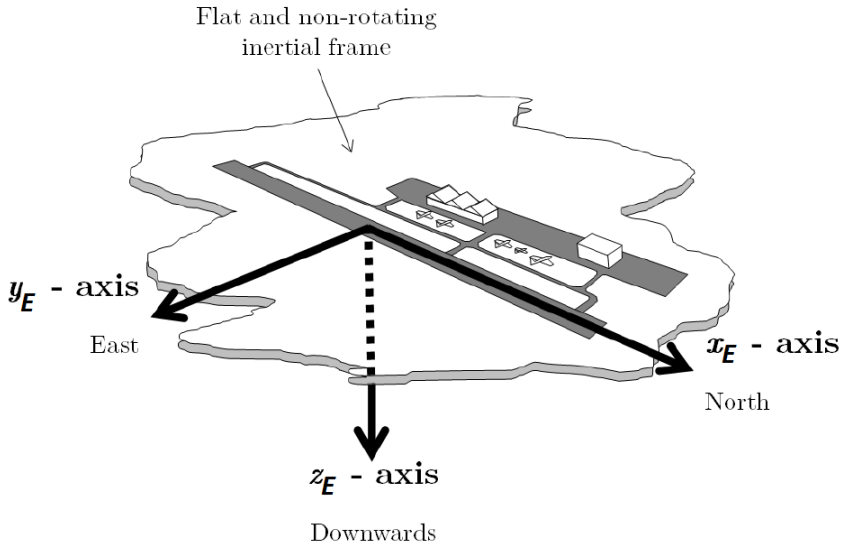

Figure 3.1: Inertial reference frame. Adapted from [3]

3.1.1 Inertial Frame

By definition, Newton's equations of motion are referenced to a fixed inertial frame. The inertial coordinate frame is defined as an earth-fixed frame with its origin at the location where the evaluation of motion begins, which is typically the starting point in a runway for the case of aircraft. It is common to approximate the inertial coordinate frame with a north-east-down (NED) reference frame, with north, indicating the $x-$direction, east indicating the $y-$direction, and down referring to the $z-$direction. The NED coordinate frame is based on a flat non-rotating earth, which is a valid assumption offering good approximation for short-duration low-speed UAV applications. The inertial reference frame is depicted in Figure 3.1. The subscript and superscript (NED) will be used to denote this coordinate frame.

3.1.2 Body-Fixed Frame

The body-fixed frame is an orthogonal frame that has its origin is at the aircraft's centre of gravity. This frame is fixed to the aircraft's body and always rotates with it. It is chosen to create symmetry about the body of the aircraft. The positive $x-$axis of this frame points towards the aircraft's nose, along some convenient reference line, such as a zero angle-of-attack line, or watermark line of the fuselage. The positive $y-$axis is pointed in

Stellenbosch University https://scholar.sun.ac.za

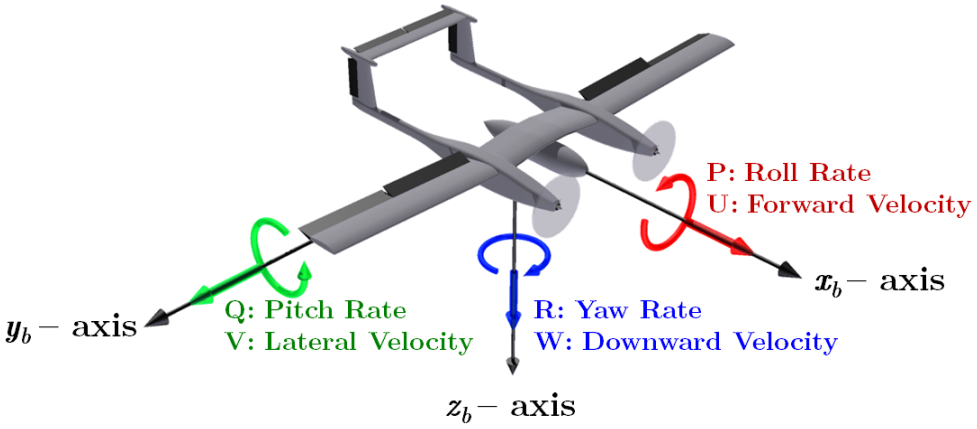

Figure 3.2: Body fixed reference frame. Adapted from [3]

the direction of the right-wing. The positive $z-$axis is normal to both axes and is pointed downward. The origin of the frame is located at the aircraft's centre of mass. The frame is denoted with the subscript and superscript b. This frame is depicted in Figure 3.2

3.1.3 Euler Angles

In this thesis, Euler angles (ψ, θ, ϕ) are used to parameterise the UAV's attitude. Just before taking off, the UAV's body reference frame will be aligned perfectly with the NED reference plane. As the UAV begins to move, its attitude is characterised by three Euler rotations ψ, θ, and ϕ, representing the yaw, pitch and roll angles respectively, referenced to the NED frame. The rotation angles are depicted in Figure 3.3. The complete rotation comes about as follows:

- Transform the NED coordinate frame into an intermediate frame 1 by rotating the frame about the z_E axis, with an angle ϕ indicating the heading of the aircraft.
- Next, rotate the frame about the new y_1 axis with an angle θ, which specifies the aircraft's elevation.
- Finally, a rotation about the new x_2 axis by a bank angle ϕ completes the transformation.

Figures 3.3 and 3.4 depicts the Euler rotations and the transformation from the NED frame to the body-fixed frame

Stellenbosch University https://scholar.sun.ac.za

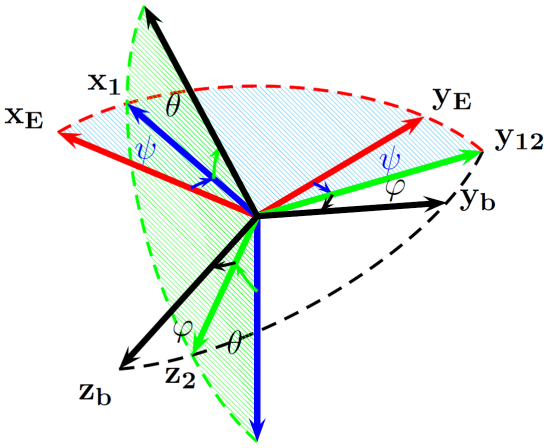

Figure 3.3: Euler rotations. Adapted from [4]

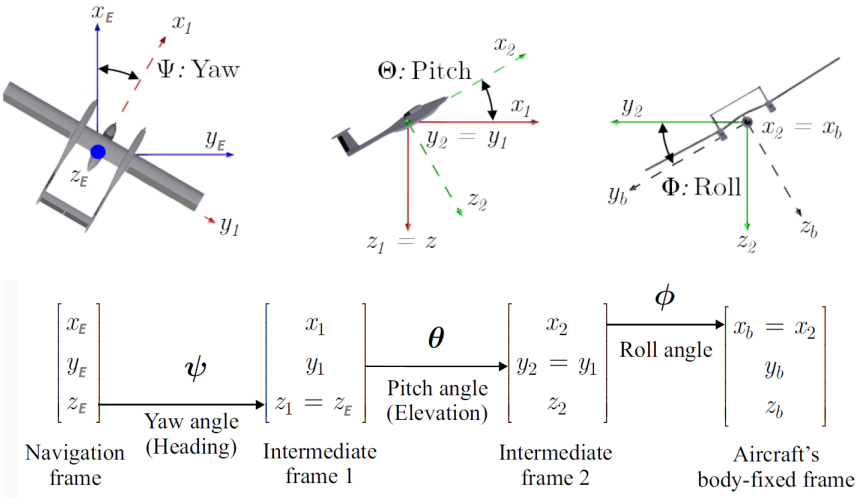

Figure 3.4: Euler angles and frame transformation (from NED to body-fixed frame). Adapted from [3]

Stellenbosch University https://scholar.sun.ac.za

3.1.4 Direction Cosine Matrices

The transformation of the coordinate frames from one to the other is archived through two mathematical operations: rotation and translation. The direction cosine matrix (DCM), which is also called the attitude transformation matrix, is used transform vectors and point coordinates from the (NED) coordinate frame to the aircraft's body-fixed frame (b) and vice versa. The three ordered sequence of Euler angle rotations depicted in Figures 3.3 and 3.4 can be represented by the following transformation matrices.

$$\mathcal{R}_{\psi} = \begin{bmatrix} \cos\psi & \sin\psi & 0 \\ -\sin\psi & \cos\psi & 0 \\ 0 & 0 & 1 \end{bmatrix} \tag{3.1.8}$$

$$\mathcal{R}_{\theta} = \begin{bmatrix} \cos\theta & 0 & -\sin\theta \\ 0 & 1 & 0 \\ \sin\theta & 0 & \cos\theta \end{bmatrix} \tag{3.1.9}$$

$$\mathcal{R}_{\phi} = \begin{bmatrix} 1 & 0 & 0 \\ 0 & \cos\phi & \sin\phi \\ 0 & -\sin\phi & \cos\phi \end{bmatrix} \tag{3.1.10}$$

The complete transformation from the inertial reference frame to UAV body-fixed frame is given by the sequence product of the above matrices as follows:

$$\mathcal{R}_{NED\to b} = \mathcal{R}_{\phi}\mathcal{R}_{\theta}\mathcal{R}_{\psi} \tag{3.1.11}$$

$$= \begin{bmatrix} \cos\theta\cos\psi & \cos\theta\sin\theta & -\sin\theta \\ \sin\phi\sin\theta\cos\psi - \cos\phi\sin\psi & \sin\phi\sin\theta\sin\psi + \cos\phi\cos\psi & \sin\phi\cos\theta \\ \cos\phi\sin\theta\cos\psi + \sin\phi\sin\psi & \cos\phi\sin\theta\sin\psi - \sin\phi\cos\phi & \cos\phi\cos\theta \end{bmatrix}$$

The DCM $\mathcal{R}_{NED\to b}$ and belongs to a class of orthonormal transformation matrices, able to rotate points without deforming them. The DCM is used to transform a vector $\boldsymbol{p}^{NED}$ expressed in the NED frame into a vector expressed in the UAV body-fixed frame $\boldsymbol{p}^{b}$ as follows:

$$\boldsymbol{p}^{b} = \mathcal{R}_{NED\to b}\boldsymbol{p}^{NED} \tag{3.1.12}$$

3.1.5 Wind Frame

As the UAV moves through its surrounding air, aerodynamic forces are generated. The aircraft's velocity relative to the surrounding air is called

Stellenbosch University https://scholar.sun.ac.za

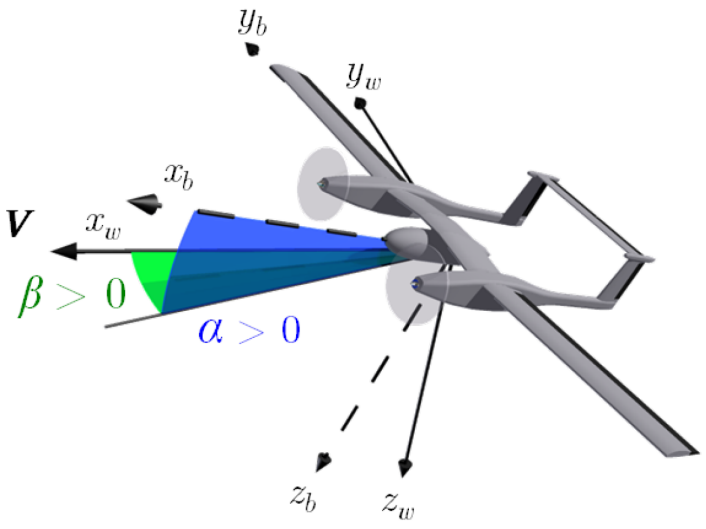

Figure 3.5: Wind coordinate axis, with a positive angle of attack and sideslip angle. Adapted from [3]

airspeed vector $\boldsymbol{V}_T$, and its magnitude is called the airspeed V_T. Lift is produced when the aircrafts' wings have a positive angle relative to the airspeed vector. This angle is called the angle of attack and represented with the symbol α. As depicted in Figure 3.5, the angle of attack is defined as the angle produced between the projection of the airspeed vector $\boldsymbol{V}_T$ onto the (x_b, z_b) plane and the x_b axis. The second angle is called the sideslip angle β, which is the angle between the airspeed vector $\boldsymbol{V}_T$ and the projection of the airspeed vector onto the (x_b, z_b) plane. The wind coordinate frame has its x_w axis aligned with the airspeed vector $\boldsymbol{V}_T$. The transformation of any vector from the body-fixed coordinate frame to the stability axis is given by

$$\boldsymbol{p}^s = \mathcal{R}_\alpha \boldsymbol{p}^b \tag{3.1.13}$$

where

$$\mathcal{R}_\alpha = \begin{bmatrix} \cos\alpha & 0 & \sin\alpha \\ 0 & 1 & 0 \\ -\sin\alpha & 0 & \cos\alpha \end{bmatrix} \tag{3.1.14}$$

As shown in Figure 3.5, the wind frame is completed by a right-handed rotation of β about the new $z-$axis from the first rotation by α. The wind

Stellenbosch University https://scholar.sun.ac.za

axis x_w is aligned with the airspeed vector $\boldsymbol{V}_T$. The transformation from stability frame to the wind frame is given by:

$$\boldsymbol{p}^w = \mathcal{R}_\beta \boldsymbol{p}^s \tag{3.1.15}$$

where

$$\mathcal{R}_\beta = \begin{bmatrix} \cos\beta & \sin\beta & 0 \\ -\sin\beta & \cos\beta & 0 \\ 0 & 0 & 1 \end{bmatrix} \tag{3.1.16}$$

The complete transformation from the body-fixed coordinate frame to the wind coordinate frame is given by

$$\boldsymbol{p}^w = \mathcal{R}_{b\to w} \boldsymbol{p}^b \tag{3.1.17}$$

where

$$\mathcal{R}_{b\to w} = \mathcal{R}_\beta \mathcal{R}_\alpha \tag{3.1.18}$$

$$= \begin{bmatrix} \cos\beta & \sin\beta & 0 \\ -\sin\beta & \cos\beta & 0 \\ 0 & 0 & 1 \end{bmatrix} \begin{bmatrix} \cos\alpha & 0 & \sin\alpha \\ 0 & 1 & 0 \\ -\sin\alpha & 0 & \cos\alpha \end{bmatrix} \tag{3.1.19}$$

$$= \begin{bmatrix} \cos\alpha\cos\beta & \sin\beta & \sin\alpha\cos\beta \\ -\sin\beta\cos\alpha & \cos\beta & -\sin\alpha\sin\beta \\ -\sin\alpha & 0 & \cos\alpha \end{bmatrix} \tag{3.1.20}$$

3.1.6 Airspeed, Ground Speed, and Wind Speed

The inertial forces that the aircraft experiences depend on velocities and accelerations relative to the inertial reference frame. On the other hand, aerodynamic forces are dependent on the aircraft's velocity relative to the surrounding air. In the absence of wind, these velocities will be the same. However, there will always be wind present, and thus it is necessary to differentiate between airspeed $\boldsymbol{V}_T$, and the ground speed, defined as the velocity with respect to the inertial frame $\boldsymbol{V}_g$. The relation between the airspeed and groundspeed is given by the expression

$$\boldsymbol{V}_T = \boldsymbol{V}_g - \boldsymbol{V}_w \tag{3.1.21}$$

Stellenbosch University https://scholar.sun.ac.za

where $\boldsymbol{V}_w$ represent the wind velocity describe with respect to the inertial frame. The ground velocity $\boldsymbol{V}_g$ can be written componentwise along the x_b, y_b, and z_b axes, expressed in the body frame

$$\boldsymbol{V}_g^b = \begin{bmatrix} u \\ v \\ w \end{bmatrix} \tag{3.1.22}$$

Likewise, the wind velocity can be written in terms of the north, east, and down components; w_n, w_e, and w_d respectively and an expressed in the body frame as

$$\boldsymbol{V}_w = \begin{bmatrix} u_w \\ v_w \\ w_w \end{bmatrix} = \mathcal{R}_{NED\to b} \begin{bmatrix} u_n \\ v_e \\ w_d \end{bmatrix} \tag{3.1.23}$$

Observe that when expressed in the wind coordinate frame, the airspeed vector $\boldsymbol{V}_T$ is given by

$$\boldsymbol{V}_T^w = \begin{bmatrix} V_T \\ 0 \\ 0 \end{bmatrix} \tag{3.1.24}$$

And by defining u_T, v_T, and w_T as the components of the airspeed vector in the body-fixed coordinate frame as

$$\boldsymbol{V}_T = \begin{bmatrix} u_T \\ v_T \\ w_T \end{bmatrix} = \begin{bmatrix} u - u_w \\ v - v_w \\ w - w_w \end{bmatrix} \tag{3.1.25}$$

Then the angle of attack and the sideslip angle can be directly used to express airspeed vector in from the airspeed magnitude as follows:

$$\boldsymbol{V}_T = \begin{bmatrix} u_T \\ v_T \\ w_T \end{bmatrix} = \mathcal{R}_{w\to b} \begin{bmatrix} V_T \\ 0 \\ 0 \end{bmatrix} \tag{3.1.26}$$

$$= \begin{bmatrix} \cos\alpha\cos\beta & -\sin\beta\cos\alpha & -\sin\alpha \\ \sin\beta & \cos\beta & 0 \\ \sin\alpha\cos\beta & -\sin\alpha\sin\beta & \cos\alpha \end{bmatrix} \begin{bmatrix} V_T \\ 0 \\ 0 \end{bmatrix}$$

which lead to the following results

$$\begin{bmatrix} u_T \\ v_T \\ w_T \end{bmatrix} = V_T \begin{bmatrix} \cos\alpha\cos\beta \\ \sin\beta \\ \sin\alpha\cos\beta \end{bmatrix} \tag{3.1.27}$$

Stellenbosch University https://scholar.sun.ac.za

Given that aerodynamic forces and moments are expressed in terms of V_T, α, and β, the above expression is inverted to result in:

$$V_T = \sqrt{u_T^2 + v_T^2 + w_T^2} \tag{3.1.28a}$$

$$\alpha = \arctan\left(\frac{w_T}{u_T}\right) \tag{3.1.28b}$$

$$\beta = \arcsin\left(\frac{v_T}{V_T}\right) \tag{3.1.28c}$$

3.2 Model of the Low Altitude Atmosphere

A key parameter affecting the aerodynamic forces is the dynamic pressure given by:

$$\bar{q} = \frac{\rho V_T}{2} \tag{3.2.1}$$

In the nonlinear simulation, the air density ρ computed in realtime at specific altitudes with atmospheric model:

$$T = T_0\left[1 + \frac{ah}{T_0}\right] \tag{3.2.2}$$

$$\rho = \frac{p_0\left[1 + \frac{ah}{T_0}\right]^{5.2561}}{RT} \tag{3.2.3}$$

where $T_0 = 288.15$ K represents temperature, and the remaining parameters are $R = 287.3\text{m}^2\text{K}^{-1}s^{-2}$, $a = -6.5 \times 10^{-3}$ K/m, and $p_0 = 1013 \times 10^2$ Nm^{-2}. For the trimmed model at an altitude of $h = 800$ m, the value of the air density is calculated as $\rho = 1.1323$ kgm^{-3}.

3.3 Forces and Moments Acting on the UAV

This section describes the external forces and moments experienced by the UAV. These forces and moments are generated primarily by gravity, engine thrust, aerodynamics, wind disturbances and turbulence.

3.3.1 Gravitational Forces and Moments

The nonlinear simulation model developed in this study assumes a flight altitude of the UAV is insignificant as compared to earth the's radius. Earth's gravitational force is act on the aircraft's' centre of gravity (CG) in

Stellenbosch University https://scholar.sun.ac.za

a downward direction. For convenience, the gravitational forces are written in the NED coordinate frame as follows:

$$\boldsymbol{F}_{grav}^{NED} = \begin{bmatrix} 0 \\ 0 \\ mg \end{bmatrix} \tag{3.3.1}$$

The gravitation forces can be expressed in the other coordinate systems by transformation with the appropriate rotation matrix. Given that the gravitational forces act on the CG, which is also chosen as that centre of the body-fixed coordinate frame, there are no moments induced by gravity, such that;

$$\boldsymbol{M}_{grav} = \begin{bmatrix} 0 & 0 & 0 \end{bmatrix}^T \tag{3.3.2}$$

3.3.2 Engine Forces and Moments

The Meraka Modular UAV studied in this thesis has two engines that are located on both sides of the aircraft and symmetrical about the $(x_b - z_b)$ plane. The thrust force vector produced by the two propellers always points in the direction of the x_b axis. The flight control system is designed to generate thrust vectors that are always equal; therefore there is no thrust vectoring used in the UAV. The thrust vector always acts through the aircraft's CG. The effects of the propellers on the moments very minimal, and considered to be zero;

$$\boldsymbol{M}_{prop} = \begin{bmatrix} 0 & 0 & 0 \end{bmatrix}^T \tag{3.3.3}$$

$$\boldsymbol{F}_{prop}^{b} = \begin{bmatrix} F_{prop} & 0 & 0 \end{bmatrix}^T \tag{3.3.4}$$

Several propulsion models can be found in the literature for the various types of aircraft engines; however, a simple first-order lag model is utilised in the nonlinear simulation model in this study. This model sufficiently captures the band-limited nature of the propulsive system in small UAVs. This model is given by:

$$\dot{F}_{prop} = -\frac{1}{\tau} F_{prop} + \frac{1}{\tau} \delta_{prop} \tag{3.3.5}$$

where F_{prop} is the magnitude of the propulsive force, δ_{prop} the propulsion command and τ the engine lag time constant.

Stellenbosch University https://scholar.sun.ac.za

3.3.3 Aerodynamic Forces and Moments

The aerodynamic forces and moments are induced by airframe's interaction with the incoming airflow. The amount of air diverted by the aircraft during flight determines the magnitude and direction of the resulting forces and moments. The total air-mass diverted by the airframe is determined by the following:

- the speed of the airflow and the air density (V_T, ρ)
- the geometrical features of the aircraft $(S_{ref}, \bar{c}, b)$
- the deflections in the control surfaces
- the orientation of the aircraft with respect to the airflow (α, β)
- the aircraft's angular rates (p, q, r)

where S_{ref} denotes the reference surface area of the aircraft's wing, $\bar{c}$ denotes the aerodynamic mean-chord and b_{ref} the reference wingspan. The forces and moments are expressed in the reference frames that makes their formulation the simplest. The aerodynamic forces, namely; drag, lift and side force, are expressed in the wind reference frame according to:

$$\boldsymbol{F}^{w}_{aero} = \bar{q} S_{ref} \begin{bmatrix} -C_D \\ C_Y \\ -C_L \end{bmatrix} \tag{3.3.6}$$

where the parameters C_L, C_D and C_Y denotes the nondimensional aerodynamic coefficients of the lift force, drag force and side force respectively. The aerodynamic force coefficients are obtained by a linear combination of control inputs and elements of the state as follows.

$$\begin{aligned}
C_D =& C_{D_0} + \frac{C_L^2}{\pi A R e} \\
C_L =& C_{L_0} + C_{L_\alpha}\alpha + \frac{\bar{c}}{2V_T} C_{L_q} q + C_{L_{\delta_{Er}}}\delta_{Er} + C_{L_{\delta_{El}}}\delta_{El} + C_{L_{\delta_{Ar}}}\delta_{Ar} + C_{L_{\delta_{Al}}}\delta_{Al} \\
C_Y =& C_{Y_\beta}\beta + \frac{b}{2V_T} C_{Y_p} p + \frac{b}{2V_T} C_{Y_r} r + C_{Y_{\delta_{Er}}}\delta_{Er} C_{Y_{\delta_{El}}}\delta_{El} + C_{Y_{\delta_{Ar}}}\delta_{Ar} + C_{Y_{\delta_{Al}}}\delta_{Al} \\
& + C_{Y_{\delta_{Rr}}}\delta_{Rr} + C_{Y_{\delta_{Rl}}}\delta_{Rl}
\end{aligned} \tag{3.3.7}$$

Stellenbosch University https://scholar.sun.ac.za

The deflections in the control surfaces and any asymmetric airflow about the airframe will induce pitching moment M, rolling moment L and yawning N moment. It is convenient to express these moments in the body-fixed reference frame as follows:

$$\boldsymbol{M}^b_{aero} = \bar{q} S_{ref} \begin{bmatrix} bC_l \\ \bar{c}C_m \\ bC_n \end{bmatrix} \tag{3.3.8}$$

where C_l, C_m and C_n denote the nondimensional aerodynamic coefficients of the rolling, pitching and yawing moments respectively. Again, these coefficients are expressed as a linear combination of the control inputs and elements of the aircraft's states:

$$\begin{aligned} C_l =& C_{l_\beta}\beta + \frac{b}{2V_T}C_{l_p}p + \frac{b}{2V_T}C_{l_r}r + C_{l_{\delta_{Er}}}\delta_{Er} + C_{l_{\delta_{El}}}\delta_{El} + C_{l_{\delta_{Ar}}}\delta_{Ar} + C_{l_{\delta_{Al}}}\delta_{Al} \\ &+ C_{l_{\delta_{Rr}}}\delta_{Rr} + C_{l_{\delta_{Rl}}}\delta_{Rl} \\ C_m =& C_{m_0} + C_{m_\alpha}\alpha + \frac{\bar{c}}{2V_T}C_{m_q}q + C_{m_{\delta_{Er}}}\delta_{Er} + C_{m_{\delta_{El}}}\delta_{El} + C_{m_{\delta_{Ar}}}\delta_{Ar} + C_{m_{\delta_{Al}}}\delta_{Al} \\ &+ C_{m_{\delta_{Rr}}}|\delta_{Rr}| + C_{m_{\delta_{Rl}}}|\delta_{Rl}| \\ C_n =& C_{n_\beta}\beta + \frac{b}{2V_T}C_{n_p}p + \frac{b}{2V_T}C_{n_r}r + C_{n_{\delta_{Er}}}\delta_{Er} + C_{n_{\delta_{El}}}\delta_{El} + C_{n_{\delta_{Ar}}}\delta_{Ar} + C_{n_{\delta_{Al}}}\delta_{Al} \\ &+ C_{n_{\delta_{Rr}}}\delta_{Rr} + C_{n_{\delta_{Rl}}}\delta_{Rl} \end{aligned} \tag{3.3.9}$$

3.4 Kinematics and Dynamics

The nonlinear simulation in this study considers a short-range flight over a small region of the earth. These flight conditions allow the following simplifying assumptions to be presumed without significant loss of accuracy in the nonlinear model, which are:

- The Earth is locally flat ($R_{earth} = \infty$)
- The earth is not rotating (there are no Coriolis accelerations from the earth's rotation). This assumption makes the earth an inertial reference frame where Newton's laws apply.
- The aircraft has a constant mass

Stellenbosch University https://scholar.sun.ac.za

- The aircraft is symmetric about the plane spanned by x_b and z_b.
- The aircraft has a rigid body

3.4.1 The Position and Propagation of the Aircraft

The realtime position vector of the aircraft in $3D$ space (x_n, y_e, z_n) is expressed in the earth-fixed inertial frame. The position vector is obtained by integrating the aircraft's ground speed. However, the translational velocity vector of the aircraft is expressed in the body-fixed coordinate frame. The expression of the position vector requires a rotational transformation of the velocity vector from the body-fixed frame to the NED coordinate frame as follows:

$$\frac{d}{dt}\begin{bmatrix} x_n \\ y_e \\ z_d \end{bmatrix} = \mathcal{R}_{b\to NED}\begin{bmatrix} u \\ v \\ w \end{bmatrix} = (\mathcal{R}_{NED\to b})^{\intercal}\begin{bmatrix} u \\ v \\ w \end{bmatrix} \tag{3.4.1}$$

3.4.2 Attitude Rates

The aircraft's angular rates are expressed in the body-fixed coordinate frame. The Euler angles are derived from three coordinate frames rotations as depicted in Figure 3.4. The angular velocities addition theorem [79] states that; for angular velocity vectors in a common coordinate frame, the resulting angular velocity of the total rotation is given by the sum of the individual rotations. The rotating frame is given by time-varying angles, (ψ, θ, ψ) and the angular velocity vector (p, q, r) can be determined as if measured in the rotating frame. Starting with the initial stationary frame and using the two intermediate frames whose relative angular velocities are given by the Euler angle rates $(\dot{\psi}, \dot{\theta}, \dot{\phi})$, the angular rates are given by the velocities addition theorem according to the following kinematic equation:

$$\begin{bmatrix} p \\ q \\ r \end{bmatrix} = \begin{bmatrix} \dot{\phi} \\ 0 \\ 0 \end{bmatrix} + \mathcal{R}_{\phi}\begin{bmatrix} 0 \\ \dot{\theta} \\ 0 \end{bmatrix} + \mathcal{R}_{\phi}\mathcal{R}_{\theta}\begin{bmatrix} 0 \\ 0 \\ \dot{\psi} \end{bmatrix} \tag{3.4.2}$$

Stellenbosch University https://scholar.sun.ac.za

$$= \begin{bmatrix} \dot{\phi} \\ 0 \\ 0 \end{bmatrix} + \begin{bmatrix} 1 & 0 & 0 \\ 0 & \cos\phi & \sin\phi \\ 0 & -\sin\phi & \cos\phi \end{bmatrix} \begin{bmatrix} 0 \\ \dot{\theta} \\ 0 \end{bmatrix} + \begin{bmatrix} 1 & 0 & 0 \\ 0 & \cos\phi & \sin\phi \\ 0 & -\sin\phi & \cos\phi \end{bmatrix} \begin{bmatrix} \cos\theta & 0 & -\sin\theta \\ 0 & 1 & 0 \\ \sin\theta & 0 & \cos\theta \end{bmatrix} \begin{bmatrix} 0 \\ 0 \\ \dot{\psi} \end{bmatrix}$$

$$= \begin{bmatrix} 1 & 0 & -\sin\theta \\ 0 & \cos\phi & \sin\phi\cos\theta \\ 0 & -\sin\theta & \cos\phi\cos\theta \end{bmatrix} \begin{bmatrix} \dot{\phi} \\ \dot{\theta} \\ \dot{\psi} \end{bmatrix}$$

The above equation is inverted and to find the propagation of the Euler angles $(\dot{\psi}, \dot{\theta}, \dot{\phi})$ in time is as follows:

$$\begin{bmatrix} \dot{\phi} \\ \dot{\theta} \\ \dot{\psi} \end{bmatrix} = \begin{bmatrix} 1 & \sin\phi\tan\theta & \cos\phi\tan\theta \\ 0 & \cos\phi & -\sin\phi \\ 0 & \sin\phi\sec\theta & \cos\phi\sec\theta \end{bmatrix} \begin{bmatrix} p \\ q \\ r \end{bmatrix} \tag{3.4.3}$$

3.4.3 Conservation of Linear Momentum

Newton's second law of motion relates the mass m of an object and the change in its velocity vector $\boldsymbol{V}_g$ to the force vectors $\boldsymbol{F}_j$ acting on the object as follows:

$$\sum_j \boldsymbol{F}_j = \left[\frac{d}{dt}\left(m\boldsymbol{V}_g\right)\right]_{NED} \tag{3.4.4}$$

The subscript (NED) denotes that the time derivative in the expression is computed in the earth-fixed inertial reference plane. However, it is convenient to express in the body-fixed reference (which rotates with the UAV) frame for control and system identification. But the Newtons' law applies to a point mass located at the object's CG in a non-rotating inertial frame.

According to Coriolis's theorem, the time derivative of any time-varying vector $\boldsymbol{p}(t)$, expressed relative to two different frames $\mathcal{F}_1$ and $\mathcal{F}_2$ is given by Equation (3.4.5).

$$\left[\frac{d}{dt}\boldsymbol{p}(t)\right]_{\mathcal{F}_1} = \left[\frac{d}{dt}\boldsymbol{p}(t)\right]_{\mathcal{F}_2} + \boldsymbol{\omega}_{\mathcal{F}_2/\mathcal{F}_1} \times \boldsymbol{p}(t) \tag{3.4.5}$$

where $\boldsymbol{\omega}_{\mathcal{F}_2/\mathcal{F}_1}$ is the rotational rate of the frame $\mathcal{F}_2$ with respect to the frame $\mathcal{F}_1$.

Stellenbosch University https://scholar.sun.ac.za

For the case of a manoeuvring aircraft, the expression (3.4.4) can be rewritten in the form (3.4.5) and expressed in the body-fixed frame denoted with the subscript b as follows

$$\frac{1}{m}\left[\sum_j \boldsymbol{F}_j\right] = \left[\frac{d}{dt}\left(\boldsymbol{V}_g\right)\right]_{NED} = \left[\frac{d}{dt}\left(\boldsymbol{V}_g\right)\right]_b + \boldsymbol{\omega}_{b/NED} \times \boldsymbol{V}_g, \tag{3.4.6}$$

where $\boldsymbol{V}_g = (u, v, w)^T$ and $\boldsymbol{\omega}_{b/NED} = (p, q, r)^T$. The subscript in $\boldsymbol{\omega}_{b/NED}$ is omitted in all expressions in the remainder of this thesis. By substitution, the below expression is obtained:

$$\frac{1}{m}\left[\boldsymbol{F}^b_{grav} + \boldsymbol{F}^b_{prop} + \boldsymbol{F}^b_{aero}\right] = \begin{bmatrix}\dot{u}\\ \dot{v}\\ \dot{w}\end{bmatrix} + \begin{bmatrix}p\\ q\\ r\end{bmatrix} \times \begin{bmatrix}u\\ v\\ w\end{bmatrix} \tag{3.4.7}$$

The gravitational and aerodynamical forces are most conveniently expressed in the (NED) and wind coordinate frames respectively. Therefore, the gravitational and aerodynamical forces as given in equations (3.3.1) and (3.3.6) are projected onto the body-fixed coordinate frame according to the following two expressions:

$$\boldsymbol{F}^b_{grav} = \mathcal{R}_{NED\to b}\begin{bmatrix}0\\ 0\\ mg\end{bmatrix} = \begin{bmatrix}-mg\sin\theta\\ mg\cos\theta\sin\phi\\ mg\cos\theta\cos\phi\end{bmatrix} \tag{3.4.8}$$

$$\boldsymbol{F}^b_{aero} = \mathcal{R}_{w\to b}\bar{q}S_{ref}\begin{bmatrix}-C_D\\ C_Y\\ -C_L\end{bmatrix} = \bar{q}S_{ref}\begin{bmatrix}\cos\alpha\cos\beta & -\sin\beta\cos\alpha & -\sin\alpha\\ \sin\beta & \cos\beta & 0\\ \sin\alpha\cos\beta & -\sin\alpha\sin\beta & \cos\alpha\end{bmatrix}\begin{bmatrix}-C_D\\ C_Y\\ -C_L\end{bmatrix} \tag{3.4.9}$$

By substituting Equations (3.4.8) and (3.4.9) into (3.4.7), expanding the cross product in and rearranging the expression results in:

$$\begin{bmatrix}\dot{u}\\ \dot{v}\\ \dot{w}\end{bmatrix} = \begin{bmatrix}rv - qw\\ pw - ru\\ qu - pv\end{bmatrix} + \begin{bmatrix}-g\sin\theta\\ g\cos\theta\sin\phi\\ g\cos\theta\cos\phi\end{bmatrix} + \frac{1}{m}\left(\begin{bmatrix}F_{prop}\\ 0\\ 0\end{bmatrix} + \mathcal{R}_{w\to b}\bar{q}S_{ref}\begin{bmatrix}-C_D\\ C_Y\\ -C_L\end{bmatrix}\right) \tag{3.4.10}$$

Stellenbosch University https://scholar.sun.ac.za

Resolving the above equations result in the individual nonlinear equations:

$$\dot{u} = rv - qw - g\sin\theta + \frac{F_{prop}}{m} + \frac{\bar{q}S}{m}\left(-C_D\cos\alpha\cos\beta - C_Y\cos\alpha\sin\beta + C_L\sin\alpha\right) \tag{3.4.11}$$

$$\dot{v} = pw - ru + g\cos\theta\sin\phi + \frac{\bar{q}S}{m}\left(-C_D\sin\beta + C_Y\cos\beta\right) \tag{3.4.12}$$

$$\dot{w} = qu - pv + g\cos\theta\cos\phi + \frac{\bar{q}S}{m}\left(-C_D\sin\alpha\cos\beta - C_Y\sin\alpha\sin\beta - C_L\cos\alpha\right) \tag{3.4.13}$$

It is convenient to express the body-fixed velocities in a polar form by the airspeed magnitude, the angle of attack and the side-slip angle, (V_T, α, β), which are directly measured by sensing equipment fixed to the UAV. The derivation of the corresponding nonlinear Equations is detailed in Appendix C

3.4.4 Conservation of Angular Momentum

Newton's second law describes rotational motion as follows:

$$\sum_j \boldsymbol{M}_j = \left[\frac{d}{dt}(\mathbf{h})\right]_{NED} \tag{3.4.14}$$

Newton's second law describes rotational motion as follows: where $\mathbf{h}$ denotes the aircraft's angular momentum and $\sum_j \boldsymbol{M}_j$ is the sum of all external moments acting on the aircraft. The time derivative of angular momentum is expressed in terms of Equation 3.4.5 to obtain:

$$\sum_j \boldsymbol{M}_j = \left[\frac{d}{dt}(\mathbf{h})\right]_b + \boldsymbol{\omega}\times\mathbf{h} \tag{3.4.15}$$

For the case of a rigid body, the angular momentum is the product of the inertia matrix $\boldsymbol{I}$ and the rotational rate: $\mathbf{h} \triangleq \boldsymbol{I}\times\boldsymbol{\omega}$. Assuming symmetry about the place x_b and z_b, $\boldsymbol{I}$ is given by:

$$\boldsymbol{I} = \begin{bmatrix} I_{xx} & 0 & -I_{xz} \\ 0 & I_{yy} & 0 \\ -I_{xz} & 0 & I_{zz} \end{bmatrix} \tag{3.4.16}$$

Expanding Equation (3.4.15) results in:

$$[\boldsymbol{M}_{grav} + \boldsymbol{M}_{prop} + \boldsymbol{M}_{aero}] = \dot{\boldsymbol{I}}\boldsymbol{\omega} + \boldsymbol{I}\dot{\boldsymbol{\omega}} + \boldsymbol{\omega}\times\boldsymbol{I}\boldsymbol{\omega} \tag{3.4.17}$$

Stellenbosch University https://scholar.sun.ac.za

Based on assumptions made in Section 3.4, we have $\boldsymbol{M}_{grav} \approx 0$, $\boldsymbol{M}_{prop} \approx 0$ and $\dot{\boldsymbol{I}} \approx 0$, resulting in:

$$\begin{bmatrix} \dot{p} \\ \dot{q} \\ \dot{r} \end{bmatrix} = \boldsymbol{I}^{-1} \left(\begin{bmatrix} L_{aero} \\ M_{aero} \\ N_{aero} \end{bmatrix} - \begin{bmatrix} p \\ q \\ r \end{bmatrix} \times \boldsymbol{I} \begin{bmatrix} p \\ q \\ r \end{bmatrix} \right) \tag{3.4.18}$$

where the operation $\boldsymbol{I}^{-1}$ is the inverse of the inertia matrix computed as follows:

$$\begin{aligned} \boldsymbol{I}^{-1} &= \frac{\text{adj}(\boldsymbol{I})}{\det(\boldsymbol{I})} \\ &= \frac{\begin{bmatrix} I_{yy}I_{zz} & 0 & I_{yy}I_{xz} \\ 0 & I_{xx}I_{zz} - I_{xz}^2 & 0 \\ I_{xz}I_{yy} & 0 & I_{xx}I_{yy} \end{bmatrix}}{I_{xx}I_{yy}I_{zz} - I_{xz}^2 I_{yy}} \\ &= \begin{bmatrix} \frac{I_{zz}}{I_D} & 0 & \frac{I_{xz}}{I_D} \\ 0 & \frac{1}{I_{yy}} & 0 \\ \frac{I_{xz}}{I_D} & 0 & \frac{I_{xx}}{I_D} \end{bmatrix} \end{aligned} \tag{3.4.19}$$

where $I_D = I_{xx}I_{zz} - I_{xz}^2$. The cross-product involving angular rates in Equation (3.4.18) can be substituted with the cross-product equivalent matrix of angular rates given by:

$$\begin{bmatrix} 0 & -r & q \\ r & 0 & -p \\ -q & p & 0 \end{bmatrix}$$

The Equation 3.4.18 can now be expressed as:

$$\begin{bmatrix} \dot{p} \\ \dot{q} \\ \dot{r} \end{bmatrix} = \begin{bmatrix} \frac{I_{zz}}{I_D} & 0 & \frac{I_{xz}}{I_D} \\ 0 & \frac{1}{I_{yy}} & 0 \\ \frac{I_{xz}}{I_D} & 0 & \frac{I_{xx}}{I_D} \end{bmatrix} \left\{ \begin{bmatrix} L_{aero} \\ M_{aero} \\ N_{aero} \end{bmatrix} - \begin{bmatrix} 0 & -r & q \\ r & 0 & -p \\ -q & p & 0 \end{bmatrix} \begin{bmatrix} I_{xx} & 0 & -I_{xz} \\ 0 & I_{yy} & 0 \\ -I_{xz} & 0 & I_{zz} \end{bmatrix} \begin{bmatrix} p \\ q \\ r \end{bmatrix} \right\} \tag{3.4.20}$$

Expanding the above results in the following differential equations:

Stellenbosch University https://scholar.sun.ac.za

$$\dot{p} = \frac{1}{I_D}\left[I_{xz}\left(I_x - I_y + I_z\right)pq - \left(I_z(I_z - I_y) + I_{xz}^2\right)qr + I_z L + I_{xz}N\right] \tag{3.4.21}$$

$$\dot{q} = \frac{1}{I_y}\left[\left(I_z - I_x\right)pr - I_{xz}\left(p^2 - r^2\right) + M\right] \tag{3.4.22}$$

$$\dot{r} = \frac{1}{I_D}\left[\left(I_x(I_x - I_y) + I_{xz}^2\right)pq - I_{xz}(I_x - I_y + I_z)qr\right] + \frac{1}{I_D}\left[I_{xz}L + I_x N\right] \tag{3.4.23}$$

3.5 Atmospheric Disturbances

This section discusses atmospheric disturbances and how they interrelate the dynamics of the aircraft. The UAV's flight will experience atmospheric disturbances in the form of wind turbulence, typically classified as wind gusts and wind shear. The wind velocity in Equation (3.1.21) in terms of steady wind and time-varying wind disturbances as:

$$\boldsymbol{V}_w = \boldsymbol{V}_{w_s} + \boldsymbol{V}_{w_g} \tag{3.5.1}$$

where $\boldsymbol{V}_{w_s}$ represents the steady ambient wind component, and $\boldsymbol{V}_{w_g}$ is a stochastic process characterising wind gusts and other disturbances in the atmosphere. The steady wind is expressed in the (NED) coordinate frame as:

$$\boldsymbol{V}_{w_s}^{NED} = \begin{bmatrix} w_{n_s} \\ w_{e_s} \\ w_{d_s} \end{bmatrix} \tag{3.5.2}$$

where w_{n_s}, w_{e_s} and w_{d_s} denote the component of the steady wind in the north, east direction, downward directions respectively. The gust components are expressed in the body-fixed coordinate frame as follows

$$\boldsymbol{V}_{w_g}^{b} = \begin{bmatrix} u_{w_g} \\ v_{w_g} \\ w_{w_g} \end{bmatrix} \tag{3.5.3}$$

3.5.1 Atmospheric Turbulence Model Theory

Empirical data show that the non-steady gust portion of the wind model can be accurately simulated by passing white noise through linear filters

Stellenbosch University https://scholar.sun.ac.za

given by the von Karmen turbulence spectrum. However, von Karmen spectrum models do not yield rational transfer functions. The Dryden transfer functions are a good approximation of the von Karmen model and are given by:

$$H_u(s) = \sigma_u \sqrt{\frac{2L_u}{\pi V_T}} \cdot \frac{1}{1 + \left(\frac{L_u}{V_T}\right) s} \tag{3.5.4}$$

$$H_v(s) = \sigma_v \sqrt{\frac{L_v}{\pi V_T}} \cdot \frac{\left(1 + \frac{\sqrt{3}L_v}{V_T} s\right)}{\left(1 + \frac{L_v}{V_T} s\right)^2} \tag{3.5.5}$$

$$H_w(s) = \sigma_w \sqrt{\frac{L_w}{\pi V_T}} \cdot \frac{\left(1 + \frac{\sqrt{3}L_w}{V_T} s\right)}{\left(1 + \frac{L_w}{V_T}\right)^2} \tag{3.5.6}$$

where σ_u, σ_v, and σ_w indicate the turbulence intensities along the along body-frame axes. The parameters L_u, L_v,and L_w represents the spatial wavelengths; and V_T is the airspeed magnitude experienced by the aircraft. The military specification MIL-F-8785C gives the parameters for the Dryden gust model. Figure 3.5.1 is a depiction of how the atmospheric disturbances enter into the nonlinear dynamic equations. The gust components in the body-fixed frame are produced by passing white noise through the Dryden filters. The total wind in the body frame is obtained by first transforming the steady wind vector from the (NED) frame into the body-fixed coordinate frame, and adding the resulting vector to the gust vector.
.

$$\boldsymbol{V}_w^b = \mathcal{R}_{NED \to b} \begin{bmatrix} u_{n_s} \\ v_{e_s} \\ w_{d_s} \end{bmatrix} + \begin{bmatrix} w_{w_g} \\ w_{w_g} \\ w_{w_g} \end{bmatrix} \tag{3.5.7}$$

where $\mathcal{R}_{NED \to b}$ is the rotation matrix from the vehicle to the body frame given in equation. For computer simulation, the Dryden filters can be written in state-space format as

Stellenbosch University https://scholar.sun.ac.za

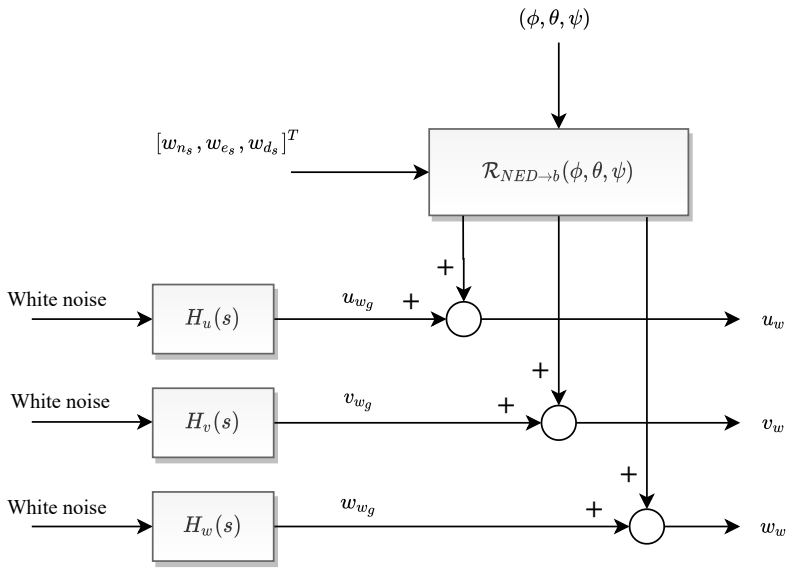

Figure 3.6: Atmospheric disturbance model with Dryden filters

$$\begin{bmatrix} \dot{u}_g(t) \\ \dot{v}_g(t) \\ \dot{v}_{g1}(t) \\ \dot{w}_g(t) \\ \dot{w}_{g1}(t) \end{bmatrix} = \begin{bmatrix} \frac{-V_T}{L_u} & 0 & 0 & 0 & 0 \\ 0 & \frac{-V_T}{L_v} & \sigma_v(1-\sqrt{3})\left(\frac{-V_T}{L_v}\right)^{3/2} & 0 & 0 \\ 0 & 0 & \frac{-V_T}{L_v} & 0 & 0 \\ 0 & 0 & 0 & \frac{-V_T}{L_w}\sigma_w(1-\sqrt{3})\left(\frac{-V_T}{L_w}\right)^{3/2} & \\ 0 & 0 & 0 & 0 & \frac{-V_T}{L_w} \end{bmatrix} \begin{bmatrix} u_g(t) \\ v_g(t) \\ v_{g1}(t) \\ w_g(t) \\ w_{g1}(t) \end{bmatrix} + \begin{bmatrix} \sigma_u\sqrt{\frac{2V_T}{\pi L_u}} \\ \sigma_v\sqrt{\frac{2V_T}{\pi L_v}} \\ 1 \\ \sigma_w\sqrt{\frac{2V_T}{\pi L_w}} \\ 1 \end{bmatrix} n(t) \tag{3.5.8}$$

where $n(t)$ is zero mean, band-limited noise with unit variance passed through the linear filters. A similar state-space model can be derived for the rotational gusts velocities using corresponding Dryden gust transfer functions. Dryden turbulence models can also be implemented using the Simulink Aerospace Toolbox package..

3.5.1.1 Low Altitude Model

The military document MIL-F-8785C specifies turbulence scale lengths for low altitudes (less than 1000 feet) according to the expressions:

Stellenbosch University https://scholar.sun.ac.za

$$L_w = h \tag{3.5.9}$$

$$L_u = L_v = \frac{h}{(0.177 + 0.000823h)^{1.2}} \tag{3.5.10}$$

where h represents the altitude. The typical wind speed at 6 meters height with the light intensity turbulence model is 7.7 m/s or 15.3 m/s with the moderate-intensity model. The turbulence intensities are given by the expressions:

$$\sigma_w = 0.1 W_{20} \tag{3.5.11}$$

$$\frac{\sigma_u}{\sigma_w} = \frac{\sigma_v}{\sigma_w} = L_v = \frac{h}{(0.177 + 0.000823h)^{0.4}} \tag{3.5.12}$$

where W_{20} is the wind speed at measured at 6 meters (20 feet).

3.5.1.2 Medium/High Altitude Model

The scale lengths and of the turbulence model for medium-to-high altitudes the are given by

$$L_u = L_v = L_w = 1750 \text{ ft} \tag{3.5.13}$$

The turbulence intensities for each for the same model are given by:

$$\sigma_u = \sigma_v = \sigma_w \tag{3.5.14}$$

The turbulence velocities and turbulence angular rates at altitudes from 1000 ft to 2000 ft are found by linear interpolation of values determined with the low-altitude model and the high-altitude model.

3.5.2 Discrete Gusts

The discrete wind gust model is incorporated into the model to simulate UAV's response to large wind disturbances. The discrete gusts are implemented with "1-cosine" build up as detailed in Equations (3.5.15)

$$V_w = \begin{cases} 0 & \text{if} \quad x < 0 \\ \frac{V_m}{2}\left(1 - \cos\left(\frac{\pi x}{d_m}\right)\right) & \text{if} \quad 0 \leq x \leq d_m \\ V_m & \text{if} \quad x > d_m \end{cases} \tag{3.5.15}$$

where V_m, d_m and x specifies the amplitude, the length and the distance travelled by the gust.

Stellenbosch University https://scholar.sun.ac.za

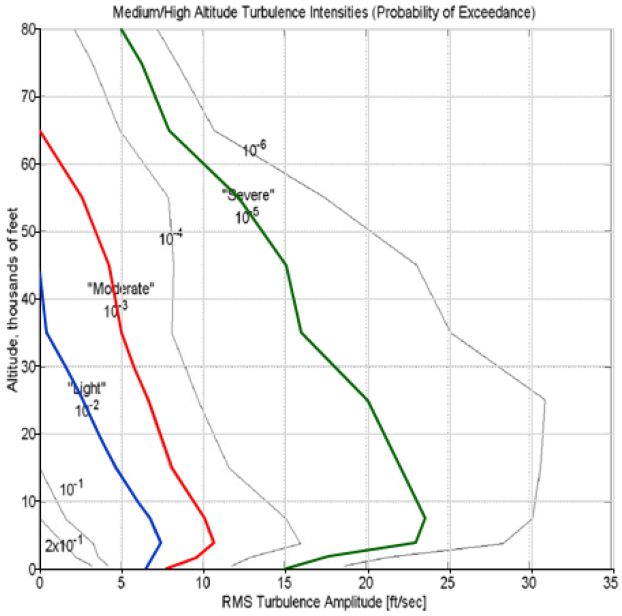

Figure 3.7: Medium/High altitudes turbulence intensities plots above 2000 feet. Adapted from [5]

3.6 Summary of the Nonlinear Aircraft Model

The complete set of 6-DoF nonlinear kinematic and dynamic equations characterising the motion of the UAV are reviewed below:

$$\begin{bmatrix} \dot{x} \\ \dot{y} \\ \dot{z} \end{bmatrix} = \begin{bmatrix} \cos\theta\cos\psi & \cos\theta\sin\theta & -\sin\theta \\ \sin\phi\sin\theta\cos\psi - \cos\phi\sin\psi & \sin\phi\sin\theta\sin\psi + \cos\phi\cos\psi & \sin\phi\cos\theta \\ \cos\phi\sin\theta\cos\psi + \sin\phi\sin\psi & \cos\phi\sin\theta\sin\psi - \sin\phi\cos\phi & \cos\phi\cos\theta \end{bmatrix} \begin{bmatrix} u \\ v \\ w \end{bmatrix} \tag{3.6.1}$$

Stellenbosch University https://scholar.sun.ac.za

$$\dot{u} = rv - qw - g\sin\theta + \frac{F_{prop}}{m} + \frac{\bar{q}S}{m}\left(-C_D\cos\alpha\cos\beta - C_Y\cos\alpha\sin\beta + C_L\sin\alpha\right) \tag{3.6.2}$$

$$\dot{v} = pw - ru + g\cos\theta\sin\phi + \frac{\bar{q}S}{m}\left(-C_D\sin\beta + C_Y\cos\beta\right) \tag{3.6.3}$$

$$\dot{w} = qu - pv + g\cos\theta\cos\phi + \frac{\bar{q}S}{m}\left(-C_D\sin\alpha\cos\beta - C_Y\sin\alpha\sin\beta - C_L\cos\alpha\right) \tag{3.6.4}$$

$$\dot{p} = \frac{1}{I_D}\left[I_{xz}\left(I_x - I_y + I_z\right)pq - \left(I_z(I_z - I_y) + I_{xz}^2\right)qr + I_zL + I_{xz}N\right] \tag{3.6.5}$$

$$\dot{q} = \frac{1}{I_y}\left[\left(I_z - I_x\right)pr - I_{xz}\left(p^2 - r^2\right) + M\right] \tag{3.6.6}$$

$$\dot{r} = \frac{1}{I_D}\left[\left(I_x(I_x - I_y) + I_{xz}^2\right)pq - I_{xz}(I_x - I_y + I_z)qr\right] + \frac{1}{I_D}\left[I_{xz}L + I_xN\right] \tag{3.6.7}$$

$$\dot{\phi} = p + q\sin\phi\tan\theta + r\cos\phi\tan\theta \tag{3.6.8}$$

$$\dot{\theta} = q\cos\phi - r\sin\phi \tag{3.6.9}$$

$$\dot{\psi} = (\sin\phi + r\cos\phi)\sec\theta \tag{3.6.10}$$

where $\theta \neq \pm\frac{\pi}{2}$. The values of the physical paramters of the Meraka Modular UAV involved in the above equations are are given in Table A.1.

3.7 Linearisation of the Nonlinear Aircraft Model

In this section, the nonlinear equations described in the previous section are linearised using small-perturbation theory. This approach assumes the motion of the aircraft consists of small deviations from and relative to the nominal flight conditions.

Some of the FDI techniques presented in this thesis are based on the linear representation of the aircraft. The TSKF requires determining the Jacobian associated with the nonlinear differential equations to characterise the evolution of the system states. The nonlinear kinematic and dynamics of equations detailed in (3.6.2) to (3.6.10) can be expressed more concisely as:

$$\dot{\boldsymbol{x}} = \boldsymbol{f}\left(\boldsymbol{x}, \boldsymbol{u}\right) \tag{3.7.1}$$

where system state $\boldsymbol{x}$ and the controls input $\boldsymbol{u}$ are chosen as:

Stellenbosch University https://scholar.sun.ac.za

$$\boldsymbol{x} = (V, \alpha, \beta, p, q, r, \phi, \theta, h)^T \tag{3.7.2}$$

$$\boldsymbol{u} = \left(\delta_{prop}, \delta_{E_r}, \delta_{E_l}, \delta_{A_r}, \delta_{A_l}, \delta_{R_r}, \delta_{R_l}\right)^T \tag{3.7.3}$$

and the vector function $\boldsymbol{f}$ characterises the nonlinear dynamic equations, $h = -z$ is the height of the aircraft's flight and δ_{prop} is the propulsive force setting. By replacing each state variable and control input as the sum of their nominal values and a small perturbation we get:

$$\boldsymbol{x} = \boldsymbol{x}_0 + \Delta\boldsymbol{x} \tag{3.7.4}$$

$$\boldsymbol{u} = \boldsymbol{u}_0 + \Delta\boldsymbol{u} \tag{3.7.5}$$

where

$$\Delta\boldsymbol{x} = (\Delta V, \Delta\alpha, \Delta\beta, \Delta p, \Delta q, \Delta r, \Delta\phi, \Delta\theta, \Delta h)^T \tag{3.7.6}$$

$$\Delta\boldsymbol{u} = \left(\Delta\delta_{prop}, \Delta\delta_{E_r}, \Delta\delta_{E_l}, \Delta\delta_{A_r}, \Delta\delta_{A_l}, \Delta\delta_{R_r}, \Delta\delta_{R_l}\right)^T \tag{3.7.7}$$

Replacing the variables in (3.7.1) with their perturbed versions and taking a Taylor series expansion yields

$$\dot{\boldsymbol{x}}_0 + \Delta\dot{\boldsymbol{x}} = \boldsymbol{f}(\boldsymbol{x}_0 + \Delta\boldsymbol{x}, \boldsymbol{u}_0 + \Delta\boldsymbol{u}) + \frac{\partial}{\partial\boldsymbol{x}}\boldsymbol{f}\bigg|_{\boldsymbol{x}_0,\boldsymbol{u}_0}\Delta\boldsymbol{x} + \frac{\partial}{\partial\boldsymbol{u}}\boldsymbol{f}\bigg|_{\boldsymbol{x}_0,\boldsymbol{u}_0}\Delta\boldsymbol{u} + H.O.T \tag{3.7.8}$$

For small perturbations from the nominal flight, the higher-order terms in the expansion can be ignored without a significant loss of accuracy. Finally, the fault-free linearised state-space model of the aircraft around the nominal operating point $(\boldsymbol{x}_0, \boldsymbol{u}_0)$, is written as:

$$\Delta\dot{\boldsymbol{x}} = \boldsymbol{A}\Delta\boldsymbol{x} + \boldsymbol{B}\Delta\boldsymbol{u} \tag{3.7.9}$$

where,

$$\boldsymbol{A} = \frac{\partial}{\partial\boldsymbol{x}}\boldsymbol{f}\bigg|_{\boldsymbol{x}_0,\boldsymbol{u}_0} \tag{3.7.10}$$

$$\boldsymbol{B} = \frac{\partial}{\partial\boldsymbol{u}}\boldsymbol{f}\bigg|_{\boldsymbol{x}_0,\boldsymbol{u}_0} \tag{3.7.11}$$

Stellenbosch University https://scholar.sun.ac.za

Since variation is fully captured in the perturbation variables $(\Delta \boldsymbol{x}_0, \Delta \boldsymbol{u}_0)$ and the nominal flight components are assumed to be constant, the following contribution is set to zero:

$$\dot{\boldsymbol{x}}_0 = \boldsymbol{f}(\boldsymbol{x}_0, \boldsymbol{u}_0) \tag{3.7.12}$$

The linearisation problem is reduced to determining the finding the vector partial derivatives of the nonlinear equations in (3.6.2) to (3.6.10). For the state vector and controls input vector in (3.7.2) and (3.7.3), the $\boldsymbol{A}$ and $\boldsymbol{B}$ are given by;

$$\boldsymbol{A} = \begin{bmatrix} A_{VV} & A_{V\alpha} & A_{V\beta} & 0 & A_{Vq} & 0 & A_{V\phi} & A_{V\theta} & 0 \\ A_{\alpha V} & A_{\alpha\alpha} & A_{\alpha\beta} & A_{\alpha p} & A_{\alpha q} & A_{\alpha r} & A_{\alpha\phi} & A_{\alpha\theta} & 0 \\ A_{\beta V} & A_{\beta\alpha} & A_{\beta\beta} & A_{\beta p} & 0 & A_{\beta r} & A_{\beta\phi} & A_{\beta\theta} & 0 \\ A_{pV} & 0 & A_{p\beta} & A_{pp} & A_{pq} & A_{pr} & 0 & 0 & 0 \\ A_{qV} & A_{q\alpha} & 0 & A_{qp} & A_{qq} & A_{qr} & 0 & 0 & 0 \\ A_{rV} & 0 & A_{r\beta} & A_{rp} & A_{rq} & A_{rr} & 0 & 0 & 0 \\ 0 & 0 & 0 & A_{\phi p} & A_{\phi q} & A_{\phi r} & A_{\phi\phi} & A_{\phi\theta} & 0 \\ 0 & 0 & 0 & 0 & A_{\theta q} & A_{\theta r} & A_{\theta\phi} & 0 & 0 \\ -A_{zV} & -A_{z\alpha} & -A_{z\beta} & 0 & 0 & 0 & -A_{z\phi} & -A_{z\theta} & 0 \end{bmatrix} \tag{3.7.13}$$

$$\boldsymbol{B} = \begin{bmatrix} B_{V\delta_T} & B_{V\delta_{Er}} & B_{V\delta_{El}} & B_{V\delta_{Ar}} & B_{V\delta_{Al}} & 0 & 0 \\ B_{\alpha\delta_T} & B_{\alpha\delta_{Er}} & B_{\alpha\delta_{El}} & B_{\alpha\delta_{Ar}} & B_{\alpha\delta_{Al}} & 0 & 0 \\ B_{\beta\delta_T} & B_{\beta\delta_{Er}} & B_{\beta\delta_{El}} & B_{\beta\delta_{Ar}} & B_{\beta\delta_{Al}} & B_{\beta\delta_{Rr}} & B_{\beta\delta_{Rl}} \\ 0 & B_{p\delta_{Er}} & B_{p\delta_{El}} & B_{p\delta_{Ar}} & B_{p\delta_{Al}} & B_{p\delta_{Rr}} & B_{p\delta_{Rl}} \\ 0 & B_{q\delta_{Er}} & B_{q\delta_{El}} & B_{q\delta_{Ar}} & B_{q\delta_{Al}} & 0 & 0 \\ 0 & B_{r\delta_{Er}} & B_{r\delta_{El}} & B_{r\delta_{Ar}} & B_{r\delta_{Al}} & B_{r\delta_{Rr}} & B_{r\delta_{Rl}} \\ 0 & 0 & 0 & 0 & 0 & 0 & 0 \\ 0 & 0 & 0 & 0 & 0 & 0 & 0 \\ 0 & 0 & 0 & 0 & 0 & 0 & 0 \end{bmatrix} \tag{3.7.14}$$

where the individual matrix elements A_{ij} and B_{ij} in (3.7.13) and (3.7.14) respectively are given by Equations (D.1) to (D.1.67). The FDI procedures considered in this thesis requires the use of a digital processor. To implement the proposed FDI algorithms in a digital environment requires the discretisation of the continuous state-space model, which is a subject of the next section.

3.8 Discretisation of the State Space Model

This section is dedicated to describing the discretisation of the continuous state-space model discussed in the previous section. The onboard proces-

Stellenbosch University https://scholar.sun.ac.za

sor in a digital environment will only sample the states of the aircraft at discrete time instances. Suppose that the onboard microprocessor samples the measurement $\boldsymbol{y}(t)$ and controls input $\boldsymbol{u}(t)$ signal at every T_s second. Then the discretised version of the continuous state-space model in Equation (3.7.9), can be written as:

$$\boldsymbol{x}_{k+1} = \boldsymbol{A}_k \boldsymbol{x}_k + \boldsymbol{B}_k \boldsymbol{u}_k + \boldsymbol{w}_k \tag{3.8.1}$$

To reconstruct the control input $\boldsymbol{u}(t)$ a sequence of discrete samples $\boldsymbol{u}_k$ are obtained with the zero-order hold technique, where the input signal has a constant value of $\boldsymbol{u}(kT_s) = \boldsymbol{u}_k$ over the given integration interval, then

$$\boldsymbol{A}_k = e^{\boldsymbol{A}T_s} \tag{3.8.2}$$

$$\boldsymbol{B}_k = \int_0^{T_s} e^{\boldsymbol{A}\tau} \boldsymbol{B} d\tau \tag{3.8.3}$$

The numerical evaluation of the discrete matrices is detailed in Appendix B.4

Stellenbosch University https://scholar.sun.ac.za

Chapter 4

Meraka UAV Actuator and Sensors FDD

This chapter is dedicated to the derivation of several Kalman filter (KF) based FDD algorithms. The chapter begins with presenting the architecture of the proposed FDD design. Next, the chapter introduces the Two-Stage Kalman filter (TSKF) approach. TSKF relies on estimating a clean (unbiased) state vector and the parameters in two separate KFs that operate interactively in parallel. The TSKF is then parameterised to characterise bias, LIP and LoE faults. As the UAV's model is highly nonlinear, the dual-unscented Kalman filter (DUKF), the nonlinear version of the TSKF, is also presented. Next, the fault isolation algorithm is described in detail. Active FDI algorithms to detect rudder faults, and to classify between bias, LIP and LoE faults are developed. The chapter concludes with fault isolation strategies for sensors by extracting fault signatures in the residuals of the KF algorithms.

4.1 The Architecture of the FDI Design

This section describes the architecture of the proposed FDD design. For convenience, the FDI architecture is presented for the TSKF case. However, the nonlinear DUKF and JUKF FDI designs will have the same architecture and structure. In the DUKF and JUKF designs, Euler's Method was utilised to propagate sigma points through the nonlinear kinematics and dynamics equations (3.6.2) to (3.6.10). The TSKF design is based on the linearised UAV model with the below state and input vectors:

Stellenbosch University https://scholar.sun.ac.za

$$\boldsymbol{x} = (V, \alpha, \beta, p, q, r, \phi, \theta)^T \tag{4.1.1}$$

$$\boldsymbol{u} = \left(\delta_{prop}, \delta_{E_r}, \delta_{E_l}, \delta_{A_r}, \delta_{A_l}, \delta_{R_r}, \delta_{R_l}\right)^T \tag{4.1.2}$$

The proposed FDI algorithm can detect, isolate and perform classification of bias, locked-in-place (LIP), and loss-of-effectiveness (LoE) fault types. These different fault types will be denoted as follows.

- Bias faults: denoted $\boldsymbol{\delta^*} = \left[\delta^*_{E_r}, \delta^*_{E_l}, \delta^*_{A_r}, \delta^*_{A_l}, \delta^*_{R_r}, \delta^*_{R_l}\right]^T$
- Stuck actuator faults: denoted $\bar{\boldsymbol{\delta}} = \left[\bar{\delta}_{E_r}, \bar{\delta}_{E_l}, \bar{\delta}_{A_r}, \bar{\delta}_{A_l}, \bar{\delta}_{R_r}, \bar{\delta}_{R_l}\right]^T$
- Loss of effectiveness: denoted $\boldsymbol{\gamma} = \left[\gamma_{E_r}, \gamma_{E_l}, \gamma_{A_r}, \gamma_{A_l}, \gamma_{R_r}, \gamma_{R_l}\right]^T$

As stated previously, in model-based FDI, the final design is dictated by the available system model. Not all six (6) control surfaces of the Meraka UAV are isolable or identifiable at the same time, when the FDI design relies on using a single model (see Section 4.2.1 on the concept of Isolability). This is because the rudders are mathematically identical and produce identical moments that cannot be distinguished. For this reason, the FDI design is split into two separate TSKF estimators, each TSKF dedicated to a subset of the six control surfaces. The first is the elevator-aileron filter, henceforth called the EA filter which monitors faults occurring in all elevators and ailerons by estimating the parameter vector $\boldsymbol{\delta^*_{EA}} = \left(\delta^*_{E_r}, \delta^*_{E_l}, \delta^*_{A_r}, \delta^*_{A_l}\right)^T$. The second is the elevator-rudder filter, henceforth called the ER filter. The purpose of the ER filter is to ensure isolation of rudder faults. The ER filter estimates faults occurring in the all elevators and rudders by estimator the fault parameter vector $\boldsymbol{\delta^*_{ER}} = \left(\delta^*_{E_r}, \delta^*_{E_l}\delta^*_{R_r}, \delta^*_{R_l}\right)^T$

The EA filter satisfies isolability test and simulation show that it can track all the three fault types investigated in this study, including faults of the same type occurring simultaneously. On the other hand, the ER filter still does not satisfy isolability conditions due to containing the twin rudders. Nevertheless, by employing active FDI (AFDI) techniques, the rudders can be isolated. It is pointed out that even though the ER filter estimates elevator fault parameters, these are ignored by the FDI, since the FDI relies on the EA filter to track elevator faults. The elevator parameters are only included in the ER filter to allow the isolation of rudder using active FDI procedures. The structure of the FDI is detailed in a flow diagram in Figure 4.1

Stellenbosch University https://scholar.sun.ac.za

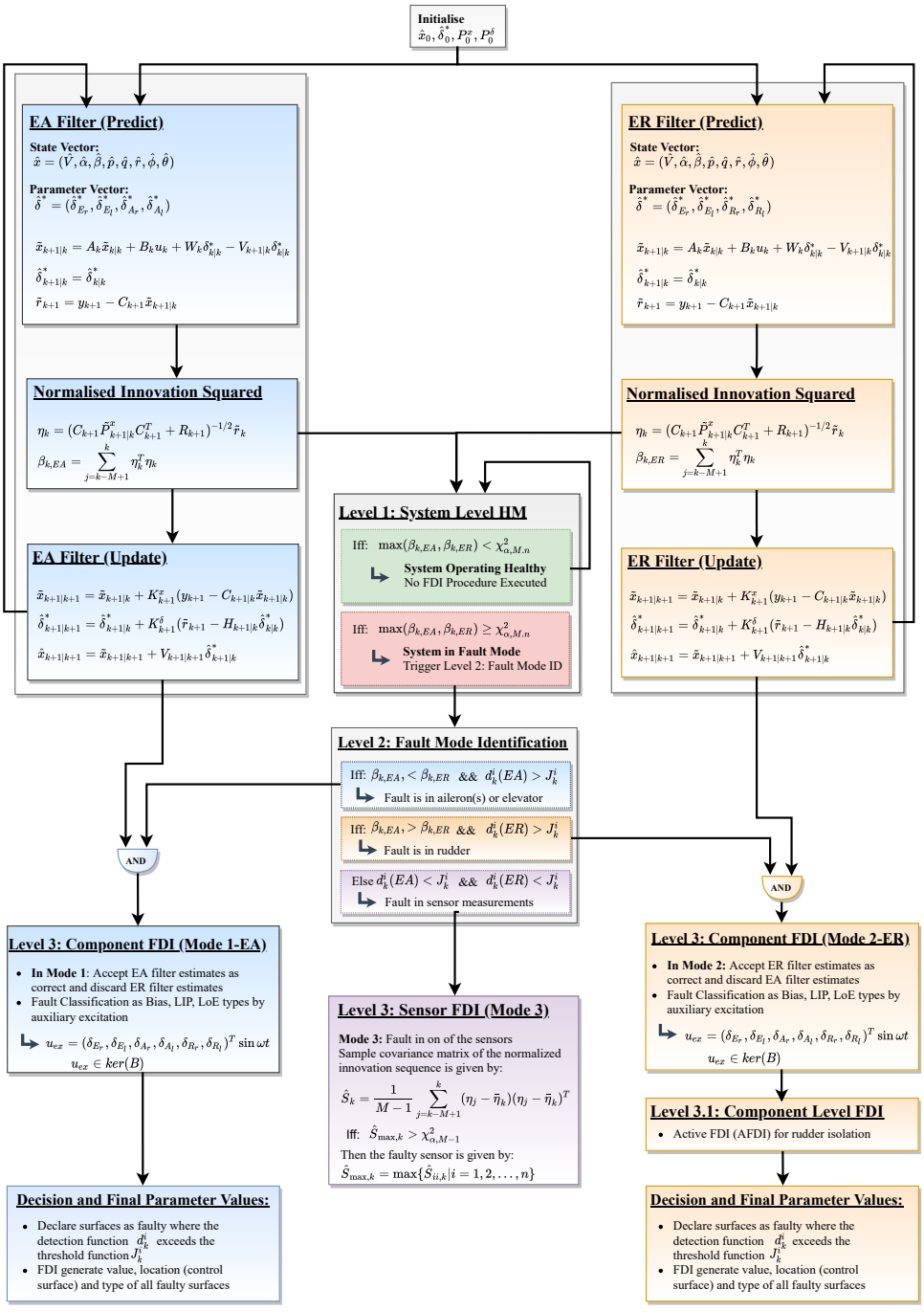

Figure 4.1: Architecture of the Fault Detection and Isolation System

4.1.1 Functionality of the FDI

The FDI design is made up of two TSKF estimators, the EA filter and the ER filters. Both filters run simultaneously to estimate their respective state vector and fault parameters online. The FDI process relies on the continu-

Stellenbosch University https://scholar.sun.ac.za

ous monitoring and extraction of fault information at every iteration. The processed information is analysed in three stages, which represents three levels of analysis, where the next level is only triggered if fault signatures are detected in the current level. The three levels begin fault detection at system level, and ends with isolating a fault to a specific control surface. In Level 1, the system detects a fault in the system, in Level 2, the FDI determines which filter is generating the correct fault parameter estimates, and in Level 3, the FDI isolates the fault to a specific control surface. See Figure 4.1 for the complete flow diagram of the FDI design

- **Level 1:** Under the Level 1 analysis, the FDI algorithm checks the normalised innovation squared (NIS) in both the EA and ER filters against a preset threshold. The NIS is calculated from the innovation sequence of the TSKF (see Section 4.9). The NIS is a χ^2-distributed random variable that indicates the unbiasedness of the innovation sequence of the KF. Provided that the TSKF is properly tuned, the NIS will have zero mean and a covariance equal to an identity matrix. A fault in a sensor or actuator will shift the mean and variance of the innovation sequence, causing the NIS to grow dramatically to a larger value that is dependent on the magnitude of the fault. The threshold set for the NIS to flag the presence of a fault can be selected for any desired significance level (in this study, a significance level of $\alpha = 0.05$ is used). If the NIS in any of the two filters has exceeded the threshold, the FDI algorithm flags a fault within the system and triggers Level 2 analysis to diagnose the fault further. If the threshold is not exceeded, the FDI does not initiate Level 2 diagnosis.
- **Level 2:** Once the NIS has flagged a fault in the system, the objective of the FDI is to determine where the fault has occurred. The purpose of the Level 2 analysis is to determine which fault Mode the system is in. The FDI will transition from Level 2 into Level 3 under one of three (3) possible Modes. Mode 1 indicates a fault detected with the EA filter, Mode 2 indicates a fault detected with the ER filter, and Mode 3 indicates a fault detected in one of the sensors. For actuator faults (Modes 1 and 2), Mode identification equates to determining which of the filters, EA or ER, is reconstructing the occurring fault correctly. This is archived by comparing the NIS of the two filters. The filter with the smallest NIS is the filter that is reconstructing the occurring fault correctly. If the NIS of the EA filter is smaller, then the system is in Fault Mode 1, the EA filter estimates are declared

Stellenbosch University https://scholar.sun.ac.za

as correct, and the ER filter estimates are discarded as incorrect. If the opposite is true, then the system is in Fault Mode 2, the ER filter estimates are declared as correct, and the EA filter estimates are discarded.

Note that the EA filter will wrongly estimate rudder faults whenever they occur, whereas the ER filter will wrongly estimate aileron faults. This is because those faults are not modelled within the respective filters. However, the NIS of the filter yielding incorrect parameter estimates will be significantly larger than the filter generating the correct fault parameter estimates. This is because the filter yielding wrong estimates will be more "biased" than the filter yielding correct estimates, which will manifest in the NIS. Thus whenever a fault occurs, the NIS in both filters will exceed the pre-selected threshold. However, the filter that is reconstructing the fault correctly will have a smaller NIS than the filter reconstructing the fault wrongly, and hence it will be selected as the correct estimator of the fault. Once the Mode is identified, the system will transition to Level 3 analysis to isolate the fault.

As stated in the previous bullet point, a sensor fault can also cause the NIS to exceed the preset threshold because a sensor failure will cause a shift in the mean and the variance of the innovation sequence. Therefore, in addition to NIS checks, Mode 1 and Mode 2 are only activated if the threshold function has exceeded within the selected filter. If none of the parameters in the EA or ER filter has exceeded the threshold function within a preset time, the FDI activates Mode 3, which indicates that the NIS shift was caused by sensor fault. In this mode, the FDI carries out a procedure to check which sensor is faulty within the Level 3 analysis.

- **Level 3:** During Level 3, the system will either be in Mode 1, Mode 2 or Mode 3, which represent faults in the EA filter, ER filter or faults in sensors respectively (see Figure 4.1 for reference). For the case of an actuator fault, the EA or the ER filter will be selected, while the other is discarded and ignored. In Mode 1 and Mode 2, statistical analysis is performed on the selected filter's fault parameters to isolate surfaces. The detection index function described in Section 4.8 is applied to all parameters. Briefly speaking, this function compares the original (fault-free) statistics of the fault parameters to their online statistics. The function is chosen to accentuate the variations in the statistical quantities of every parameter from their fault-free values.

Stellenbosch University https://scholar.sun.ac.za

If there are no shifts in the fault parameters' statistics, this function will remain in the close to zero. If there is a fault, the function will vary dramatically from zeros by large orders of magnitude. A high threshold value can be set for the detection index function, to avoid false alarms to due variations caused by noise. All the parameters that exceed this threshold in the active (selected) filter are declared as faulty. Next, the fault classification procedure described in Section 4.6 is carried out to specify the type of fault that has occurred. If the fault is in the ER filter, the active-FDI procedure described in Section 4.6.2 is finally carried out to isolate the specific rudder.

If Mode 3 is active, to isolate sensor faults, the FDI checks the statistics of the innovation channel (the statistics of individual elements of the innovation vector). The FDI computes a statistical variable that is a ratio of a sampled innovation variance versus theoretical variance (see Section 4.10). If this function exceeds a preset threshold, then a fault is declared in the sensor within the corresponding innovation channel. The algorithm assumes one sensor fault at any given time time. Therefore, only the largest statistical function to exceed the threshold is declared to indicate a sensor fault.

4.2 Modelling Faults with the Kalman Filter

The FDD algorithms presented in the upcoming sections rely on the simultaneous online reconstruction of the system states and fault parameters. Consider a discrete state-space linear representation of a healthy UAV described in the form

$$\begin{aligned} \boldsymbol{x}_{k+1} &= \boldsymbol{A}_k \boldsymbol{x}_k + \boldsymbol{B}_k \boldsymbol{u}_k + \boldsymbol{w}_k^x \\ \boldsymbol{y}_{k+1} &= \boldsymbol{C}_k \boldsymbol{x}_{k+1} + \boldsymbol{v}_{k+1} \end{aligned} \tag{4.2.1}$$

where, $\boldsymbol{x}_k$ is the $n \times 1$ state vector, $\boldsymbol{y}_k$ is the $m \times 1$ measurement vector, and $\boldsymbol{u}_k$ is the $l \times 1$ control input. The Kalman filter (KF) could be directly applied to Equation (4.2.1) to estimate system states for system identification or FTC. However, the KF requires an accurate characterisation of both the dynamical and statistical model parameters. Such a model is never available in practice. In a UAV, degradation and malfunctioning in the plant, actuators and sensors will cause changes in the modelled parameters. Some changes can manifest as the unknown constant or time-varying bias in the system dynamics and observations or as multiplicative varia-

Stellenbosch University https://scholar.sun.ac.za

tions. Faults can be modelled as parameter variations by extending (4.2.1) as follows

$$\begin{aligned} \boldsymbol{x}_{k+1} &= \left(\boldsymbol{A}_k + \Delta\boldsymbol{A}_k^f\right)\boldsymbol{x}_k + \left(\boldsymbol{B}_k + \Delta\boldsymbol{B}_k^f\right)\boldsymbol{u}_k + \boldsymbol{E}_k\boldsymbol{b}_k + \boldsymbol{w}_k^x \\ \boldsymbol{y}_{k+1} &= \left(\boldsymbol{C}_k + \Delta\boldsymbol{C}_k^f\right)\boldsymbol{x}_{k+1} + \boldsymbol{F}_k\boldsymbol{b}_k + \boldsymbol{v}_{k+1} \end{aligned} \tag{4.2.2}$$

The terms $\Delta\boldsymbol{A}_k^f$, $\Delta\boldsymbol{B}_k^f$, and $\Delta\boldsymbol{C}_k^f$, represent multiplicative faults in the UAV whereas $\boldsymbol{b}_k$, represents additive faults, which enter the process through the matrix $\boldsymbol{E}_k$. Multiplicative faults are characterised by their direct influence on system stability. Regardless, both additive and multiplicative faults will cause serious degradation of the Kalman filter, if parameter changes are not incorporated into the filtering problem. For most systems, it is possible to make some simplifying assumptions to allow modelling multiplicative as additive faults [42]. If only additive actuator faults are of interest, the following simplified model is considered.

$$\begin{aligned} \boldsymbol{x}_{k+1} &= \boldsymbol{A}_k\boldsymbol{x}_k + \boldsymbol{B}_k\boldsymbol{u}_k + \boldsymbol{E}_k\boldsymbol{b}_k + \boldsymbol{w}_k^x \\ \boldsymbol{y}_{k+1} &= \boldsymbol{C}_k\boldsymbol{x}_{k+1} + \boldsymbol{F}_k\boldsymbol{b}_k + \boldsymbol{v}_{k+1} \end{aligned} \tag{4.2.3}$$

and

$$\boldsymbol{b}_{k+1} = \boldsymbol{b}_k + \boldsymbol{w}_k^b \begin{cases} \boldsymbol{b}_k = 0 & k < k_F \\ \boldsymbol{b}_k \neq 0 & k \geq k_F \end{cases} \tag{4.2.4}$$

Where $\boldsymbol{b}_k$ is the $p \times 1$ bias vector with an unknown magnitude. All matrices have the appropriate dimensions. The noise sequences $\boldsymbol{w}_k^x$, $\boldsymbol{w}_k^b$, and $\boldsymbol{v}_k$ are zero mean uncorrelated Gaussian random sequences with

$$E\left\{\begin{bmatrix} \boldsymbol{w}_k^x \\ \boldsymbol{w}_k^b \\ \boldsymbol{v}_k \end{bmatrix}\begin{bmatrix} (\boldsymbol{w}_k^x)^T & (\boldsymbol{w}_k^b)^T & (\boldsymbol{v}_k)^T \end{bmatrix}\right\} = \begin{bmatrix} \boldsymbol{Q}_k^x & \boldsymbol{0} & \boldsymbol{0} \\ \boldsymbol{0} & \boldsymbol{Q}_k^b & \boldsymbol{0} \\ \boldsymbol{0} & \boldsymbol{0} & \boldsymbol{R}_k \end{bmatrix} \tag{4.2.5}$$

To account for the unknown fault vector $\boldsymbol{b}_k$ in (4.2.4), the augmented state Kalman filter (ASKF) may be used to jointly estimate the state and bias together by augmenting the bias into the state vector resulting in an augmented state $\bar{\boldsymbol{x}}_k = \begin{bmatrix} \boldsymbol{x}_k \\ \boldsymbol{b}_k \end{bmatrix}$. This results in a new vector size of $n + p$ and the following fault model:

Stellenbosch University https://scholar.sun.ac.za

$$\begin{bmatrix} \boldsymbol{x}_{k+1} \\ \boldsymbol{b}_k + 1 \end{bmatrix} = \begin{bmatrix} \boldsymbol{A}_k & \boldsymbol{E}_k \\ \boldsymbol{0} & \boldsymbol{I} \end{bmatrix} \begin{bmatrix} \boldsymbol{x}_k \\ \boldsymbol{b}_k \end{bmatrix} + \begin{bmatrix} \boldsymbol{B}_k \\ \boldsymbol{0} \end{bmatrix} \boldsymbol{u}_k + \begin{bmatrix} \boldsymbol{w}_k^x \\ \boldsymbol{w}_k^b \end{bmatrix} \tag{4.2.6}$$

$$\boldsymbol{y}_{k+1} = \begin{bmatrix} \boldsymbol{C}_k & \boldsymbol{F}_k \end{bmatrix} \begin{bmatrix} \boldsymbol{x}_{k+1} \\ \boldsymbol{b}_k \end{bmatrix} + \boldsymbol{v}_{k+1} \tag{4.2.7}$$

The above formulation is convenient because it models faults additive bias terms and allows direct implementation of well-known algorithms, such as the Kalman filter, to estimate the bias vector. The problem statement is the design of the fault input matrices $\boldsymbol{E}_k$ and $\boldsymbol{F}_k$. As pointed out in [80], the design of a model-based FDI is highly dependent on the particular fault of interest, the plant system, and the availability of a mathematical mapping of the fault to some measurable system behaviour. The upcoming sections show how both bias faults, locked-in-place, and loss-of-effectiveness (LoE) faults in the control surfaces can both be formulated in the additive structure in (4.2.6).

4.2.1 Fault Detectability and Isolability

Characterising the plant in with respect to the expected fault parameters is not sufficient to guarantee fault isolation. If the faults are not mutually "isolable", then multiple models or a hybrid model is required. There are several definitions of fault detectability and fault isolability in literature, which are very similar. In [34, 35] detectability and isolability conditions were derived for the Unknown Input Observers (UIO) based on the concepts of observability and controllability. A more general definition is the so-called structural fault identifiability derived in [42], which refers to the same concept. Briefly, structural fault identifiability is the characterisation of system structure that is required to reconstruct faults based on measured system output. Mathematically, this represents the mapping that relates system outputs to the faults under consideration. If the mapping is unique for each fault parameter, then the faults are identifiable.

This thesis is concerned with the isolability of the discrete state-space structure in Equations (4.2.6) and (4.2.21), which are identical. For this structure, when parametrised with additive faults of dimension l, then the l faults are isolable if and only if.

$$rank \begin{bmatrix} \boldsymbol{A} - \boldsymbol{z}\boldsymbol{I} & \boldsymbol{E} \\ \boldsymbol{C} & \boldsymbol{F} \end{bmatrix} = n + l \tag{4.2.8}$$

Stellenbosch University https://scholar.sun.ac.za

where z to denotes the complex variable from the $z-$transform in a discrete-time system. In this thesis, identifiability and isolability are used interchangeably since these concepts are similar. It is pointed out that not all the control surfaces are identifiable when treated jointly within one model. This is because the rudders produce identical moments which cannot be distinguished. For this reason, the FDI system is split into two separate EA filter and ER filter (See Section 4.1)

4.2.2 Saturation of Surfaces and Controller Assumptions

The FDI algorithms presented in this thesis requires that the aircraft maintains stability after the fault. If stability is maintained, the algorithm can reconstruct LIP, LoE and bias faults. To counter the effect of actuator faults, the feedback controller may saturate the healthy control surfaces, further reducing the controller capabilities. Consider that the flight envelope of the aircraft is given by:

$$\boldsymbol{\chi}_{\phi} = \left\{ \boldsymbol{x} \leq R^{n} \quad : \quad \boldsymbol{x}_{min} \leq \boldsymbol{x} \leq \boldsymbol{x}_{max} \right\} \tag{4.2.9}$$

for the nominal pre-fault operating point $\{\boldsymbol{x}_0, \boldsymbol{u}_0\}$, where $\boldsymbol{u}_0$ denotes the trim deflections of control surfaces at the nominal state $\boldsymbol{x}_0$. At the time t_F when a control surface is biased by an internal fault or is locked-in-place, the equilibrium state of the moments and forces are violated. A failure will cause the state vector to transition from the nominal point $\boldsymbol{x}_0$. After t_F, a new operating point $\{\boldsymbol{x}_0^f, \boldsymbol{u}_0^h\}$ must exist, where $\boldsymbol{x}_0^f$ and $\boldsymbol{u}_0^h$ represents a new post-fault operating point and the trim deflections of the healthy controls surfaces respectively. If the control surface is stuck a large deflection angle (such as hard-over fault), a saturation of healthy surfaces may occur. During fault-free conditions, the actuator deflections are bounded by $U_{i,min} \leq u_i \leq U_{i,max}$. After a stuck fault, the post-failure reduced saturation levels depicted in Figure 4.2.2 are given by:

$$u_{i+} = U_{i_{max}} - u_{i_e} \tag{4.2.10}$$

$$u_{i-} = U_{i_{min}} - u_{i_e} \tag{4.2.11}$$

The FDI algorithm functions most reliably under the following conditions:

- Stability is maintained automatically using the redundant (duplicate) or remaining healthy control surfaces.

Stellenbosch University https://scholar.sun.ac.za

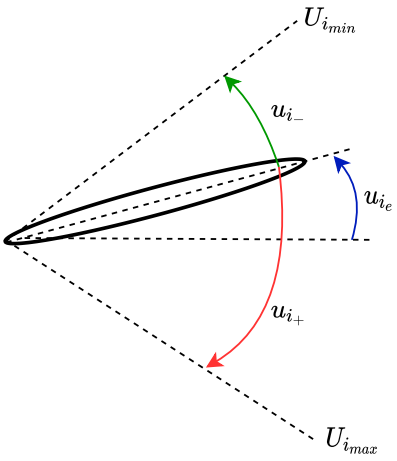

Figure 4.2: Reduced saturation levels post- stuck fault failure

- The faulty actuator is stuck at an angle where the fault nominal controller does not force the saturation of the other control surfaces. In other words, the healthy control surfaces must cancel out the effects of the failed control surface and still be able to maintain system stability (even at some reduced performance capabilities).

4.2.3 Actuator Bias Faults Model

Before a fault occurs, all control surfaces' actual deflections will follow their respective control command signals. Malfunctioning actuator servo-loops can result in unwanted actuation, inducing biases between the command signals and the actual control surface deflections. An example is the Oscillatory Failure Case (OFC) mainly caused by faulty electronic components or actuator mechanical parts generating spurious signals [2]. The bias could appear abruptly and then assume a constant value, or it could be varying slowly. In the context of this thesis, "varying slowly" means slower than the dynamics of the Kalman filter algorithm, such that the moving bias can be tracked accurately. The fault parameter is modelled as $p-$dimensional vector comprised of bias magnitudes of p actuators as:

The magnitudes of the biases are random and are independent of the control command signal. Thus, the biases become part system states which can be estimated. The faulty surfaces' actual deflections are partly con-

Stellenbosch University https://scholar.sun.ac.za

tributed by the control command signals and partly by the bias vector $\boldsymbol{\delta}^*$. This leads to a state augmentation problem as follows:

$$\bar{\boldsymbol{x}}_k = \begin{bmatrix} \boldsymbol{x}_k \\ \boldsymbol{\delta}^* \end{bmatrix} \tag{4.2.12}$$

where

$$\boldsymbol{\delta^*} = \left(\delta^*_{E_r}, \delta^*_{E_l}, \delta^*_{A_r}, \delta^*_{A_l}\right)^T. \tag{4.2.13}$$

for the case of the EA filter, and

$$\boldsymbol{\delta^*} = \left(\delta^*_{E_r}, \delta^*_{E_l}, \delta^*_{R_r}, \delta^*_{R_l}\right)^T. \tag{4.2.14}$$

for the case of the ER filter. This leads to a state augmentation problem of the same structure as (4.2.6). The fault input matrix $\boldsymbol{E}_k$ is submatrix of the controls input matrix, which is concatenated into the system states transition matrix, where:

$$\boldsymbol{E}_k = \begin{bmatrix} \boldsymbol{b}_i & \cdots & \boldsymbol{b}_j \end{bmatrix} \tag{4.2.15}$$

where $\boldsymbol{b}_i, \ldots, \boldsymbol{b}_j$ are the ith to jth columns of the input matrix $\boldsymbol{B}_k$ corresponding to the control surfaces whose bias faults are of interest (corresponding to parameter vector $\boldsymbol{\delta}^*$). Since there's no real knowledge about the evolution of the bias fault, its description as a random in the following form is appropriate:

$$\boldsymbol{\delta}^*_{k+1} = \boldsymbol{\delta}^*_k + \boldsymbol{w}^{\delta^*}_k \tag{4.2.16}$$

Provided that the identifiability or isolability condition is satisfied in the EA filter, the structure in (4.2.6) can be applied to the Kalman filter to estimate all bias faults simultaneously without the need for the MM approach.

4.2.4 Modeling Stuck Actuator Faults

The formulation of LIP faults relies on the duplex redundancy configuration in the Meraka UAV's control surfaces. In the absence of redundancy, a stuck actuator fault, such as a hard-over, will cause a "jump" [80] in the system mode, altering its behaviour differently than a parametric fault. However, in a duplex or triplex redundancy configuration where backup actuators can quickly correct the effects of a stuck actuator, a LIP actuator fault will it will manifest as a gain and offset error which may be modelled as a bias for constant commands using the same structure in (4.2.6).

Stellenbosch University https://scholar.sun.ac.za

First, consider that an identical pair of healthy control surfaces (such as two identical elevators) are given the same control command signal. Then the control effort will be shared equally by the two control surfaces, provided they have identical aerodynamic coefficients. If one of the surfaces "jumps" to an arbitrary position and gets stuck, the autopilot will command a new trim-deflection setting to both control surfaces to correct the resultant trim offsets. The stuck actuator will not respond, whereas the healthy actuator will take over the effort of two control actuators to correct the offset. This will result in a mismatch (bias) between the control command signal and the stuck-position of the faulty surface. This observation allows the design of an FDI for LIP faults based on the same model structure in (4.2.6) and (4.2.21).

Note that if this structure is applied to the case of a LIP fault, the TSKF will compute a LIP position that is twice the true LIP position. This is due to the healthy actuator carrying the duty of two control surfaces or removing the moments induced by the stuck actuator, then finding a new post-fault trim setting. This creates a separation angle (bias) between the healthy and the faulty actuators, which is twice the faulty surface's stuck-position. To enable the TSKF model to estimate the stuck position correctly, a hybrid multi-mode switching model approach described in Section 4.6 is utilised. Once a LIP fault has been detected and isolated to a specific surface, the column corresponding to the stuck actuator in $\boldsymbol{B}_k$ is nulled, such that the stuck position is completely estimated as part of the augmented state. This results in the correct estimation of the stuck position, provided saturation has been avoided.

4.2.5 Modeling Actuator Loss of Effectiveness (Gain Loss) Faults

Next, the loss-of-effectiveness in the control surface actuators is considered. Under the fault-free conditions, the control surfaces' true deflection angles will follow the control command signals. In this case, it can be said that the actuator is 100% effective. When a failure occurs, such as partial mechanical blockage, voltage reduction, or amplifier saturation in the servos systems, the actuators cannot entirely follow the control command signal. This represents a gain-loss that scales down the one-to-one relationship between the command signal and control surface deflection position. This fault is called loss-of-effectiveness. Revisiting the model in Equation in (4.2.1), the control input matrix can be parameterised by mul-

Stellenbosch University https://scholar.sun.ac.za

tiplicative fault parameters as follows:

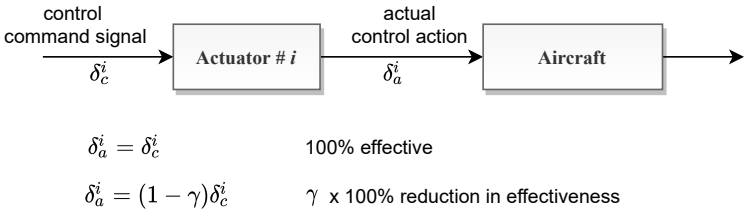

Figure 4.3: Loss of effectiveness fault in a actuator

$$\boldsymbol{x}_{k+1} = \boldsymbol{A}_k \boldsymbol{x}_k + \boldsymbol{B}_k^f \boldsymbol{u}_k + \boldsymbol{w}_k^x \tag{4.2.17}$$

where $\boldsymbol{B}_k^f$ represents the post-fault control input matrix, which can be related to the nominal, fault-free control input matrix $\boldsymbol{B}_k$ with respect to control effectiveness factors γ_k^i , $i = 1, 2, \cdots, p$ as follows:

$$\boldsymbol{B}_k^f = \boldsymbol{B}_k \left(\boldsymbol{I} - \boldsymbol{\Gamma}_k \right), \quad \text{where } \boldsymbol{\Gamma}_k = \begin{bmatrix} \gamma_k^1 & 0 & \cdots & 0 \\ 0 & \gamma_k^2 & \cdots & 0 \\ \vdots & \ddots & \ddots & \vdots \\ 0 & 0 & \cdots & \gamma_k^l \end{bmatrix} \tag{4.2.18}$$

where $\gamma_k^i = 0$, $i = 1, 2, \cdots, l$ represents the ith healthy actuator and $\gamma_k^i = 1$ represents the total failure of the ith actuator. Therefore a partial loss in control effectiveness of the actuator is represented by $0 \leq \gamma_k^i \leq 1$. This formulation is illustrated in Figure 4.3. When characterised as per Equation (4.2.17), the control effectiveness parameter appears as multiplicative with respect to the input. It would be beneficial to characterise the control effectiveness in vector or additive form such that it may be estimated with the KF methods. By matrix multiplication in (4.2.17), we get:

$$\boldsymbol{x}_{k+1} = \boldsymbol{A}_k \boldsymbol{x}_k + \boldsymbol{B}_k \boldsymbol{u}_k - \boldsymbol{B}_k \boldsymbol{\Gamma}_k \boldsymbol{u}_k + \boldsymbol{w}_k^x \tag{4.2.19}$$

Stellenbosch University https://scholar.sun.ac.za

Note that because the control effectiveness parameters matrix is diagonal, $\boldsymbol{\Gamma}_k \boldsymbol{u}_k$ and $\boldsymbol{U}_k \boldsymbol{\gamma}_k$ are mathematically equivalent, where

$$\boldsymbol{U}_k = \begin{bmatrix} u_k^1 & 0 & \cdots & 0 \\ 0 & u_k^2 & \cdots & 0 \\ \vdots & \ddots & \ddots & \vdots \\ 0 & 0 & \cdots & u_k^l \end{bmatrix}, \quad \boldsymbol{\gamma}_k = \begin{bmatrix} \gamma_k^1 \\ \gamma_k^2 \\ \vdots \\ \gamma_k^l \end{bmatrix} \tag{4.2.20}$$

By defining the time-varying fault matrix $\boldsymbol{E}_k = -\boldsymbol{B}_k \boldsymbol{U}_k$, the loss-of-effectiveness model can finally be written in the same format as (4.2.3) as follows

$$\begin{aligned} \boldsymbol{x}_{k+1} =& \boldsymbol{A}_k \boldsymbol{x}_k + \boldsymbol{B}_k \boldsymbol{u}_k + \boldsymbol{E}_k \boldsymbol{\gamma}_k + \boldsymbol{w}_k^x \\ \boldsymbol{\gamma}_{k+1} =& \boldsymbol{\gamma}_k + \boldsymbol{w}_k^\gamma \quad \begin{cases} \boldsymbol{\gamma}_k = 0 & , \quad k < k_F \quad \text{fault-free} \\ \boldsymbol{\gamma}_k \neq 0 & , \quad k \geq k_F \quad \text{under fault} \end{cases} \\ \boldsymbol{y}_{k+1} =& \boldsymbol{C}_k \boldsymbol{x}_{k+1} + \boldsymbol{v}_{k+1} \end{aligned} \tag{4.2.21}$$

The objective is to estimate control effectiveness parameter $\boldsymbol{\gamma}_k$ so that reconfiguration controllers can be synthesised to eliminate the effects of gain loss in the control loops.

4.3 The Two-Stage Kalman Filter

The Equation (4.2.6) describes the evolution of the fault parameter and its interaction with system states and control inputs. However, in this thesis, fault parameters will not be estimated within the augmented state Kalman filter (ASKF), which relies on a larger augmented state vector $\bar{\boldsymbol{x}}_k$ with a size $n + p$. If p is almost as large as n, as is the case in this study where $n = p = 8$, the size of the augmented state vector is increased significantly. The computational requirements of the ASKF will thus be excessive. Moreover, numerical problems will arise in ill-conditioned systems [81].

To address some of these problems, Friedland [82] proposed the two-stage Kalman filter (TSKF) in which the state vector and the bias are decoupled and estimated in parallel, but separately. The approach employs two reduced-order KFs to estimate the system state and bias separately. In [83, 84], Ignani and Keller proposed an alternative derivation to Friedland's TSKF for the case of an unknown constant bias. Later works derived the TSKF approach for an unknown random bias [81, 85].

Stellenbosch University https://scholar.sun.ac.za

Figure 4.2 shows a schematic flow diagram of the TSKF, and the complete algorithm for its implementation is given in Equations (4.3.2) to (4.3.18) below. Note how the TSKF follows the familiar "predict" and "update" sequence of the Kalman filter. The time-update equations are denoted with the subscript $(k+1|k)$, and the measurement-update equations are subscripted $(k+1|k+1)$

In the time update stage, the TSKF predicts a "bias-free" state estimate $\tilde{\boldsymbol{x}}$ that is "oblivious" to faults in the system. This results in residuals $\tilde{\boldsymbol{r}}$ that are significantly larger in the presence of faults than the regular KF. This is especially beneficial for the FDI problem, where residuals are used to detect the presence of faults. The TSKF relies on coupling Equations (4.3.14) to (4.3.16), which are calculated at every time step to "correct" the bias-free state estimate. The last state estimate in Equation (4.3.18) is the corrected state that should be used for feedback regulation or system identification, rather than the bias-free updated state in (4.3.4)

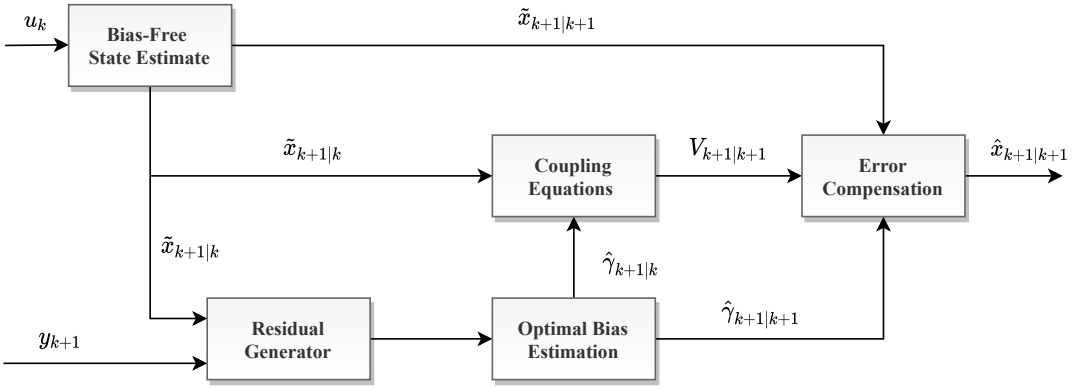

Figure 4.4: The Two Stage Kalman filter flow diagram

Stellenbosch University https://scholar.sun.ac.za

Bias-free state estimate

$$\tilde{\boldsymbol{x}}_{k+1|k} = \boldsymbol{A}_k \tilde{\boldsymbol{x}}_{k|k} + \boldsymbol{B}_k \boldsymbol{u}_k + \boldsymbol{W}_k \boldsymbol{\gamma}_{k|k} - \boldsymbol{V}_{k+1|k} \boldsymbol{\gamma}_{k|k} \tag{4.3.1}$$

$$\tilde{\boldsymbol{P}}^x_{k+1|k} = \boldsymbol{A}_k \tilde{\boldsymbol{P}}^x_{k|k} \boldsymbol{A}_k^T + \boldsymbol{Q}^x_k + \boldsymbol{W}_k \boldsymbol{P}^\gamma_{k|k} \boldsymbol{W}_k^T - \boldsymbol{V}_{k+1|k} \boldsymbol{P}^\gamma_{k+1|k} \boldsymbol{V}^T_{k+1|k} \tag{4.3.2}$$

$$\tilde{\boldsymbol{x}}_{k+1|k+1} = \tilde{\boldsymbol{x}}_{k+1|k} + \tilde{\boldsymbol{K}}^x_{k+1} \left(\boldsymbol{y}_{k+1} - \boldsymbol{C}_{k+1|k} \tilde{\boldsymbol{x}}_{k+1|k} \right) \tag{4.3.3}$$

$$\tilde{\boldsymbol{K}}^x_{k+1} = \tilde{\boldsymbol{P}}^x_{k+1|k} + \boldsymbol{C}^T_{k+1} \left(\boldsymbol{C}_{k+1} \tilde{\boldsymbol{P}}^x_{k+1|k} \boldsymbol{C}^T_{k+1} + \boldsymbol{R}_{k+1} \right)^{-1} \tag{4.3.4}$$

$$\tilde{\boldsymbol{P}}^x_{k+1|k+1} = \left(\boldsymbol{I} - \tilde{\boldsymbol{K}}^x_{k+1} \boldsymbol{C}_{k+1} \right) \tilde{\boldsymbol{P}}^x_{k+1|k} \tag{4.3.5}$$

Find the bias-free residual and its covariance

$$\tilde{\boldsymbol{r}}_{k+1} = \boldsymbol{y}_{k+1} - \boldsymbol{C}_{k+1} \tilde{\boldsymbol{x}}_{k+1|k} \tag{4.3.6}$$

$$\tilde{\boldsymbol{S}}_{k+1} = \boldsymbol{C}_{k+1} \tilde{\boldsymbol{P}}^x_{k+1|k} \boldsymbol{C}^T_{k+1} + \boldsymbol{R}_{k+1} \tag{4.3.7}$$

The optimal bias estimate is given by

$$\hat{\boldsymbol{\gamma}}_{k+1|k} = \hat{\boldsymbol{\gamma}}_{k|k} \tag{4.3.8}$$

$$\boldsymbol{P}^\gamma_{k+1|1} = \boldsymbol{P}^\gamma_{k|k} + \boldsymbol{Q}^\gamma_k \tag{4.3.9}$$

$$\hat{\boldsymbol{\gamma}}_{k+1|k+1} = \hat{\boldsymbol{\gamma}}_{k+1|k} + \boldsymbol{K}^\gamma_{k+1} \left(\tilde{\boldsymbol{r}}_{k+1} - \boldsymbol{H}_{k+1|k} \hat{\boldsymbol{\gamma}}_{k|k} \right) \tag{4.3.10}$$

$$\boldsymbol{K}^\gamma_{k+1} = \boldsymbol{P}^\gamma_{k+1|k} \boldsymbol{H}^T_{k+1|k} \left(\boldsymbol{H}_{k+1|k} \boldsymbol{P}^\gamma_{k+1|k} \boldsymbol{H}^T_{k+1|k} + \tilde{\boldsymbol{S}}_{k+1} \right)^{-1} \tag{4.3.11}$$

$$\tilde{\boldsymbol{P}}^\gamma_{\boldsymbol{k+1|k+1}} = \left(\boldsymbol{I} - \tilde{\boldsymbol{K}}^\gamma_{\boldsymbol{k+1}} \boldsymbol{H}_{\boldsymbol{k+1|k}} \right) \tilde{\boldsymbol{P}}^\gamma_{\boldsymbol{k+1|k}} \tag{4.3.12}$$

The coupling equations are

$$\boldsymbol{W}_k = \boldsymbol{A}_k \boldsymbol{V}_{k|k} - \boldsymbol{B}_k \boldsymbol{U}_k \tag{4.3.13}$$

$$\boldsymbol{V}_{k+1|k} = \boldsymbol{W}_k \boldsymbol{P}^\gamma_{k|k} \left(\boldsymbol{P}^\gamma_{k+1|k} \right)^{-1} \tag{4.3.14}$$

$$\boldsymbol{H}_{k+1|k} = \boldsymbol{C}_{k+1} \boldsymbol{V}_{k+1|k} \tag{4.3.15}$$

$$\boldsymbol{V}_{k+1|k+1} = \boldsymbol{V}_{k+1|k} - \tilde{\boldsymbol{K}}^{\boldsymbol{x}}_{\boldsymbol{k+1}} \boldsymbol{H}_{\boldsymbol{k+1|k}} \tag{4.3.16}$$

Stellenbosch University https://scholar.sun.ac.za

Finally, the compensated state and error covariance are

$$\hat{\boldsymbol{x}}_{k+1|k+1} = \tilde{\boldsymbol{x}}_{k+1|k+1} + \boldsymbol{V}_{k+1|k+1}\hat{\boldsymbol{\gamma}}_{k+1|k+1} \tag{4.3.17}$$

$$\boldsymbol{P}_{k+1|k+1} = \tilde{\boldsymbol{P}}^{x}_{k+1|k+1} + \boldsymbol{V}_{k+1|k+1}\boldsymbol{P}^{\gamma}_{k+1|k+1} + \boldsymbol{V}^{T}_{k+1|k+1} \tag{4.3.18}$$

The above TSKF equations are written with respect to the effectiveness factor parameter $\boldsymbol{\gamma}$, but they can be applied to bias and stuck faults by simply substituting the fault matrix $(-\boldsymbol{B}_k\boldsymbol{U}_k)$ in (4.3.14) with the input matrix $\boldsymbol{B}_k$. For convenience, the rest of the derivations and descriptions relating to fault parameters will be presented with respect to the effectiveness factor $\boldsymbol{\gamma}$. However, the algorithms can be applied to any of the three fault types studied in this thesis.

Since it is not possible to describe the evolution of faults deterministically, they are modelled as a random vector with additive noise covariance as shown in Equations (4.2.4) and (4.2.21). A small initial estimate covariance of the fault parameter $\boldsymbol{P}^{\gamma}_{0}$ should be selected because no faults are expected at the start of the algorithm. When faults occur, the fault parameters will jump abruptly. This requires selecting a large process noise covariance matrix $\boldsymbol{Q}^{\gamma}$ to ensure the fast-tracking of such abrupt changes in the fault parameter. However, a large covariance matrix will result in the filter being too sensitive to external excitation from process noise and measurement errors in the steady-state and initialisation phases. This will result in erratic behaviour in the fault parameters, resulting in the FDI algorithm being overly sensitive to external disturbances. The selection of an appropriate $\boldsymbol{Q}^{\gamma}$ is amongst the primary design objectives in the FDI design that is based on the KF approach. A fitting parameter covariance matrix $\boldsymbol{Q}^{\gamma}$ is a trade-off between desired filter convergence rate (mean detection time of the FDI) and tolerable noise sensitivity (false detection rate and parameter estimate accuracy).

Since $\boldsymbol{Q}^{\gamma}$ influences $\boldsymbol{P}^{\gamma}$ additively, a large $\boldsymbol{Q}^{\gamma}$ makes the algorithm extremely noise-sensitive resulting in the "blow-up" of the parameter estimate. Even slight excitation in the direction of large elements of the $\boldsymbol{P}^{\gamma}$ matrix may result in a dramatic behaviour in the parameter estimates. To address this problem, the thesis proposes an adaptive procedure to estimate the fault parameter, which is the subject of the next section.

Stellenbosch University https://scholar.sun.ac.za

4.4 Adaptive Estimation of Fault Parameter

In this section, enhancements are added to the FDI algorithm to make it more responsive to abrupt changes in fault parameters, while remaining insensitive to external noise excitation in the absence of faults. Not all control surfaces will always fail at the same time. There will be substantial differences in the abrupt behaviour and variations rates between all or subsets of parameters during faults. When a fault occurs, system parameters associated with the failed control surfaces will vary more rapidly than parameters associated with healthy control surfaces. The adaptation methods developed should be tailored to affect the individual or group of parameters associated with the occurring faults.

4.4.1 P-Adaptation: by Parameter Estimate Covariance Matrix

Forgetting factor algorithms have been applied to tackle the adaptation problem. These techniques involve discounting past information to allow the filtering algorithm to maintain the ability to respond to fast changes in the system. The covariance of the fault parameter determines the rate of the filter in estimating such parameter. Thus the forgetting factor can be attached to the time propagation of the parameter covariance as follows:

$$\boldsymbol{P}^{\gamma}_{k+1|k} = \frac{\boldsymbol{P}^{\gamma}_{k|k}}{\lambda} + \boldsymbol{Q}^{\gamma}_{k} \quad , 0 < \lambda \leq 1 \tag{4.4.1}$$

However, as single forgetting factor such as in (4.4.1) above will scale all parameters uniformly in time and space. This is against the argument made previously that fault parameters will vary in a non-uniform fashion over time. A better solution is to introduce multiple forgetting factors tailored to each parameter. This enables tuning the forgetting factors based on knowledge about the rate of variations in each individual parameter.

There are many multiple forgetting methods in literature with varying complexities and performances. However, the fundamental concepts are similar. Briefly, the forgetting approach applied should avoid the loss of tracking capability on the one hand, and unbounded growth of the $\boldsymbol{P}^{\gamma}$ matrix. This means that the covariance matrix should neither be too large (aggressive and sensitive to noise) nor too small (nonresponsive to actual abrupt faults). To this effect, in [36] it is suggested to constrain the covariance within prescribed boundaries as follows:

$$\sigma_{min}\boldsymbol{I} \leq \boldsymbol{P}^{\gamma}_{k+1|k} \leq \sigma_{max}\boldsymbol{I} \tag{4.4.2}$$

Stellenbosch University https://scholar.sun.ac.za

where σ_{min} and σ_{max} are positive constants such that $0 < \sigma_{min} < \sigma_{max} < \infty$, and $\boldsymbol{I}$ is an identity matrix. The constrained matrix in (4.4.2) allows a spectral factorization as follows

$$\boldsymbol{P}^{\gamma}_{k|k} = \sum_{i=1}^{l} \alpha^{i}_{k|k} \boldsymbol{e}^{i}_{k} \left(\boldsymbol{e}^{i}_{k}\right)^{T} \quad , \quad \|\boldsymbol{e}^{1}_{k}\| = \cdots = \|\boldsymbol{e}^{l}_{k}\| = 1 \tag{4.4.3}$$

where $\alpha^{1}_{k|k}, \ldots, \alpha^{l}_{k|k}$ are the eigenvalues of $\boldsymbol{P}^{\gamma}_{k|k}$ and $e^{1}_{k|k}, \ldots, e^{l}_{k|k}$ are the respective normalized eigenvectors. Substituting (4.4.3) into (4.4.1) gives

$$\boldsymbol{P}^{\gamma}_{k|k} = \sum_{i=1}^{l} \frac{\alpha^{i}_{k|k}}{\lambda^{i}_{k}} \boldsymbol{e}^{i}_{k} \left(\boldsymbol{e}^{i}_{k}\right)^{T} \quad , \quad 0 < \lambda^{i}_{k} \leq 1 \tag{4.4.4}$$

In [36], it is shown that by selecting the forgetting factor λ^{i}_{k} as a decreasing function of the amount of information received in the direction e^{i}_{k} , these bounds are met. The eigenvalues α^{i}_{k} of the covariance $\boldsymbol{P}^{\gamma}_{k|k}$ are measure of the variance in the direction of e^{i}_{k} . Therefore the forgetting factor λ^{i}_{k} scales the eigenvalues without violating the bounds in (4.4.2)

$$\lambda^{i}_{k} = \begin{cases} 1 & \text{if} \quad \alpha^{i}_{k|k} > \alpha_{max} \\ \alpha^{i}_{k|k} \left[\alpha_{min} + \frac{\alpha_{max} - \alpha_{min}}{\alpha_{max}} \alpha^{i}_{k|k}\right]^{-1} & \text{if} \quad \alpha^{i}_{k|k} \leq \alpha_{max} \end{cases} \tag{4.4.5}$$

Replacing (4.3.9) with (4.4.4), will turn the TSKF into an adaptive TSKF (ATSKF). The forgetting factor causes the filter to lose its steady-state optimality, resulting in reduced estimation accuracy. Nonetheless, this is a fair trade-off as the filter is now more responsive to abrupt changes by not learning the parameter too well. It is highlighted that the bounds in (4.4.2) get rid of the off-diagonal elements of the parameter covariance matrix. This causes the filter to lose its ability to quickly estimate fault parameters that are dependant on the cross-correlations characterised by the off-diagonal elements. Moreover, when there is high coupling between surfaces, as is the case with the Meraka UAV, eliminating the off-diagonal elements of $\boldsymbol{P}^{\gamma}_{k+1|k}$ results in the loss of all information about coupling between state variables. In this thesis, the forgetting factor presented in this section worked well in isolating and distinguishing between the right and left elevator faults. The next section presents a novel multiple forgetting factor approach, which preserves the cross-coupling between all parameters.

Stellenbosch University https://scholar.sun.ac.za

4.4.2 Q-Adaptation: by Additive Noise Covariance

As pointed out in [73], the forgetting factors as given in the expression (4.4.5) is equivalent to adding a noise term with a time-varying covariance to the algorithm. If we denote the equivalent noise covariance as $\hat{\boldsymbol{Q}}_k^{\gamma}$, then it can be related to the forgetting factor by:

$$\hat{\boldsymbol{Q}}_k^{\gamma} = \sum_{i=1}^{l} \left(\frac{1}{\lambda_k^i} - 1 \right) \alpha_{k|k}^i e_k^i (e_k^i)^T \geq 0 \tag{4.4.6}$$

This observation justifies developing an adaptation technique based on a time-varying noise covariance. The novel approach proposed in this study is based on monitoring the evolution of the fault parameters and scaling the additive covariance matrix $\boldsymbol{Q}_k^{\gamma}$ in directions along which the parameter variations are most significant. The TSKF already has the ability to detect changes and estimate fault parameters. However, parameter estimates may be too slow or too sensitive to noise, depending on the size of the $\boldsymbol{Q}_k^{\gamma}$ matrix. By experimentation, a conservative (not too small and not too large) is usually found. Suppose that there exists a conservative $\boldsymbol{Q}_0^{\gamma}$ matrix that is sufficiently small to minimise noise sensitivity in steady-state, and sufficiently large to track changes in fault parameters, yet not aggressive enough to track faults as quickly as required for FDI purposes. Actually, such a matrix needs to be found by experimentation as part of the normal KF design process in any case. This matrix can then be scaled in the direction of parameter variation whenever the FDI algorithm detects a fault, allowing the KF to track occurring faults faster. To this effect, the following realtime statistics of the fault parameters are defined to quantify parameter variations.

- Firstly, the initial variances of the fault parameters during the fault free conditions as follows

$$\sigma_{\hat{\gamma}_0^i}^2 = \frac{1}{N_1 - 1} \sum_{j=1}^{N_1} \left[\hat{\gamma}_j^i - \bar{\mu}_{\hat{\gamma}_0^i} \right]^2 \tag{4.4.7}$$

  where $\bar{\mu}_{\hat{\gamma}_0^i}$ are the means of the fault parameters over the initial sampling size of length N_1

$$\bar{\mu}_{\hat{\gamma}_0^i} = \frac{1}{N_1} \sum_{j=1}^{N_1} \hat{\gamma}_j^i \tag{4.4.8}$$

Stellenbosch University https://scholar.sun.ac.za

The sample size should be selected to be long enough to collect sufficient statistics in the variation of the fault parameters during fault free conditions.

- Next, a rolling variance of the fault parameters are defined as:

$$\sigma^2_{\hat{\gamma}^i_k\,II} = \frac{1}{N_2 - 1} \sum_{j=k-N_2+1}^{k} \left[\hat{\gamma}^i_j - \bar{\mu}_{\hat{\gamma}^i_k}\right]^2 \tag{4.4.9}$$

- Next we define a function ϑ_γ, as the ratio between the initial fault-free parameter variance and the moving variance as:

$$\vartheta_{\gamma^i_k} = \frac{\sigma^2_{\hat{\gamma}^i_k\,II}}{\sigma^2_{\hat{\gamma}^i_0}} \tag{4.4.10}$$

The moving variance tracks variation rates over the evaluation window N_2, and thus old data outside the evaluation window is discounted or "forgotten". If there are no abrupt changes in the parameter statistics within the moving window N_2, the ratio ϑ_γ is expected to be close to unity. This ratio ϑ_γ is here called the normalised moving variance, normalised by the system's "original" fault free variance. This parameter is expected to be close to unity when there are no significant changes in the parameter's second moment statistic and larger than unity when there are high variations. This provides a basis for a scaling factor based on this ratio.

Since $\boldsymbol{Q}^\gamma_k$ is a symmetric positive definite matrix, by spectral factorisation it can be written as follows:

$$\boldsymbol{Q}^\gamma_k = \sum_{i=1}^{l} \sigma^i_{k|k} \boldsymbol{q}^i_k \left(\boldsymbol{q}^i_k\right)^T \tag{4.4.11}$$

with eigenvalues $\sigma^1_{k|k}, \ldots, \sigma^l_{k|k}$ and corresponding orthonormal eigenvectors $q^1_{k|k}, \ldots, q^l_{k|k}$. Then an adaptive $\boldsymbol{Q}^\gamma_k$ is given by:

$$\boldsymbol{Q}^\gamma_k = \sum_{i=1}^{l} \Lambda^i_k \sigma^i_{k|k} \boldsymbol{q}^i_k \left(\boldsymbol{q}^i_k\right)^T \tag{4.4.12}$$

where

$$\Lambda^i_k = \begin{cases} \max\left(1, \vartheta_{\gamma^i_k}\right), & \vartheta_{\gamma^i_k} < \vartheta_{\gamma^i_{max}} \\ \vartheta_{\gamma^i_{max}} & \vartheta_{\gamma^i_k} \geq \vartheta_{\gamma^i_{max}} \end{cases} \tag{4.4.13}$$

Stellenbosch University https://scholar.sun.ac.za

In application, the ratio ϑ_γ may vary in the fault-free mode for other reasons than faults, such as noise disturbances. However, in the presence of faults, the variations will be much more significant since the noise statistics are already captured in $\sigma^2_{\hat{\gamma}_0^i}$. Therefore, the FDI does not trigger the $\boldsymbol{Q}_k^\gamma$ – scaling algorithm unless significantly large values of ϑ_γ are detected. The scaling limits are $\vartheta_{\gamma^i_{max}}$ included to avoid over-scaling $\boldsymbol{Q}_k^\gamma$ which would lead to blowing up of estimated fault parameters.

4.5 Adaptation Filtering of the State

For similar reasons discussed in the previous section, adaptive procedures for the state estimation equations in the TSKF are developed.

4.5.1 State Adaptation Based on a Single Factor

The innovation of the TSKF can be affected by several factors, including unmodelled dynamics, measurement errors, poor approximations or shifts in the system. From (4.3.7), it is clear that the covariance of the innovation sequence is affected by the estimate covariance and the measurement covariance. If the system dynamics are known precisely, the theoretical innovation covariance will closely approximate the real innovation covariance. However, in practice, the true nonlinear model is never available, and a simplified model is typically used. Consequently, the innovation covariance may grow when affected by the state estimation error or measurement errors. This observation provides the basis for comparing the real and theoretical covariances of the innovation sequence online to construct adaptive procedures. Let the sampled innovation sequence covariance be given by:

$$\bar{\boldsymbol{S}}_k = \frac{1}{L-1} \sum_{j=k-L+1}^{k} \tilde{\boldsymbol{r}}_k \tilde{\boldsymbol{r}}_k^T \tag{4.5.1}$$

$$\alpha_k = \max\left\{1, \frac{\text{tr}(\bar{\boldsymbol{S}}_k)}{\text{tr}(\tilde{\boldsymbol{S}}_k)}\right\} \tag{4.5.2}$$

When the theoretical innovation covariance increases due to unmodelled behaviour, the true sampled innovation covariance $\bar{\boldsymbol{S}}_k$, could be used to find the scalar α_k. The effects of incomplete knowledge in the dynamic equation can be compensated by increasing the magnitude of $\tilde{\boldsymbol{P}}^x_{k+1|k}$. Thus the adaptive approach could be based on increasing the predicted estimate error covariance by defining $\bar{\boldsymbol{P}}^x_{k+1|k} \equiv \lambda^x_k \tilde{\boldsymbol{P}}^x_{k+1|k}$. Then $\lambda^x_k \geq 1$ and

Stellenbosch University https://scholar.sun.ac.za

serves as a forgetting factor by scaling up the predicted covariance. The sampled covariance $\bar{\boldsymbol{S}}_{k+1|k}$ is given by the following two equations:

$$\bar{\boldsymbol{S}}_{k+1} = \boldsymbol{C}_{k+1}\bar{\boldsymbol{P}}^{x}_{k+1|k}\boldsymbol{C}^{T}_{k+1} + \boldsymbol{R}_{k+1} \tag{4.5.3}$$

$$= \boldsymbol{C}_{k+1}(\lambda^{x}_{k}\tilde{\boldsymbol{P}}^{x}_{k+1|k})\boldsymbol{C}^{T}_{k+1} + \boldsymbol{R}_{k+1} \tag{4.5.4}$$

and

$$\bar{\boldsymbol{S}}_{k+1} = \alpha_k\tilde{\boldsymbol{S}}_{k+1} \tag{4.5.5}$$

$$= \alpha_k(\boldsymbol{C}_{k+1}\tilde{\boldsymbol{P}}^{x}_{k+1|k}\boldsymbol{C}^{T}_{k+1} + \boldsymbol{R}_{k+1}) \tag{4.5.6}$$

Combining the above results we get

$$\alpha_k(\boldsymbol{C}_{k+1}\tilde{\boldsymbol{P}}^{x}_{k+1|k}\boldsymbol{C}^{T}_{k+1} + \boldsymbol{R}_{k+1}) = \lambda^{x}_{k}\boldsymbol{C}_{k+1}\tilde{\boldsymbol{P}}^{x}_{k+1|k}\boldsymbol{C}^{T}_{k+1} + \boldsymbol{R}_{k+1} \tag{4.5.7}$$

$$\lambda^{x}_{k} \approx \frac{\text{tr}\left[\alpha_k\boldsymbol{C}_{k+1}\tilde{\boldsymbol{P}}^{x}_{k+1|k}\boldsymbol{C}^{T}_{k+1} + (\alpha_k - 1)\boldsymbol{R}_{k+1}\right]}{\text{tr}\left[\boldsymbol{C}_{k+1}\tilde{\boldsymbol{P}}^{x}_{k+1|k}\boldsymbol{C}^{T}_{k+1}\right]} \tag{4.5.8}$$

The solution given by (4.5.8) is an approximation of λ^{x}_{k}. However, if we trust the sensing devices more, then the scaling should be limited to the predicted estimate error covariance and $\boldsymbol{R}_{k+1}$ does not form part of the adaptation. In this study, we trust the sensing equipment more due to their high accuracy, and we opt to adapt to modelling errors in the stochastic model. When R_{k+1} is ignored, the above equation becomes $\lambda^{x}_{k} = \alpha_k$. Regardless, the adaptation (scaling) philosophy typically requires to trust either the process and adapt for measurements errors or vice versa. As pointed out in [86], the simultaneous adaptation of both the process and measurements based on matching covariances is questionable since these covariance matrices affect each other. Then the estimates error covariance is $\bar{\boldsymbol{P}}^{x}_{k+1|k} \equiv \lambda^{x}_{k}\tilde{\boldsymbol{P}}^{x}_{k+1|k}$. The value of λ^{x}_{k} should be estimated online using (4.5.2) and plugged into Equation (4.3.3) to add state estimate adaptation.

4.5.2 Multiple Forgetting Factors by Q-Adaptation

The previous section derived adaptation procedure based on a single forgetting factor. Following arguments made previously in sections 4.4.1 and 4.4.2, in complex multivariate systems, adaptation procedures should be tailored in the direction of flow of information, such that each state weighted

Stellenbosch University https://scholar.sun.ac.za

the differently depending on observations. Thus a matrix of multiple forgetting factors should be used. Similar to the single factor case, the approach is based on matching the sampled innovation covariance to the theoretical as follows.

$$\bar{\boldsymbol{S}}_k = \frac{1}{L-1}\sum_{j=k-L+1}^{k} \tilde{\boldsymbol{r}}_k \tilde{\boldsymbol{r}}_k^T = \boldsymbol{C}_{k+1}\tilde{\boldsymbol{P}}^x_{k+1|k}\boldsymbol{C}^T_{k+1} + \boldsymbol{R}_{k+1} \tag{4.5.9}$$

This time, a $\boldsymbol{Q}-$ adaptation procedure is derived by finding an appropriate multiplier matrix for the $\boldsymbol{Q}-$ matrix such that the sampled innovation covariance matrix closely matches the theoretical one. A matrix $\boldsymbol{\Sigma}$ is constructed with multiple forgetting factors as follows:

$$\frac{1}{L-1}\sum_{j=k-L+1}^{k} \tilde{\boldsymbol{r}}_k \tilde{\boldsymbol{r}}_k^T = \boldsymbol{C}_{k+1}\left(\boldsymbol{A}_k\tilde{\boldsymbol{P}}^x_{k|k}\boldsymbol{A}^T_k + \boldsymbol{\Sigma}_k\boldsymbol{Q}^x_k + \boldsymbol{W}_k\boldsymbol{P}^\gamma_{k|k}\boldsymbol{W}^T_k - \boldsymbol{V}_{k+1|k}\boldsymbol{P}^\gamma_{k+1|k}\boldsymbol{V}^T_{k+1|k}\right)\boldsymbol{C}^T_{k+1} + \boldsymbol{R}_{k+1} \tag{4.5.10}$$

For a specific case in this thesis, where the the observation matrix is identity, as simpler forgetting matrix is

$$\boldsymbol{\Sigma}_k = \left(\frac{1}{L-1}\sum_{j=k-L+1}^{k} \tilde{\boldsymbol{r}}_k \tilde{\boldsymbol{r}}_k^T - \boldsymbol{A}_k\tilde{\boldsymbol{P}}^x_{k|k}\boldsymbol{A}^T_k - \boldsymbol{W}_k\boldsymbol{P}^\gamma_{k|k}\boldsymbol{W}^T_k + \boldsymbol{V}_{k+1|k}\boldsymbol{P}^\gamma_{k+1|k}\boldsymbol{V}^T_{k+1|k} - \boldsymbol{R}_{k+1}\right) \times (\boldsymbol{Q}^x_k)^{-1} \tag{4.5.11}$$

The sampled covariance is nevertheless an approximation over a moving window of length L. Also, $\boldsymbol{\Sigma}$ is evaluated using an online computer which can have round-off errors; causing the resulting matrix to be non-diagonal or have diagonal elements that are smaller than one or negative. Therefore a modified scaling matrix is constructed as follows:

$$\boldsymbol{\Sigma}^*_k = \text{diag}\begin{bmatrix}\lambda^{*1}_k & \lambda^{*2}_k & \cdots & \lambda^{*n}_k\end{bmatrix} \tag{4.5.12}$$

$$\lambda^{*i}_k = \max\{1, \Sigma_{ii}\}, \quad i = 1, \cdots, n \tag{4.5.13}$$

The scalar Σ_{ii} are taken from the diagonal elements of the matrix $\boldsymbol{\Sigma}$. This matrix multiplier is incorporated into (4.3.3) for adaptive state estimation.

4.6 Hybrid Switching Model Formulation

It was shown in sections 4.2.3, 4.2.4 and 4.2.5 that the bias fault, LIP fault and the LoE fault can be tracked using the same structure in (4.2.4) and

Stellenbosch University https://scholar.sun.ac.za

(4.2.21). The only difference in the models for estimating bias, LIP and LoE faults is the fault entry matrix $\boldsymbol{E}_k$, and the fact that the column in the controls input matrix $\boldsymbol{B}_k$ corresponding to the stuck actuator is nulled in the case of a LIP fault. Instead of having three designs for bias, LIP and LoE faults, and hybrid, multiple mode switching model is utilised to track all fault types. The Hybrid approach eliminates the need for multiple designs or models and reduces computational requirements. The approach is based on the assumption that the UAV can be sufficiently expressed at any given time by a stochastic hybrid system denoted as $\boldsymbol{\mathcal{H}}$

$$\boldsymbol{\mathcal{H}}: \begin{cases} \boldsymbol{x}_{k+1} = & \boldsymbol{A}_k(p_{k+1})\boldsymbol{x}_k + \boldsymbol{B}_k(p_{k+1})\boldsymbol{u}_k + \boldsymbol{w}_k \\ \boldsymbol{y}_k = & \boldsymbol{C}_k(p_k)\boldsymbol{x}_k + \boldsymbol{v}_k \end{cases} \tag{4.6.1}$$

where $p_k \in \boldsymbol{\mathcal{H}} \subseteq \mathbb{R}^l$ represents the unknown plant parameters which may vary in time in an abrupt fashion and represents the various failure scenarios. Suppose that a set of finite p linear models can be designed to represent all possible modes of the hybrid system $\boldsymbol{\mathcal{H}}$. Let $\mathcal{M}$ be a finite set of p models:

$$\mathcal{M}: \left\{M_1, \ldots, M_p\right\} \tag{4.6.2}$$

such that the model in (4.2.3) is re-written as a hybrid jump ("switching") model as follows:

$$\mathcal{M}: \begin{cases} \boldsymbol{x}_{k+1} = & \boldsymbol{A}_k\boldsymbol{x}_k + \left(\boldsymbol{B}_k - \mathcal{B}_{j,k}\right)\boldsymbol{u}_k + \mathcal{E}_k\boldsymbol{b}_k + \boldsymbol{w}_k^x \\ \boldsymbol{y}_{k+1} = & \boldsymbol{C}_k\boldsymbol{x}_{k+1} + \boldsymbol{v}_{k+1} \end{cases} \tag{4.6.3}$$

where $\mathcal{B}_{j,k}$ and $\mathcal{E}_{j,k}$ corresponds to the parameter set $\boldsymbol{p}_i \in \boldsymbol{\mathcal{H}}$ representing mode changes in the system for every actuator failure. In this thesis, $\mathcal{B}_{j,k}$ is chosen as a matrix of the same dimensions as the control input matrix $\boldsymbol{B}_k$. The hybrid system's nominal model is chosen to match the bias TSKF estimator in Section 4.2.3. Thus the nominal (initial) value of $\mathcal{B}_{j,k}$ is a zero matrix, and the nominal value of $\mathcal{E}_{j,k}$ is a submatrix of the controls input matrix $\boldsymbol{B}_k$ chosen appropriately for the EA and ER filters as described in section 4.2.3.

In the event of a LIP fault, the matrix $\mathcal{B}_{j,k}$ is chosen annihilate the appropriate column of the control matrix. To speak again, $\mathcal{B}_{j,k}$ is chosen with zero values in all elements with the exception of the j_{th} column, corresponding the j_{th} stuck actuator, which is chosen as equal to the j_{th} column in matrix $\boldsymbol{B}_k$ corresponding to the same stuck actuator. The arithmetic difference between $\boldsymbol{B}_k$ and $\mathcal{B}_{j,k}$ matrices results in the effects of the

Stellenbosch University https://scholar.sun.ac.za

failed actuator being completely removed from the $\boldsymbol{B}_k$ matrix, such that it is completely estimated in the "augmented" state parameter vector. This formulation is fitting because after the actuator is stuck, it no longer responds to control commands and therefore no longer forms part of the control input dynamics. In the event of an LoE fault, the switching occurs in $\mathcal{E}_{j,k}$. Following the explanation in Section 4.2.5, the fault input matrix will transition to $\mathcal{E}_{j,k} = -\boldsymbol{B}_k \boldsymbol{U}_k$.

The next problem is to select a switching logic for the hybrid system. The detection index function d_k^i described in section 4.8 already reliably isolates all considered faults. The detection index function and the classification technique described in section 4.6.1 are used to isolate the faulty surface and determine the type of fault. Based on this information, the hybrid model switches appropriately to reconstruct the fault correctly.

4.6.1 Active FDI for Fault Classification and Hybrid Switching

This section describes the active FDI strategy utilised for the classification of bias, LIP and LoE faults. The model structure in 4.2.6 can detect bias, LoE and LIP faults. The nominal (default) model is chosen as the bias estimator. Therefore, if a bias fault occurs, it will be isolated and reconstructed without any switching in the hybrid model. In the event of a LIP fault, the nominal model will also isolate the fault correctly; however, the fault parameters estimates will be exaggerated and incorrect. For the case of an LoE fault, the fault parameter will be time-varying and incorrect, coupled into the input. To reconstruct the LoE and LIP faults correctly, the hybrid model needs to switch to a different mode by adjusting either the $\boldsymbol{B}_k$ matrix or the fault input matrix $\boldsymbol{E}_k$.

At time t_D, when a fault is detected with the detection function, the active FDI procedure is triggered and initiates the fault classification procedure. Auxiliary excitation signals are injected to extract fault signatures from the system. The excitation signals are chosen as sinusoidal with a frequency ω and amplitudes chosen in the kernel of the $\boldsymbol{B}$ matrix as follows:

$$\boldsymbol{u}_{ex} = \left(\delta_{E_r}, \delta_{E_l}, \delta_{A_r}, \delta_{A_l}, \delta_{R_r}, \delta_{R_l}\right)^T \sin \omega t \tag{4.6.4}$$

where $\boldsymbol{u}_{ex} \in ker(\boldsymbol{B})$. The null space will always exist under "fault-free" conditions due to the duplex redundancy configuration and symmetric surfaces. In the case of a bias fault, $\boldsymbol{u}_{ex}$ represents orthogonal signals injected into the controls, which will cancel out each other in the aircraft's dynamic behaviour. If the fault is a LIP or LoE type, the auxiliary controls

Stellenbosch University https://scholar.sun.ac.za

excitation signals cannot fulfil $\boldsymbol{u}_{ex} \in ker(\boldsymbol{B})$ because of a stuck surface or a partially responsive surface. Consequently, the excitation frequency ω will propagate through the system and appear in the measured signals and parameter estimates. The classification process consists of detecting the presence of the excitation frequency in any of the measured signals or calculated signals, for example, the estimate of the faulty control surface $\hat{\delta^*}_k$. If the frequency is absent in $\hat{\delta^*}_k$ over the excitation window, the fault is declared as bias type, and no mode switching occurs. If the excitation frequency ω is present in $\hat{\delta^*}_k$, then the fault is either LIP or LoE type.

To determine if the fault is LIP or LoE, a new excitation signal which can be of the same frequency ω is now injected into a single surface that failed. If the fault is LIP type, there will be no response in the system. If the fault is an LoE type, the excitation frequency ω will be present again in the $\hat{\delta^*}_k$ parameter. In this way, the FDI distinguished between the three types of control surface faults.

Note that the classification and the FDI algorithm can run in parallel. Indeed the auxiliary sinusoidal excitation allows the TSKF to learn the new state and parameters faster, which improves the reliability of the FDI.

4.6.2 Active Fault Detection and Isolation for Rudder Faults

The two rudders in the Meraka UAV are mathematically identical and are not isolable within one structure. Nevertheless, due to the similarity, when there is a fault on one rudder, the ER filter will estimate a parameter that is half of the true fault size but in the correct direction of deflection in both rudders. This is useful information that can be used to isolate the failed rudder actively by using the following approach.

4.6.2.1 For Bias Faults

This approach relies on the observation that the ER filter will estimate a false elevator bias whenever there is a rudder bias fault. Unlike with the elevators and ailerons, all the moments generated by the right and left rudders are always identical, making it impossible to isolate rudder faults by only tracking their effects on the moments. This is due to the two rudders being equivalent in their mathematical characterisation. To achieve rudder fault isolation, active FDI (AFDI) algorithms are developed. In the case of a bias fault, the nonlinear relationship between rudder deflection and pitching moment is assessed online to extract fault signatures. Due to the rudders being located above the centre of mass on the Meraka UAV,

Stellenbosch University https://scholar.sun.ac.za

any rudder deflection in any direction will cause a positive pitching moment. The rudder-induced pitching moment is modelled as a function of the absolute value of rudder deflection in this study, i.e. $C_m = \boldsymbol{f}(\mid \delta_R \mid)$,for the nonlinear simulation model.

The AFDI technique developed to isolate rudder bias faults functions by tracking the effects of the rudders on the pitching moment. A bias fault on one of the rudders will offset trim and cause unwanted pitching. Because the UAV is fitted with a feedback controller, the elevator will compensate for the rudder induced pitch and find a new "biased" elevator trim setting. As a result, the ER filter will estimate a false elevator bias (*pseudo-elevator bias*), which in truth, represents right or left rudder fault. The ER filter will still detect and reconstruct rudder faults but attribute half of the actual bias magnitude to both rudders, regardless of which of the two is faulty. The AFDI approach monitors this behaviour in the *pseudo-elevator bias* to determine which rudder is truly faulty.

Firstly, the FDI algorithm is able to identify the presence of *pseudo-elevator bias* and distinguish it from a real elevator bias, since the FDI relies on the EA filter to track elevator faults. In other words, if there is a real (true) elevator fault, it will appear in the EA filter and will be isolated correctly.

In the case of the ER filter, since a fault in either of the rudders will induce the *pseudo-elevator bias*, the same faulty rudder can be used to remove the *pseudo-elevator bias* by forcing the faulty rudder to a correct trim setting that induces no pitch. This is realised with an active FDI strategy which injects auxiliary signals into the rudders to remove any rudder induced pitching moment.

The rudder whose auxiliary excitation restores or approximates the original "pre-fault" elevator trim setting (the rudder whose auxiliary manipulation can eliminate the *pseudo-elevator bias*) is declared as the rudder with a bias fault. Note that if the "healthy" rudder is actively injected, the *pseudo-elevator bias* bias can only increase. In contrast, if the faulty rudder is injected, the *pseudo-elevator bias* can either increase or decrease down to zero. This is the distinguishing factor that allows the active isolation of the faulty rudder. The decrease in the *pseudo-elevator bias* to zero lets the FDI know that the biased rudder was deflected back to the unbiased trim or zero deflection, resulting in the elevator reverting to the original trim setting. With the elevator back at the trim setting, the *pseudo-elevator bias* disappears, and the rudder that removed its effect is declared as the one having a bias fault.

Stellenbosch University https://scholar.sun.ac.za

4.6.2.2 For Stuck Faults

Once a locked-in-place fault is detected in either of the rudders and classified as such, the stuck-actuator isolation procedure is triggered. This procedure works by injecting the excitation signal into any of the two rudders. The excitation is chosen at a frequency ω_R. If the excitation is injected into the stuck rudder, there will be no response observed from the systems states and parameter estimates, in which case the injected control surface will be declared as the stuck surface. On the other hand, if the excitation is injected on a healthy rudder, the excitation signal frequency of ω_R will propagate through the system and be observed in the measurements and the fault parameter estimates. If the frequency ω_R is detected in the system, then the opposite rudder will be declared as stuck.

4.7 Joint Unscented Kalman Filter (JUKF) and Dual Unscented Kalman Filter (DUKF)

The Kalman filter and the Extended Kalman filter (EKF) have been widely applied to nonlinear dynamic systems in various applications and have gained popularity among researchers and industry [3, 71, 73, 80, 87]. In KF and the EKF, the state distribution is approximated by Gaussian random variable (GRV), relying only on first-order statistics of the system. Moreover, the approach may require large Jacobian matrices, which may be challenging to attain. The KF approach also requires that the chosen system model is differentiable.

The UKF characterises the mean and covariance of the GRV differently, using a set of sample points selected through a deliberate procedure, and passed through the nonlinear function to accurately capture posterior mean and covariance to the 3rd order for any nonlinearity. [74–77]. In this thesis, the application of the UKF to simultaneous state and parameter estimation for FDD is investigated. The TSEKF yielded good results for fault parameter estimation and faults isolation. Nevertheless, highly coupled behaviour was observed between the left and right ailerons, which required intricate bias adaptation techniques to improve their isolation. The Dual Unscented Kalman filter and Joint-Unscented Kalman filter initially investigated in [76], are applied to a nonlinear stochastic aircraft model with split control surfaces.

Stellenbosch University https://scholar.sun.ac.za

4.7.1 Unscented Transformation (UT)

The unscented transform (UT) is a technique for estimating the statistics of a random variable after it has gone through a nonlinear transformation [74, 75]. The basis for the UT is the very intuitive idea that it should be easier to approximate a given distribution than it is to approximate an arbitrary nonlinear function. Consider transforming a random variable $\boldsymbol{x}$ of dimension L through a nonlinear function, $\boldsymbol{y} = \boldsymbol{f}(\boldsymbol{x})$. If the random variable $\boldsymbol{x}$ has a known mean $\bar{\boldsymbol{x}}$ and covariance $\boldsymbol{P}_x$, then the transformation is realised by forming a matrix $\mathcal{X}$ of $2L+1$ sigma vectors $\mathcal{X}_i$ according to the following:

$$\begin{aligned}
\boldsymbol{\mathcal{X}}_0 &= \bar{\boldsymbol{x}} \\
\boldsymbol{\mathcal{X}}_i &= \bar{\boldsymbol{x}} + \left(\sqrt{(L+\lambda)\boldsymbol{P}_x}\right)_i \qquad i = 1, \cdots, L \\
\boldsymbol{\mathcal{X}}_i &= \bar{\boldsymbol{x}} - \left(\sqrt{(L+\lambda)\boldsymbol{P}_x}\right)_i \qquad i = L+1, \cdots, 2L
\end{aligned} \tag{4.7.1}$$

With the weights W_i of the state and covariance are given by

$$\begin{aligned}
W_0^{(m)} &= \frac{\lambda}{L+\lambda} \\
W_0^{(c)} &= \frac{\lambda}{L+\lambda} + \left(1 - \rho^2 + \sigma\right) \\
W_i^{(m)} &= \sigma_i^{(c)} \frac{\lambda}{2(L+\lambda)} \qquad i = 1, \cdots, 2L
\end{aligned} \tag{4.7.2}$$

where $\lambda = \rho^2(L+\kappa) - L$ is a scaling parameter and ρ determines the how the sigma points are spread around the mean $\bar{\boldsymbol{x}}$. The κ is a secondary scaling parameter and σ is to incorporate prior knowledge of the distribution of $\boldsymbol{x}$. The $\left(\sqrt{(L+\lambda)\boldsymbol{P}_x}\right)_i$ is the ith column of the matrix square root of the weighted covariance matrix . Secondly, sigma points are propagated through the nonlinear function to yield a cloud of transformed points from which $\bar{\boldsymbol{y}}$ and $\boldsymbol{P}_y$ can be determined:

$$\boldsymbol{\mathcal{Y}}_i = \boldsymbol{f}(\boldsymbol{\mathcal{X}}_i) \quad , \quad i = 0, \cdots, 2L \tag{4.7.3}$$

and the mean and covariance for y are approximated using a weighted sample mean and covariance of the posterior sigma points,

$$\bar{\boldsymbol{y}} \approx \sum_{i=0}^{2L} W_i^{(m)} \boldsymbol{\mathcal{Y}}_i \tag{4.7.4}$$

$$\boldsymbol{P}_y \approx \sum_{i=0}^{2L} W_i^{(m)} (\boldsymbol{\mathcal{Y}}_i - \bar{\boldsymbol{y}})(\boldsymbol{\mathcal{Y}}_i - \bar{\boldsymbol{y}})^T \tag{4.7.5}$$

where $\bar{\boldsymbol{y}}$ is the mean and $\boldsymbol{P}_y$ is covariance of $\boldsymbol{y}$.

Stellenbosch University https://scholar.sun.ac.za

4.7.2 State Estimation with Unscented Kalman filter

The unscented Kalman Filter (UKF) follows directly from the unscented transformation. The UT technique is simply adopted in the familiar recursive Kalman filter framework to estimate the state:

$$\hat{\boldsymbol{x}}_k = \boldsymbol{x}_{\boldsymbol{predicted,k}} + \boldsymbol{\mathcal{K}}_k(\boldsymbol{y}_k - \boldsymbol{y}_{\boldsymbol{predicted,k}}) \tag{4.7.6}$$

where $\boldsymbol{\mathcal{K}}_k = \boldsymbol{P}_{x_k y_k}\boldsymbol{P}^{-1}_{\tilde{y}_k \tilde{y}_k}$, and the state random variable is augmented with the process and measurement noise variables as follows:

$$\bar{\boldsymbol{x}}_k = \begin{bmatrix} \boldsymbol{x}_k \\ \boldsymbol{w}^x_k \\ \boldsymbol{v}_k \end{bmatrix} \tag{4.7.7}$$

The unscented transformation is now applied to the augmented state random variable by applying the Equations 4.7.1 and the sigma points are calculated based on this augmented state RV. The dimension of the augmented state and matrices are increased according. The complete equations for the implementation of the UKF procedures is given in Table 4.1 for iterations, $k \in [1, \ldots, \infty]$. Rather that finding the true matrix square root of $\eta\boldsymbol{P}$ in (4.7.1) and Tables 4.1 and 4.2, an alternative definition of the matrix square $\boldsymbol{R} = \sqrt{\boldsymbol{P}}$ computes a result such that $\boldsymbol{P} = \boldsymbol{R}\boldsymbol{R}^T$ is utilized. This yields a numerically stable solution found as the lower-triangular Cholesky factorisation provided that $\boldsymbol{P}$ is positive definite.

4.7.3 Parameter Estimation with Unscented Kalman filter

To estimate parameters with UKF procedure requires a nonlinear function that maps $\boldsymbol{y}_k = \boldsymbol{G}(\boldsymbol{x}_k, \boldsymbol{w})$ where $\boldsymbol{x}_k$ is the known input variable and $\boldsymbol{G}(.)$ is the nonlinear map which has been parameterised by the unknown vector $\boldsymbol{w}$. Consider that the nonlinear function maps known inputs and known or desired observations $\{\boldsymbol{x}_k, \boldsymbol{d}_k\}$. The error between the observations and the nonlinear mapping function is given by

$$\boldsymbol{e}_k = \boldsymbol{d}_k - \boldsymbol{G}(\boldsymbol{x}_k, \boldsymbol{w}_k) \tag{4.7.8}$$

The UKF algorithm provides an estimate of the parameters $\boldsymbol{w}_k$ which minimises the expected squared error of (4.7.8). With the, we write an new state transition function to estimate the unknown parameter set as follows

Stellenbosch University https://scholar.sun.ac.za

Table 4.1: State Estimation with Unscented Kalman filter

UKF algorithm for state estimation

Initialise the state vector and covariance with

$$\hat{\boldsymbol{x}}_0 = E\{\boldsymbol{x}_0\}$$
$$\hat{\boldsymbol{x}}^a = E\{\boldsymbol{x}^a\} = \left[\hat{\boldsymbol{x}}_0^T, \mathbf{0}, \mathbf{0}\right]^T$$
$$\boldsymbol{P}_0 = E\left\{(\boldsymbol{x}_0 - \hat{\boldsymbol{x}}_0)(\boldsymbol{x}_0 - \hat{\boldsymbol{x}}_0)^T\right\}$$
$$\boldsymbol{P}_0^a = E\{(\boldsymbol{x}_0^a - \hat{\boldsymbol{x}}_0^a)(\boldsymbol{x}_0^a - \hat{\boldsymbol{x}}_0^a)^T\} = \begin{bmatrix} \boldsymbol{P} & \mathbf{0} & \mathbf{0} \\ \mathbf{0} & \boldsymbol{Q}^x & \mathbf{0} \\ \mathbf{0} & \mathbf{0} & \boldsymbol{R} \end{bmatrix}$$

For $k \in \{1, \cdots, N\}$ calculate the *sigma points* of the state mean and covariance

$$\boldsymbol{\mathcal{X}}_{\boldsymbol{k-1}}^{\boldsymbol{a}} = \left[\hat{\boldsymbol{x}}_{k-1}^a \quad \hat{\boldsymbol{x}}_{k-1}^a + \eta\sqrt{\boldsymbol{P}_{k-1}^a} \quad \hat{\boldsymbol{x}}_{k-1}^a - \eta\sqrt{\boldsymbol{P}_{k-1}^a}\right]$$

For $k \in \{1, \cdots, N\}$ calculate the *time update* of the state vector and covariance

$$\begin{aligned}
\mathcal{X}_{k|k-1}^x &= \boldsymbol{f}\left(\mathcal{X}_{k-1}^x, \boldsymbol{u}_{k-1}, \mathcal{X}_{k-1}^w\right) \\
\boldsymbol{\mathcal{Y}} &= \boldsymbol{h}\left(\mathcal{X}_{i,k|k-1}^x, \boldsymbol{u}_{k-1}, \mathcal{X}_{k-1}^w\right) \\
\hat{\boldsymbol{x}}_{k|k-1}^- &= \sum_{i=0}^{2L} W_i^{(m)} \mathcal{X}_{i,k|k-1}^x \\
\hat{\boldsymbol{y}}_{k|k-1}^- &= \sum_{i=0}^{2L} W_i^{(m)} \boldsymbol{\mathcal{Y}}_{i,k|k-1}^x \\
\boldsymbol{P}_{k+1|k} &= \sum_{i=0}^{(2L)} W_i^{(c)} \left(\mathcal{X}_{i,k|k-1}^x - \hat{\boldsymbol{x}}_k^-\right)\left(\mathcal{X}_{i,k|k-1}^x - \hat{\boldsymbol{x}}_k^-\right)^T
\end{aligned}$$

For $k \in \{1, \cdots, N\}$ calculate the *measurement update* of the state and covariance

$$\begin{aligned}
\boldsymbol{P}_{\tilde{y}_k \tilde{y}_k} &= \sum_{i=0}^{2L} W_i^{(c)} \left(\boldsymbol{\mathcal{Y}}_{i,k|k-1} - \hat{\boldsymbol{y}}_k^-\right)\left(\boldsymbol{\mathcal{Y}}_{i,k|k-1} - \hat{\boldsymbol{y}}_k^-\right)^T \\
\boldsymbol{P}_{x_k y_k} &= \sum_{i=0}^{2L} W_i^{(c)} \left(\boldsymbol{\mathcal{X}}_{i,k|k-1} - \hat{\boldsymbol{x}}_k^-\right)\left(\boldsymbol{\mathcal{Y}}_{i,k|k-1} - \hat{\boldsymbol{y}}_k^-\right)^T \\
\boldsymbol{\mathcal{K}}^x &= \boldsymbol{P}_{x_k y_k} \boldsymbol{P}_{\tilde{y}_k \tilde{y}_k}^{-1} \\
\hat{\boldsymbol{x}}_k &= \hat{\boldsymbol{x}}_k^- + \boldsymbol{\mathcal{K}}^x(\boldsymbol{y}_k - \hat{\boldsymbol{y}}_k^-) \\
\boldsymbol{P}_{k+1|k+1} &= \boldsymbol{P}_k^- - \boldsymbol{\mathcal{K}}^x \boldsymbol{P}_{\tilde{y}_k \tilde{y}_k} \boldsymbol{\mathcal{K}}^T
\end{aligned}$$

where $\eta = \sqrt{L + \lambda}$, $\boldsymbol{x}^a = [\boldsymbol{x}, \boldsymbol{w}^x, \boldsymbol{v}]$, $\mathcal{X}^a = [(\mathcal{X}^x)^T, (\mathcal{X}^{w^x})^T, (\mathcal{X}^v)^T]$ λ is the composite scaling parameter, L is the dimension of augmented states, N is the total number of sample data $\boldsymbol{Q}^x$ is process noise covariance matrix,$\boldsymbol{R}$ is measurement noise covariance matrix and W_i indicates the UT weights

Stellenbosch University https://scholar.sun.ac.za

Table 4.2: Parameter Estimation with Unscented Kalman filter

UKF algorithm for parameter estimation

Initialise the parameters vector and its covariance by
$\hat{\boldsymbol{w}}_0 = E\{\boldsymbol{w}_0\}$
$\boldsymbol{P}_0^w = E\Big\{(\boldsymbol{w}_0 - \hat{\boldsymbol{w}}_0)(\boldsymbol{w}_0 - \hat{\boldsymbol{w}}_0)^T\Big\}$
For $k \in \{1, \cdots, N\}$, calculate the *sigma points* from the parameter mean and covariance

$$
\begin{aligned}
\hat{\boldsymbol{w}}_k^- &= \hat{\boldsymbol{w}}_{k-1}^- \\
\boldsymbol{P}_{w_k}^{w-} &= \boldsymbol{P}_{k-1}^w + \boldsymbol{Q}_{k-1}^w \\
\boldsymbol{\mathcal{W}}_{k|k-1} &= \left[\hat{\boldsymbol{w}}_{k-1}^- \quad \hat{\boldsymbol{w}}_{k-1}^- + \eta\sqrt{\boldsymbol{P}_{k-1}^{w-}} \quad \hat{\boldsymbol{w}}_{k-1}^- - \eta\sqrt{\boldsymbol{P}_{k-1}^{w-}}\right] \\
\boldsymbol{\mathcal{D}}_{k|k-1} &= \boldsymbol{G}\left(\boldsymbol{x}_k, \boldsymbol{\mathcal{W}}_{k|k-1}\right)
\end{aligned}
$$

For $k \in \{1, \cdots, N\}$, calculate the *time update* of the parameter vector and covariance

Option 1: $\hat{\boldsymbol{d}}_k = \sum_{i=0}^{2L} W_i^{(m)} \boldsymbol{\mathcal{D}}_{i,k|k-1}$

Option 2: $\hat{\boldsymbol{d}}_k = \boldsymbol{G}\left(\boldsymbol{x}_k, \hat{\boldsymbol{w}}_k^-\right)$

For $k \in \{1, \cdots, N\}$ calculate the *measurement update* of the parameter vector and covariance

$$
\begin{aligned}
\boldsymbol{P}_{\tilde{d}_k \tilde{d}_k} &= \sum_{i=0}^{2L} W_i^{(c)} \left(\boldsymbol{\mathcal{D}}_{i,k|k-1} - \hat{\boldsymbol{d}}_k\right)\left(\boldsymbol{\mathcal{D}}_{i,k|k-1} - \hat{\boldsymbol{d}}_k\right)^T + \boldsymbol{R}_k^e \\
\boldsymbol{P}_{w_k d_k} &= \sum_{i=0}^{2L} W_i^{(c)} \left(\boldsymbol{\mathcal{W}}_{i,k|k-1} - \hat{\boldsymbol{w}}_k^-\right)\left(\boldsymbol{\mathcal{D}}_{i,k|k-1} - \hat{\boldsymbol{d}}_k^-\right)^T \\
\boldsymbol{\mathcal{K}}_k^w &= \boldsymbol{P}_{w_k d_k} \boldsymbol{P}_{\tilde{d}_k \tilde{d}_k}^{-1} \\
\hat{\boldsymbol{w}}_k &= \hat{\boldsymbol{w}}_k^- + \boldsymbol{\mathcal{K}}^w(\boldsymbol{d}_k - \hat{\boldsymbol{d}}_k^-) \\
\boldsymbol{P}_k^w &= \boldsymbol{P}_k^{w-} - \boldsymbol{\mathcal{K}}^w \boldsymbol{P}_{\tilde{d}_k \tilde{d}_k} \left(\boldsymbol{\mathcal{K}}^w\right)^T
\end{aligned}
$$

where $\eta = \sqrt{L + \lambda}$, λ is the composite scaling parameter, L is the dimension of parameter being estimated, N is the total number of sample data. $\boldsymbol{Q}^w$ is the artificial process-noise covariance and $\boldsymbol{R}_k^e$ is the observation-noise covariance and W_i indicates the UT weights

Stellenbosch University https://scholar.sun.ac.za

$$\boldsymbol{w}_{k+1} = \boldsymbol{w}_k + \boldsymbol{r}_k \tag{4.7.9}$$

$$\boldsymbol{d}_k = \boldsymbol{G}(\boldsymbol{x}_k, \boldsymbol{w}_k) + \boldsymbol{e}_k \tag{4.7.10}$$

Again, since there's no information about the evolution of the unknown parameter $\boldsymbol{w}_k$, we define it as a stationary process with identity state transition matrix, with additive process noise $\boldsymbol{r}_k$. The complete parameter estimation UKF procedure is detailed in Table 4.2

4.7.4 Joint and Dual UKF

The conjoint state-parameter problem consists of simultaneously estimating the clean state $\boldsymbol{x}_k$ and the model parameters $\boldsymbol{w}$ from the noisy data $\boldsymbol{y}_k$. In the preceding sections, the case of separate state and parameter was presented. This technique is also available in the UKF environment, in the forms commonly known as the Joint-UKF and Dual-UKF. Briefly, the Joint-UKF is analogous to the Augmented-EKF, whereas the Dual-UKF [76, 77] is similar to the TSKF where two filters run simultaneously to estimate the state and unknown parameters.

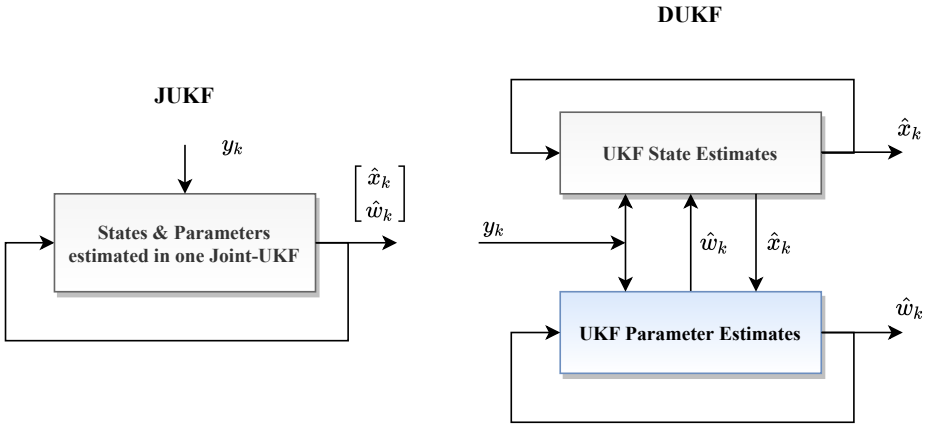

Figure 4.5: A comparison between the Joint-UKF and the Dual-UKF

The key to the DUKF approach is that the state filter utilises the previous estimate of the parameter $\hat{\boldsymbol{w}}_{k-1}$, generated by the parameter UKF that is running in parallel with the state UKF. The DUKF see the parameter estimate as a known input rather than a random variable. Likewise, the parameter filter utilised the previous estimate of the state, $\hat{\boldsymbol{x}}_{k-1}$ which is treated as a known input in the observation equation. This result is the

Stellenbosch University https://scholar.sun.ac.za

iterative online exchange of estimates between the filters in Table 4.1 and Table 4.2.

With the joint-UKF [76] filter, the system states and unknown parameters are estimated together in a larger concatenated vector $\bar{\boldsymbol{x}} = \left(\boldsymbol{x}_k^T, \boldsymbol{w}_k^T\right)^T$. Then the standard algorithm for UKF state estimation in Table 4.1 is applied to the augmented state.

$$\begin{bmatrix} \boldsymbol{x}_{k+1} \\ \boldsymbol{w}_{k+1} \end{bmatrix} = \begin{bmatrix} \boldsymbol{f}\left(\boldsymbol{x}_k, \boldsymbol{w}_k^x, \boldsymbol{v}_k, \boldsymbol{w}_k\right) \\ \boldsymbol{w}_k \end{bmatrix} + \begin{bmatrix} \boldsymbol{0} \\ \boldsymbol{r}_k \end{bmatrix} \tag{4.7.11}$$

Because the joint-UKF augments the state variable and unknown parameter into one vector, the UKF captures the cross-covariance between the state and parameter estimates in the off-diagonal blocks due to:

$$\boldsymbol{P}_{\bar{\boldsymbol{x}}_k} = \begin{bmatrix} \boldsymbol{P}_{\boldsymbol{x}_k} & \boldsymbol{P}_{\boldsymbol{x}_k \boldsymbol{w}_k} \\ \boldsymbol{P}_{\boldsymbol{w}_k \boldsymbol{x}_k} & \boldsymbol{P}_{\boldsymbol{w}_k} \end{bmatrix} \tag{4.7.12}$$

With this formulation, the Joint-UKF to computes cross-correlation between the states and the parameter estimates. Per contra, the DUKF decouples the dual estimation problem by treating the parameter estimate as a known fixed value and not as a random variable in the state filter, and the state estimate as a fixed, known value (and not as a random variable) in the parameter filter. This effectively equates the off-diagonal blocks $\boldsymbol{P}_{\boldsymbol{w}_k \boldsymbol{x}_k} = \boldsymbol{P}_{\boldsymbol{x}_k \boldsymbol{w}_k} = \boldsymbol{0}$. Consequently, the DUKF filters are each less sensitive to erratic behaviour in the other, which is an attractive property for reliable FDD design.

4.8 Actuator Fault Isolation

The fault isolation algorithm is a simple statistical hypothesis test based on preselected thresholds. The TSKF and DUKF already provide estimates of fault parameters, including their magnitude and direction, and can distinguish between control surfaces by tracking their influence on the moments. Therefore, only basic threshold-based isolation techniques are required. The isolation scheme is based on comparing the evolution of the statistical quantities of the fault parameters, calculated online during system operation, to their known initial statistics under fault-free conditions. Firstly, the system has a trial period where the statistics (mean and variance) of each parameter are collected under fault-free conditions. Once known, then the realtime variations in the statistics of the fault parameters can be compared to their initial values. Enough time should be allowed

Stellenbosch University https://scholar.sun.ac.za

to capture accurate statistics of the fault-free conditions. This can be easily done both in simulation and on the real control system. The fault-free statistics must be collected under worst-case scenario to capture for system variations in the extreme direction.

- **Fault-free Statistics**

  In the first stage, the mean and variance of the fault the parameters calculated under the fault-free conditions:

$$\hat{\gamma}_k \sim \mathcal{N}\left(\bar{\boldsymbol{\mu}}_{\hat{\gamma}_0}, \boldsymbol{\sigma}^2_{\hat{\gamma}_0}\right) \tag{4.8.1}$$

  where $\hat{\gamma}_k \in \mathbb{R}^l$ is the estimate of the fault parameter at time t_k. The vector $\bar{\boldsymbol{\mu}}_{\hat{\gamma}_0} = \begin{bmatrix} \bar{\mu}_{\hat{\gamma}_0^1} & \bar{\mu}_{\hat{\gamma}_0^2} & \cdots & \bar{\mu}_{\hat{\gamma}_0^l} \end{bmatrix}^T$ and the matrix $\boldsymbol{\sigma}^2_{\hat{\gamma}_0} = \text{diag}\begin{bmatrix} \sigma^2_{\hat{\gamma}_0^1} & \sigma^2_{\hat{\gamma}_0^2} & \cdots & \sigma^2_{\hat{\gamma}_0^l} \end{bmatrix}$ are the mean and variance of the fault parameter respectively. These values are obtained for $i = 1, \ldots, l$ by

$$\bar{\mu}_{\hat{\gamma}_0^i} = \frac{1}{N_1} \sum_{j=1}^{N_1} \hat{\gamma}_j^i \tag{4.8.2}$$

$$\sigma^2_{\hat{\gamma}_0^i} = \frac{1}{N_1 - 1} \sum_{j=1}^{N_1} \left[\hat{\gamma}_j^i - \bar{\mu}_{\hat{\gamma}_0^i}\right]^2 \tag{4.8.3}$$

  where N_1 is the sample size, which is selected to ensure capturing the accurate statistics of the normal (fault-free) conditions

- **Online Statistics & Isolation Decision**

  In the second part of the analysis, the same statistical quantities are determined under online to detect abnormal (faulty) conditions. We define a moving window of size N_2 and derive the following statistical quantities:

$$\bar{\mu}_{\hat{\gamma}_k^i} = \frac{1}{N_2} \sum_{j=k-N_2+1}^{k} \hat{\gamma}_j^i \tag{4.8.4}$$

$$= \bar{\mu}_{\hat{\gamma}_{k-1}^i} - \frac{1}{N_2}\left[\hat{\gamma}_{k-N_2}^i - \hat{\gamma}_k^i\right] \tag{4.8.5}$$

Stellenbosch University https://scholar.sun.ac.za

$$\sigma^2_{\hat{\gamma}^i_k\, I} = \frac{1}{N_2 - 1} \sum_{j=k-N_2+1}^{k} \left[\hat{\gamma}^i_j - \bar{\mu}_{\hat{\gamma}^i_0}\right]^2 \tag{4.8.6}$$

$$= \sigma^2_{\hat{\gamma}^i_{k-1}\, I} - \frac{1}{N_2 - 1}\left[(\hat{\gamma}^i_{k-N_2})^2 - (\hat{\gamma}^i_k)^2 - 2\bar{\mu}_{\hat{\gamma}^i_k}\varepsilon^i_k\right] \tag{4.8.7}$$

$$\sigma^2_{\hat{\gamma}^i_k\, II} = \frac{1}{N_2 - 1} \sum_{j=k-N_2+1}^{k} \left[\hat{\gamma}^i_j - \bar{\mu}_{\hat{\gamma}^i_k}\right]^2 \tag{4.8.8}$$

$$= \sigma^2_{\hat{\gamma}^i_{k-1}\, II} + \frac{1}{N_2 - 1}\left[2\bar{\mu}^i_{\hat{\gamma}\, k-1}\varepsilon^i_k - (\hat{\gamma}^i_{k-N_2})^2 + (\hat{\gamma}^i_k)^2 - \frac{1}{N_2 - 1}(\varepsilon^i_k)^2\right] \tag{4.8.9}$$

where $\varepsilon^i_k = \hat{\gamma}^i_{k-N_2} - \hat{\gamma}^i_k$, and N_2 is the length of the moving window. The quantity $\sigma^2_{\hat{\gamma}^i_k\, I}$ represents the variance of "fault-free" of parameters, and $\sigma^2_{\hat{\gamma}^i_k\, II}$ is the variance from the moving mean, i.e. moving variance of fault parameters.

Now we define the following detection index function, which is chosen to accentuate the variations in the statistical quantities of parameters from their fault-free values:

$$d^i_k = \frac{\sigma^2_{\hat{\gamma}^i_k\, I}}{\sigma^2_{\hat{\gamma}^i_0}} - \ln\frac{\sigma^2_{\hat{\gamma}^i_k\, II}}{\sigma^2_{\hat{\gamma}^i_0}} - 1, \qquad i = 1, \cdots, l \tag{4.8.10}$$

This index is calculated at every time-step k and is used to declare fault in the ith actuator whenever a preset threshold is $\boldsymbol{J}_i$ exceeded

$$\mathcal{H}_0 \text{ :system operates normally, and} \tag{4.8.11}$$

$$\mathcal{H}_1 \text{ :fault has occurred in the } i\text{th actuator.} \tag{4.8.12}$$

$$\mathcal{H}_0 : \; d^i_k \leq \boldsymbol{J}_i \quad \forall k \tag{4.8.13}$$

$$\mathcal{H}_1 : \; d^i_k > \boldsymbol{J}_i \quad \exists k \tag{4.8.14}$$

where $\mathcal{H}_0$ indicates that no significant statistical shifts observed in the ith actuator and thus no fault declared in the actuator; and $\mathcal{H}_1$ indicates that significant statistical shifts observed in the ith actuator and thus a fault is declared in that actuator.

Stellenbosch University https://scholar.sun.ac.za

4.8.1 Adaptive Isolation Threshold

It noted that the function 4.8.10, when simplified, has the form $x^2 - \ln x^2 - 1$ and d_k^i grows both quadratically and logarithmically as a function of fault size. Faults of small magnitudes will generate smaller d_k^i and vice versa. If J_i is set too high, then small faults will be missed resulting in high missed detection rates. If set too low, there will be high false detection rates due to transient jumps in the strongly coupled parameters or jumps caused by noise. Simulations show that a fault in any control surface will cause a transient response in the rest. The related surfaces (e.g. right and left ailerons) will particularly induce large transients that eventually disappear. These transients trigger false alarms if J_i is set too low. Consequently, it is impossible to set a static threshold of J_i that works for all fault sizes. To solve this problem, the thesis proposed the following adaptive threshold function.

$$J_k^i = J_0^i + \nu^i \beta_k \tag{4.8.15}$$

where J_0^i is the minimum isolation threshold selected for the ith to ensure that small-sized faults can be isolated. In 5.8, β_k represents the normalised innovation squared (NIS) which is a χ^2- distributed random variable and is a measure of the unbiasedness of the innovation. When the KF is set correctly, the NIS will have zero mean and covariance equal to identity ($\boldsymbol{I}$). If there is a fault present in the system affecting the mean and variance of the innovation, the NIS will grow and a larger value dependent on the fault. Since β_k varies as a function of fault size, when larger faults occur, J_k^i will grow significantly, and a higher alarm threshold will set due to the variables $\nu^i \beta_k$. This greatly improves the reliability, sensitivity and robustness of the FDI by reducing false alarms and missed detections.

4.9 Normalised Innovation Squared

As stated in the preceding section, the FDI utilised the normalised innovation squared (NIS), to detect the presence of an actuator or sensor fault in the system. Under the Level 1 analysis, the FDI algorithm checks the normalised innovation squared (NIS) in both the EA and ER filters against a probabilistically preset threshold. The NIS is calculated from the innovation sequence of the TSKF. The NIS is a χ^2-distributed random variable that represents the unbiasedness of the innovation sequence of the KF.

Stellenbosch University https://scholar.sun.ac.za

Provided that the TSKF is tuned correctly, the unbiased NIS will have zero mean and covariance equal to the identity matrix.

Firstly, a normalised innovation sequence is defined by the following:

$$\boldsymbol{\eta}_k = \left(\boldsymbol{C}_{k+1}\tilde{\boldsymbol{P}}^x_{k+1|k}\boldsymbol{C}^T_{k+1} + \boldsymbol{R}_{k+1}\right)^{-1/2}\tilde{\boldsymbol{r}}_k \tag{4.9.1}$$

If the Kalman filter has been correctly tuned by the appropriate selection of the $\boldsymbol{Q}^x$, $\boldsymbol{Q}^\gamma$, and $\boldsymbol{R}$, matrices, then then it follows by definition that $E\{\boldsymbol{\eta}^T_k\boldsymbol{\eta}_k\} = \boldsymbol{I}$ (a unit matrix). Both actuator and sensor fault faults will influence the mean of the innovation sequence, and to the detect that shift, we define the following function, which is the NIS of the Kalman filter:

$$\beta_k = \sum_{j=k-M+1}^{k} \boldsymbol{\eta}^T_k\boldsymbol{\eta}_k \tag{4.9.2}$$

$$= \sum_{j=k-M+1}^{k} \tilde{\boldsymbol{r}}^T_k\left(\boldsymbol{C}_{k+1}\tilde{\boldsymbol{P}}^x_{k+1|k}\boldsymbol{C}^T_{k+1} + \boldsymbol{R}_{k+1}\right)^{-1}_k\tilde{\boldsymbol{r}}_k \tag{4.9.3}$$

where M above is the rolling window in which the normalised innovation squared is evaluated every at every iteration. It turns out that this function has a χ^2 distribution with $M \times n$ degrees of freedom, where n is the vector size of the innovation sequence (See Appendix E.1). Since this function is affected by both actuator or sensor faults, we use it to detect a system-level (which we call *Level-1* analysis) by setting up the following two hypotheses:

$$\mathcal{H}_0 : \textit{system operates normally, and} \tag{4.9.4}$$

$$\mathcal{H}_1 : \textit{fault occurs in the system.} \tag{4.9.5}$$

To evaluate the hypotheses, we use the select a desired significance level α for $\mathcal{H}_1$ (such as $\alpha = 0.05$), and and use the χ^2 PDF to an appropriate threshold by:

$$P\{\chi^2 > \chi^2_{\alpha,M.s}\} = \alpha; \quad 0 < \alpha < 1 \tag{4.9.6}$$

If the calculated value of β_k is greater than the threshold value $\chi^2_{\alpha,M.s}$ then the hypothesis $\mathcal{H}_1$ is true as follows

$$\mathcal{H}_0 : \beta_k \leq \chi^2_{\alpha,M.s} \quad \forall k \tag{4.9.7}$$

$$\mathcal{H}_1 : \beta_k > \chi^2_{\alpha,M.s} \quad \exists k \tag{4.9.8}$$

Stellenbosch University https://scholar.sun.ac.za

4.10 Sensor Fault Isolation Algorithm

To isolate the sensor faults in the innovation channel affecting the characteristics of the sequence $\bar{\boldsymbol{\eta}}_k$, we construct the following sample covariance matrix of the normalized innovation sequence as follows:

$$\hat{\boldsymbol{S}}_k = \frac{1}{M-1} \sum_{j=k-M+1}^{k} (\boldsymbol{\eta}_j - \bar{\boldsymbol{\eta}}_k)(\boldsymbol{\eta}_j - \bar{\boldsymbol{\eta}}_k)^T \tag{4.10.1}$$

where $\bar{\boldsymbol{\eta}}_k = \frac{1}{M} \sum_{j=k-M+1}^{k} \boldsymbol{\eta}_j$ is the moving average of the innovation sequence, sample over M iterations

To isolate the faulty sensor, we define a statistical variable as the ratio between the sampled and theoretical variances $\hat{\sigma}_i^2/\sigma_i^2$. This function can then be used to detect changes in each channel of the innovation sequence to isolate the failed sensor. Since $\boldsymbol{\eta}_k \sim \mathcal{N}(0, \sigma_i)$, it follows that

$$\frac{\boldsymbol{v}_i}{\sigma_i^2} \sim \chi^2_{\alpha,M-1}, \quad \forall i, \quad i = 1, 2, \cdots, n \tag{4.10.2}$$

where $\boldsymbol{v}_i = (M-1)\hat{\sigma}_i$. Since $\sigma_i^2 = 1$ for normalized innovation sequence it follows that,

$$v_i \sim \chi^2_{\alpha,M-1}, \quad \forall i, \quad i = 1, 2, \cdots, n \tag{4.10.3}$$

By selecting level of significance as α we can find the threshold as follows:

$$P\{\chi^2 > \chi^2_{\alpha,M-1}\} = \alpha; \quad 0 < \alpha < 1 \tag{4.10.4}$$

The above equation allows selecting an appropriate threshold $\chi^2_{\alpha,M-1}$ for a desired significance level. If a fault occurs, it will change the mean and variance of the innovation sequence, and the statistics v_i will exceed the threshold value $\chi^2_{\alpha,M-1}$ depending on $(1-\alpha)$, and degree of freedom $(M-1)$.

As detailed in Appendix E.2, as soon as the statistical function v_i exceeds the threshold $\chi^2_{\alpha,M-1}$ the fault should be immediately detected, because once N reaches M $(N = M)$, the statistical function will start to decrease.

The sample variances of each innovation channel $\hat{\sigma}_i^2$ are simply the diagonal components of the sampled covariance normalised innovation matrix $\hat{\boldsymbol{S}}_k$. Thus there is no need to individually calculate these statistics for each measurement in the innovation vector. However, the diagonal of the normalised innovation matrix $\hat{\boldsymbol{S}}_k$ need to be multiplied by $M-1$ to get

Stellenbosch University https://scholar.sun.ac.za

the correct values. For fault isolation, these values should be compared with $\chi^2_{\alpha,M-1}$ and with one each other. The algorithm assumes only one sensor fault at any given time, so only the largest statistical function to exceed the threshold is declared to reflect a sensor fault. The decision logic is as follows; if $\hat{\boldsymbol{S}}_{\max,k} > \chi^2_{\alpha,M-1}$, where $\hat{\boldsymbol{S}}_{\max,k} = \max\{\hat{\boldsymbol{S}}_{ii,k} | i = 1, 2, \ldots, n\}$, the hypothesis $\mathcal{H}_1$ is true for the ith sensor associated with $\hat{\boldsymbol{S}}_{\max,k}$. $\hat{\boldsymbol{S}}_{ii,k}$ represents the iith component of $\hat{\boldsymbol{S}}_k$

Stellenbosch University https://scholar.sun.ac.za

Chapter 5

Simulations

In this section, the proposed FDD algorithms are tested and evaluated for reliability and robustness in a high fidelity nonlinear simulated environment. Firstly, a description of the nonlinear stochastic aircraft model is given. A layout of the simulation campaign to validate and test the reliability of the FDD algorithm is outlined. Simulation results for various fault scenarios and fault types are presented. Performance results from 1000 Monte-Carlo simulations are presented for the three fault types considered.

5.1 Nonlinear Simulation Environment

The high-fidelity nonlinear aircraft model was designed with software packages MATLAB® and Simulink ® and incorporates the nonlinear kinematic and dynamic equation presented in Chapter 3. Figure 5.1 shows the nonlinear model is embedded with atmospheric disturbance models, including turbulence, gusts and wind shear, sensor noise model, actuator, and control surface nonlinearities such as saturation and abrupt, discontinuous failures.

In practice, there are multiple sources of error in UAV sensors. These may be random, such as electrical noise, or maybe caused by nonlinearity, temperature sensitivity, or cross-axis sensitivity which are more deterministic. To simulate sensor measurement noise, Gaussian noise with zero mean and sensor dependant variance is superimposed onto the system states. The sensor variances are chosen based on typical industry standard specifications for commercially available sensors used in low-cost UAVs for each sensing device. The sensors modelled includes rate gyros, pressure sensors, and magnetometers.

Stellenbosch University https://scholar.sun.ac.za

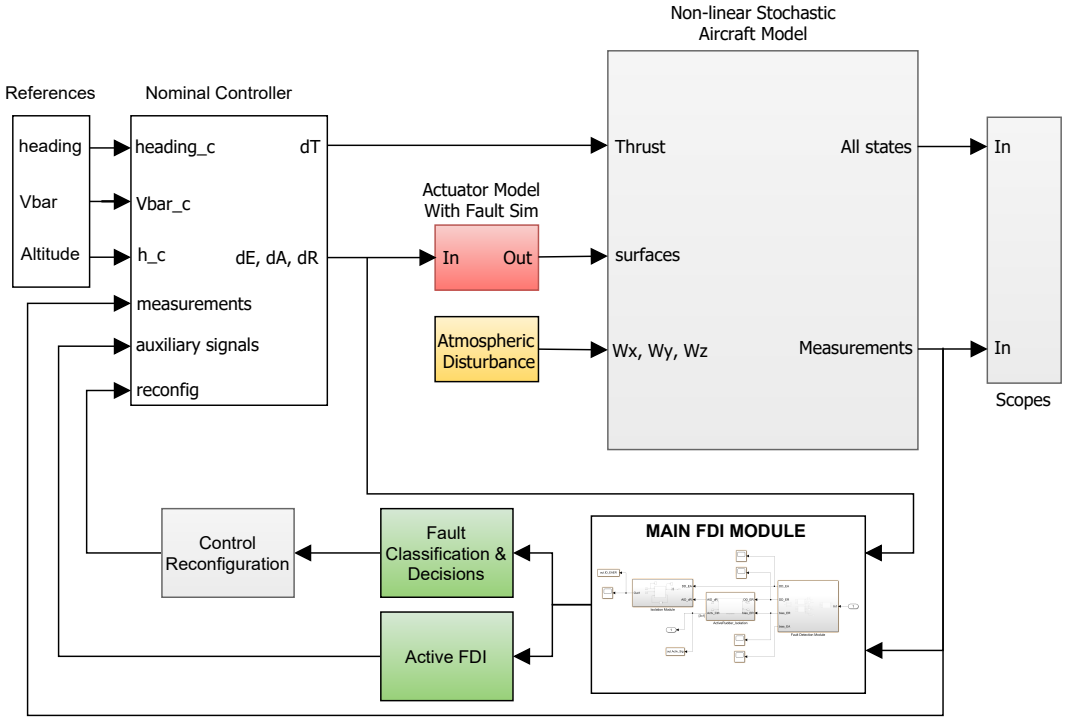

Figure 5.1: High-fidelity nonlinear dynamic model simulation, with autopilot controller and FDI module

The wind is modelled as having a steady component plus atmospheric disturbances. Gust components are produced by passing white noise through the Dryden filters. The Dryden gust model parameters are defined in the MIL-F-8785C specification. Angular rates turbulence, discrete gust buildup, and wind shear models are embedded into the nonlinear equation using the Aerospace Blockset in Simulink. Steady wind components are rotated from the inertial frame to the body frame and added to the gust components to produce the total wind experienced by the UAV model. The nonlinear simulated aircraft is fitted with an autopilot controller, and faults are routinely introduced during straight and level trimmed flight.

5.1.1 Simulation Tests Methodology

During each failure scenario, system states, system inputs, and estimates of the reconstructed fault parameters are captured and recorded for presentation in this section. Based on this data, performance indexes are calculated to evaluate the performance and reliability of the FDD design. Firstly, the chapter presents selected demonstrative results to illustrate the robustness introduced by the proposed FDI algorithm. Secondly, a valida-

Stellenbosch University https://scholar.sun.ac.za

tion campaign is performed in a Monte Carlo framework to truly test the reliability of the FDI and expose the FDD algorithm not only to fault scenarios of different types and magnitudes, but also to scenarios where all or a subset of the aircraft model parameters and disturbances are scattered, each with its own statistical distribution (means dispersion). The validation campaign is performed for bias, LoE and LIP actuator faults. The FDD's reliability is evaluated through a Monte-Carlo statistical analysis from a set of 1000 fault scenarios that occur randomly in the left or right elevator, aileron or rudder. Each of the six control surfaces has an equal probability of failure during each run, and only one controlled surface failure can fail at a time during the MC campaign. Each failure scenario is performed with randomly distributed turbulence profiles, aircraft mass, centre-of-gravity locations, aerodynamic coefficients, trimmed height and speed. The characteristics of the parameter distributions are given in Table 5.1

Table 5.1: Distributions of the Meraka aircraft parameters, an fault magnitudes during MC simulations

Parameter	**Distribution**	**mean**	α	**min**	**max**
Long. wind	normal	6m/s	2m/s	N/A	N/A
Lat. wind	normal	6m/s	2m/s	N/A	N/A
Mass	uniform	N/A	N/A	23 kg	27 kg
CG	uniform	N/A	N/A	95%	105%
Aero. coeffs.	uniform	N/A	N/A	98%	102%)
Bias	uniform	N/A	N/A	1°	5°
LIP	uniform	N/A	N/A	1°	5°
LoE	uniform	N/A	N/A	40%	95%

5.2 Simulation of Bias Faults

In this section, bias faults are simulated, and the results are presented. If a bias fault is detected, the hybrid FDI model remains in the nominal state, and no switching occurs. As pointed out in the preceding sections, for the case of a bias fault, the orthogonal excitation signals in the AFDI will cancel each other out, and the frequency of the test signal will not be present in the parameter estimate. This phenomenon is illustrated through simulations in this chapter.

Stellenbosch University https://scholar.sun.ac.za

5.2.1 Single Elevator Fault with and without Adaptive Procedures

In this simulation test, a single bias fault of $5°$ is induced in the right elevator at time $t_F = 20s$, and the results are presented. The main purpose of the simulation test is to demonstrate the capabilities of the FDI algorithm in isolating and reconstructing a single bias fault. The second objective is to compare the FDI's performance with and without the proposed $\boldsymbol{Q}^{\gamma}$ - adaptation technique.

Thus, a total of three simulation tests are carried out in this experiment. The first experiment is carried out without any adaptation procedure. The second carried out with the $\boldsymbol{P}^{\gamma}$ - adaptation procedure proposed by Wu[73], and the third is carried out with the novel $\boldsymbol{Q}^{\gamma}$ - adaptation procedure proposed in this thesis. The experimental setup for all three scenarios are identical. In all test cases, a $5°$ fault is induced in the right elevator while the simulated flight conditions and aircraft parameters are kept the same.

The simulations' test criteria is to compare effectiveness in fault isolation and accuracy in reconstructing the fault parameter. Figures 5.2, 5.3 and 5.4 show the the first, second and third experiments respectively. The

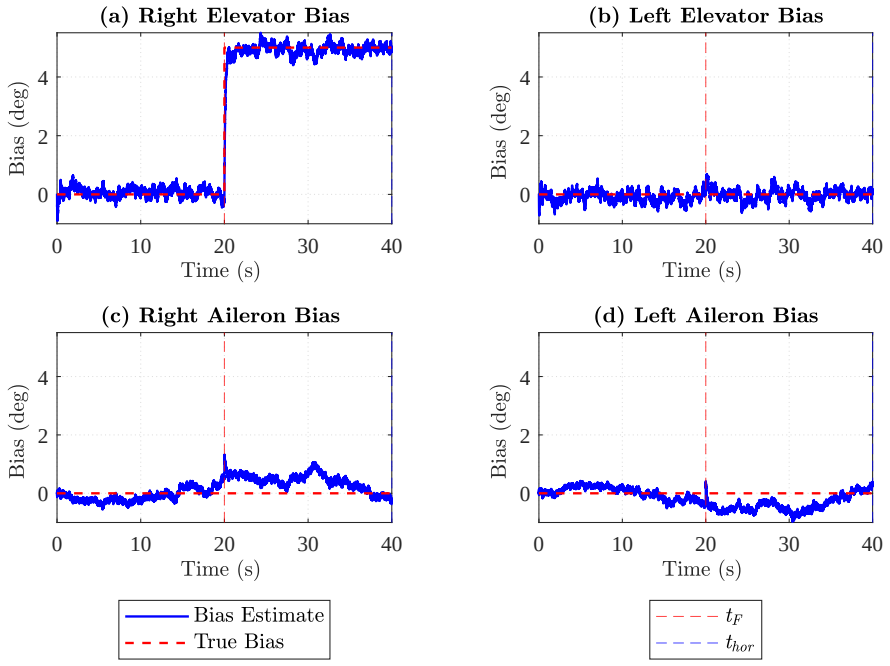

Figure 5.2: Single fault scenario of $5°$ bias fault in the right elevator. The fault is reconstructed with the EA filter without any forgetting factor adaptation

Stellenbosch University https://scholar.sun.ac.za

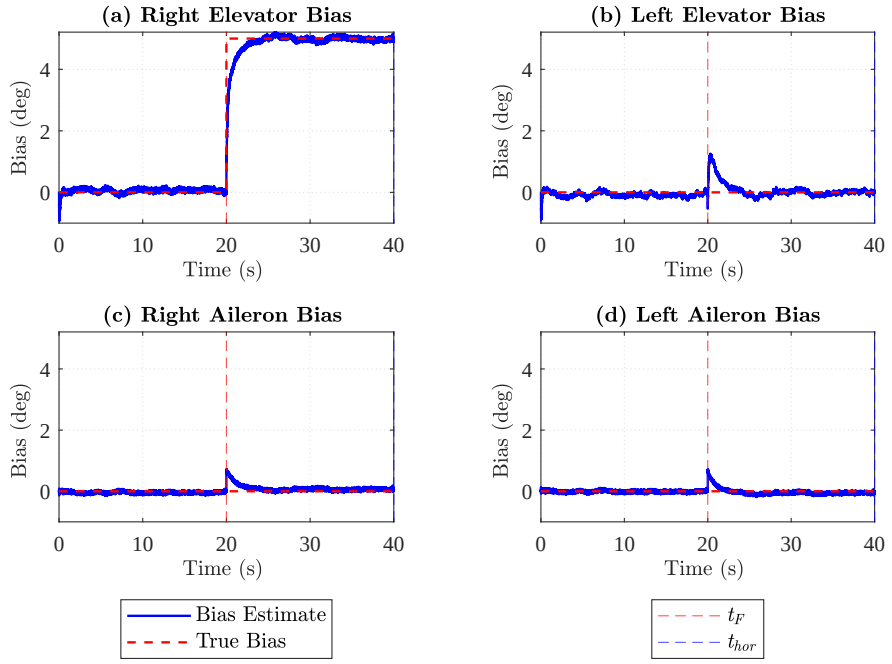

Figure 5.3: Single fault scenario of 5° bias fault in the right elevator. The fault is reconstructed with the EA filter with the forgetting factor applied to the $\boldsymbol{P}_k^{\gamma}$ matrix

results in Figure 5.2 are based on the non-adaptive TSKF. The results in Figure 5.3 are based on the $\boldsymbol{P}_k^{\gamma}$ covariance matrix of the bias estimate error in accordance with Equation (4.4.4). Finally, the results in Figure 5.4 are based on the $\boldsymbol{Q}_k^{\gamma}$ additive noise covariance matrix fault parameter in accordance with Equation (4.4.11).

As seen in Figure 5.2 plot (a), the 5° bias fault in the right elevator is sufficiently reconstructed by the EA filter. Moreover, the fault is tracked at a fast rate. Note also, the left elevator parameter estimate in 5.2 plot (b), remained insensitive to the presence of the fault in the right surface. Nevertheless, all fault estimates show noise sensitivity, which is more pronounced in the aileron parameters, appearing as a common-mode bias. As mentioned in Chapter 4, in the non-adaptive TSKF, the $\boldsymbol{Q}_k^{\gamma}$ matrix has to be set high enough to ensure the TSKF tracks the abrupt faults. However, this results in noise sensitivity during steady state. This phenomenon can be observed in Figure 5.2 plots (c) and (d), where the aileron estimates continually blows-up symmetrically around zero.

A closer inspection of plots in 5.2 (a) and (b) reveal that a common-mode drift is also present in the elevator fault estimates. However, this behaviour is prevalent in the aileron parameters estimates due to the strong

Stellenbosch University https://scholar.sun.ac.za

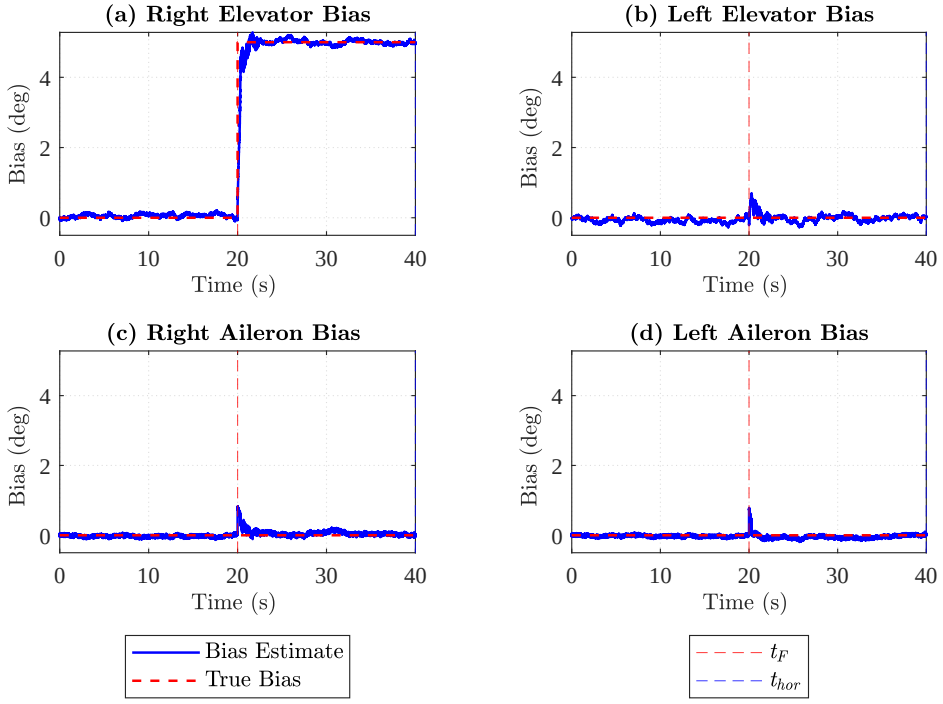

Figure 5.4: Single fault scenario of 5° bias fault in the right elevator. The fault is reconstructed with the EA filter with the forgetting factor applied to the $\boldsymbol{Q}_k^{\gamma}$ matrix

coupling effect in the ailerons. The noise sensitivity is induced by strong excitation from wind disturbances as well as sensor noise. It is noteworthy that in small UAVs, winds can amount to 15 to 60% of the vehicle airspeed and atmospheric disturbances represent significant system noise. A study in [88], shows a correlation between size reduction and reduced handling capabilities in small UAVs.

Two adaptive methods were considered to address the noise sensitivity. From plots in Figure 5.3 it is evident that the forgetting factor described in Equation (4.4.5) is capable of removing noise sensitivity and reconstruct parameters with higher accuracy and resolution. However, a minor loss in tracking ability can be observed in Figure 5.3 plots (a) and (b), and a larger and wider jump is observed in the healthy elevator in Figure 5.3 plot (b), as the FDI tries to figure out which elevator has failed.

As detailed in Chapter 4, the forgetting factor proposed by Wu [73] is based on constraining the fault estimate error covariance matrix within some bounds given by $\sigma_{min}\boldsymbol{I} \leq \boldsymbol{P}_{k+1|k}^{\gamma} \leq \sigma_{max}\boldsymbol{I}$. These constraints ultimately removes the off-diagonal components from the covariance matrix, needed to capture any cross-correlation (interaction between surfaces and

Stellenbosch University https://scholar.sun.ac.za

aircraft dynamics) between parameters needed to allow correct tracking of parameters.

In this thesis, an adaptation technique that does not reduce the filter's tracking ability is proposed. Moreover, the algorithm also reduces the sensitivity to noise during steady-state. The technique relies on adapting the $\boldsymbol{Q}_k^\gamma$ in the direction of information flow during the evolution of the fault parameters. The $\boldsymbol{P}_k^\gamma$ matrix is kept intact to ensure cross-correlation between all parameters is tracked by the TSKF algorithm (see 4.4.2).

The simulation results for the same single fault scenario considered before are shown in Figures 5.4. Again, the only difference between the simulation and preceding ones is the adaptation technique. The approach relies upon selecting a small initial $\boldsymbol{Q}_k^\gamma$ to ensure noise insensitivity and bumping up the same matrix in the direction of parameter variation. Note that parameter variations will increase signification during faults.

In Figure 5.4, we see increased activity just after time t_F, especially in the faulty control surface in plot (a). After a fault is detected, the $\boldsymbol{Q}_k^\gamma$ becomes more aggressive in the direction of the faulty surface, allowing faster tracking in proportion to parameter variation. This is archived by scaling up the eigenvalues of $\boldsymbol{Q}_k^\gamma$ corresponding to normalised unit eigenvectors in the direction of variation. Because the adaptation algorithm is based on moving variances, this gives the algorithm the ability to discount old data outside the evaluation window. When the moving window's variation ceases, adaptation will also cease, by which time the TSKF would have hopefully found the true estimate of the fault parameters. This algorithm greatly enhances the weaknesses observed in the non-adaptive TSKF and in the $\boldsymbol{P}_k^\gamma$ forgetting factor approach. This improvement will be more evident in the case of an aileron fault, which is discussed in the next section.

5.2.2 Single Aileron Fault with and without Adaptive Procedures

In this simulation test, the setup, simulated environment, flight conditions and aircraft parameters are the same as the previous section, except that test bias faults of $5°$ are injected into the right aileron. Again, a total of three simulation tests are carried out. The first experiment is carried out without any adaptation procedure. The second carried out with the $\boldsymbol{P}^\gamma$ - adaptation, and the third is carried out with the $\boldsymbol{Q}^\gamma$ - adaptation procedure

Stellenbosch University https://scholar.sun.ac.za

proposed in this thesis. For three tests, a $5°$ fault is induced in the right aileron.

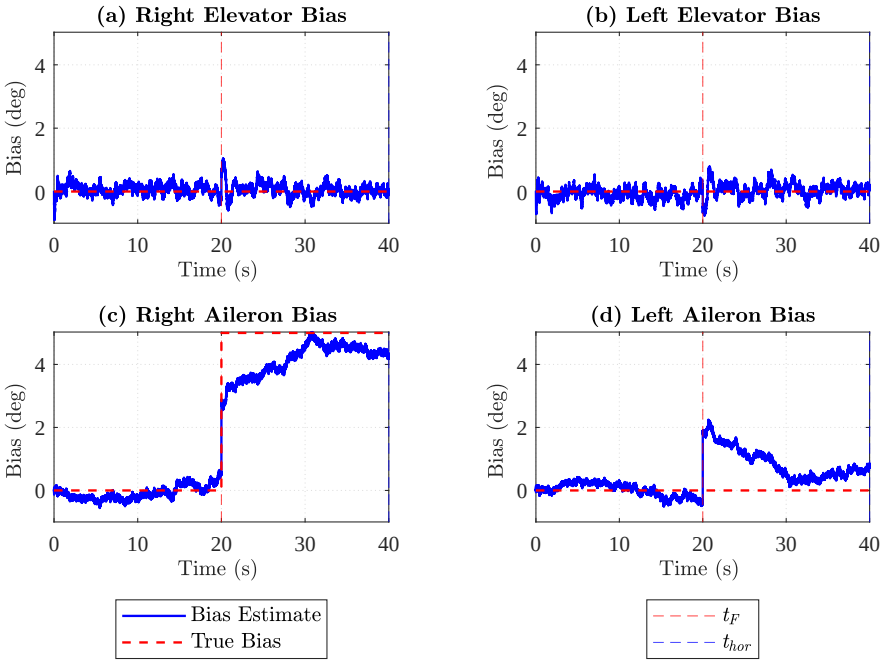

Figure 5.5: Single fault scenario of $5°$ bias fault in the right aileron. The fault is reconstructed with the EA filter without any forgetting factor adaptation

Figure 5.5 shows simulation results where the test was carried out without any adaptation procedure. Similar to the previous section, the fault estimates display noise sensitivity. The FDI is reconstructing the fault in the right aileron, with slower tracking capabilities than it was the case for the elevator fault. The ailerons dynamics appears to be highly coupled with high symmetry. This results in a significant spike in the "healthy" aileron as seen in Figure 5.5 plot (d). The FDI also takes longer to distinguish between the failed (right) and the healthy (left) aileron, has high noise sensitivity and is subject to a significant common-mode-bias superimposed on the aileron parameters. The fault parameter reached the correct value in $10s$, as compared to the elevator (previous section), which occurred within less than $1s$. This slower performance is simply a property of the ailerons owing to their dynamics. Nevertheless, the performance may be improved with adaptation procedures.

Figure 5.6 shows simulation results where the test was carried out with the $\boldsymbol{P}^{\gamma}$ - adaptation procedure incorporated. As seen, the common-mode-

Stellenbosch University https://scholar.sun.ac.za

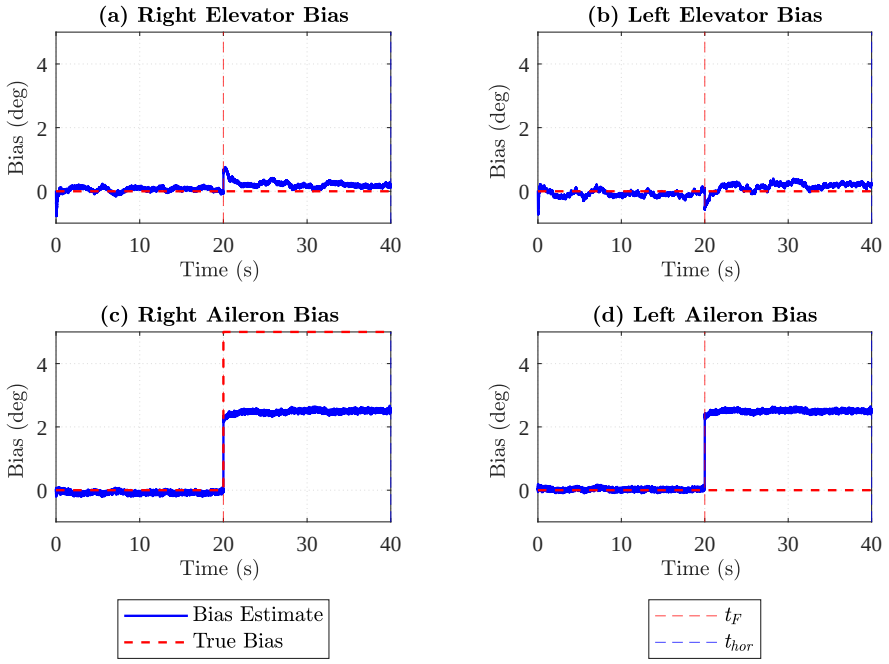

Figure 5.6: Single fault scenario of $5°$ bias fault in the right aileron. The fault is reconstructed with the EA filter with the forgetting factor applied to the $\boldsymbol{P}_k^{\gamma}$ matrix

bias and noise sensitivity have been significantly reduced in the steady-state. The FDI has lost its ability to distinguish between the right and the left ailerons and wrongly assigns half the true magnitude to both ailerons.

To state again, this is due to the $\boldsymbol{P}^{\gamma}$ - adaptation procedure constraining parameter estimate error covariance matrix within the boundaries $\sigma_{min}\boldsymbol{I} \leq \boldsymbol{P}_{k+1|k}^{\gamma} \leq \sigma_{max}\boldsymbol{I}$. This constraint makes the off-diagonal zero, removing information about the evolution of the parameters needed for correct tracking of faults. The $\boldsymbol{P}^{\gamma}$ - adaptation procedure improves robustness against noise but greatly degrades the filter's tracking abilities and affects the system's isolabilty properties as seen in Figure 5.6 plot (c) and (d), where the FDI can no longer distinguish between the left and right ailerons. The observation of these deficiencies motivated developing the proposed $\boldsymbol{Q}^{\gamma}$ - adaptation procedure in this thesis.

Figure 5.7 shows simulation results where the test was carried out with $\boldsymbol{Q}^{\gamma}$ - adaptation. The algorithm shows excellent robustness against noise during steady-state. After the fault occurs at time $t_F = 20s$, there is increased activity in the right aileron's fault parameter due to the activation of the adaptation procedure until the variation of parameters has reduced.

Stellenbosch University https://scholar.sun.ac.za

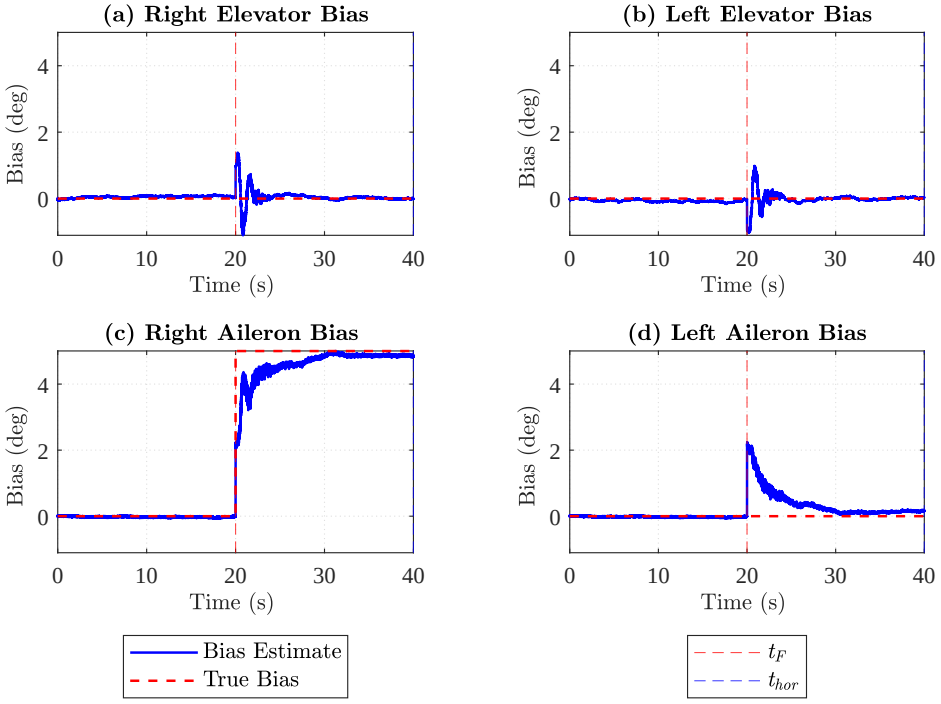

Figure 5.7: Single fault scenario of $5°$ bias fault in the right aileron. The fault is reconstructed with the EA filter with the forgetting factor applied to the $\boldsymbol{Q}_k^{\gamma}$ matrix

The $\boldsymbol{Q}_k^{\gamma}$ - adaptation procedure proposed in this thesis enhanced the filter's tracking ability, and isolability aileron is preserved. The approach displays great robustness against noise, parameter tracking ability, selectivity between opposite surfaces and sensitivity to faults. Now that the superiority of the $\boldsymbol{Q}_k^{\gamma}$ - adaptation procedure has been demonstrated, it is noted that most of the upcoming simulations are based only on the $\boldsymbol{Q}_k^{\gamma}$ - adaptation procedure.

5.2.3 Fault Detection Function and Adaptive Threshold

The purpose of this test is to demonstrate the performance of the fault detection function d_k in Equation (4.8.10), the evolution of the NIS during faults, and the adaptive isolation threshold function, which is derived based on the NIS. The simulation plots presented in this section were extracted from the same simulation trial in the previous section, where a $5°$ was injected into the right aileron.

In the previous section, the simulation for the case of an aileron failure in Figure 5.5, with a non-adaptive FDI, represents the worst performance observed with this FDI configuration. The parameter estimates

Stellenbosch University https://scholar.sun.ac.za

were noisy, and there was a significant jump in the healthy (left) aileron parameter, which could potentially cause false detections by exceeding the threshold function. Therefore, this case is ideal for testing the effectiveness of the adaptive threshold function.

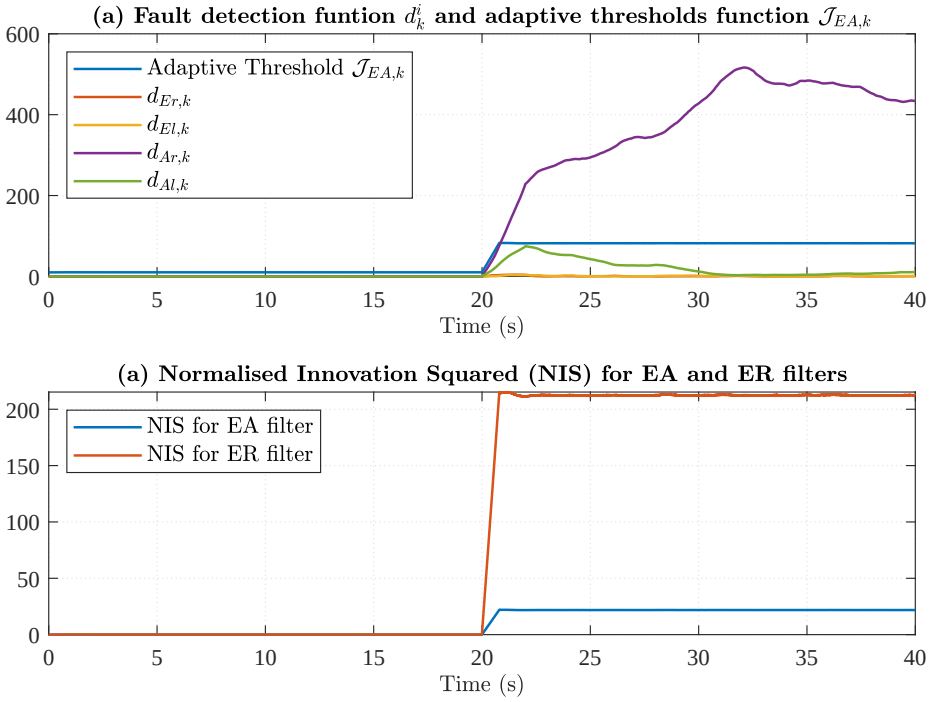

Figure 5.8: (a) Evolution of the fault detection function and adaptive isolation threshold during a right aileron fault at 20 seconds **(b)** normalised innovation squared functions for EA and ER filters with right aileron fault at 20 seconds

Figure 5.8 (b) depicts the evolution of the detection function, the NIS, and the adaptive threshold during the right aileron fault scenario in Figure 5.5. At time $t_F = 20s$, a fault occurs in the right aileron. Observe in the bottom plots of Figure 5.5 (b) that NIS for both the EA and ER filter rise to large values after $t_F = 20s$. We know that the EA filter will estimate aileron faults correctly. Thus even though the NIS for both filters exceed the threshold $\chi^2_{\alpha,M.s}$, the NIS for the ER filter assumed a significantly larger final value because the ER filter is more biased (that is, it is giving wrong estimates because there is no fault in the ER). This behaviour enables the FDI to select the correct filter during the Level 2 analysis by comparing their NIS.

Observe in Figure 5.8 (b) in the top plots that at $t_F = 20s$, the fault detection function $d_{Ar,k}$ of the right aileron grows much higher value than in

Stellenbosch University https://scholar.sun.ac.za

its pre-fault state. The function remains large and grows or declines based on the evolution of the δ^*_{Ar} fault parameter. It is noted that the fault parameter for the left (healthy) aileron also had a significant jump at $t_F = 20s$ (Figure 5.5 plot (d)). Therefore its corresponding detection function $d_{Al,k}$ in Figure 5.8 jumped to larger values after $t_F = 20s$, and after peaking, it started to decline in response to the left aileron's fault parameter δ^*_{Al}. It is this momentary rise in the function $d_{Al,k}$ that can cause false detections if a static threshold is selected.

Observe that the adaptive threshold function (represented by the blue line) was a small value before $t_F = 20s$. Indeed, the additive constant in the threshold function must be set to a small value to ensure that small faults are not missed. However, at time $t_F = 20s$, the adaptive threshold function sets a new threshold dependent on the fault size. More precisely, the new threshold is dependant on the biasedness in the Kalman filter, which is th

5.2.4 Multiple Fault Scenarios and Fault Isolation

A major advantage of the proposed FDD approach is its ability to detect multiple faults occurring simultaneously. The purpose of the simulation tests in the section is to demonstrate the proposed FDI's ability to detect multiple faults. While the FDI can detect multiple faults occurring at different timestamps, the simulations consider faults occurring simultaneously. Faults of different magnitudes are injected into the two ailerons and two elevators simultaneously at time $t_F = 20s$.

Simulations reveal that the detection of multiple faults may be simpler with this approach. Part of the reason is that; multiple faults result in larger perturbation in the system, which results in significant excitation and coupling effects, enabling the TSKF to learn the new system states and parameters quicker.

Figure 5.9 depicts simulation results for the case where a non-adaptive FDI was used, while Figure 5.10 depicts the case where $\boldsymbol{Q}^{\gamma}_{k}$ - adaptation was used. Comparing Figures 5.9 and 5.10, it is clear that the adaptive FDI once again displays significant improvement in noise sensitivity, without loss of tracking capabilities or accuracy in reconstructing parameters. Moreover, due to each fault parameter having individual adaptive thresholds, multiple faults of different sizes are isolated without computing probabilities, which is typically required with MM and IMM ap-

Stellenbosch University https://scholar.sun.ac.za

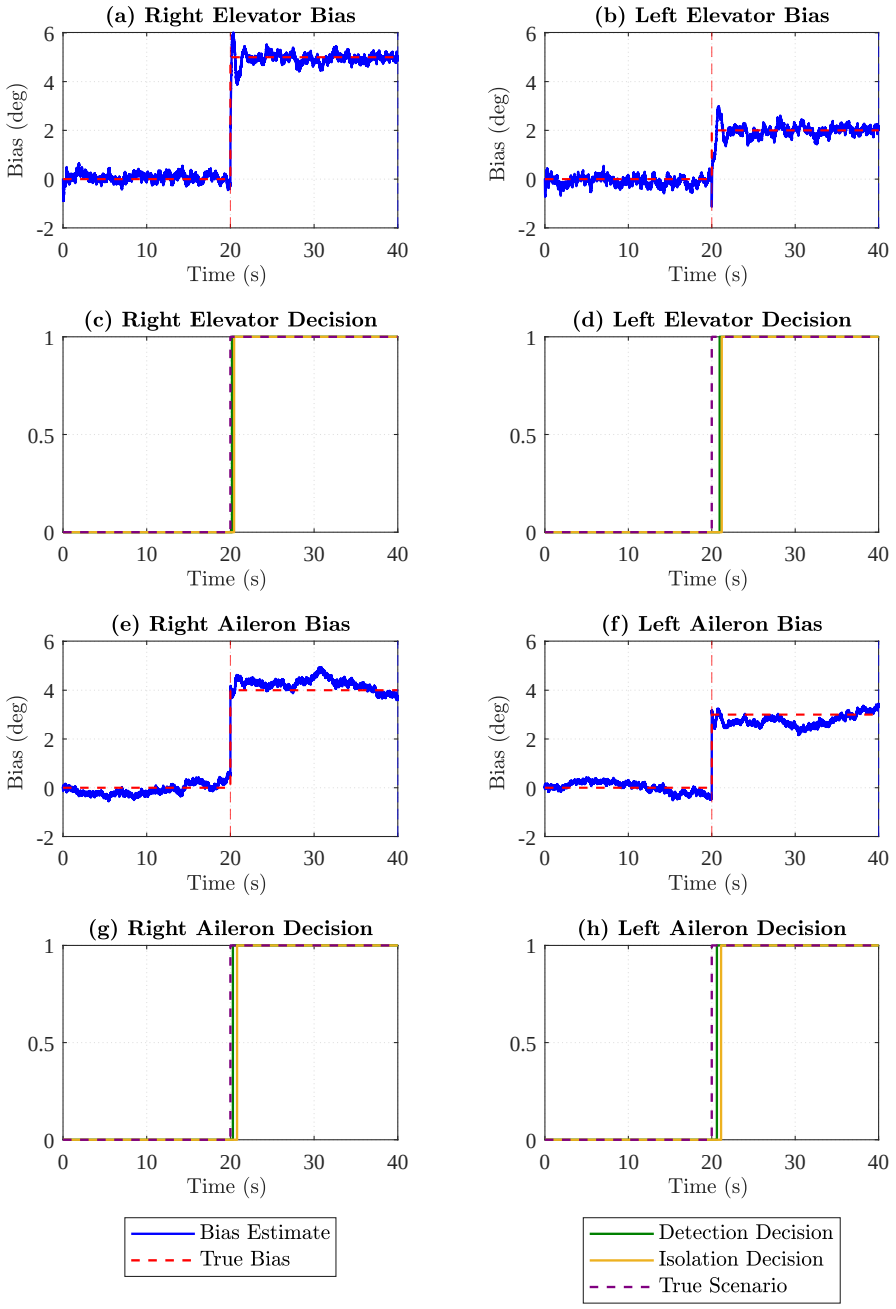

Figure 5.9: Multiple faults scenario both ailerons and elevators for the non-additive FDI case. See plot titles and legends for identification.

proaches. The simulation shows that the FDI is sensitive and robust without complex MM algorithms.

Stellenbosch University https://scholar.sun.ac.za

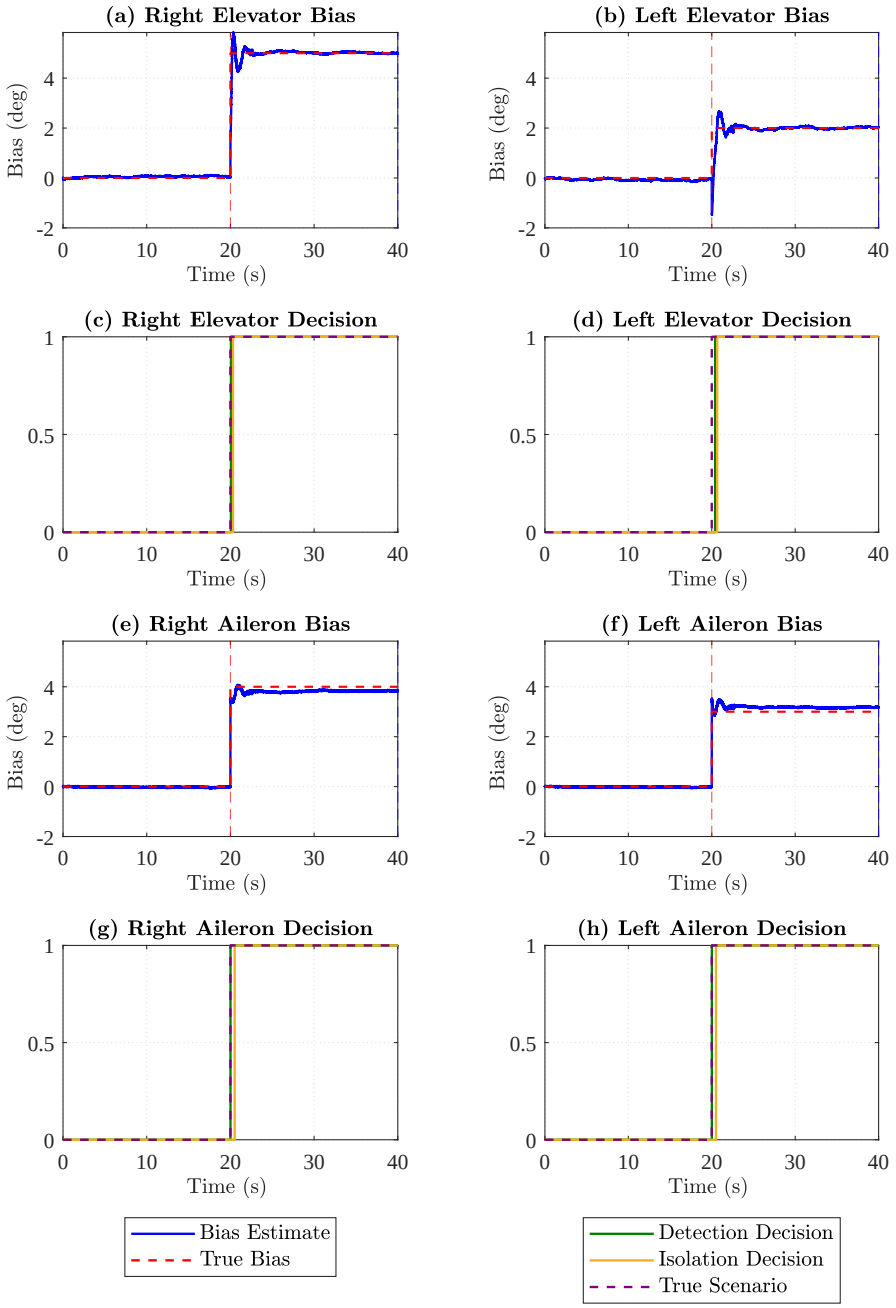

Figure 5.10: Multiple faults scenario both ailerons and elevators for the Q_k^γ - adaptation case. See plot titles and legends for identification.

In this section, the FDI's ability to detect and isolate the faults is demonstrated in the simulation plots. The algorithm for detecting and isolating faults was presented in section 4.8, and demonstrated in Figure 5.8.

Stellenbosch University https://scholar.sun.ac.za

As seen in Figures 5.9 and 5.10, all faults are detected and isolated very quickly within $3s$. As seen, each fault is isolated at a different time because each parameter evolves independently. Within $1 - 3s$, four control surfaces are detected for faults and their fault magnitudes reconstructed with high accuracy. In this section, simulations confirmed fast fault detection and isolation, while the FDI does not lose its noise-insensitivity, robustness and accuracy in reconstructing the fault parameters.

5.2.5 DUKF and JUKF Simulations

The purpose of this section is to make basic comparisons between the four KF approaches discussed in this thesis; namely, the TSKF, the adaptive-TSKF (ATSKF), the DUKF and the Joint-UKF. For this comparison campaign, each KF approach is subjected to an identical simulated environment with a single fault. Moreover, the UKF and the KF approaches were given the same initial covariance matrices. An elevator bias fault of $5°$ was injected at time $t_F = 20s$ in each of the four cases. During each test, simulation data were collected for analysis.

Figure 5.12 shows the results of the four simulated cases on the same plot. Note that only the faulty (right) elevator parameters are plotted in the figure. As expected, the non-adaptive TSKF displays high sensitivity

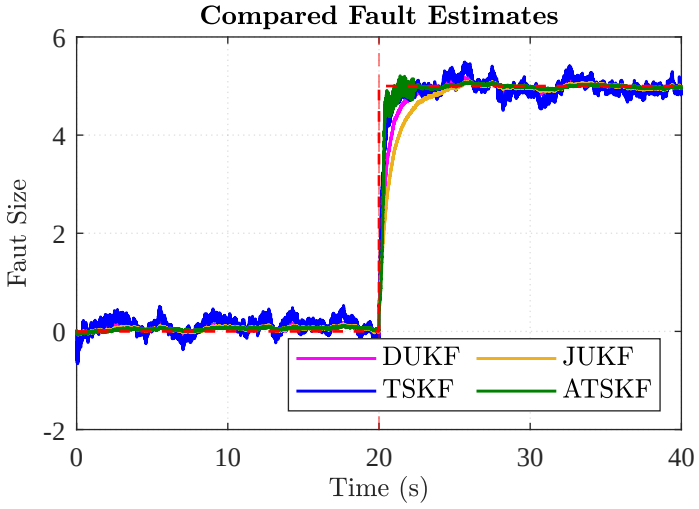

Figure 5.11: A comparison between the TSKF, ATSKF, JUKF and DUKF with elevator bias fault of $5°$

Stellenbosch University https://scholar.sun.ac.za

to noise. Nevertheless, the performance levels appear acceptable for practical use (for the case of an elevator fault).

The DUKF and Joint-UKF show similar performances, with high accuracy in reconstructing the fault parameter and tracking ability. The ATSKF displays superior performance in comparison with the other three techniques. The ASTKF signal is insensitive to noise in the steady-state. However, during the transition after the fault occurred, it shows aggressive behaviour, which disappears once the fault has been sufficiently reconstructed. This is a clear indication that the FDI adapts the $\boldsymbol{Q}_k^{\gamma}$ matrix whenever it searches for the change in the parameters. This characteristic makes the ATSKF very sensitive to occurring faults.

In the presented simulation, there is minimal difference between DUKF and JUKF, which appear to generate better results than the non-adaptive TSKF. Due to its adaptive behaviour, the ATSKF displays greater tracking during the transition to find the new parameter value. This quality gives it improved sensitivity and robustness.

5.2.6 Sensitivity and Specificity Test of the FDI

The purpose of the following simulations is to test the algorithm for its sensitivity (a measure of true positive detection capability) and specificity (a measure of true negative detection capability). Not only is it important to correctly detect the faults, but it is also critical to detect the absence of faults correctly. High false alarm rates in automated systems will result in unnecessary response based on wrong information, and in complex systems, may result in severe or catastrophic failures.

To test the sensitivity and specificity of the FDI, faults are injected in the two elevators and two ailerons sequentially. In this simulation test, at every 50 seconds interval, a positive bias of $5°$ or negative bias of $-5°$ are injected and cleared sequentially, starting with the right elevator and ending with the left aileron. The simulation of sequential faults that appear and disappear is a good way to test the FDI's ability to detect and clear faults.

Figure 5.13 depicts the simulated results with the non-adaptive TSKF, while Figure 5.14 depicts the adaptive counterpart. Figure 5.12 depicts the system states' responses under the sequential fault scenario. In Figure 5.13, from $t = 450s$ to $t = 500s$ a positive bias occurs in the right aileron, which is isolated relatively quickly. When the fault clears, the FDI algorithms correctly clears the fault. From $t = 550s$ to $t = 600s$ when a

Stellenbosch University https://scholar.sun.ac.za

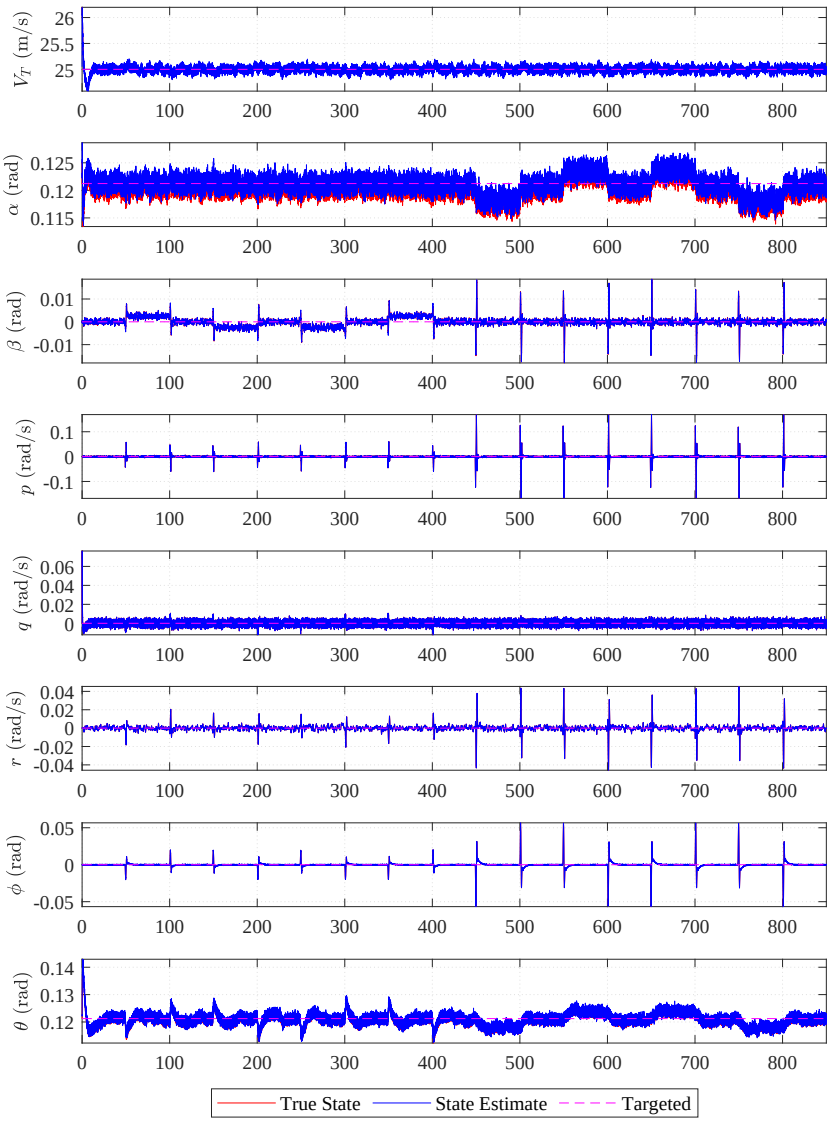

Figure 5.12: Response of the system states in the presence of elevator and aileron faults

negative bias fault occurs in the right aileron, there are multiple intermittent false detections in the left aileron just after $550s$. Moreover, the decision logic does not isolate the true fault in the right aileron until halfway through the fault, at approximately 575 seconds. This observation indicates that the TSKF based FDI is expected to have high false detection rates and missed detection rates for faults occurring in the aileron.

Stellenbosch University https://scholar.sun.ac.za

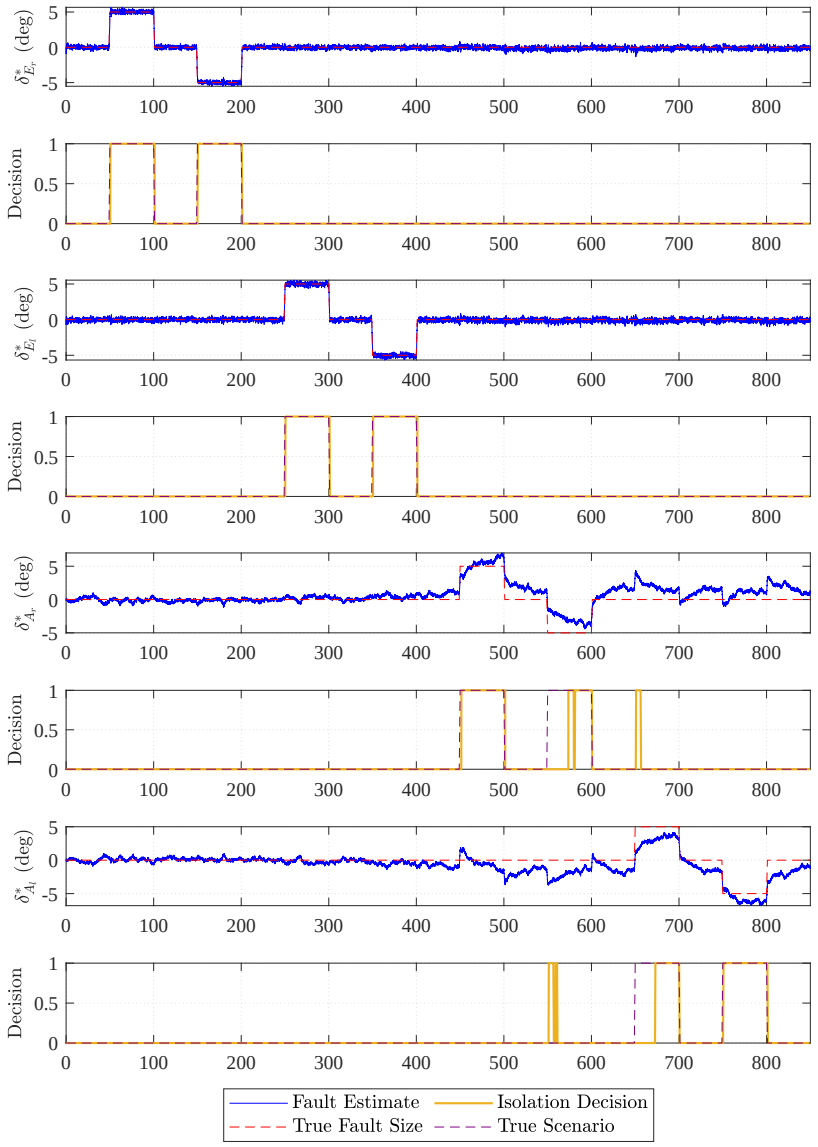

Figure 5.13: Sequential faults in the elevators and ailerons simulated with the non-adaptive TSKF

From Figure 5.14, it can be seen that there are no missed detections or false alarms, despite the transient behaviour in the aileron parameters after $450s$. The transient responses in the aileron during no-fault condition are not large enough to cause false detections. Moreover, a much cleaner evolution of the fault parameters is observed in both the elevator and aileron parameters. This indicates that the root-mean-squared error

Stellenbosch University https://scholar.sun.ac.za

(RMSE) associated with these signals is small. This is particularly important for FTC, where accurate parameter estimates will improve control reconfiguration capabilities. This section demonstrated that the adaptive TSKF proposed in this thesis has greater sensitivity and specificity than the standard TSKF.

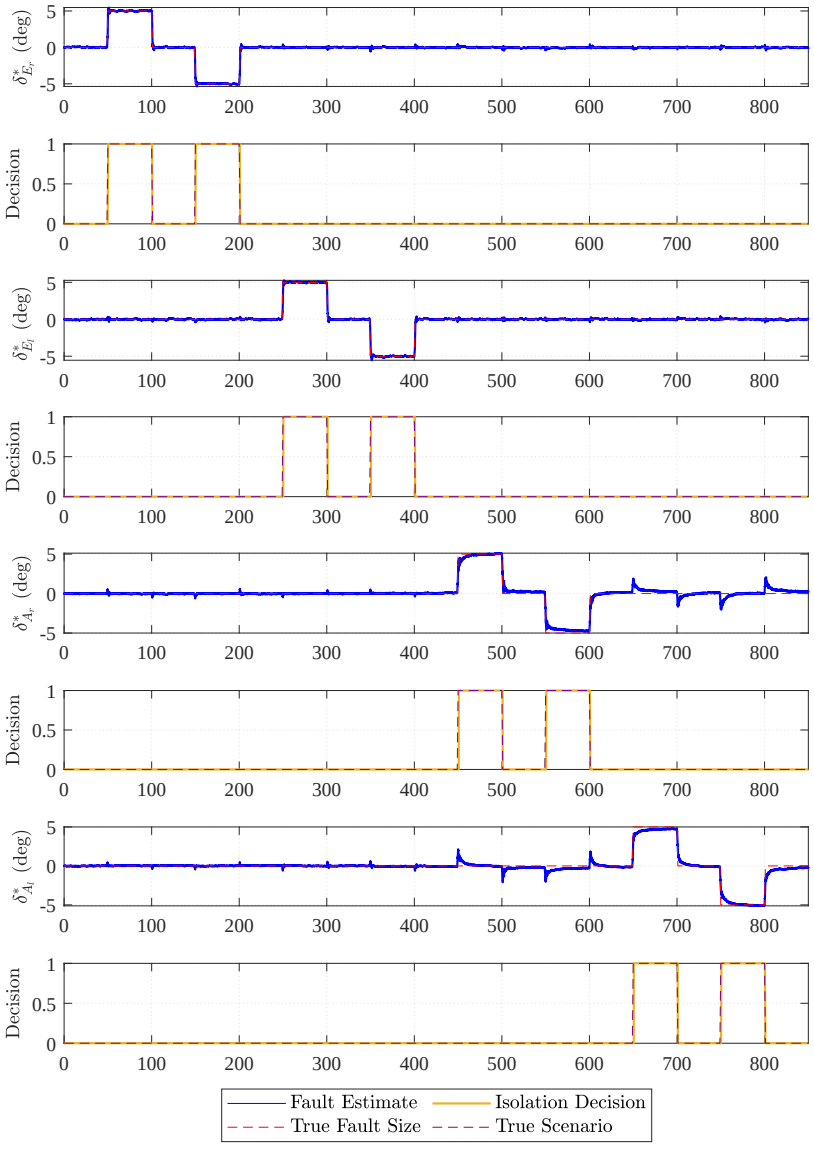

Figure 5.14: Sequential faults in the elevators and ailerons simulated with the adaptive TSKF

Stellenbosch University https://scholar.sun.ac.za

5.3 Active Fault Detection and Isolation

This section presents the simulation results of the two distinct active-FDI designs are proposed in this thesis for two purposes. The first AFDI design ensures the isolation of the two identical rudders, which do not satisfy the isolability condition within the ER structure. The second AFDI design is intended for fault classification as either bias, stuck actuator or LIP faults.

5.3.1 AFDI for Rudder Isolation

The purpose of the simulation tests in this section is to validate the effectiveness of the AFDI rudder isolation technique for bias faults. Recall that the AFDI for rudder isolation relies on randomly selecting one of the rudders, assuming that it is faulty, and attempting to extract fault signatures from it. If the AFDI's initial guess is incorrect, it will move on to the next rudders and attempt to extract the same fault signatures. Therefore two cases were considered in the simulation tests in this section. The first case simulates the scenario where the AFDI's initial guess was correct (that is, the AFDI diagnosed the failed rudder first), depicted in Figure 5.15, and the second case is where the initial guess was incorrect, depicted in Figure 5.15

As stated previously, the algorithm utilised the NIS to determine that the system is in Mode 2; that is, the ER filter is generating the correct fault parameter estimates. As seen in Figure 5.15, a fault of 5° occurs at time $t_F = 20s$ in the right rudder. Recall that the ER filter also estimates the *pseudo-elevator bias*, which the FDI algorithm knows is not the true elevator bias because the system is in Mode 2 (it is only the elevator bias parameters generated with EA filter that are considered correct by the algorithm). As discussed previously, at this point, the FDI algorithm knows that the ER filter is estimating half of the true rudder bias and attributing it to both rudders equally.

Almost immediately after t_F, left and right rudder faults are detected by adaptive threshold function (the green line in the plots indicates the detection signal). After the detection of a rudder fault, the AFDI module is triggered for fault isolation. Firstly, the AFDI allows $3s$ for the rudder bias estimate to settle, then samples its value and stores it in its memory. Next, the AFDI commands a deflection equal to twice the negative of the stored value in one of the rudders in an attempt command the biased rudder to a true zero (trim) deflection, to eliminate the *pseudo-elevator bias* from the ER filter. If the AFDI's initial guess is correct, the absolute value of

Stellenbosch University https://scholar.sun.ac.za

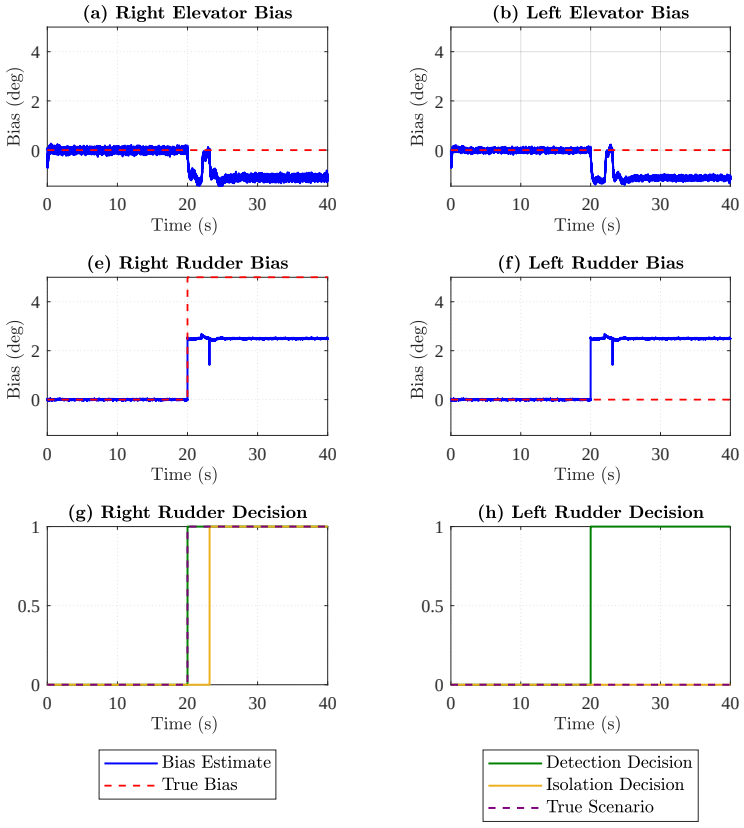

Figure 5.15: Correct isolation of a $5°$ rudder fault where the AFDI algorithm's initial guess was correct

the *pseudo-elevator bias* will start to decrease towards zero. As soon as the *pseudo-elevator bias* reaches the zero mark, the AFDI declares the surface as faulty, and isolation occurs.

Figure 5.15 depicts the first scenario where the AFDI's initial guess was correct. In Figure 5.15 (a), it is seen that the *pseudo-elevator bias* starts to move towards a zero value approximately $3s$ after detection, without increasing first. This indicates that the AFDI's initial guess was correct. As soon as the *pseudo-elevator bias* reaches zero, the right rudder is isolated as faulty (the yellow line in plot (g) indicates the isolation signal)

Figure 5.16 depicts the second case where the AFDI's initial guess is wrong. As the right rudder (healthy) is deflected, the rudder induced pitch increases the *pseudo-elevator bias* in the ER filter (note the increase absolute value of *pseudo-elevator bias* in plot (a) of Figure 5.16). The increase in the magnitude of the *pseudo-elevator bias* indicates that more rudder induced pitch is introduced due to diagnosing and manipulating the wrong

Stellenbosch University https://scholar.sun.ac.za

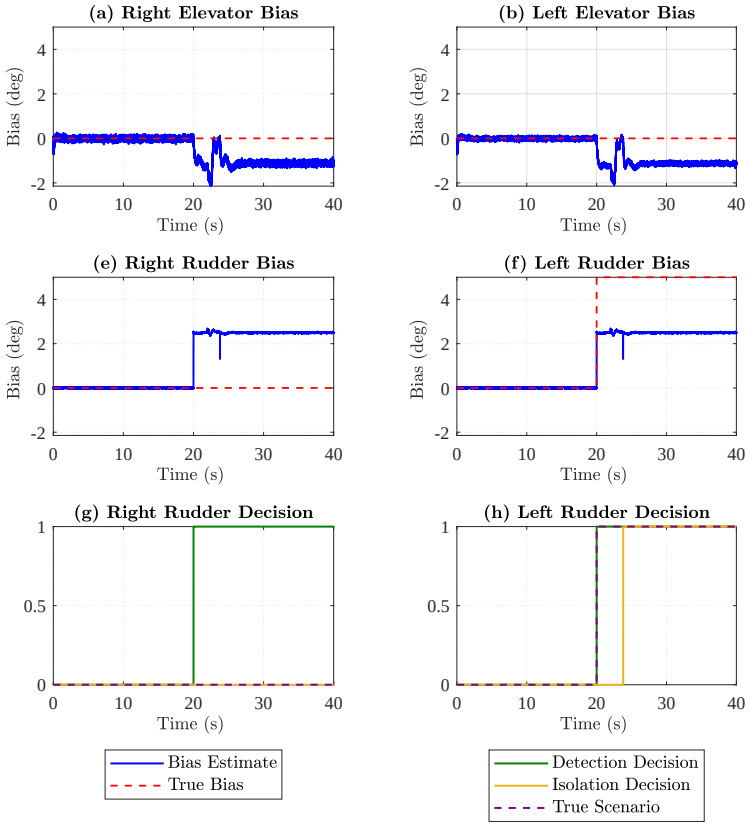

Figure 5.16: Correct isolation of a $5°$ rudder fault where the AFDI algorithm's initial guess was incorrect

(healthy) rudder. After failing to remove the *pseudo-elevator bias* at the initial attempt, the AFDI switches to the left rudder and attempts to reduce the *pseudo-elevator bias* with it. As observed, the *pseudo-elevator bias* is reduced after the initial increase, and a fault is isolated in the right rudder.

In this section, the AFDI for rudder isolation was demonstrated. Simulation reveals that the rudder bias isolation technique by eliminating the 5.16 yields reliable FDI and high isolation rates. The AFDI requires $3s$ to sample the half-rudder bias, which results in increased isolation times. However, the procedure displays high detection rates and low false detection rates.

5.3.2 AFDI for Classification of Stuck Actuators

The purpose of this section is to test the fault classification capabilities of the AFDI. As discussed, the model structure in Equation (4.2.6) can detect bias and LIP faults. The nominal (default) model is chosen as the

Stellenbosch University https://scholar.sun.ac.za

bias estimator. Hence, in previous sections, bias faults were reconstructed without any switching to the hybrid model. LIP faults will also be detected with the nominal model. However, the parameter estimates will be twice the true fault size (see section 4.2.4)

To reconstruct LIP faults correctly, the hybrid model needs to switch to a different mode by adjusting the $\boldsymbol{B}_k$ matrix appropriately. At time t_D, when a fault is detected with the detection function, the active FDI procedure is triggered and initiates the fault classification procedure. Auxiliary sinusoidal excitation signals with a frequency ω and amplitudes chosen in the kernel of the $\boldsymbol{B}$ are injected into the control surfaces.

If the fault is a bias type, $\boldsymbol{u}_{ex}$ represents orthogonal signals injected into the controls, which will cancel out. If the fault is a LIP, the auxiliary controls excitation signals cannot fulfil $\boldsymbol{u}_{ex} \in ker(\boldsymbol{B})$ and the excitation frequency ω will propagate through the system and appear in the measured signals and parameter estimate $\hat{\delta^*}_k$.

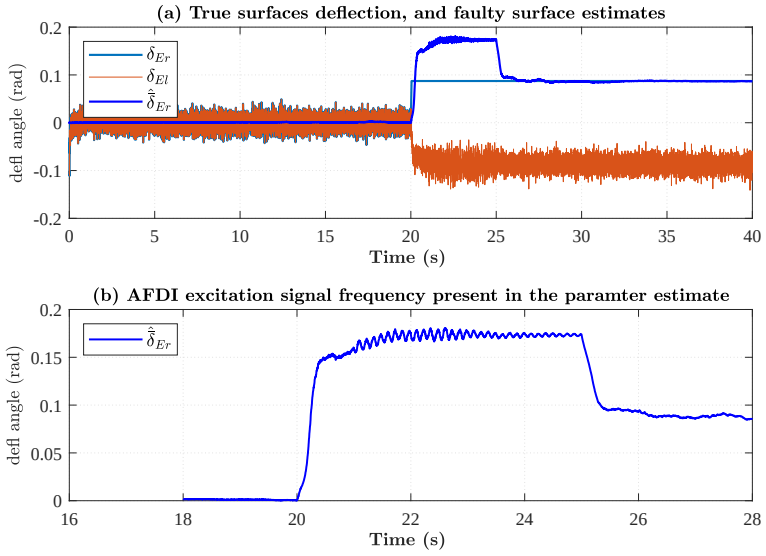

Figure 5.17: Classification of a LIP fault in the right elevator, stuck at $5°$

Figure 5.17 shows the fault classification AFDI technique in action for the case of LIP fault in the right elevator, stuck at $5°$ (0.0873 rad). In plot (a), it is seen that at $t_F = 20s$ the right elevator gets stuck at 0.0873 rad. The nominal model detects that a fault has occurred. The plot (a) shows that the estimator generates approximately twice the true fault magnitude. Note there is some activity in the fault parameter signal shortly after $t_F = 20s$. Plot (b) is a zoomed-out version of plot (a) between $18s$ and

Stellenbosch University https://scholar.sun.ac.za

$28s$. A closer look reveals that there is a sinusoidal signal with a fixed frequency superimposed on the parameter estimate $\hat{\delta^*}_k$. This is the propagation of the auxiliary excitation signal injected into the controls for fault classification. This indicates that the kernel test $\boldsymbol{u}_{ex} \in ker(\boldsymbol{B})$ has failed due to the fault being LIP type. If the fault was a bias type, the observed sinusoidal excitation in the parameter estimate $\hat{\delta^*}_k$ would be absent due to the orthogonal signals cancelling out. Indeed, all previous bias simulations had the AFDI classification active after a fault detection. However, the excitation frequency was not present in the parameter estimates due to orthogonal cancellation in the case of bias faults

Once the AFDI detects the excitation frequency in $\hat{\delta^*}_k$, the fault is classified as a LIP type, and the hybrid model switches by eliminating the column corresponding to $\hat{\delta^*}_k$ from the $\boldsymbol{B}$ matrix. In the simulation, switching occurs at approximately $25s$. As seen in the plots in Figure 5.17, the correct stuck position of the right elevator is estimated after $25s$.

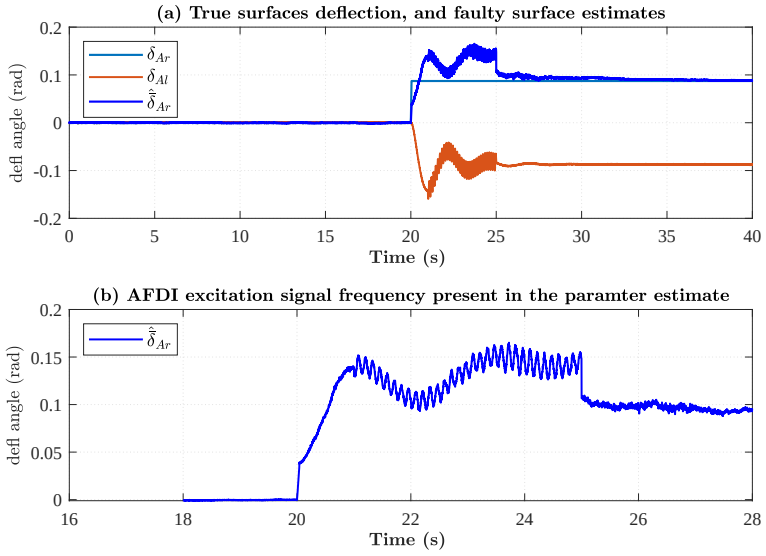

Figure 5.18: Classification of a LIP fault in the right aileron, stuck at $5°$

Figure 5.18 depicts the same simulation but with the fault in the right aileron instead. As seen in plot (b), the excitation signal frequency is even more pronounced and appears in both left and right ailerons due to the heavy coupling between the two surfaces.

This section presented simulation results that validated the fault classification procedure and the hybrid switching model. The approach retains

Stellenbosch University https://scholar.sun.ac.za

the bias estimator's reliability features and incorporates auxiliary excitation and switching with the hybrid model. The method shows better accuracy of the reconstructed signal than MM or IMM approaches (see [3]) where a single parameter is augmented in a MM environment, in contrast to augmenting multiple parameters in a single model environment. By augmenting multiple parameters, the KF can track their interaction and cross-correlations within the system and account for the effect of multiple parameters in the system, thereby generating accurate estimates.

5.4 Loss of Effectiveness Faults

The purpose of the following simulations is to test the FDI design in detecting and isolating LoE faults. At the same time, the sensitivity specificity of the FDI is tested. Faults are injected in the two elevators and two ailerons sequentially. In this simulation test, at every 50 seconds interval, a loss-of-effectiveness of 40%, followed by 80% are injected and cleared from the surfaces sequentially, starting with the right elevator and ending with the left aileron.

Recall that the to correctly estimate LoE faults, the EA and ER filters rely on having a time-varying fault entry matrix given by $\boldsymbol{E}_k = -\boldsymbol{B}_k \boldsymbol{U}_k$ (see section 4.2.21). Figure 5.19 depicts the simulated results of the LoE sequential fault simulation. The presented results were obtained using the novel adaptive procedure proposed in this thesis. Similar to previous observations in previous sections, the parameter estimates for the elevator faults yield better tracking ability, robustness against noise, and sensitivity to occurring faults and specificity.

On the other hand, significant transient responses can be observed in the opposite healthy aileron during any aileron fault triggers. As a result, there are three false alarms in the ailerons during the $850s$ long simulation. However, these false alarm periods are very brief and could be avoided by adding a delay in the isolation algorithm. However, a delay will increase the mean time required to isolate a fault, which may be more undesirable. Consequently, the designer must choose if the FDI will accept some level of false detections, or if isolation can be delayed to avoid false alarms by carrying out consistency checks.

The presented simulations reveal that LoE fault can be tracked accurately with a single EA filter. The FDI design displays high sensitivity to occurring faults and specificity.

Stellenbosch University https://scholar.sun.ac.za

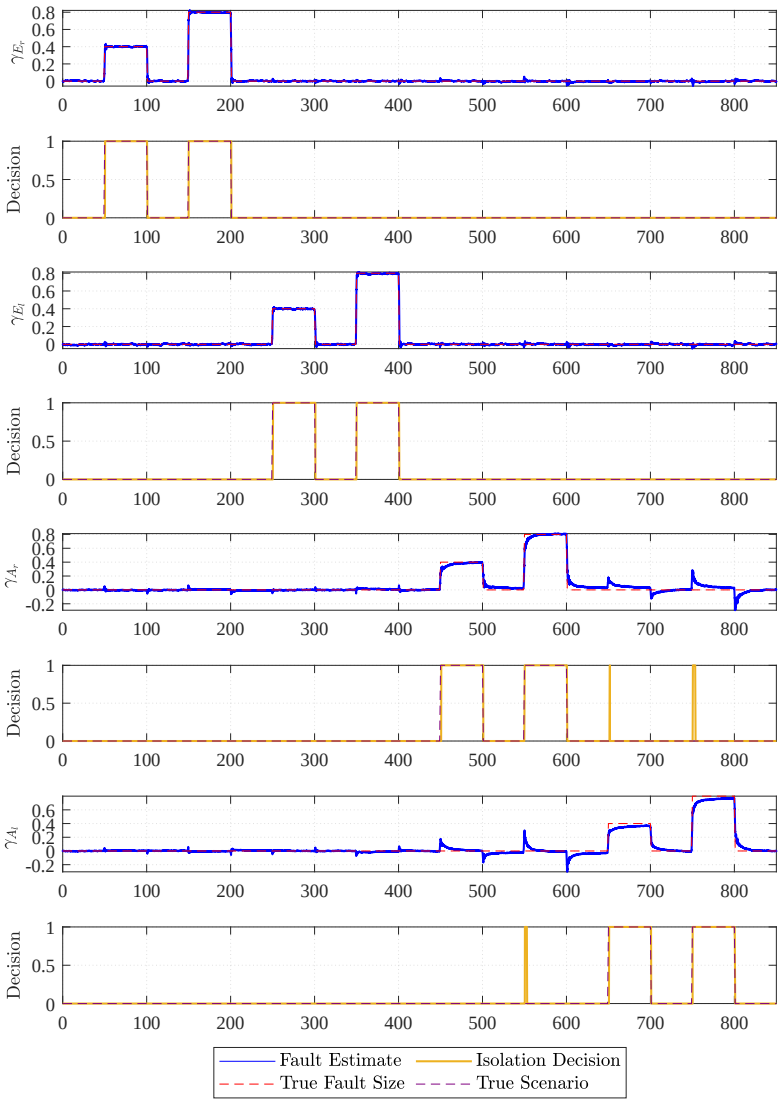

Figure 5.19: Sequential LoE faults in the elevators and ailerons simulated with the adaptive TSKF

5.5 Monte Carlo Simulation

In this section, a Monte Carlo simulation campaign is carried to test the FDI design. The purpose of the Monte Carlo campaign is to validate the proposed FDI algorithms' performance and reliability. During each failure scenario, estimates of the reconstructed fault parameters are recorded. The performance indexes defined in section 2.4.2 are calculated with each MC run to evaluate the performance and reliability of the FDD design. The

Stellenbosch University https://scholar.sun.ac.za

MC simulation exposes the FDD algorithm to different faults, while the aircraft model parameters and disturbances are scattered, each with its own statistical distribution.

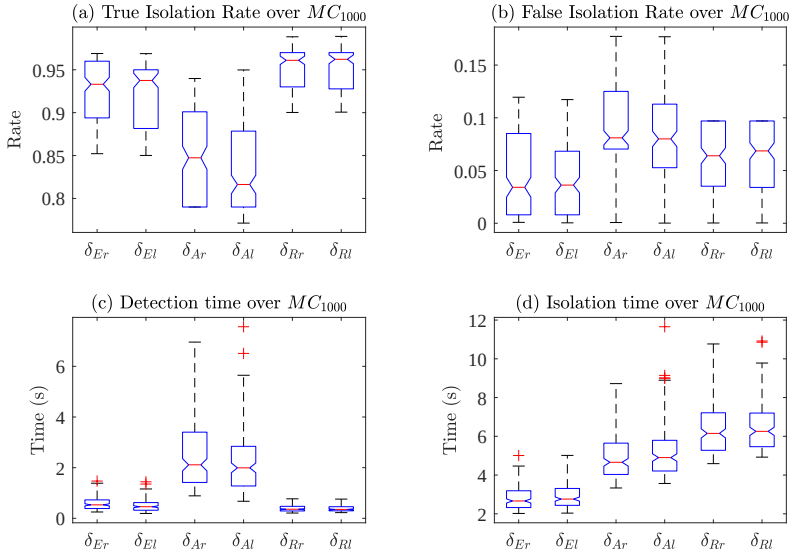

Figure 5.20: FDI Performance indices for the six control surfaces over $n_{mc} = 1000$ simulations of bias faults

The validation campaign is performed for bias, LoE and LIP actuator faults separately. The FDD's reliability is evaluated through a Monte-Carlo statistical analysis from a set of 1000 fault scenarios that occur randomly in the left or right elevator, aileron or rudder. Each of the six control surfaces has an equal probability of failure during each run, and only one surface can fail at any given time. Each failure scenario is performed with randomly distributed turbulence profiles, aircraft mass, centre-of-gravity locations, aerodynamic coefficients, trimmed height and speed. The characteristics of the parameter distributions are given in Table 5.1

Figure 5.20 depicts the calculated FDI performance indices of all control surfaces over the $n_{mc} = 1000$ simulations for the case of bias faults. From plot (a) in Figure 5.20, it is evident that the rudder has the highest true isolation rate. In previous simulations, it was observed that the rudder had the least sensitivity to noise, and faults were detected quickly (and isolated late due to AFDI tests). The less noisy the parameter signal is, the less false detections can be expected. The rudder is already detected at a high rate. Once a rudder fault is detected, AFDI techniques are applied to the ER filter by analysing the *pseudo-elevator bias* until the failed rudder

Stellenbosch University https://scholar.sun.ac.za

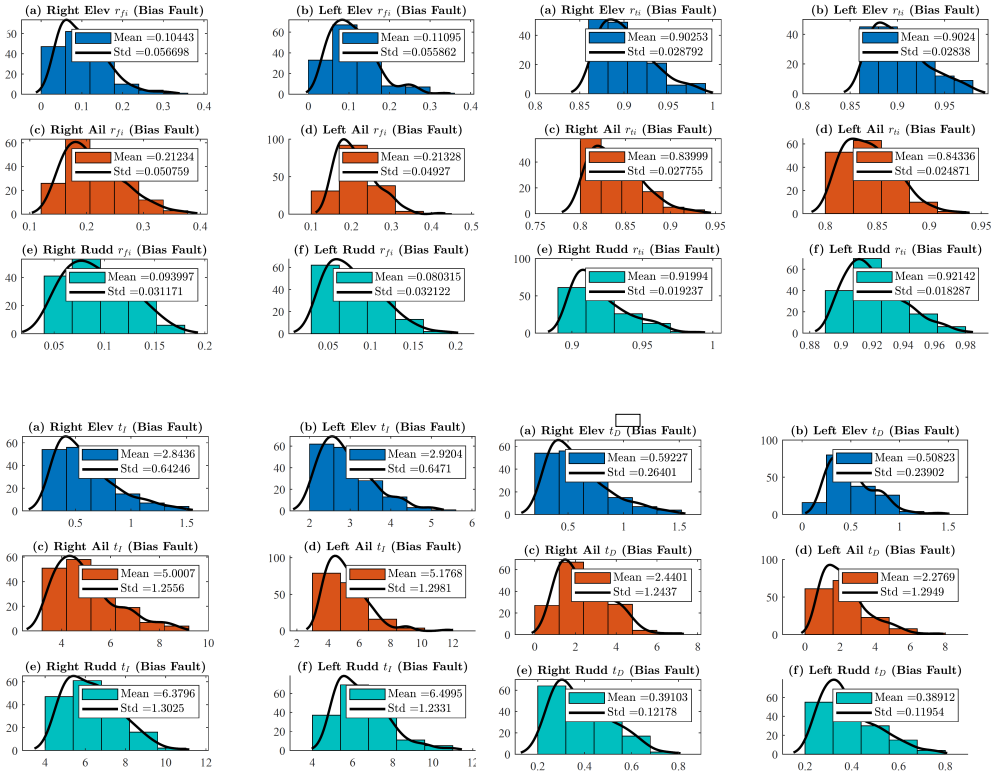

Figure 5.21: FDI Performance indices for the six control surfaces over $n_{mc} = 1000$ simulations of bias faults depicted in histograms

is isolated. For this reason, the rudder has the highest true-isolation rate. The elevator has the second-best isolation rate because the elevator fault parameter is less sensitive to noise than the aileron, which results in better accuracy when reconstructing the fault parameters.

False isolation rate is the can be explained in the same way. When true isolation rate is high, false isolation rate must be low. From examining the boxes and whiskers' lengths, it is observed that performance indices for the aileron have the highest variations. This is expected, given that aileron parameters display high variations and common-mode-bias. Figure 5.21 depicts the same FDI performance indexes in histograms. The histograms also show the mean and standard deviation of all the performance indices within a kernel distribution.

Considering plot (c) in Figure 5.20, it is noted that the rudder has the shortest detection time, followed by the elevator. Detection is particularly fast in the rudder because the ER filter does not have to distinguish between the left and right rudders. More precisely, it cannot distinguish between them, which leads to fast isolation. Recall how the aileron fault

Stellenbosch University https://scholar.sun.ac.za

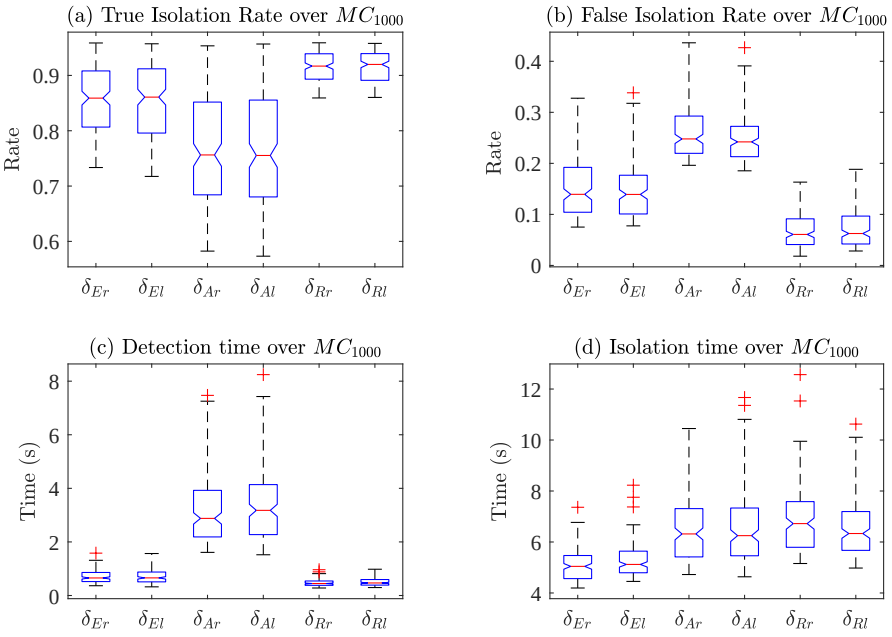

Figure 5.22: FDI Performance indices for the six control surfaces over $n_{mc} = 1000$ simulations of LIP faults

parameters slowly tracked the occurring fault due to the high coupling between the right and left surfaces. This problem is absent in the rudder. While the rudders are detected the fastest, they are isolated very late (see plot (c) in Figure 5.20), due to the delays associated with the AFDI algorithm. As expected, the elevator has the second-best detection time, followed by the aileron with the worst (plot (c)). Note how the aileron's isolation time is faster than the rudder's. This is because there are no delays introduced by AFDI in the aileron isolation process. The ailerons are only isolated using the adaptive threshold function without AFDI.

Figure 5.22 depicts the same performance indices for the case of LIP faults. The detection time, true isolation and false isolation rates are similar to the results obtained for bias fault MC simulations. Note the increase in isolation time. The increase is due to the AFDI step required to switch the hybrid model and reconstruct the fault parameter correctly. Figure 5.23 displays similar results to the bias MC simulation case.

In this section, the performance and reliability of the FDI were tested and found perform with reliability. The highest average for true isolation rate is 92%, while the smallest average for isolation time is approximately $2.9s$. Note that these are averages, and there are cases where isolation oc-

Stellenbosch University https://scholar.sun.ac.za

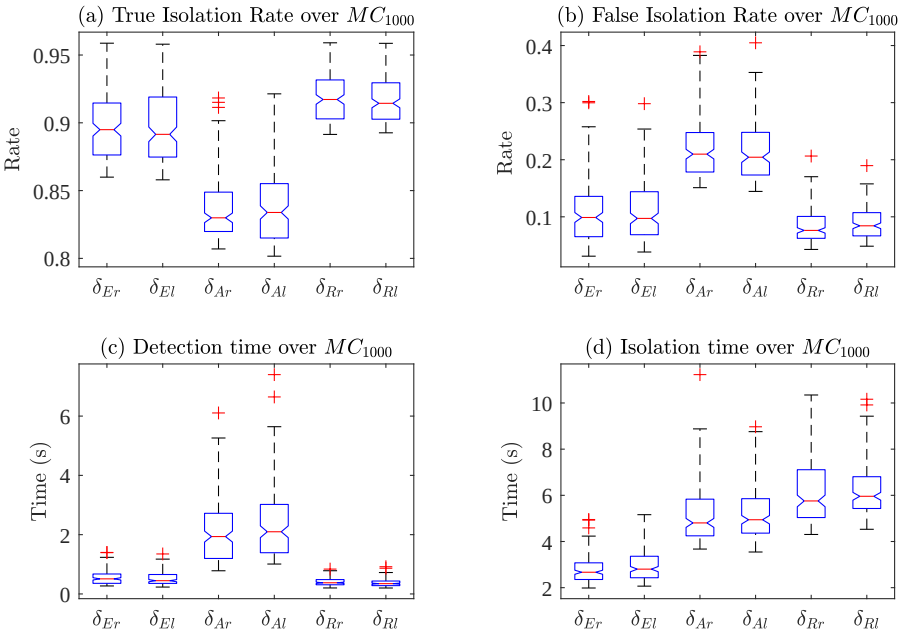

Figure 5.23: FDI Performance indices for the six control surfaces over $n_{mc} = 1000$ simulations of LoE faults

curs within less than $1s$. The FDI displays excellent sensitivity and selectivity, which makes it reliable.

Stellenbosch University https://scholar.sun.ac.za

Chapter 6

Conclusion and Recommendations

This thesis presented the design, implementation and validation model-based approaches to fault detection and isolation applicable to small-sized unmanned aerial vehicles. This chapter is dedicated to providing a summary of the findings and conclusions made from simulation tests.

6.1 Conclusions

This thesis provided theoretical analyses and simulation results in the fault detection and isolation of faults in UAVs. The study presented various model-based FDI approaches in detail to establish a foundation for the research and aid in selecting the most efficient methods for FDI design in this thesis. Model model-based FDI was preferred because it offers a cost-effective, iterative and efficient FDI design process, verifiable in high fidelity computer-aided simulation (CAS) without additional hardware.

The scenarios discussed in this thesis show that the FDI design developed can detect and isolate faults in all the control surfaces, including faults of different magnitudes, type, and multiple faults are isolated concurrently. Moreover, the algorithm only relies on two TSKF filters. The TSKF solves deficiencies faced with the augmented state Kalman filter (ASKF), namely, numerical instability in ill-conditioned systems, and computational inefficiency where large parameter vectors are augmented. The TSKF approach utilises two parallel reduced-order KFs to estimate the system state and the parameter vectors separately.

To further reduce computational loads in the FDI design, a multi-mode hybrid switching model was developed to track bias, LoE and LIP faults

Stellenbosch University https://scholar.sun.ac.za

within a single model-based FDI design, rather than using the MM or IMM approach. The UAV's two rudders were found not to be "isolable" because they produce identical moments. A novel active AFDI method was developed to isolate rudder actuator faults.

The FDI displayed high noise sensitivity under the severe Dryden turbulence model, resulting in high false detection and missed detection rates. To tackle this problem novel adaptive technique was developed to improve the robustness and sensitivity of the FDI. Unlike most methods that rely on a single scaling factor, the method developed in this thesis adaptation technique employs multiple factors to weight the spread of fault parameter covariance matrix in the flow of information, resulting in selective adaptation.

All fault parameters vary independently throughout their evolution since surfaces will not always fail at the same time. Thus parameter variations are nonuniform in time and space. While conducting the research, it was found that a static alarm threshold induced extremely high false alarms or missed alarms when set to low or too high, respectively, which made the original FDI design impractical. A novel adaptive threshold function based on the normalised innovation squared (NIS) was developed. The adaptive threshold function resulted in significant improvement of the true isolation rate and reduced false isolation rates.

A Monte Carlo test campaign was carried out to test the FDI's performance and reliability. The presented KF based algorithms show great capabilities in reliably isolating faults and reconstructing fault parameters. The highest average for true isolation rate is 92%, while the fastest average for isolation time is approximately $2.9s$. Again, these are averages, meaning the algorithm is capable of achieving higher detection rates and faster detection times in other fault scenarios. The adaptive methods developed in this thesis display great robustness against noise, sensitivity to faults and selectivity in the absence of fault. Having met these requirements, it can be said that the FDI design is reliable.

6.2 Recommendation for Future Work

The methods developed here were only tested on a trimmed straight and level flight as the nominal. However, lading and take-off represent the most challenging stages in flight, with various safety challenges due to ground effects and shear. The methods developed here and other FDI methods should be investigated for landing and take-off scenarios.

Stellenbosch University https://scholar.sun.ac.za

The ailerons show heavy coupling and symmetry in dynamic behaviour. Under severe turbulence models, aileron parameter estimates suffer from a common-mode-bias and the "blow up" effect. Algorithms should be developed to detect and filter out the common-mode-bias in similarly coupled and symmetric parameters.

The AFDI methods developed in this thesis assume that the auxiliary signals will not saturate the control surfaces. However, during a fault, the aircraft's control capabilities are already reduced, and some control surfaces may be close to their saturation levels. Auxillary AFDI methods that take into account the saturation levels of the controls surfaces must be developed. In other words, the FDI shall compute new post-fault saturation levels based on the post-fault trim settings. These saturation levels are not to be exceeded when auxiliary excitation or control reconfiguration is carried out. The saturation levels can also be part of the data that the FDI feeds to the FTC.

The FDI developed in this thesis can detect multiple faults concurrently, provided they are of the same type. AFDI strategies must be developed to diagnose different types of faults occurring at the same time.

Stellenbosch University https://scholar.sun.ac.za

Appendices

Stellenbosch University https://scholar.sun.ac.za

Appendix A

Meraka UAV Physical Model Parameters

The physical parameters of the Meraka Modular UAV as shown in Table A.1. These parameters are adopted from previous works at ESL as detailed in [3, 26]

Table A.1: Meraka Aircraft Physical Model Parameters

Parameter	Value	Unit	Definition
m	26	kg	aircraft mass
$\boldsymbol{I}$	$\boldsymbol{I} = \begin{pmatrix} 8.53 & 0 & 0.95 \\ 0 & 11.58 & 0 \\ 0.95 & 0 & 13.67 \end{pmatrix}$	kg.m^2	aircraft inertia matrix
S	1.44	m^2	Wing Reference Area
$\bar{c}$	0.36	m	Mean Aerodynamic Chord
b	4	m	Wing Span
AR	11.11	[-]	Wing Aspect Ratio
e_0	0.85	[-]	Oswald Efficiency Factor

Stellenbosch University https://scholar.sun.ac.za

Table A.2: Aerodynamic Coefficients of the Meraka Aircraft Model

Drag Force	Value	Lateral Force	Value	Lift Force	Value
C_{D_0}	0.06	C_{Y_0}	0	C_{Y_0}	0
e_0	0.85	C_{Y_β}	-0.3894	C_{L_α}	5.5579
		C_{Y_p}	0.0492	C_{L_q}	8.0469
		C_{Y_r}	0.2440	$C_{L_{\delta_{Er}}}$	0.4046
		$C_{Y_{\delta_{Er}}}$	-0.0098	$C_{L_{\delta_{El}}}$	0.4046
		$C_{Y_{\delta_{El}}}$	0.0098	$C_{L_{\delta_{Ar}}}$	0.1636
		$C_{Y_{\delta_{Ar}}}$	-0.0060	$C_{L_{\delta_{Al}}}$	-0.1636
		$C_{Y_{\delta_{Al}}}$	-0.0060		
		$C_{Y_{\delta_{Rr}}}$	0.1077		
		$C_{Y_{\delta_{Rl}}}$	0.1077		
Roll	**Value**	**Pitch**	**Value**	**Yaw**	**Value**
C_{l_0}	0	C_{M_0}	0	C_{n_0}	0
C_{l_β}	-0.0715	C_{M_α}	-2.7695	C_{n_β}	0.1022
C_{l_p}	-0.6219	C_{M_q}	-18.2810	C_{n_p}	-0.0636
C_{l_r}	0.1946	$C_{M_{\delta_{Er}}}$	-0.7864	C_{n_r}	-0.0853
$C_{l_{\delta_{Er}}}$	-0.0826	$C_{M_{\delta_{El}}}$	-0.7864	$C_{n_{\delta_{Er}}}$	-0.0052
$C_{l_{\delta_{El}}}$	0.0826	$C_{M_{\delta_{Ar}}}$	-0.0151	$C_{n_{\delta_{El}}}$	0.0052
$C_{l_{\delta_{Ar}}}$	-0.4752	$C_{M_{\delta_{Al}}}$	0.0151	$C_{n_{\delta_{Ar}}}$	-0.0099
$C_{l_{\delta_{Al}}}$	-0.4752	$C_{M_{\delta_{Rr}}}$	0.0030	$C_{n_{\delta_{Al}}}$	-0.0099
$C_{l_{\delta_{Rr}}}$	0.0363	$C_{M_{\delta_{Rl}}}$	0.0030	$C_{n_{\delta_{Rr}}}$	-0.3866
$C_{l_{\delta_{Rl}}}$	0.0363			$C_{n_{\delta_{Rl}}}$	-0.3866

Stellenbosch University https://scholar.sun.ac.za

Appendix B

Discretisation of Continuous Stochastic Systems

B.1 Analytical Solution of the Continuous Model

Suppose the controlled system can be expressed as follows:

$$\dot{\boldsymbol{x}}(t) = \boldsymbol{A}\boldsymbol{x}(t) + \boldsymbol{B}\boldsymbol{u}(t) + \boldsymbol{G}\boldsymbol{w}(t) \tag{B.1.1}$$

$$\boldsymbol{y}(t) = \boldsymbol{C}\boldsymbol{x}(t) + v(t) \tag{B.1.2}$$

Let $\boldsymbol{x}(\boldsymbol{0}) \sim (\bar{\boldsymbol{x}}_0, \boldsymbol{P}_0)$, $\boldsymbol{w}(t) \sim (\boldsymbol{0}, \boldsymbol{Q})$, $\boldsymbol{v}(t) \sim (\boldsymbol{0}, \boldsymbol{R})$, where $\boldsymbol{w}(t)$ and $\boldsymbol{v}(t)$ are white uncorrelated noise processes. Several problems in control systems require estimating the state $\boldsymbol{x}(t)$. Suppose the digital computer samples the input signal $\boldsymbol{u}(t)$ and measurement signal $\boldsymbol{y}(t)$ at a sampling rate of Ts second. The discrete Kalman filter requires the discretization of the continuous plant. This requires a solution to (B.1.1)

Its is known that the matrix exponential is given by:

$$\frac{d}{dt} e^{\boldsymbol{A}t} = \boldsymbol{A} e^{\boldsymbol{A}t} = e^{\boldsymbol{A}t} \boldsymbol{A} \tag{B.1.3}$$

and by pre-multiplying the model we get

$$e^{-\boldsymbol{A}t} \dot{\boldsymbol{x}}(t) = e^{-\boldsymbol{A}t} \boldsymbol{A}\boldsymbol{x}(t) + e^{-\boldsymbol{A}t} \boldsymbol{B}\boldsymbol{u}(t) + e^{-\boldsymbol{A}t} \boldsymbol{G}\boldsymbol{w}(t) \tag{B.1.4}$$

which becomes

$$e^{-\boldsymbol{A}t} \dot{\boldsymbol{x}}(t) - e^{-\boldsymbol{A}t} \boldsymbol{A}\boldsymbol{x}(t) = e^{-\boldsymbol{A}t} \boldsymbol{B}\boldsymbol{u}(t) + e^{-\boldsymbol{A}t} \boldsymbol{G}\boldsymbol{w}(t) \tag{B.1.5}$$

$$\frac{d(e^{-\boldsymbol{A}t} \boldsymbol{x}(t)}{dt} = e^{-\boldsymbol{A}t} \boldsymbol{B}\boldsymbol{u}(t) + e^{-\boldsymbol{A}t} \boldsymbol{G}\boldsymbol{w}(t) \tag{B.1.6}$$

Stellenbosch University https://scholar.sun.ac.za

Integrating the expression over the time interval $[t_0, t]$ results in

$$\int_{t_0}^{t} \frac{d(e^{-\boldsymbol{A}\tau}\boldsymbol{x}(\tau)}{d\tau} d\tau = \int_{t_0}^{t} e^{-\boldsymbol{A}\tau}\boldsymbol{B}\boldsymbol{u}(\tau)d\tau + \int_{t_0}^{t} e^{-\boldsymbol{A}\tau}\boldsymbol{G}\boldsymbol{w}(\tau)d\tau \tag{B.1.7}$$

$$e^{-\boldsymbol{A}(t-t_0)}\boldsymbol{x}(t-t_0) - \boldsymbol{x}(t_0) = \int_{t_0}^{t} e^{-\boldsymbol{A}\tau}\boldsymbol{B}\boldsymbol{u}(\tau)d\tau + \int_{t_0}^{t} e^{-\boldsymbol{A}\tau}\boldsymbol{G}\boldsymbol{w}(\tau)d\tau \tag{B.1.8}$$

$$\boldsymbol{x}(t) = e^{\boldsymbol{A}(t-t_0)}\boldsymbol{x}(t_0) + \int_{t_0}^{t} e^{\boldsymbol{A}(t-\tau)}\boldsymbol{B}\boldsymbol{u}(\tau)d\tau + \int_{t_0}^{t} e^{\boldsymbol{A}(t-\tau)}\boldsymbol{G}\boldsymbol{w}(\tau)d\tau \tag{B.1.9}$$

This last expression is the solution to B.1.1

B.2 Discretisation of the Continuous Model

The state propagation between samples is expressed by letting $t_0 = kT$ and $t = (k+1)Ts$ where k is an integer. The sampled state is then define as $\boldsymbol{x}_k \triangleq \boldsymbol{x}(kTs)$ which results in the expression:

$$\boldsymbol{x}_{k+1} = e^{\boldsymbol{A}Ts}\boldsymbol{x}_k + \int_{kTs}^{(k+1)Ts} e^{\boldsymbol{A}[(k+1)Ts-\tau]}\boldsymbol{B}\boldsymbol{u}(\tau)d\tau + \int_{kTs}^{(k+1)Ts} e^{\boldsymbol{A}[(k+1)Ts-\tau]}\boldsymbol{G}\boldsymbol{w}(\tau)d\tau \tag{B.2.1}$$

If the control input $\boldsymbol{u}(t)$ is reconstructed from the discrete control sequence $\boldsymbol{u}_k$ by using a zero-order hold sampling, then $\boldsymbol{u}(\tau)$ has a constant value of $\boldsymbol{u}(kT_s) = \boldsymbol{u}_k$ over the integration interval. The third term in the above can be thought of as smoothed out (low-pass filtered) version of the continuous white process noise $\boldsymbol{w}(t)$ that has been scaled by the matrix $\boldsymbol{G}$. It can be shown that this term indicates a discrete white noise sequence. Hence, if the discrete noise is defined as

$$\boldsymbol{w}_k = \int_{kTs}^{(k+1)Ts} e^{\boldsymbol{A}[(k+1)Ts-\tau]}\boldsymbol{G}\boldsymbol{w}(\tau)d\tau \tag{B.2.2}$$

Thus the equation in (B.2.1) becomes

$$\boldsymbol{x}_{k+1} = e^{\boldsymbol{A}Ts}\boldsymbol{x}_k + \int_{kTs}^{(k+1)Ts} e^{\boldsymbol{A}[(k+1)Ts-\tau]}\boldsymbol{B}d\tau \cdot \boldsymbol{u}_k + \boldsymbol{w}_k \tag{B.2.3}$$

On changing variables twice ($\lambda = \tau - kTs$ and then $\tau = Ts - \lambda$), we obtain

$$\boldsymbol{x}_{k+1} = e^{\boldsymbol{A}Ts}\boldsymbol{x}_k + \int_{0}^{Ts} e^{\boldsymbol{A}\tau}\boldsymbol{B}d\tau \cdot \boldsymbol{u}_k + \boldsymbol{w}_k \tag{B.2.4}$$

Stellenbosch University https://scholar.sun.ac.za

This is the sampled version of B.1.1, which we can write as

$$\boldsymbol{x}_{k+1} = \boldsymbol{A}_k \boldsymbol{x}_k + \boldsymbol{B}_k \boldsymbol{u}_k + \boldsymbol{w}_k \tag{B.2.5}$$

where

$$\boldsymbol{A}_k = e^{\boldsymbol{A}Ts} \tag{B.2.6}$$

$$\boldsymbol{B}_k = \int_0^{Ts} e^{\boldsymbol{A}\tau} \boldsymbol{B} d\tau \tag{B.2.7}$$

B.3 Propagation of Covariance Matrices

The covariance $\boldsymbol{Q}_k$ of the new noise sequence $\boldsymbol{w}_k$ is given by

$$\boldsymbol{Q}_k = E\{\boldsymbol{w}_k \boldsymbol{w}_k^T\} \tag{B.3.1}$$

$$= \int \int_{kT}^{(k+1)T} e^{\boldsymbol{A}[(k+1)T-\tau]} E\{\boldsymbol{G}\boldsymbol{w}_k \boldsymbol{w}_k^T \boldsymbol{G}^T\} e^{\boldsymbol{A}^T[(k+1)T-\tau]} d\tau \tag{B.3.2}$$

Where

$$E\{\boldsymbol{w}_k \boldsymbol{w}_k^T\} = \boldsymbol{Q}\delta(\tau - \alpha) \tag{B.3.3}$$

By substitution we obtain

$$\boldsymbol{Q}_k = \int_{kT}^{(k+1)T} e^{\boldsymbol{A}[(k+1)T-\tau]} \boldsymbol{G}\boldsymbol{Q}\boldsymbol{G}^T e^{\boldsymbol{A}^T[(k+1)T-\tau]} d\tau \tag{B.3.4}$$

Adjusting the variables two times similarly to the previous above results in

$$\boldsymbol{Q}_k = \int_0^T e^{\boldsymbol{A}\tau} \boldsymbol{G}\boldsymbol{Q}\boldsymbol{G}^T e^{\boldsymbol{A}^T\tau} d\tau \tag{B.3.5}$$

To obtain the covariance $\boldsymbol{R}_k$ of $\boldsymbol{v}_k$ the following expression is defined

$$\prod(t) = \begin{cases} 1, & -1/2 \leq t \leq 1/2 \\ 0, & \text{otherwise} \end{cases} \tag{B.3.6}$$

It is notefd that the $\lim_{T\to 0}(1/T)\Pi(t/T) = \delta(t)$, is the Kronecker delta. Thus covariance associated with $\boldsymbol{v}_k$ is expressed as:

$$\boldsymbol{R}_v(k) = \boldsymbol{R}_k \delta(k) \tag{B.3.7}$$

As $\delta(k)$ is equal to one (1) when $k = 0$, then the covariance will equal $\boldsymbol{R}_k$, wich is a finite matrix. The noise parameter $\boldsymbol{v}(t)$, has a covariance equal to $\boldsymbol{R}\delta(t)$, with $\boldsymbol{R}$ denoting its spectral density. This results in:

$$\boldsymbol{R}\delta(t) = \lim_{T\to 0} (\boldsymbol{R}T) \frac{1}{T} \prod \left(\frac{t}{T}\right) \tag{B.3.8}$$

Stellenbosch University https://scholar.sun.ac.za

resulting in

$$\boldsymbol{R}_k = \frac{\boldsymbol{R}}{T} \tag{B.3.9}$$

B.4 Numerical Evaluation of Discrete Matrices

The discretisation presented in previous chapters may not be trackable because of the errors associated with the matrix exponential and integral calculations. However, there are some elegant tricks to evaluate these integrals if they are needed once-off. With respect to the $\boldsymbol{A}_k$ and $\boldsymbol{B}_k$ matrices, the following property can be used to obtain a solution faster.

$$e^{\boldsymbol{M}} = \begin{pmatrix} \boldsymbol{A}_k & \boldsymbol{B}_k \\ 0 & \boldsymbol{I} \end{pmatrix} \tag{B.4.1}$$

where $\boldsymbol{M} = \begin{pmatrix} \boldsymbol{A} & \boldsymbol{B} \\ 0 & 0 \end{pmatrix} Ts$

Charles F. Van Loan's article in 1978 presented a technique for calculating the integrals in (B.2.7) and (B.3.5) using matrix exponentials. The computation relies on $\boldsymbol{Q}$ being positive semi-definite which is already a property of the process noise covariance matrix. The technique requires a) calculating the exponential of $\boldsymbol{M}$, which a triangular block matrix formed with matrices representing the relation of the forms in (B.2.7) and (B.3.5) and b) combing the resultant matrices to find the integrals. The formulation is given by:

$$\exp\left\{ \begin{pmatrix} -\boldsymbol{A} & \boldsymbol{Q}_c^T \\ 0 & \boldsymbol{A}^T \end{pmatrix} Ts \right\} = \begin{pmatrix} \boldsymbol{F}_2 & \boldsymbol{G}_2 \\ 0 & \boldsymbol{F}_3 \end{pmatrix} \tag{B.4.2}$$

Then it can be shown that:

$$\boldsymbol{Q}_k = \boldsymbol{F}_3^T \boldsymbol{G}_2 \tag{B.4.3}$$

For the stochastic model in (B.1.1), Van Loan's results can be implemented with the MATLAB function `expm()` by choosing $\boldsymbol{Q}_c$ as $\boldsymbol{G}\boldsymbol{Q}\boldsymbol{G}^T$ and extracting partitioned matrices from the result. When $\boldsymbol{A}_k$ and $\boldsymbol{B}_k$ do not need not to be calculated at every iteration k, the MATLAB function `expm()` can be used. The discrete transition, input and process noise covariance matrices as derived in this Appendix **??** can be approximated as the first few terms of the infinite series expansions for the sampled matrices as

Stellenbosch University https://scholar.sun.ac.za

$$\boldsymbol{A}_k = \boldsymbol{I} + \boldsymbol{A}Ts + \frac{\boldsymbol{A}^2 Ts^2}{2!} + \cdots \tag{B.4.4}$$

$$\boldsymbol{B}_k = \boldsymbol{B}Ts + \frac{\boldsymbol{A}\boldsymbol{B}Ts^2}{2!} + \cdots \tag{B.4.5}$$

$$\boldsymbol{Q}_k = \boldsymbol{G}\boldsymbol{Q}\boldsymbol{G}^T Ts + \frac{\left(\boldsymbol{A}\boldsymbol{G}\boldsymbol{Q}\boldsymbol{G}^T + \boldsymbol{G}\boldsymbol{Q}\boldsymbol{G}^T\boldsymbol{A}^T\right)Ts^2}{2!} + \cdots \tag{B.4.6}$$

The terms with the order T^2 or higher can be neglected, which is *Euler's approximation*. With Euler's method, it is noted that noise covariance matrix $\boldsymbol{Q}_k$ is a result of multiplication by Ts and measurement noise covariance $\boldsymbol{R}_k$ is given by division with T.

Stellenbosch University https://scholar.sun.ac.za

Appendix C

Airspeed Equations

We recall Newton's of motion derived in the inertial reference frame as follows

$$\sum_j \boldsymbol{F}_j = \left[\frac{d}{dt}\left(m\boldsymbol{V}\right)\right]_i \tag{C.0.1}$$

The subscript i denotes the inertial reference frame, which in this study was approximated with the NED reference frame.

$$\frac{1}{m}\sum_j \boldsymbol{F}_j = \left[\frac{d}{dt}\boldsymbol{V}\right]_b + \boldsymbol{\omega}_{b/i} \times \boldsymbol{V} \tag{C.0.2}$$

Coriolis's theorem allows the characterisation of motion within a frame of reference that rotates with respect to an inertial frame. In the case of the aircraft, the body reference frame is rotating with the aircraft, with respect to the inertial reference frame. This leads to the following expression.

$$\frac{1}{m}\sum_j \boldsymbol{F}_j = \left[\frac{d}{dt}\boldsymbol{V}\right]_w + \boldsymbol{\omega}_{w/b} \times \boldsymbol{V} + \boldsymbol{\omega}_{b/i} \times \boldsymbol{V} \tag{C.0.3}$$

By the same principle, the above call all be projected to the wind reference frame as follows:

$$\frac{1}{m}\sum_j \boldsymbol{F}_j^w = \left[\frac{d}{dt}\boldsymbol{V}^w\right]_w + \boldsymbol{\omega}_{w/b}^w \times \boldsymbol{V}^w + \boldsymbol{\omega}_{b/i}^w \times \boldsymbol{V}^w \tag{C.0.4}$$

Expanding the different contribution to the net force acting on the aircraft lead to the following expression.

$$\left[\frac{d}{dt}\boldsymbol{V}^w\right]_w = \frac{1}{m}\left(m\boldsymbol{g}^w + \boldsymbol{F}_{\boldsymbol{engine}}^w + \boldsymbol{F}_{\boldsymbol{aero}}^w\right) - \boldsymbol{\omega}_{w/b}^w \times \boldsymbol{V}^w - \boldsymbol{\omega}_{b/i}^w \times \boldsymbol{V}^w \tag{C.0.5}$$

Stellenbosch University https://scholar.sun.ac.za

where

$$\boldsymbol{g}^w = \begin{pmatrix} g_x^w \\ g_y^w \\ g_z^w \end{pmatrix} = \mathcal{R}_b^w \mathcal{R}_i^b \begin{pmatrix} 0 \\ 0 \\ g \end{pmatrix} \tag{C.0.6}$$

$$= g \begin{pmatrix} \sin\alpha\cos\beta\cos\theta\cos\phi + \sin\beta\cos\theta\sin\phi - \cos\alpha\cos\beta\sin\theta \\ \cos\alpha\sin\beta\sin\theta + \cos\beta\cos\theta\sin\phi - \sin\alpha\sin\beta\cos\theta\cos\phi \\ \sin\alpha\sin\theta + \cos\alpha\cos\theta\cos\phi \end{pmatrix} \tag{C.0.7}$$

and

$$\boldsymbol{F}_{\boldsymbol{aero}}^w = \bar{q}S \begin{pmatrix} -C_D \\ C_Y \\ -C_L \end{pmatrix}, \quad \boldsymbol{F}_{\boldsymbol{engine}}^w = \mathcal{R}_b^w \begin{pmatrix} F_{prop} \\ 0 \\ 0 \end{pmatrix} \tag{C.0.8}$$

and

$$\boldsymbol{\omega}_{w/b}^w = \begin{pmatrix} 0 \\ 0 \\ \dot{\beta} \end{pmatrix} + \begin{pmatrix} \cos\beta & \sin\beta & 0 \\ -\sin\beta & \cos\beta & 0 \\ 0 & 0 & 1 \end{pmatrix} \begin{pmatrix} 0 \\ -\dot{\alpha} \\ 0 \end{pmatrix} = \begin{pmatrix} -\dot{\alpha}\sin\beta \\ -\dot{\alpha}\cos\beta \\ \dot{\beta} \end{pmatrix} \tag{C.0.9}$$

and

$$\boldsymbol{\omega}_{b/i}^w = \begin{pmatrix} p^w \\ q^w \\ r^w \end{pmatrix} = \mathcal{R}_b^w \begin{pmatrix} p \\ q \\ r \end{pmatrix}, \quad \boldsymbol{V}^w = \begin{pmatrix} V_T \\ 0 \\ 0 \end{pmatrix} \tag{C.0.10}$$

Substituting the expressions (C.0.6) to (C.0.10) into (C.0.5) yields

$$\begin{aligned} \begin{pmatrix} \dot{V}_T \\ 0 \\ 0 \end{pmatrix} =& \frac{1}{m} \left[F_{prop} \begin{pmatrix} \cos\alpha\cos\beta \\ -\sin\beta\cos\alpha \\ -\sin\alpha \end{pmatrix} + \bar{q}S \begin{pmatrix} -C_D \\ C_Y \\ -C_L \end{pmatrix} \right] + \begin{pmatrix} g_x^w \\ g_y^w \\ g_z^w \end{pmatrix} \\ & - \begin{pmatrix} p^w \\ q^w \\ r^w \end{pmatrix} \times \begin{pmatrix} V_T \\ 0 \\ 0 \end{pmatrix} - \begin{pmatrix} -\dot{\alpha}\sin\beta \\ -\dot{\alpha}\cos\beta \\ \dot{\beta} \end{pmatrix} \times \begin{pmatrix} V_T \\ 0 \\ 0 \end{pmatrix} \end{aligned} \tag{C.0.11}$$

Stellenbosch University https://scholar.sun.ac.za

Computing the cross-products results in

$$\begin{aligned}\begin{pmatrix}\dot{V}_T\\0\\0\end{pmatrix} =&\frac{1}{m}\left[F_{prop}\begin{pmatrix}\cos\alpha\cos\beta\\-\sin\beta\cos\alpha\\-\sin\alpha\end{pmatrix}+\bar{q}S\begin{pmatrix}-C_D\\C_Y\\-C_L\end{pmatrix}\right]+\begin{pmatrix}g_x^w\\g_y^w\\g_z^w\end{pmatrix}\\&-\begin{pmatrix}0\\r^wV_T\\-q^wV_T\end{pmatrix}-\begin{pmatrix}0\\\dot{\beta}V_T\\\dot{\alpha}\cos\beta V_T\end{pmatrix}\end{aligned} \tag{C.0.12}$$

Finally, the three differential equation for the airspeed, angle of attack and sideslip angle can be obtained from the above as follows

$$\dot{V}_T = \frac{1}{m}\left(-\bar{q}SC_D + F_{prop}\cos\alpha\cos\beta\right) + g_x^w \tag{C.0.13}$$

$$\dot{\alpha} = \frac{1}{mV_T\cos\beta}\left(-\bar{q}SC_L - F_{prop}\sin\alpha + mg_z^w\right) + q - \tan\beta(p\cos\alpha + r\sin\alpha) \tag{C.0.14}$$

$$\dot{\beta} = \frac{1}{mV_T}\left(\bar{q}SC_Y - F_{prop}\cos\alpha\sin\beta + mg_y^w\right) + p\sin\alpha - r\cos\alpha \tag{C.0.15}$$

Stellenbosch University https://scholar.sun.ac.za

Appendix D

Linearisation of the Aircraft Model

D.1 Partial Derivatives of the Elements of the State Matrices

$$\begin{aligned} A_{VV} =& \frac{\partial}{\partial V_T}\dot{V}_T\bigg|_{\boldsymbol{x}_0,\boldsymbol{u}_0} \\ =& \frac{1}{m}\left[-\frac{\partial}{\partial V_T}\left(\frac{\rho V_T^2}{2}SC_D\right) + F_{prop}\frac{\partial}{\partial V_T}\left(\frac{u}{V_T}\right)\right] \\ =& -\frac{1}{m}\left[\rho S V_0 C_D + \bar{q}SC_{D_V}\right] - \frac{F_{prop}\cos\alpha_0\cos\beta_0}{mV_0} \end{aligned} \tag{D.1.1}$$

$$\begin{aligned} A_{V\alpha} =& \frac{\partial}{\partial \alpha}\dot{V}_T\bigg|_{\boldsymbol{x}_0,\boldsymbol{u}_0} \\ =& \frac{1}{m}\left[-\frac{\partial}{\partial \alpha}(\bar{q}SC_D) + F_{prop}\frac{\partial}{\partial \alpha}(\cos\alpha)\cos\beta\right] + \frac{\partial}{\partial \alpha}(g_x^w) \\ =& -\frac{\bar{q}S}{m}\cdot\frac{2C_{L_0}}{\pi Ae}\cdot C_{L_\alpha} - \frac{F_{prop}\sin\alpha_0\cos\beta_0}{m} \\ &+ g(\cos\alpha_0\cos\beta_0\cos\phi_0\cos\theta_0 + \sin\alpha_0\cos\beta_0\sin\theta_0) \end{aligned} \tag{D.1.2}$$

$$\begin{aligned} A_{V\beta} =& \frac{\partial}{\partial \beta}\dot{V}_T\bigg|_{\boldsymbol{x}_0,\boldsymbol{u}_0} \\ =& -\frac{F_{prop}\cos\alpha_0\sin\beta_0}{m} \\ &+ g(-\sin\alpha_0\sin\beta_0\cos\phi_0\cos\theta_0 + \cos\beta_0\sin\phi_0\cos\theta_0 + \cos\alpha_0\sin\beta_0\sin\theta_0) \end{aligned} \tag{D.1.3}$$

Stellenbosch University https://scholar.sun.ac.za

$$A_{V_q} = \frac{\partial}{\partial q}\dot{V}_T\bigg|_{\boldsymbol{x}_0,\boldsymbol{u}_0} = -\frac{\bar{q}S\bar{c}}{mV_0}\cdot\frac{C_{L_0}}{\pi Ae}\cdot C_{L_q} \tag{D.1.4}$$

$$A_{V_\phi} = \frac{\partial}{\partial \phi}\dot{V}_T\bigg|_{\boldsymbol{x}_0,\boldsymbol{u}_0} = g(-\sin\alpha_0\cos\beta_0\cos\theta_0\sin\phi_0 + \sin\beta_0\cos\theta_0\cos\phi_0) \tag{D.1.5}$$

$$A_{V_\theta} = \frac{\partial}{\partial \theta}\dot{V}_T\bigg|_{\boldsymbol{x}_0,\boldsymbol{u}_0} = -g(\sin\alpha_0\cos\beta_0\cos\phi_0\sin\theta_0 + \sin\beta_0\sin\phi_0\sin\theta_0 + \cos\alpha_0\cos\beta_0\cos\theta_0) \tag{D.1.6}$$

$$B_{V_{\delta_T}} = \frac{\partial}{\partial \delta_T}\dot{V}_T\bigg|_{\boldsymbol{x}_0,\boldsymbol{u}_0} = \frac{\cos\alpha_0\cos\beta_0}{m} \tag{D.1.7}$$

$$B_{V_{\delta_{Ei}}} = \frac{\partial}{\partial \delta_{Ei}}\dot{V}_T\bigg|_{\boldsymbol{x}_0,\boldsymbol{u}_0} = \frac{\bar{q}S}{m}\left[-\frac{2C_L}{\pi Ae}\right]C_{L_{\delta_{Ei}}} \tag{D.1.8}$$

$$B_{V_{\delta_{Ai}}} = \frac{\partial}{\partial \delta_{Ai}}\dot{V}_T\bigg|_{\boldsymbol{x}_0,\boldsymbol{u}_0} = \frac{\bar{q}S}{m}\left[-\frac{2C_L}{\pi Ae}\right]C_{L_{\delta_{Ai}}} \tag{D.1.9}$$

$$A_{\alpha V} = \frac{\partial}{\partial V_T}\dot{\alpha}\bigg|_{\boldsymbol{x}_0,\boldsymbol{u}_0} = \frac{-1}{mV_0\cos\beta_0}\left[\bar{q}SC_L - F_{prop}\sin\alpha_0 + mg(\sin\alpha_0\sin\theta_0 + \cos\alpha_0\cos\phi_0\cos\theta_0)\right] \tag{D.1.10}$$

$$A_{\alpha\alpha} = \frac{\partial}{\partial \alpha}\dot{\alpha}\bigg|_{\boldsymbol{x}_0,\boldsymbol{u}_0} = \frac{-1}{mV_0\cos\beta_0}\left[\bar{q}SC_{L_\alpha} + F_{prop}\cos\alpha_0 + mg(\sin\alpha_0\cos\phi_0\cos\theta_0 - \cos\alpha_0\sin\theta_0)\right] + (p_0\sin\alpha_0 - r_0\cos\alpha_0)\tan\beta_0 \tag{D.1.11}$$

Stellenbosch University https://scholar.sun.ac.za

$$\begin{aligned} A_{\alpha\beta} =& \frac{\partial}{\partial\beta}\dot{\alpha}\bigg|_{\boldsymbol{x}_0,\boldsymbol{u}_0} \\ =& \frac{-\sin\beta_0}{mV_0\cos^2\beta_0}\left[\bar{q}SC_L + F_{prop}\sin\alpha_0 - mg(\cos\alpha_0\cos\phi_0\cos\theta_0 + \sin\alpha_0\sin\theta_0)\right] \\ & - \frac{(p_0\cos\alpha_0 + r_0\sin\alpha_0)}{\cos^2\beta_0} \end{aligned} \tag{D.1.12}$$

$$\begin{aligned} A_{\alpha p} =& \frac{\partial}{\partial p}\dot{\alpha}\bigg|_{\boldsymbol{x}_0,\boldsymbol{u}_0} \\ =& -\cos\alpha_0\tan\beta_0 \end{aligned} \tag{D.1.13}$$

$$\begin{aligned} A_{\alpha q} =& \frac{\partial}{\partial}\dot{\alpha}\bigg|_{\boldsymbol{x}_0,\boldsymbol{u}_0} \\ =& 1 - \frac{\bar{q}S\bar{c}}{2mV_0^2\cos\beta_0}C_{L_q} \end{aligned} \tag{D.1.14}$$

$$\begin{aligned} A_{\alpha r} =& \frac{\partial}{\partial r}\dot{\alpha}\bigg|_{\boldsymbol{x}_0,\boldsymbol{u}_0} \\ =& -\sin\alpha_0\tan\beta_0 \end{aligned} \tag{D.1.15}$$

$$\begin{aligned} A_{\alpha\theta} =& \frac{\partial}{\partial\theta}\dot{\alpha}\bigg|_{\boldsymbol{x}_0,\boldsymbol{u}_0} \\ =& \frac{g}{V_0\cos\beta_0}\left[\sin\alpha_0\cos\theta_0 - \cos\alpha_0\cos\phi_0\cos\theta_0\right] \end{aligned} \tag{D.1.16}$$

$$\begin{aligned} A_{\alpha\phi} =& \frac{\partial}{\partial\phi}\dot{\alpha}\bigg|_{\boldsymbol{x}_0,\boldsymbol{u}_0} \\ =& \frac{-g}{V_0\cos\beta_0}\cos\alpha_0\sin\phi_0\cos\theta_0 \end{aligned} \tag{D.1.17}$$

$$\begin{aligned} B_{\alpha\delta_T} =& \frac{\partial}{\partial\delta_T}\dot{\alpha}\bigg|_{\boldsymbol{x}_0,\boldsymbol{u}_0} \\ =& -\frac{\sin\alpha_0}{mV_0\cos\beta_0} \end{aligned} \tag{D.1.18}$$

Stellenbosch University https://scholar.sun.ac.za

$$\begin{aligned} B_{\alpha\delta_{Ei}} =& \frac{\partial}{\partial \delta_{Ei}} \dot{\alpha} \Big|_{\boldsymbol{x}_0, \boldsymbol{u}_0} \\ =& -\frac{\bar{q}S}{mV_0 \cos\beta_0} C_{L_{\delta_{Ei}}} \end{aligned} \tag{D.1.19}$$

$$\begin{aligned} B_{\alpha\delta_{Ai}} =& \frac{\partial}{\partial \delta_{Ai}} \dot{\alpha} \Big|_{\boldsymbol{x}_0, \boldsymbol{u}_0} \\ =& -\frac{\bar{q}S}{mV_0 \cos\beta_0} C_{L_{\delta_{Ai}}} \end{aligned} \tag{D.1.20}$$

$$\begin{aligned} A_{\beta V} =& \frac{\partial}{\partial V_T} \dot{\beta} \Big|_{\boldsymbol{x}_0, \boldsymbol{u}_0} \\ =& \frac{\bar{q}SC_Y}{mV_0^2} + \frac{\bar{q}SC_{Y_V}}{mV_0} + \frac{F_{prop}\cos\alpha_0 \sin\beta_0}{mV_0^2} \end{aligned} \tag{D.1.21}$$

$$\begin{aligned} A_{\beta\alpha} =& \frac{\partial}{\partial \alpha} \dot{\beta} \Big|_{\boldsymbol{x}_0, \boldsymbol{u}_0} \\ =& \frac{F_{prop}\sin\alpha_0 \sin\beta_0}{mV_0} + p_0 \cos\alpha_0 + r_0 \sin\alpha_0 \\ & - \frac{g}{V_0}(\sin\alpha_0 \sin\beta_0 \sin\theta_0 + \cos\alpha_0 \sin\beta_0 \cos\theta_0 \cos\phi_0) \end{aligned} \tag{D.1.22}$$

$$\begin{aligned} A_{\beta\beta} =& \frac{\partial}{\partial \beta} \dot{\beta} \Big|_{\boldsymbol{x}_0, \boldsymbol{u}_0} \\ =& \frac{\bar{q}S}{mV_0} \cdot C_{Y_\beta} - \frac{F_{prop}\cos\alpha_0 \cos\beta_0}{mV_0} \\ & + \frac{g}{V_0}(\cos\alpha_0 \cos\beta_0 \sin\theta_0 - \sin\beta_0 \cos\theta_0 \sin\phi_0 - \sin\alpha_0 \cos\beta_0 \cos\theta_0 \cos\phi_0) \end{aligned} \tag{D.1.23}$$

$$\begin{aligned} A_{\beta p} =& \frac{\partial}{\partial p} \dot{\beta} \Big|_{\boldsymbol{x}_0, \boldsymbol{u}_0} \\ =& \frac{\bar{q}Sb}{2mV_0^2} \cdot C_{Y_p} + \sin\alpha_0 \end{aligned} \tag{D.1.24}$$

$$\begin{aligned} A_{\beta r} =& \frac{\partial}{\partial r} \dot{\beta} \Big|_{\boldsymbol{x}_0, \boldsymbol{u}_0} \\ =& \frac{\bar{q}Sb}{2mV_0^2} \cdot C_{Y_r} - \cos\alpha_0 \end{aligned} \tag{D.1.25}$$

Stellenbosch University https://scholar.sun.ac.za

$$\begin{aligned} A_{\beta\theta} =& \frac{\partial}{\partial\theta}\dot{\beta}\bigg|_{\boldsymbol{x}_0,\boldsymbol{u}_0} \\ =& \frac{g}{V_0}(\cos\alpha_0 \sin\beta_0 \cos\theta_0 - \cos\beta_0 \sin\theta_0 \sin\phi_0 + \sin\alpha_0 \sin\beta_0 \sin\theta_0 \cos\phi_0) \end{aligned} \tag{D.1.26}$$

$$\begin{aligned} A_{\beta\phi} =& \frac{\partial}{\partial\phi}\dot{\beta}\bigg|_{\boldsymbol{x}_0,\boldsymbol{u}_0} \\ =& \frac{g}{V_0}(\cos\beta_0 \cos\theta_0 \cos\phi_0 + \sin\alpha_0 \sin\beta_0 \cos\theta_0 \sin\phi_0) \end{aligned} \tag{D.1.27}$$

$$\begin{aligned} B_{\beta\delta_T} =& \frac{\partial}{\partial\delta_T}\dot{\beta}\bigg|_{\boldsymbol{x}_0,\boldsymbol{u}_0} \\ =& \frac{-\cos\alpha_0 \sin\beta_0}{mV_0} \end{aligned} \tag{D.1.28}$$

$$\begin{aligned} B_{\beta\delta_{Ei}} =& \frac{\partial}{\partial\delta_{Ei}}\dot{\beta}\bigg|_{\boldsymbol{x}_0,\boldsymbol{u}_0} \\ =& \frac{\bar{q}S}{mV_0}\cdot C_{Y_{\delta_{Ei}}} \end{aligned} \tag{D.1.29}$$

$$\begin{aligned} B_{\beta\delta_{Ai}} =& \frac{\partial}{\partial\delta_{Ai}}\dot{\beta}\bigg|_{(\boldsymbol{x}_0,\boldsymbol{u}_0)} \\ =& \frac{\bar{q}S}{mV_0}\cdot C_{Y_{\delta_{Ai}}} \end{aligned} \tag{D.1.30}$$

$$\begin{aligned} B_{\beta\delta_{Ri}} =& \frac{\partial}{\partial\delta_{Ri}}\dot{\beta}\bigg|_{\boldsymbol{x}_0,\boldsymbol{u}_0} \\ =& \frac{\bar{q}S}{mV_0}\cdot C_{Y_{\delta_{Ri}}} \end{aligned} \tag{D.1.31}$$

$$\begin{aligned} A_{pV} =& \frac{\partial}{\partial V_T}\dot{p}\bigg|_{\boldsymbol{x}_0,\boldsymbol{u}_0} \\ =& \frac{Sb}{I_D}\left[I_z(\rho V_0 C_l + \bar{q}C_{l_V}) + I_{xz}(\rho V_0 C_n + \bar{q}C_{n_V})\right] \end{aligned} \tag{D.1.32}$$

$$\begin{aligned} A_{p\beta} =& \frac{\partial}{\partial\beta}\dot{p}\bigg|_{\boldsymbol{x}_0,\boldsymbol{u}_0} \\ =& \frac{\bar{q}Sb}{I_D}\left[I_z C_{l_\beta} + I_{xz}C_{n_\beta}\right] \end{aligned} \tag{D.1.33}$$

Stellenbosch University https://scholar.sun.ac.za

$$\begin{aligned} A_{pp} =& \frac{\partial}{\partial p}\dot{p}\bigg|_{\boldsymbol{x}_0,\boldsymbol{u}_0} \\ =& \frac{I_{xz}(I_x - I_y + I_z)q_0}{I_D} + \frac{\bar{q}Sb^2}{2I_D V_0}\left[I_z C_{l_p} + I_{xz} C_{n_p}\right] \end{aligned} \tag{D.1.34}$$

$$\begin{aligned} A_{pq} =& \frac{\partial}{\partial q}\dot{p}\bigg|_{\boldsymbol{x}_0,\boldsymbol{u}_0} \\ =& \frac{1}{I_D}\left[I_{xz}(I_x - I_y + I_z)p_0 - \left(I_z(I_z - I_y) + I_{xz}^2\right) r_0\right] \end{aligned} \tag{D.1.35}$$

$$\begin{aligned} A_{pr} =& \frac{\partial}{\partial r}\dot{p}\bigg|_{\boldsymbol{x}_0,\boldsymbol{u}_0} \\ =& -\frac{\left[I_z(I_z - I_y) + I_{xz}^2\right] q_0}{I_D} + \frac{\bar{q}Sb^2}{2I_D V_0}\left[I_z C_{l_r} + I_{xz} C_{n_r}\right] \end{aligned} \tag{D.1.36}$$

$$\begin{aligned} B_{p\delta_{Ei}} =& \frac{\partial}{\partial \delta_{Ei}}\dot{p}\bigg|_{\boldsymbol{x}_0,\boldsymbol{u}_0} \\ =& \frac{\bar{q}Sb}{I_D}\left[I_z C_{l_{\delta_{Ei}}} + I_{xz} C_{n_{\delta_{Ei}}}\right] \end{aligned} \tag{D.1.37}$$

$$\begin{aligned} B_{p\delta_{Ai}} =& \frac{\partial}{\partial \delta_{Ai}}\dot{p}\bigg|_{\boldsymbol{x}_0,\boldsymbol{u}_0} \\ =& \frac{\bar{q}Sb}{I_D}\left[I_z C_{l_{\delta_{Ai}}} + I_{xz} C_{n_{\delta_{Ai}}}\right] \end{aligned} \tag{D.1.38}$$

$$\begin{aligned} B_{p\delta_{Ri}} =& \frac{\partial}{\partial \delta_{Ri}}\dot{p}\bigg|_{\boldsymbol{x}_0,\boldsymbol{u}_0} \\ =& \frac{\bar{q}Sb}{I_D}\left[I_z C_{l_{\delta_{Ri}}} + I_{xz} C_{n_{\delta_{Ri}}}\right] \end{aligned} \tag{D.1.39}$$

$$\begin{aligned} A_{qV} =& \frac{\partial}{\partial V_T}\dot{q}\bigg|_{\boldsymbol{x}_0,\boldsymbol{u}_0} \\ =& 2\frac{\bar{q}S\bar{c}}{I_y V_0} C_{m_0} \end{aligned} \tag{D.1.40}$$

$$\begin{aligned} A_{q\alpha} =& \frac{\partial}{\partial \alpha}\dot{q}\bigg|_{\boldsymbol{x}_0,\boldsymbol{u}_0} \\ =& \frac{\bar{q}S\bar{c}}{I_y} C_{m_\alpha} \end{aligned} \tag{D.1.41}$$

Stellenbosch University https://scholar.sun.ac.za

$$A_{qp} = \frac{\partial}{\partial p}\dot{q}\bigg|_{\boldsymbol{x}_0,\boldsymbol{u}_0}$$
$$= \frac{1}{I_y}\left[(I_z - I_x)r_0 - 2p_0 I_{xz}\right] \tag{D.1.42}$$

$$A_{qq} = \frac{\partial}{\partial q}\dot{q}\bigg|_{\boldsymbol{x}_0,\boldsymbol{u}_0}$$
$$= \frac{\bar{q}S\bar{c}}{I_y}\cdot\frac{\bar{c}}{2V_0}C_{m_q} \tag{D.1.43}$$

$$A_{qr} = \frac{\partial}{\partial p}\dot{r}\bigg|_{\boldsymbol{x}_0,\boldsymbol{u}_0}$$
$$= \frac{1}{I_y}\left[(I_z - I_x)p_0 + 2r_0 I_{xz}\right] \tag{D.1.44}$$

$$B_{q\delta_{Ei}} = \frac{\partial}{\partial \delta_{Ei}}\dot{p}\bigg|_{\boldsymbol{x}_0,\boldsymbol{u}_0}$$
$$= \frac{\bar{q}S\bar{c}}{I_y}C_{m_{\delta_{Ei}}} \tag{D.1.45}$$

$$B_{q\delta_{Ai}} = \frac{\partial}{\partial \delta_{Ai}}\dot{p}\bigg|_{\boldsymbol{x}_0,\boldsymbol{u}_0}$$
$$= \frac{\bar{q}S\bar{c}}{I_y}C_{m_{\delta_{Ai}}} \tag{D.1.46}$$

$$A_{rV} = \frac{\partial}{\partial V_T}\dot{r}\bigg|_{\boldsymbol{x}_0,\boldsymbol{u}_0}$$
$$= \frac{Sb}{I_D}\left[I_{xz}(\rho V_0 C_l + \bar{q}C_{l_V}) + I_x(\rho V_0 C_n + \bar{q}C_{n_V})\right] \tag{D.1.47}$$

$$A_{r\beta} = \frac{\partial}{\partial \beta}\dot{r}\bigg|_{\boldsymbol{x}_0,\boldsymbol{u}_0}$$
$$= \frac{\bar{q}Sb}{I_D}\left[I_{xz}C_{l_\beta} + I_x C_{n_\beta}\right] \tag{D.1.48}$$

$$A_{rp} = \frac{\partial}{\partial p}\dot{r}\bigg|_{\boldsymbol{x}_0,\boldsymbol{u}_0}$$
$$= \frac{\left[I_x(I_x - I_y) + I_{xz}^2\right]q_0}{I_D} + \frac{\bar{q}Sb^2}{2I_D V_0}\left[I_{xz}C_{l_p} + I_x C_{n_p}\right] \tag{D.1.49}$$

Stellenbosch University https://scholar.sun.ac.za

$$\begin{aligned} A_{rq} =& \frac{\partial}{\partial q}\dot{r}\bigg|_{\boldsymbol{x}_0,\boldsymbol{u}_0} \\ =& \frac{1}{I_D}\left[\left(I_x(I_x - I_y) + I_{xz}^2\right)p_0 - I_{xz}(I_x - I_y + I_z)r_0\right] \end{aligned} \tag{D.1.50}$$

$$\begin{aligned} A_{rr} =& \frac{\partial}{\partial r}\dot{r}\bigg|_{\boldsymbol{x}_0,\boldsymbol{u}_0} \\ =& -\frac{I_{xz}(I_x - I_y + I_z)q_0}{I_D} + \frac{\bar{q}Sb^2}{2I_D V_0}\left[I_{xz}C_{l_r} + I_x C_{n_r}\right] \end{aligned} \tag{D.1.51}$$

$$\begin{aligned} B_{r\delta_{Ei}} =& \frac{\partial}{\partial \delta_{Ei}}\dot{r}\bigg|_{\boldsymbol{x}_0,\boldsymbol{u}_0} \\ =& \frac{\bar{q}Sb}{I_D}\left[I_{xz}C_{l_{\delta_{Ei}}} + I_x C_{n_{\delta_{Ei}}}\right] \end{aligned} \tag{D.1.52}$$

$$\begin{aligned} B_{r\delta_{Ai}} =& \frac{\partial}{\partial \delta_{Ai}}\dot{r}\bigg|_{\boldsymbol{x}_0,\boldsymbol{u}_0} \\ =& \frac{\bar{q}Sb}{I_D}\left[I_{xz}C_{l_{\delta_{Ai}}} + I_x C_{n_{\delta_{Ai}}}\right] \end{aligned} \tag{D.1.53}$$

$$\begin{aligned} B_{r\delta_{Ri}} =& \frac{\partial}{\partial \delta_{Ri}}\dot{r}\bigg|_{\boldsymbol{x}_0,\boldsymbol{u}_0} \\ =& \frac{\bar{q}Sb}{I_D}\left[I_{xz}C_{l_{\delta_{Ri}}} + I_x C_{n_{\delta_{Ri}}}\right] \end{aligned} \tag{D.1.54}$$

$$\begin{aligned} A_{\theta q} =& \frac{\partial}{\partial q}\dot{\theta}\bigg|_{\boldsymbol{x}_0,\boldsymbol{u}_0} \\ =& \cos\phi_0 \end{aligned} \tag{D.1.55}$$

$$\begin{aligned} A_{\theta r} =& \frac{\partial}{\partial r}\dot{\theta}\bigg|_{\boldsymbol{x}_0,\boldsymbol{u}_0} \\ =& -\sin\phi_0 \end{aligned} \tag{D.1.56}$$

$$\begin{aligned} A_{\theta\phi} =& \frac{\partial}{\partial \phi}\dot{\theta}\bigg|_{\boldsymbol{x}_0,\boldsymbol{u}_0} \\ =& -q_0\sin\phi_0 - r_0\cos\phi_0 \end{aligned} \tag{D.1.57}$$

Stellenbosch University https://scholar.sun.ac.za

$$A_{\phi p} = \frac{\partial}{\partial p}\dot{\phi}\bigg|_{\mathbf{x}_0,\mathbf{u}_0} = 1 \tag{D.1.58}$$

$$A_{\phi q} = \frac{\partial}{\partial q}\dot{\phi}\bigg|_{\mathbf{x}_0,\mathbf{u}_0} = \sin\phi_0 \tan\theta_0 \tag{D.1.59}$$

$$A_{\phi r} = \frac{\partial}{\partial r}\dot{\phi}\bigg|_{\mathbf{x}_0,\mathbf{u}_0} = \cos\phi_0 \tan\theta_0 \tag{D.1.60}$$

$$A_{\phi\theta} = \frac{\partial}{\partial \theta}\dot{\phi}\bigg|_{\mathbf{x}_0,\mathbf{u}_0} = \frac{q_0 \sin\phi_0 + r_0 \cos\phi_0}{\cos^2\theta_0} \tag{D.1.61}$$

$$A_{\phi\phi} = \frac{\partial}{\partial \phi}\dot{\phi}\bigg|_{\mathbf{x}_0,\mathbf{u}_0} = q_0 \cos\phi_0 \tan\theta_0 - r_0 \sin\phi_0 \tan\theta_0 \tag{D.1.62}$$

$$A_{zV} = \frac{\partial}{\partial V_T}\dot{z}\bigg|_{\mathbf{x}_0,\mathbf{u}_0} = -\cos\alpha_0 \cos\beta_0 \sin\theta_0 + \sin\beta_0 \sin\phi_0 \cos\theta_0 + \sin\alpha_0 \cos\beta_0 \cos\phi_0 \cos\theta_0 \tag{D.1.63}$$

$$A_{z\alpha} = \frac{\partial}{\partial \alpha}\dot{z}\bigg|_{\mathbf{x}_0,\mathbf{u}_0} = V_0\left(\sin\alpha_0 \cos\beta_0 \sin\theta_0 + \cos\alpha_0 \cos\beta_0 \cos\phi_0 \cos\theta_0\right) \tag{D.1.64}$$

$$A_{z\beta} = \frac{\partial}{\partial \beta}\dot{z}\bigg|_{\mathbf{x}_0,\mathbf{u}_0} = V_0\left(\cos\alpha_0 \sin\beta_0 \sin\theta_0 + \cos\beta_0 \sin\phi_0 \cos\theta_0 - \sin\alpha_0 \sin\beta_0 \cos\phi_0 \cos\theta_0\right) \tag{D.1.65}$$

Stellenbosch University https://scholar.sun.ac.za

$$\begin{aligned} A_{z\theta} =& \frac{\partial}{\partial \theta} \dot{z} \Big|_{\boldsymbol{x}_0, \boldsymbol{u}_0} \\ =& - V_0 \left(\cos \alpha_0 \cos \beta_0 \cos \theta_0 + \sin \beta_0 \sin \phi_0 \sin \theta_0 + \sin \alpha_0 \cos \beta_0 \cos \phi_0 \sin \theta_0 \right) \end{aligned} \tag{D.1.66}$$

$$\begin{aligned} A_{z\phi} =& \frac{\partial}{\partial \phi} \dot{z} \Big|_{\boldsymbol{x}_0, \boldsymbol{u}_0} \\ =& V_0 \left(\sin \beta_0 \cos \phi_0 \cos \theta_0 - \sin \alpha_0 \cos \beta_0 \sin \phi_0 \cos \theta_0 \right) \end{aligned} \tag{D.1.67}$$

Stellenbosch University https://scholar.sun.ac.za

Appendix E

The Kalman Filter Innovation Sequence

E.1 Normalised Innovation Squared

For a multi-output model, define

$$\eta_k = \boldsymbol{M}_k \tilde{\boldsymbol{r}}_k \tag{E.1.1}$$

The mean of $\boldsymbol{\eta}_k$ is $E\{\boldsymbol{\eta}_k\} = E\{\boldsymbol{M}_k \tilde{\boldsymbol{r}}_k\} = 0$
The covariance of $\boldsymbol{\eta}_k$ is $\boldsymbol{S}_{\eta,k} = E\{\boldsymbol{M}_k \tilde{\boldsymbol{r}}_k \tilde{\boldsymbol{r}}_k^T \boldsymbol{M}_k^T\} = \boldsymbol{M}_k \tilde{S}_k \boldsymbol{M}_k^T$
Since it is a linear $\boldsymbol{\eta}_k$ is a combination of Gaussians, then it is also Gaussian

If $\boldsymbol{M}_k$ is defined such that $\boldsymbol{M}_k^T \boldsymbol{M}_k = \tilde{S}_k^{-1}$, then

- $\boldsymbol{M}_k$ is the lower-triangular Cholesky factor of $\tilde{S}_k^{-1}$
- And we have $\boldsymbol{\eta}_k \sim \mathcal{N}(\boldsymbol{0},\, \boldsymbol{I})$ because

$$\boldsymbol{S}_{\eta,k} = \boldsymbol{M}_k (\boldsymbol{M}_k^T \boldsymbol{M}_k)^{-1} \boldsymbol{M}_k^T = \boldsymbol{M}_k \boldsymbol{M}_k^{-1} \boldsymbol{M}_k^{-T} \boldsymbol{M}_k^T = \boldsymbol{I} \tag{E.1.2}$$

If we further compute normalized innovation squared

$$\beta_k = \sum_{j=k-M+1}^{k} \boldsymbol{\eta}_k^T \boldsymbol{\eta}_k = \sum_{j=k-M+1}^{k} \tilde{\boldsymbol{r}}_k^T \tilde{\boldsymbol{S}}_k^{-1} \tilde{\boldsymbol{r}}_k \tag{E.1.3}$$

then β_k is the sum of squares of independent $\mathcal{N}(0,1)$ random variables. Then, β_k is a chi-square random variable with n degrees of freedom, where n is the dimension of the innovation vector.

Stellenbosch University https://scholar.sun.ac.za

E.2 Sensor Isolation and NIS Shifts

Using (4.10.3), it can be shown that the NIS's variation is predictable. Consider a shift in NIS at time τ, and that $\tilde{\boldsymbol{\eta}}_k$ signify the unchanged normalized innovation sequence, then the changed normalized innovation sequence is given by

$$\boldsymbol{\eta}_k = \tilde{\boldsymbol{\eta}}_k \quad k = 1, 2, \ldots, \tau - 1 \tag{E.2.1}$$

$$\boldsymbol{\eta}_k = \tilde{\boldsymbol{\eta}}_k + \boldsymbol{\mu}_{k-\tau} \quad k = \tau, \tau + 1, \ldots \tag{E.2.2}$$

where $\mu(.)$ is an unknown change and may vary with respect to time, but there exists a quantity $L > 0$ such that $|\mu(j)| < L, \forall j$. The above yield,

$$\boldsymbol{\eta}_k \sim \mathcal{N}(0, 1) \quad k = 1, 2, \ldots, \tau - 1 \tag{E.2.3}$$

$$\boldsymbol{\eta}_k \sim \mathcal{N}(0, 1) + \boldsymbol{\mu}_{k-\tau} \quad k = \tau, \tau + 1, \ldots \tag{E.2.4}$$

Consider that the window from $j = k \grave{} M + 1$ to k is given by N. Given that $k < \tau$ then the expectation is $E\{v\} = M \grave{} 1$ In the event of a fault, this expectation of can be determined by the following theorem. Theorem: When $k \geq \tau$, i.e. the hypothesis $\mathcal{H}_1$ is true, the following equation is also true,

$$E\{v_k\} = (M-1)\sigma^2 + E\left\{ \sum_{j=k-M+1}^{k} \left(\mu_{j-\tau} - \frac{\sum_{j=k-M+1}^{k} \mu_{j-\tau}}{M} \right)^2 \right\} \tag{E.2.5}$$

$$\mu_{j-\tau} = \begin{cases} 0 & j < \tau \\ \mu^* = \text{constant} & j \geq \tau \end{cases}$$

The proof is given in

Let the number of shifted innovation values from$j = k \grave{} M + 1$ to k in a window be denoted by N. If $N < M$, then

$$\left(\mu_{j-\tau} - \frac{\sum_{j=k-M+1}^{k} \mu_{j-\tau}}{M} \right)^2 = \left(\mu_{j-\tau} - \frac{N\mu^*}{M} \right)^2 \geq 0 \tag{E.2.6}$$

and a shift in the innovation sequence will cause an asymptotic increase in the expected value of the statistics v_k , and v_k will exceed the threshold $\chi^2_{\alpha,M-1}$. The larger μ^* the faster detection is.

The optimal (maximum) value N is $N = M/2$

Stellenbosch University https://scholar.sun.ac.za

Bibliography

[1] Coordinated, A.: Risk-based approach to improving global aviation safety/2011 state of global aviation safety. *ICAO-Montreal, Quebec, Canada*, vol. 80, 2011.

[2] Zolghadri, A., Henry, D., Cieslak, J., Efimov, D. Goupil, P.: *Fault diagnosis and fault-tolerant control and guidance for aerospace vehicles*. Springer, 2014.

[3] Odendaal, H.M.: *An analysis and comparison of two methods for UAV actuator fault detection and isolation*. Ph.D. thesis, Stellenbosch: Stellenbosch University, 2012.

[4] Bateman, F., Noura, H. Ouladsine, M.: Fault diagnosis and fault-tolerant control strategy for the aerosonde UAV. *IEEE Transactions on Aerospace and Electronic Systems*, vol. 47, no. 3, pp. 2119–2137, 2011.

[5] Continous, D.W.T.M.: Mathworks.

[6] Circular, I.: 328, unmanned aircraft systems (uas). *Montreal, Canada: International Civil Aviation Organization (ICAO)*, 2011.

[7] Tice, B.P.: Unmanned aerial vehicles: The force multiplier of the 1990s. *Airpower Journal*, vol. 5, no. 1, pp. 41–55, 1991.

[8] Tsach, S., Peled, A., Penn, D., Keshales, B. Guedj, R.: Development trends for next generation of UAV systems. In: *AIAA Infotech@ Aerospace 2007 Conference and Exhibit*, p. 2762. 2007.

[9] Group, E.R.P.A.S.S. *et al.*: Roadmap for the integration of civil remotely-piloted aircraft systems into the European Aviation System. *Final report from the European RPAS Steering Group*, 2013.

Stellenbosch University https://scholar.sun.ac.za

[10] of Transportation, U.D.: *Integration of Civil Unmanned Aircraft Systems (UAS) in the National Airspace System (NAS) Roadmap*. CreateSpace Independent Publishing Platform, 2015. ISBN 9781511523226.

[11] Undertaking, S.J.: U-space blueprint. *SESAR Joint Undertaking. Accessed September*, vol. 18, 2017.

[12] Undertaking, S.J.: European atm master plan: Roadmap for the safe integration of drones into all classes of airspace. *SESAR Joint Undertaking: Brussels, Belgium*, 2018.

[13] Murray, C.C. Chu, A.G.: The flying sidekick traveling salesman problem: Optimization of drone-assisted parcel delivery. *Transportation Research Part C: Emerging Technologies*, vol. 54, pp. 86–109, 2015.

[14] Welch, A.: A cost-benefit analysis of Amazon Prime Air. 2015.

[15] Agatz, N., Bouman, P. Schmidt, M.: Optimization approaches for the traveling salesman problem with drone. *Transportation Science*, 2018.

[16] Ingham, L.A.: *Considerations for a Roadmap for the Operation of Unmanned Aerial Vehicles (UAV) in South African Airspace, 2008*. Ph.D. thesis, PhD thesis in Universiteit Stellenbosch University, 2008.

[17] Maneschijn, A.: *A framework and criteria for the operability of Unmanned Aircraft Systems*. Ph.D. thesis, Stellenbosch: University of Stellenbosch, 2010.

[18] SACAA. `http://www.caa.co.za/`. Accessed: 2020-08-26.

[19] Weatherington, D. Deputy, U.: Unmanned aircraft systems roadmap, 2005-2030. *Deputy, UAV Planning Task Force, OUSD (AT&L)*, 2005.

[20] Burcham Jr, F.W., Maine, T.A., Fullerton, C.G. Webb, L.D.: Development and flight evaluation of an emergency digital flight control system using only engine thrust on an F-15 airplane. 1996.

[21] Belcastro, C. Foster, J.: Aircraft loss-of-control accident analysis. In: *AIAA Guidance, Navigation, and Control Conference*, p. 8004. 2010.

[22] Edwards, C., Lombaerts, T., Smaili, H. *et al.*: Fault tolerant flight control. *Lecture Notes in Control and Information Sciences*, vol. 399, pp. 1–560, 2010.

Stellenbosch University https://scholar.sun.ac.za

[23] Galison, P.: An accident of history. In: *Atmospheric flight in the twentieth century*, pp. 3–43. Springer, 2000.

[24] Aircraft Accident Report. Tech. Rep., National Trasnportation Safety Board, 1979.

[25] Peddle, I.K.: Fault Tolerant Control: Overview and Research at Stellenbosch University. . Tech. Rep., IASSA, 2009.

[26] Pietersen, W.H.: *System identification for fault tolerant control of unmanned aerial vehicles*. Ph.D. thesis, Stellenbosch: University of Stellenbosch, 2010.

[27] Basson, W.A.: *Fault tolerant adaptive control of an unmanned aerial vehicle*. Ph.D. thesis, Stellenbosch: Stellenbosch University, 2011.

[28] Basson, L.: *Control allocation as part of a fault-tolerant control architecture for UAVs*. Ph.D. thesis, Stellenbosch: University of Stellenbosch, 2011.

[29] Appel, J.-P.: *Online system identification for fault tolerant control of unmanned aerial vehicles*. Ph.D. thesis, Stellenbosch: Stellenbosch University, 2013.

[30] Hugo, G.: *Autonomous landing of a fixed-Wing unmanned aircraft with partialwing and stabiliser losses*. Ph.D. thesis, Stellenbosch: Stellenbosch University, 2017.

[31] Li, K. Chen, G.: Analysis of parachute recovery process for uav based on launch rocket. In: *IOP Conference Series: Materials Science and Engineering*, vol. 569, p. 032066. IOP Publishing, 2019.

[32] Bleier, M., Settele, F., Krauss, M., Knoll, A. Schilling, K.: Risk assessment of flight paths for automatic emergency parachute deployment in uavs. *IFAC-PapersOnLine*, vol. 48, no. 9, pp. 180–185, 2015.

[33] Mejias, L. Eng, P.: Controlled emergency landing of an unpowered unmanned aerial system. *Journal of Intelligent & Robotic Systems*, vol. 70, no. 1-4, pp. 421–435, 2013.

[34] Chen, J., Patton, R.J. Zhang, H.-Y.: Design of unknown input observers and robust fault detection filters. *International Journal of control*, vol. 63, no. 1, pp. 85–105, 1996.

Stellenbosch University https://scholar.sun.ac.za

[35] Basseville, M.: On fault detectability and isolability. *European Journal of Control*, vol. 7, no. 6, pp. 625–637, 2001.

[36] Parkum, J., Poulsen, N.K. Holst, J.: Selective forgetting in adaptive procedures. *IFAC Proceedings Volumes*, vol. 23, no. 8, pp. 137–142, 1990.

[37] Isermann, R. Balle, P.: Trends in the application of model-based fault detection and diagnosis of technical processes. *Control engineering practice*, vol. 5, no. 5, pp. 709–719, 1997.

[38] Zhang, Y. Jiang, J.: Bibliographical review on reconfigurable fault-tolerant control systems. *Annual reviews in control*, vol. 32, no. 2, pp. 229–252, 2008.

[39] Isermann, R.: Model-based fault-detection and diagnosis–status and applications. *Annual Reviews in control*, vol. 29, no. 1, pp. 71–85, 2005.

[40] Blanke, M., Kinnaert, M., Lunze, J., Staroswiecki, M. Schröder, J.: *Diagnosis and fault-tolerant control*, vol. 2. Springer, 2006.

[41] Bokor, J. Szabó, Z.: Fault detection and isolation in nonlinear systems. *Annual Reviews in Control*, vol. 33, no. 2, pp. 113–123, 2009.

[42] Ding, S.X.: *Model-based fault diagnosis techniques: design schemes, algorithms, and tools*. Springer Science & Business Media, 2008.

[43] Hwang, I., Kim, S., Kim, Y. Seah, C.E.: A survey of fault detection, isolation, and reconfiguration methods. *IEEE transactions on control systems technology*, vol. 18, no. 3, pp. 636–653, 2010.

[44] Venkatasubramanian, V., Rengaswamy, R., Kavuri, S.N. Yin, K.: A review of process fault detection and diagnosis: Part III: Process history based methods. *Computers & chemical engineering*, vol. 27, no. 3, pp. 327–346, 2003.

[45] Basseville, M., Nikiforov, I.V. *et al.*: *Detection of abrupt changes: theory and application*, vol. 104. Prentice Hall Englewood Cliffs, 1993.

[46] Patton, R.J., Frank, P.M. Clarke, R.N.: *Fault diagnosis in dynamic systems: theory and application*. Prentice-Hall, Inc., 1989.

[47] Patton, R.J. Chen, J.: A review of parity space approaches to fault diagnosis. *IFAC Proceedings Volumes*, vol. 24, no. 6, pp. 65–81, 1991.

Stellenbosch University https://scholar.sun.ac.za

[48] Chen, J. Patton, R.J.: *Robust model-based fault diagnosis for dynamic systems*, vol. 3. Springer Science & Business Media, 2012.

[49] Lunze, J. Richter, J.: Control reconfiguration: Survey of methods and open problems. *Ruhr–University, Bochum*, 2006.

[50] Goupil, P.: AIRBUS state of the art and practices on FDI and FTC in flight control system. *Control Engineering Practice*, vol. 19, no. 6, pp. 524–539, 2011.

[51] Yeh, Y.C.: Design considerations in Boeing 777 fly-by-wire computers. In: *High-Assurance Systems Engineering Symposium, 1998. Proceedings. Third IEEE International*, pp. 64–72. IEEE, 1998.

[52] Kinnan, L.M.: Use of multicore processors in avionics systems and its potential impact on implementation and certification. In: *Digital Avionics Systems Conference, 2009. DASC'09. IEEE/AIAA 28th*, pp. 1–E. IEEE, 2009.

[53] Takats, I.J. Chenoweth, C.C.: Multiple-voting fault detection system for flight critical actuation control systems. December 28 1993. US Patent 5,274,554.

[54] Kohlmeier-Beckmann, C. Kessler, J.: System and method for detecting faults in an aircraft electrical power system. January 20 2005. US Patent App. 10/894,869.

[55] Goupil, P.: Oscillatory failure case detection in the A380 electrical flight control system by analytical redundancy. *Control Engineering Practice*, vol. 18, no. 9, pp. 1110–1119, 2010.

[56] Bernard, D., Dorais, G., Gamble, E., Kanefsky, B., Kurien, J., Man, G., Millar, W., Muscettola, N., Nayak, P., Rajan, K. *et al.*: Spacecraft autonomy flight experience: The DS1 Remote Agent experiment. 1999.

[57] Straub, J.: A review of spacecraft AI control systems. In: *Proc. 15th World Multi-Conference on Systemics, Cybernetics and Informatics*. 2011.

[58] Shafto, M.G. Korsmeyer, D.J.: NASA's Contributions to Information Technology: A View From Ames Research Center.

[59] Roemer, M.J. Tang, L.: Integrated vehicle health and fault contingency management for UAVs. In: *Handbook of Unmanned Aerial Vehicles*, pp. 999–1025. Springer, 2015.

Stellenbosch University https://scholar.sun.ac.za

[60] Skardon, J.A.: The Apollo story: what the watchdogs missed. *Columbia Journalism Review*, vol. 6, pp. 11–15, 1967.

[61] Marzat, J., Piet-Lahanier, H., Damongeot, F. Walter, E.: Model-based fault diagnosis for aerospace systems: a survey. *Proceedings of the Institution of Mechanical Engineers, Part G: Journal of aerospace engineering*, vol. 226, no. 10, pp. 1329–1360, 2012.

[62] Sadeghzadeh, I. Zhang, Y.: A review on fault-tolerant control for unmanned aerial vehicles (UAVs). In: *Infotech@ Aerospace 2011*, p. 1472. 2011.

[63] Beard, R.V.: *Failure accomodation in linear systems through self-reorganization*. Ph.D. thesis, Massachusetts Institute of Technology, 1971.

[64] Zhang, Y.M.: Fault Detection and Diagnosis for NASA GTMUAV with Dual Unscented Kalman Filter. In: *Handbook of Unmanned Aerial Vehicles*, pp. 1157–1181. Springer, 2015.

[65] Chow, E.Y.E.Y. Willsky, A.S.: Analytical redundancy and the design of robust failure detection systems. *IEEE Transactions on automatic control*, vol. 29, no. 7, pp. 603–614, 1984.

[66] Gertler, J. Singer, D.: A New Structural Framework for Parity Equation-based Failure Detection. *Automatica*, vol. 26, no. 2, pp. 381–388, 1990.

[67] Gertler, J.J. Kunwer, M.M.: Optimal residual decoupling for robust fault diagnosis. *International Journal of Control*, vol. 61, no. 2, pp. 395–421, 1995.

[68] Delmaire, G., Cassar, J.-P. Staroswiecki, M.: Comparison of identification and parity space approaches for failure detection in single input single output systems. In: *IEEE Conf. On Control Applications, Glasgow, Grande-Bretagne*, pp. 865–870. 1994.

[69] Staroswiecki, M., Cassar, J.P. Cocquempot, V.: Generation of optimal structured residuals in the parity space. *IFAC Proceedings Volumes*, vol. 26, no. 2, pp. 535–542, 1993.

[70] Frank, P.M.: On-line fault detection in uncertain nonlinear systems using diagnostic observers: a survey. *International journal of systems science*, vol. 25, no. 12, pp. 2129–2154, 1994.

Stellenbosch University https://scholar.sun.ac.za

[71] Ducard, G.J.J.: *Fault-tolerant flight control and guidance systems: Practical methods for small unmanned aerial vehicles*. Springer Science & Business Media, 2009.

[72] Sobahni-Tehrani, E.: *Fault detection, isolation, and identification for nonlinear systems using a hybrid approach*. Ph.D. thesis, Concordia University, 2008.

[73] Wu, N.E., Zhang, Y. Zhou, K.: Control effectiveness estimation using an adaptive Kalman estimator. In: *Intelligent Control (ISIC), 1998. Held jointly with IEEE International Symposium on Computational Intelligence in Robotics and Automation (CIRA), Intelligent Systems and Semiotics (ISAS), Proceedings*, pp. 181–186. IEEE, 1998.

[74] Julier, S.J. Uhlmann, J.K.: New extension of the Kalman filter to nonlinear systems. In: *Signal processing, sensor fusion, and target recognition VI*, vol. 3068, pp. 182–194. International Society for Optics and Photonics, 1997.

[75] Julier, S.J., Uhlmann, J.K. Durrant-Whyte, H.F.: A new approach for filtering nonlinear systems. In: *American Control Conference, Proceedings of the 1995*, vol. 3, pp. 1628–1632. IEEE, 1995.

[76] Van Der Merwe, R. Wan, E.A.: The square-root unscented kalman filter for state and parameter-estimation. In: *2001 IEEE international conference on acoustics, speech, and signal processing. Proceedings (Cat. No. 01CH37221)*, vol. 6, pp. 3461–3464. IEEE, 2001.

[77] VanDyke, M.C., Schwartz, J.L., Hall, C.D. *et al.*: Unscented kalman filtering for spacecraft attitude state and parameter estimation. *Advances in the Astronautical Sciences*, vol. 118, no. 1, pp. 217–228, 2004.

[78] Nelson, R.C.: *Flight stability and automatic control*, vol. 2. WCB/McGraw Hill New York, 1998.

[79] Rogers, R.M.: *Applied mathematics in integrated navigation systems*. American Institute of Aeronautics and Astronautics, 2007.

[80] Zhang, Y. Li, X.R.: Detection and diagnosis of sensor and actuator failures using imm estimator. *IEEE Transactions on aerospace and electronic systems*, vol. 34, no. 4, pp. 1293–1313, 1998.

Stellenbosch University https://scholar.sun.ac.za

[81] Keller, J.-Y. Darouach, M.: Optimal two-stage kalman filter in the presence of random bias. *Automatica*, vol. 33, no. 9, pp. 1745–1748, 1997.

[82] Friedland, B.: Treatment of bias in recursive filtering. *IEEE Transactions on Automatic Control*, vol. 14, no. 4, pp. 359–367, 1969.

[83] Keller, J.-Y., Summerer, L. Darouach, M.: Extension of friedland's bias filtering technique to discrete-time systems with unknown inputs. *International journal of systems science*, vol. 27, no. 12, pp. 1219–1229, 1996.

[84] Ignagni, M.: An alternate derivation and extension of friendland's two-stage kalman estimator. *IEEE Transactions on Automatic Control*, vol. 26, no. 3, pp. 746–750, 1981.

[85] Ignagni, M.: Optimal and suboptimal separate-bias kalman estimators for a stochastic bias. *IEEE Transactions on Automatic Control*, vol. 45, no. 3, pp. 547–551, 2000.

[86] Almagbile, A., Wang, J. Ding, W.: Evaluating the performances of adaptive kalman filter methods in gps/ins integration. *Journal of Global Positioning Systems*, vol. 9, no. 1, pp. 33–40, 2010.

[87] Maybeck, P.S.: Multiple model adaptive algorithms for detecting and compensating sensor and actuator/surface failures in aircraft flight control systems. *International Journal of Robust and nonlinear control*, vol. 9, no. 14, pp. 1051–1070, 1999.

[88] Pisano, W. Lawrence, D.: Control limitations of small unmanned aerial vehicles in turbulent environments. In: *AIAA Guidance, Navigation, and Control Conference*, p. 5909. 2009.